Theoretical Simulation, Manufacture and Experimental Evaluation of a Free-Piston Stirling Engine Electric Generator

by
Bernabé Jean Gerard de la Bat

Dissertation presented for the degree of
Doctor of Philosophy in the Faculty of Engineering at
Stellenbosch University

Supervisor: Prof. T.M. Harms
Co-supervisors: Mr R.T. Dobson
Dr A.J. Bell

December 2019

Declaration

By submitting this dissertation electronically, I declare that the entirety of the work contained therein is my own, original work, that I am the sole author thereof (save to the extent explicitly otherwise stated), that reproduction and publication thereof by Stellenbosch University will not infringe any third party rights and that I have not previously in its entirety or in part submitted it for obtaining any qualification.

Date: December 2019

Abstract

Theoretical simulation, manufacture and experimental evaluation of a free-piston Stirling engine electric generator

B.J.G. de la Bat

A Stirling engine is a suitable candidate for heat and electrical power co-generation when integrated with a parabolic-dish solar concentrator. Such solar systems are envisaged as being a viable option for micro off-grid co-generation using smart energy control strategies in developing countries rich in solar irradiance. This dissertation presents the theoretical simulation, fabrication and experimental evaluation of a novel prototype free-piston Stirling engine electric generator.

The theoretical model was developed from first principles, by discretising the working fluid into a network of one-dimensional control volumes. By applying the conservation of mass, momentum and energy and applicable property functions to each control volume, a system of non-linear time-dependent partial differential equations was generated. These equations were solved sequentially using a fully-explicit numerical method with linear upwind-differencing and by employing a backwards-staggered velocity scheme. A transient electromagnetic finite element analysis of the linear generator was performed and is represented in the theoretical simulation model through generator characteristic functions. A novel experimental engine prototype was manufactured that includes a linear motor attached to the displacer shaft. Finite element analyses were used to design the strength and safety-critical mechanical components of the engine. The electromechanical, flexure spring stiffness and displacer and piston mechanical friction characterising equations of the theoretical model were matched to the as-built engine by direct experimentation. Seven selected experimental test runs were used to establish whether the theoretical model is capable of emulating the behaviour of the as-manufactured engine, with hot-end temperatures varied between 300 and 600 °C and working fluid charge pressures between 1.0 and 2.0 MPa. Self-sustained, closed-circuit operation of the engine was achieved at a hot-end temperature of 470 °C and charge pressure of 1.7 MPa absolute, with a peak electrical output power of approximately 73 W.

A good correlation between experimental and simulation results was demonstrated for several operating conditions, thereby validating the theoretical simulation model. It is concluded that it is critical to ensure proper alignment of the moving parts so that internal sliding friction may be minimised. To achieve continuous and sustained operation without piston-casing collisions, it is recommended that an electronic feedback control system be integrated to the existing engine.

Uittreksel

Teoretiese simulasie, vervaardiging and eksperimentele evaluering van 'n vry-suier Stirling enjin elektriese kragopwekker

B.J.G. de la Bat

'n Stirling enjin is 'n geskikte kandidaat vir gekombineerde warmte en elektriese kragopwekking tesame met die gebruik van 'n paraboliese sonkrag konsentreer skottel. Só 'n stelsel word beoog as 'n lewensvatbare oplossing vir mikro kragopwekking in ontwikkelende lande waar sonkrag vollop beskikbaar is. Hierdie proefskrif dokumenteer die teoretiese simulasie, vervaardiging en eksperimentele evaluering van 'n nuwe prototipe vry-suier Stirling enjin elektriese kragopwekker.

Die teoretiese simulasiemodel is vanuit eerste beginsels afgelei deur die werkvloeistof in 'n netwerk van eendimensionele kontrolevolumes te verdeel. Die beginsels van behoud van massa, momentum en energie, asook toepaslike eienskapsvergelykings is dan aan elke kontrolevolume toegeken om sodoende 'n stelsel van nie-lineêre, tydafhanklike parsiële differensiaalvergelykings af te lei. Hierdie tydsafhanklike vergelykings was opgelos deur gebruik te maak van 'n volledig-eksplisiete numeriese metode met windopse-verskilvorming en 'n terugwaards-gestapelde snelheidskema. 'n Ongestadigde elektromagnetiese eindige element analise was uitgevoer om die werking van die lineêre elektriese kragopwekker te simuleer. Die kragopwekker word in die teoretiese model verteenwoordig deur gebruik te maak van analitiese kragopwekkerkenmerkende funksies. 'n Nuwe eksperimentele enjin prototipe was gemasjineer. Eindige element analises was gebruik om die sterkte en veiligheidskritieke meganiese komponente van die enjin te ontwerp. Die elektromeganiese, veërbuigstyfheid en verplaser- en krag-suier meganiese wrywing eienskappe was vasgestel deur eksperimentele ondersoeke van die soos-vervaardigde enjin. Sewe uitgekiesde eksperimentele toetslope was gebruik om vas te stel of die teoretiese model in staat is om die gedrag van die vervaardigde enjin na te boots. In hierdie toetse is die verwarmer temperatuur gewissel tussen 300 en 600 °C en die werkvloeistof lugdruk gewissel tussen 1.0 en 2.0 MPa. Selfonderhoudbare, geslote-stroom werking van die enjin was behaal met 'n temperatuur van 470 °C en 'n lugdruk van 1.7 MPa. By hierdie toestande is 'n piek elektriese krag uitset van 73 W behaal.

'n Goeie korrelasie tussen eksperimentele en simulasie resultate was getoon vir 'n reeks werkstoestande, wat die teoretiese model valideer. Daar is tot die gevolgtrekking gekom dat dit noodsaaklik is om die belyning en passing van die bewegende suiers te verbeter om ten einde interne glywrywing te minimaliseer. Dit word aangebeveel om vir die bestaande prototipe 'n elektroniese terugvoerbeheerstelsel te ontwikkel sodat volhoubare enjine werking sonder suier botsings kan verseker word.

Acknowledgements

The author would like to express his sincerest gratitude towards the following people and institutions for their inputs in this study:

My supervisors, Prof. Thomas Harms, Mr Robert Dobson and Dr Arthur Bell, for providing me with expert technical and scientific guidance throughout this study. Mr Dobson, in particular, who has guided me on this academic journey since my final year of undergraduate study: Thank you for all the interesting and intellectual discussions that we could have shared; it has awakened in me a deep appreciation for science, technology and academia. Thank you also, Prof. Harms and Dr Bell, for providing me with your guidance during the later stages of my graduate studies. I will forever be indebted to the opportunity that you have afforded me.

The Solar Thermal Energy Research Group (STERG) at Stellenbosch University, for facilitating this research.

The Department of Mechanical and Mechatronic Engineering workshop at Stellenbosch University and its staff, especially Ferdie Zietsman, Cobus Zietzman and Juliun Stanfliet, for their help pertaining to the manufacturing and experimental aspects of this study.

My parents, Bernabé and Anita. Thank you for your unconditional love, motivation and financial support. You have eagerly supported my full-time studies over the last nine years, for which I will forever be grateful.

My colleagues and the many more friends I have made during my time at University. Thank you for the late-morning coffees, "Neelsie" lunch breaks, intellectual discussions (and debates), and your general support of my work.

Lastly, I would like to thank my most fond supporter, Elbie, for unconditionally supporting and believing in me, always, without falter. Your affection, support, kindness and understanding have carried me throughout my graduate studies. Words cannot express my gratitude.

In loving memory of my grandmother,
Connie de la Bat

Table of Contents

List of Figures

List of Tables

Nomenclature

Constants

g	Gravitational acceleration	[m/s^2]
σ	Stefan-Boltzmann constant	[W/m^{2}K^4]

Variables

A	Area	[m^2]
A_x	Cross-sectional area	[m^2]
A_z	Surface area in z-direction	[m^2]
a	Acceleration	[m/s^2]
B	Magnetic flux density	[Wb]
C_f	Skin coefficient of friction	[−]
C_t	Tuning capacitor	[F]
c_p	Specific heat at constant pressure	[J/kg K]
c_v	Specific heat at constant temperature	[J/kg K]
c_{vis}	Viscous damping coefficient	[N s/m]
cc	Cubic centimetres	[cm^3]
d	Diameter	[m]
d_h	Hydraulic diameter	[m]
emf	Electromotive force	[V]
F	Force	[N]
f	Frequency	[Hz]
G	Variable transformer voltage	[V]
h	Convective heat transfer coefficient	[W/m^{2}K]
I	Electrical heater current	[A]
i	Linear generator or motor current	[A]
J	Colburn J number	[−]
k	Thermal conductivity	[W/m K]
k	Spring constant	[N/m]
L	Inductance	[H]
l	Length	[m]
m	Mass	[kg]
$\dot{m}$	Mass flow rate	[kg/s]
N	Number of control volumes, coil turns	[−]
Nu	Nusselt number	[−]
P	Power	[W]
P	Pressure	[Pa]
Pr	Prandtl number	[−]
p_f	Fin pitch	[mm]
p_w	Wetted perimeter	[m]
Q	Heat transfer	[J]
$\dot{Q}$	Heat transfer rate	[W]
R	Electrical resistance	[Ω]

R	Thermal heat transfer resistance	[K/W]
Re	Reynolds number	[−]
R_g	Specific gas constant of helium	[J/kg K]
St	Stanton number	[−]
T	Temperature	[°C]
t	Thickness	[mm]
t	Time	[s]
u	Specific internal energy	[J/kg]
V	Volume	[m^3]
V	Voltage	[V]
v	Velocity	[m/s]
$\dot{W}$	Boundary work rate	[W]
x	Displacement	[m]
$\dot{x}$	Velocity	[m/s]
$\ddot{x}$	Acceleration	[m/s^2]
Z	Impedance	[Ω]

Greek symbols

α	Phase difference between pressure swing and piston motion	[°]
β	Phase difference between pressure swing and displacer motion	[°]
γ	Adiabatic index	[−]
ε	Void fraction	[−]
η	Efficiency	[−]
θ	Phase difference between piston and displacer	[°]
θ	Rotation angle	[rad]
Φ	Phase difference	[°]
ϕ	Magnetic flux	[Wb]
λ	Flux linkage	[Wb Turns]
μ	Dynamic viscosity	[kg/m s]
ρ	Density	[kg/m^3]
τ	Shear stress	[N/m^2]
ω_n	Natural frequency	[Hz]

Vectors and tensors

$\boldsymbol{B}$	Magnetic flux density	[Wb]
$\boldsymbol{i}$	Electrical current	[A]
$\overrightarrow{v}$	Velocity vector	[m/s]
$\overrightarrow{\tau}$	Stress tensor	[N/m^2]

Subscripts

0	Initial
a	Axial
b	Base
bc	Bore cylinder
bs	Backspace
c	Compression space
cw	Casing wall
d	Displacer
dp	Between displacer and piston

e	Expansion space
f	Flow, fin, flexure spring, friction
g	Gas, generator
h	Heater, hot-end, hot-side
i	Inlet, i-th Numbered scalar control volume
j	j-th Numbered vector control volume, interface node
k	Cooler, cold-end, cold-side
L	Load
m	Magnet, magnetic, motor
OC	Open-circuit
o	Outlet, outside
p	Piston
r	Regenerator
rm	Regenerator mesh
s	Shaft
T	Terminal
w	Water, wire
wl	Wall
wd	Displacer length
wp	Piston length

Superscripts

t	Denotes the current time-step
Δt	Finite time-step duration

Acronyms and abbreviations

AC	Alternating current
AISI	American Iron and Steel Institute
API	Armoured Polyesterimide
ASC	Advanced Stirling Converter
ASRG	Advanced Stirling Radioisotope Generator
AWG	American Wire Gauge
CFL	Courant-Friedrichs-Lewy
CHP	Combined heat and power
cDAQ	Compact data acquisition
DAQ	Data acquisition
DC	Direct current
FEA	Finite element analysis
FEM	Finite element method
FPSE	Free piston Stirling engine
HX	Heat exchanger
LHS	Left-hand side
MTI	Mechanical Technology Incorporated
NASA	National Aeronautics and Space Administration
PTFE	Polytetrafluoroethylene
RHS	Right-hand side
RTG	Radioisotope Thermoelectric Generator
SEP	Sound Engineering Practice
TESS	Thermal energy storage system

1. Introduction

Energy is the *lifeblood* of our modern society; it is a vital requirement for the functioning of nearly all forms of productive means and it impacts all sectors of our economies, from best business practices through healthcare, transportation and agriculture, to education, communication and leisure, to name only a few (Hudson, 2013). The depletion of earth's conventional energy resources, combined with the global increase in greenhouse gas emissions, has over the last decade spurted an increased urgency to accelerate research and development efforts into more renewable and sustainable energy alternatives. However, in spite of the advancements that are being made towards sustainable energy generation in developed economies, the World Bank (2017) estimates that approximately 57 percent of the 1.07 billion people living in Sub-Saharan Africa are still without grid-tied electrification and live in conditions of extreme poverty. Millions of people lose their lives every year for reasons either directly or indirectly related to extreme energy poverty (Stevens *et al.*, 2016). Consequently, it should come as no surprise that *Sustainable Energy Generation* has been identified as one of the United Nations' seventeen Sustainability Development Goals, which is aimed at improving the livelihoods of *all* people (wealthy and poor) around the globe (United Nations, 2015).

One solution to extending sustainable electrification to rural and off-grid communities is the deployment of *smart* energy management infrastructure, i.e. *smart-grids*, by which two-way communication and intelligent sharing of a network of limited resources can be accomplished within a decentralised community (Camarinha-Matos, 2016). As motivated by Craig (2018), solar-powered micro-grids should be considered a viable solution to accelerating rural electrification in areas rich with solar irradiation, including rural South Africa. In addition to the development of new technologies to distribute renewable energy more efficiently, investigation of existing technologies for more efficient generation and usage may be as important in addressing these significant environmental and socio-economic challenges. Owing to its high thermal efficiency, fuel flexibility and nearly zero maintenance requirement, free-piston Stirling engines (FPSEs) have in recent years attracted renewed interest worldwide for uses specifically relating to micro-Combined Heat and Power (mCHP) generation (Murugan and Horák, 2016; Shunmin *et al.*, 2018). In particular, Stellenbosch University has identified the use of a FPSE as a viable candidate for mCHP cogeneration (Prinsloo, 2018), with the local development of such a system utilising concentrated solar power to generate up to 3 kW of electrical and 10 kW usable thermal heat being envisaged for rural South Africa (Kayofa, 2015).

First patented by the Reverend Robert Stirling in 1816 as an alternative to the steam engine, a Stirling engine is a closed-cycle external combustion heat engine that converts thermal heat into usable mechanical (or electrical) energy via the cyclic expansion and contraction of a hermetically sealed gas working fluid (Organ, 1992). By employing internal heat regeneration, Stirling engines are known to achieve thermal efficiencies closest to that of Carnot, with net efficiencies in the

range of 25 to 32 % not being uncommon (Organ, 2014). In 1964 Professor William Beale from Ohio University brought forward a unique modification to the Stirling engine (Beale, 1969), by replacing the conventional crank mechanism of a Stirling engine with *flexure springs* being attached to the respective pistons. This modification distinguishes the *free-piston* Stirling engine from the more traditional *kinematic* Stirling engine. Moreover, the elimination of rotary components eliminates piston side-load forces, rotary wear and the requirement for wet lubricants, thereby leading to considerably prolonged engine lifetimes and increased reliability (Alger, 1988). Since FPSEs derive heat from external sources, they have been applied to a range of applications including waste heat recovery and utilisation (Senda, 2012), bio-mass or methane combustion (Renzi and Brandoni, 2014) and even nuclear thermal heating (Gibson *et al.*, 2017). When combined with a parabolic-dish solar concentrator, FPSEs are well-suited to supplying both usable electric power and hot water as micro co-generation systems (Caballero *et al.*, 2017).

South Africa has in recent years become a testing ground for novel solar power applications – this includes technology developments relating to Stirling engines. For example in 2012, Ripasso Energy (now Swedish Stirling AB) commissioned a test facility in Upington, South Africa, and demonstrated a world-leading solar-to-grid energy efficiency of 32 % for their 33 kW_e dish-Stirling engine. Since then Ripasso has expanded their market interest to waste-heat recovery utilisation and in 2017, launched its first commercially available *PWR BLOK 400-F*: a container-based array of Stirling generators capable of delivering a net output of 400 kW. In 2018, Afarak's Mogale ferroalloy processing plant in South Africa signed an agreement for seven such PWR BLOK units to deliver a total of 2.8 MW_e *clean* electricity from recovered waste heat (Steyn, 2019). In June 2019, Ripasso announced the signing of an exclusivity agreement to negotiate the installation of 25 PWB BLOK units at Glencore South Africa's Lydenburg smelting facility (Bulbulia, 2018). Targetting dispatchable concentrated solar power electrification in Sub-Saharan Africa, the Swedish-based Azelio (previously Cleanergy) in 2018 demonstrated the integration of a Stirling generator with an aluminium-silica latent heat storage system as being a viable solution to rural electrification (Azelio, 2019). In May 2019, Azelio announced at a press-release the preliminary signing of a sales agreement with Pasanté AB to develop its technology for the electrification of rural African hospitals.

The aforementioned examples illustrate the current breakthroughs in waste-heat recovery and localised solar thermal electrification that well-established Stirling engine companies are, at the time of writing, actively pursuing to make into the sustainable and renewable energy markets. However, despite the distinct advantage of increased reliability that free-piston Stirling engines may well hold over their kinematic counterparts, research and development efforts into actual and operational FPSEs have remained limited in the existing published literature.

1.1. Motivation

In spite of the notable advantages of high thermal efficiency, quiet operation, zero maintenance and being adaptable to nearly any high-temperature heat source, com-

mercial adoption of FPSEs into the energy market has historically been unsuccessful (Qiu *et al.*, 2019). For example, in 2012 Infinia Corporation, a fore-runner in the development of FPSEs who were marketing their FPSE technology for remote solar power electricity generation, filed for Chapter 11 bankruptcy (CSP World, 2013). Moreover, at the time of writing, the only commercially available FPSE units were that of Microgen Engine Corporation (2018) and Qnergy (2018), despite ongoing government-funded research in the United States (ARPA-E, 2019) towards developing a natural-gas-fuelled FPSE for residential micro heat and power application. A consequence of this poor market penetration is that the existing published literature still remains limited on undisclosed experimental test data or validated numerical models (Shunmin *et al.*, 2018). Of the existing models available from literature, most are validated against dated test results from the 1980s performed on General Motors' GPU-3 kinematic Stirling engine, with the majority of these models considering the engine thermodynamics and kinematics in a decoupled manner.

To address this knowledge shortfall, and in so doing provide a foundation from which ultimately a *task-suited* engine may be developed, this study considers the theoretical simulation, manufacture and experimental evaluation of a free-piston Stirling engine electric generator. As concluded from the literature study in Chapter 2, it is hypothesised that the complete modelling of a FPSE should capture and emulate the inherent coupling that exists between the gas thermodynamics, piston and displacer kinematics and linear generator electrodynamics so that the underlying engine working mechanism can be studied in its entirety. Additionally, by developing a unique and fully-testable experimental prototype as a *technology demonstrator* to validate this model against, this study aims to gain insight into critical design and manufacturing considerations.

1.2. Aim and objectives

The preceding considerations lead to the primary aim of this study, which is to:

Provide a validated, in-depth theoretical simulation model of a free-piston Stirling engine electric generator that is capable of simulating the linked thermodynamic, kinematic and electrodynamic engine behaviour from first principles.

To realise this aim, the principal research objectives are defined as follows:

- Derive a comprehensive theoretical simulation model of a free-piston Stirling engine electric generator that is based on fundamental thermodynamic, fluid mechanic and electrodynamic theory.
- Design and manufacture a testable prototype free-piston Stirling engine electric generator and identify key complexities associated with the manufacture of such an engine.
- Evaluate the performance of the prototype engine by operating it under controlled conditions and in so doing, validate the underlying theoretical model.

The successful completion of these objectives will not only deliver a practical and usable free-piston Stirling engine design tool, but also a *technology demonstrator unit* that may be thoroughly studied to understand and describe free-piston Stirling engine dynamics. It should be emphasised that the aim of this study has *not* been the development of an optimised engine, but rather to provide a knowledge foundation around which future planned research and development efforts may be centred.

1.3. Original research contributions

The novelty of this dissertation lies in the development of a validated theoretical simulation model that emulates, from first principles, the transient and intrinsically linked interaction between the working gas thermodynamics, the non-linearised engine kinematics, and the linear generator electrodynamics of a free-piston Stirling engine to a fair degree of accuracy. A unique approach to characterising and linking the linear generator performance and electromagnetic force interaction to the piston dynamics is outlined in this study. By inferring generator characteristic equations from a transient finite element analysis of the linear generator, the generator performance is accurately emulated in the numerical simulation program. This allows the linked thermodynamic and electrodynamic behaviour of the engine to be studied in a relatively computationally inexpensive way, whilst retaining the real generator induced currents and electromagnetic forces acting on the piston.

To validate its underlying theoretical basis, a unique engine prototype has been designed and manufactured from the ground-up. This novel prototype for the first time includes an internally located displacer motor, which has allowed the engine to be tested under operating parameters where self-sustained engine operation would otherwise not be possible. The lab-based test engine has been experimentally characterised and operationally test-proven over a range of setup conditions. A qualitative comparison of modelled results to seven selected test cases has been performed to verify that the model is capable of emulating the experiment. The study presents experimental results of real-time engine dynamics. This includes the measurement of engine temperature, pressure swing, displacements, load voltage, current and electrical power output, all contributing to the limited existing knowledge base surrounding FPSE experimental test results.

It is to the author's best knowledge that no such comprehensive and validated model is currently available in the published literature. Therefore, this study presents a significant contribution to the limited body of literature surrounding the modelling of free-piston Stirling engine operational mechanics. The computer simulation program developed throughout this study requires *only* that the engine heater and cooling water inlet temperature be specified. Accordingly, the time-dependent engine motion and generator load power evolve naturally as simulation outputs, therefore the model is capable of emulating the *real* dynamic behaviour of such an engine. It is ultimately envisaged that the use of this validated model will form a powerful design tool from which an optimised and task-suited FPSE may be developed.

2. A review of applicable literature

The literature review presents a short history of Stirling engines up to the advent of the free-piston variant. The working principle of the engine is discussed and the idealised Stirling cycle is presented. An overview of published theoretical modelling techniques is presented. The chapter concludes that only a nodal analysis model is deemed capable of capturing the coupled thermodynamic and *free* engine kinematics; thus it is preferred for the accurate simulation-study of a free-piston Stirling engine.

2.1. A brief history of Stirling engines

The invention of the Stirling engine, then coined simply as a 'hot air engine with economiser', was pioneered by Reverend Robert Stirling in the early 1800s as a safer alternative to early steam engines (Walker, 1980). A steam engine functions by extracting the mechanical work done by the expansion of steam in a closed cylinder-piston arrangement, but Stirling adopted this mechanism so that air could be used. The expansion and contraction of air as the working fluid is more stable and safer than steam as it does not undergo any phase change. Air is also not corrosive, thereby leaving the machine integrity unchanged. However, due to the poor metallurgical knowledge of the time, Stirling's engines were limited to low hot-end temperatures and working fluid pressures, leading to low power generating capacities. With the advent of the Bessemer process in 1856 to mass produce low cost, higher quality steel, steam engines became significantly safer and subsequently the dominant driving force behind the first industrial revolution (Hart-Davis, 2012).

Stirling engines would again see renewed interest in the mid 1930s from the Philips Research Laboratory in Eindhoven, Netherlands. Their objective was to develop a small and quiet thermally-driven electric generator for off-grid application (Hargreaves, 1991). This work led to the development of the *rhombic* drive system by which the displacer and piston are interconnected in an arrangement that nearly eliminates any displacer or piston side loads whilst reducing the overall size of such engines considerably (Meijer, 1960). Philips continued the development of its Stirling engines well into the 1960s when General Motors Corporation also became involved. Originally developed for the United States Army in 1965 as part of a $3\,\mathrm{kW_e}$ generator set, General Motors' Ground Power Unit-3 (GPU-3) Stirling engine, which employs the rhombic drive crankshaft previously pioneered by Philips, became arguably one of the most well documented Stirling engines to date, as having being studied extensively by NASA's Lewis Research Center in the late 1970s (Thieme, 1979, 1981). During this period of peak development, Stirling engines even received specialised interest for their application relating to deep space exploration and for use in nuclear-powered submarines (Jakubowski, 1980; Organ, 1992). New technological advancements in metallurgy and machining precision allowed engine designers to explore the high thermal efficiencies associated with Stirling engines and apply this to nearly any task imaginable, including automotive and residential power

generating application. It was during this period of heightened development that Professor William Beale (1969) from Ohio University realised that a Stirling engine could function even in the absence of a mechanical drive system linking the piston and displacer motions. In replacing the rhombic drive mechanism of a Philips engine with respective *flexure springs* attached to the displacer and piston, Beale invented the first *free-piston* variant – eliminating the previous requirements of expensive rolling seals used on both the Philips and GPU-3 engines. This breakthrough in Stirling technology ultimately led Beale to found Sunpower Incorporated (2016), which has ever since been a leading developer of free-piston machines.

2.2. Free-piston Stirling engines

A free-piston Stirling engine (FPSE) is a variant of the Stirling engine in which the piston and displacer are not interlinked by a mechanical crank: the power piston is essentially *free* of any mechanical linkages and its motion is only dependent on the magnetically coupled generator load and working fluid pressure forces. Both the piston and displacer resonate in a shared natural frequency, deriving power from an oscillatory pressure variation (called pressure swing) that is induced by the cyclic heating and cooling of a gas working fluid. Flexure springs attached to the respective displacer and piston cyclically store and release mechanical energy, analogous to the angular momentum stored in the flywheel of a kinematic Stirling engine. Traditionally, power is extracted from the engine by means of a linear alternator that is coupled to the power piston. In contrast to their kinematic counterparts that operate at fixed strokes but variable speeds, FPSEs operate at fixed frequencies, but the displacer and piston strokes may vary depending on operating conditions. By actively modifying the generator load and current draw, the power piston (and indirectly the displacer) may be influenced to oscillate within a predefined stroke range. In addition to the compactness of these engines, the removal of the crankshaft eliminates crank stresses and rotary wear, thereby eliminating the requirement for wet lubricants. Close-tolerance hydrodynamic gas bearings are traditionally employed to ensure nearly zero contact friction with the displacer and power piston. To demonstrate the long engine life expectancy, NASA's Glenn Research Centre has been operating its Technology Demonstrator Converters (TDCs) since early 2003, and in 2018, surpassed more than one hundred thousand hours of accumulated operation without any signs of significant internal wear (SpaceFlight Insider, 2018).

As shown by Figure 2.1, for example, the entire engine is hermetically sealed within a pressure-retaining casing and is typically charged with helium gas as the working fluid. Due to the additional benefits of no required servicing and extremely long engine lifetimes, silent operation and flexibility to be used with a wide range of external heat sources, FPSEs may often be preferred over kinematic type engines for applications ranging from a few Watts to 10 kW. They are also especially fitting for niche applications where engine servicing is not possible. Since the late 1970s, NASA has extensively researched FPSEs for use as electricity (and heat) generating devices in deep space exploration (Dochat, 1987). Under contract from NASA and the U.S. Department of Energy, Mechanical Technology Incorporated (MTI) invested considerable effort in the development of FPSEs suited for both concentrated solar

power application (Dochat, 1979) and for use in envisaged deep space missions as the primary electrical generator (Dhar, 1999). As early as 1977, MTI had demonstrated the operation of a 2 kW FPSE with an attached linear alternator (Goldwater *et al.*, 1977), and by September 1993, had succeeded in developing a 25 kW_e prototype that operated under a mean charge pressure of 15 MPa with helium gas as the working fluid. Also in pursuit of this undertaking, Sunpower Inc. developed the RE-1000 Stirling engine, documented by Schreiber and Geng (1987), which remains arguably one of the most extensively studied experimental free-piston Stirling engines to date.

From 1999 to 2006, NASA's Glenn Research Center actively supported the development of a 110 W_e high-efficiency Stirling Radioisotope Generator, which was envisaged as a more efficient replacement to conventional Radioisotope Thermoelectric Generators (RTGs) currently being used for deep space application (Oriti and Scott, 2011; Wilson *et al.*, 2016). Sunpower Inc. replaced Infinia Corporation as the primary contractor for the development of an *Advanced Stirling Radioisotope Generator* (ASRG) in 2006. But despite the significant progress made in this undertaking, due to budget constraints from the U.S. Department of Energy, the contract was terminated prematurely in 2013 (Schmitz *et al.*, 2016; Wilson *et al.*, 2016) and as a result the engine never flight-tested. Nevertheless, in 2015, work on the ASRG was redirected to NASA's Kilopower Development Program (Gibson *et al.*, 2015, 2017) which, at the time of writing, envisages using an array of fission-powered Advanced Stirling Convertor (ASC) units to produce between 1 and 10 kW_e of reliable, zero-maintenance power for future planetary exploration missions. In March 2018, the first round of experimental tests on the so-called Kilopower Reactor Using Stirling

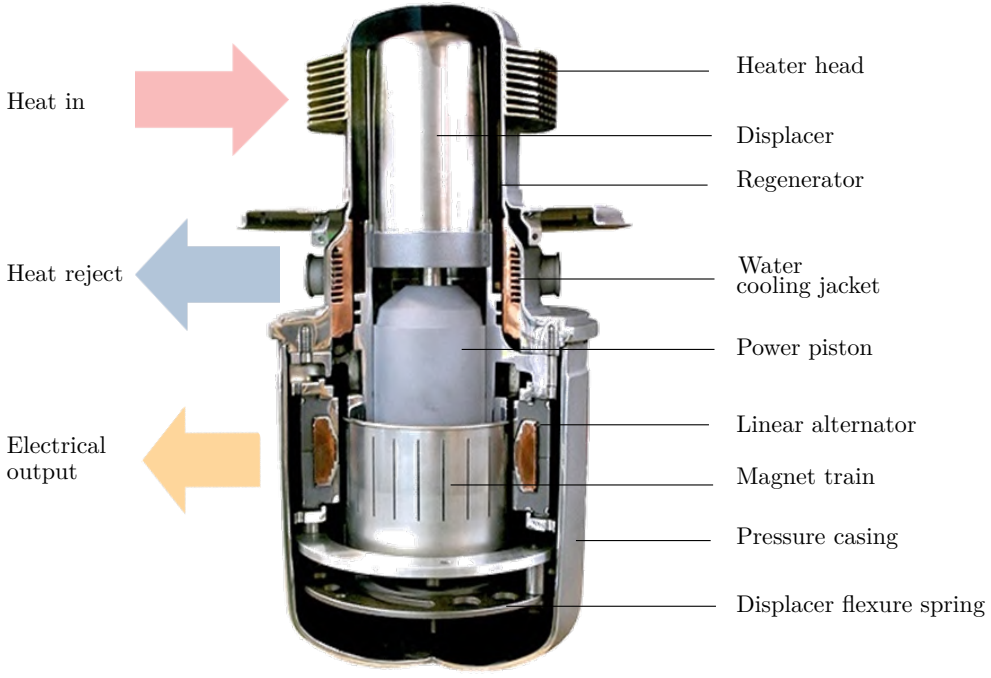

Figure 2.1: Photograph of the 1.0 kW_e Microgen free-Piston Stirling engine (Image adapted from Ökofen, 2018)

TechnologY (KRUSTY) was successfully completed (Gibson *et al.*, 2018) in which Stirling simulators were used to investigate the performance of such an envisaged reactor.

Relating to the commercial energy sector, development efforts have focused mainly on cogeneration systems that deliver both electricity and hot water from virtually any high-temperature heat source. Based on Sunpower's P2A engine, Microgen Engine Corporation (2018) developed a commercially available $1\,kW_e$, $3\,kW_{th}$ micro-combined heat and power (mCHP) FPSE. Microgen has successfully integrated its product for a range of domestic energy applications, also including for use in remote power systems with either combustion or concentrated solar power heating. Qnergy (2018), who in 2013 acquired former Infinia Corporation's intellectual assets, has recently launched its $7\,kW_e$ *PowerGen* cogeneration FPSE into this same market space. An example of this technology has been demonstrated by Qnergy at the *Snowbasin Resort* in Utah, United States, where as a pilot to their Remote Power Systems Division, such a cogeneration unit has been delivering a net amount of $130\,kW\,h$ of electrical power daily using natural gas combustion as the heat source (Collins, 2019).

Based on the developments by Sunpower and Infinia (previously Stirling Technology Company), primarily two competing configurations of FPSE have become well-known for use in mCHP application. As shown in Figure 2.2, in the *Beta* configuration the displacer and piston are both located in a single bore-cylinder arrangement. Typically the displacer shaft is located through the power piston; both the power piston and displacer may be 'sprung to ground' using flexure springs. Compact FPSEs like the $1.0\,kW_e$ P2A FPSE developed by Sunpower are typically based on this configuration. Interestingly, the P2A engine has no flexure spring attached to

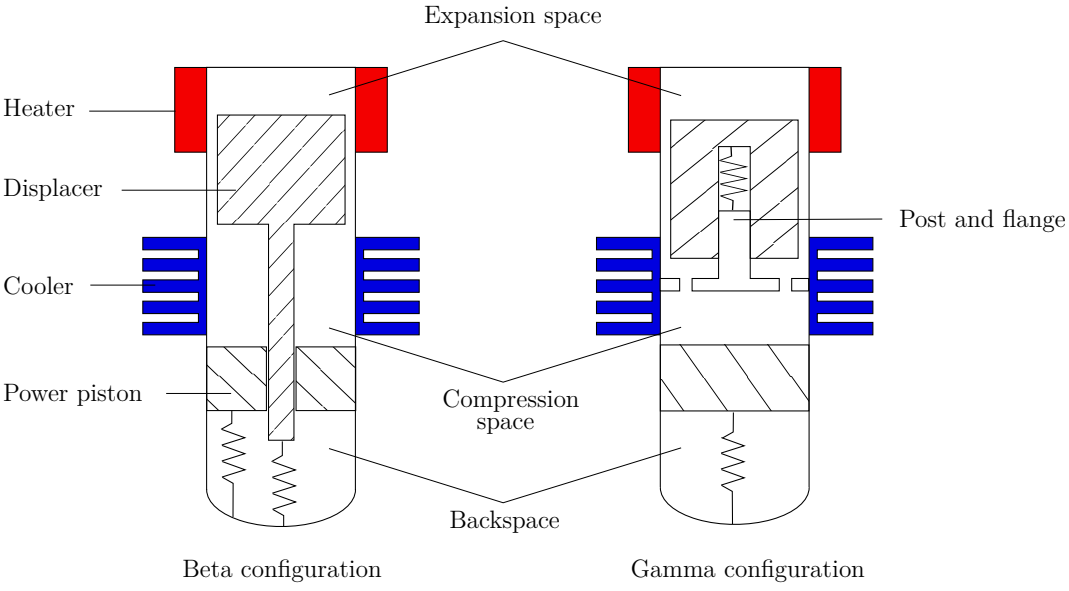

Figure 2.2: Comparison of the Beta configuration FPSE with displacer shaft through power piston, and the Gamma configuration with fixed displacer post

the power piston, as the generator magnetic forces are sufficient to centre the piston, thus adding to the simplicity and longevity of its design. In the *Gamma* configuration, the displacer and piston are not necessarily located within the same bore. The illustration shows the displacer to be located about a stationary post and flange setup. This arrangement partially relaxes the otherwise stringent requirement on precision-machined tolerances between piston, displacer and bore cylinder and consequently allows for a more modular design. Infinia Corporation (now Qnergy) has successfully developed a flexure-supported Stirling engine based on this geometry.

2.3. Working principle of the ideal Stirling cycle

In this section, the working principle of the Stirling engine is illustrated by depicting the thermodynamic processes of the Stirling cycle on accompanying pressure-volume and temperature-entropy diagrams. As shown by Figure 2.3, the most basic Stirling engine consists of an enclosed displacer and power piston that move 90° out of phase with one another in a common frequency (the piston lags behind the displacer). The displacer 'shuttles' the working fluid back and forth between the hot- and cold-ends of the engine, and in doing so, the working fluid is thermally expanded and contracted. Thermal expansion of the working fluid forces the power piston outwards in an *expansion stroke*, whereas thermal contraction pulls the power piston inwards in the *compression stroke*. Mechanical work is derived from the power piston through a piston-coupled linear electric generator. Figure 2.3 further shows how the idealised Stirling cycle may be represented by four thermodynamic phases, indicated by positions one to four on the accompanying pressure-volume (PV) and temperature-entropy (TS) diagrams. The PV diagram depicts both the idealisation of the Stirling cycle, which is also the idealised Carnot cycle, as well as the more realistic elliptically shaped cycle that results from finite-time thermodynamics. The idealised Stirling cycle can briefly be described by the steps:

$1 \rightarrow 2$ **Isothermal compression**: The working fluid is compressed isothermally during the *compression stroke*. This is accomplished by the inward movement of the piston. The effect on the PV and TS diagrams should be noted.

$2 \rightarrow 3$ **Constant volume heat addition**: The working fluid is shuttled by the displacer from the cold-end to the hot-end. In Stirling engines the working fluid usually passes through a regenerator that is located in between the heater and the cooler, improving the overall efficiency of the cycle by aiding in heat recovery. As the bulk of the working fluid enters the hot-end and is heated, the working fluid pressure increases.

$3 \rightarrow 4$ **Isothermal expansion**: The working fluid is expanded isothermally during the *expansion stroke*. This is accomplished by the outward movement of the displacer and piston.

$4 \rightarrow 1$ **Constant volume heat rejection**: The displacer shuttles the working fluid from the hot-end to the cold-end. Typically the displacer starts this movement whilst the piston is still expanding. The working fluid effectively rejects its heat in a constant volume process as shown.

As the engine undergoes isothermal expansion or compression, heat is either supplied or removed from the working fluid by the heater and cooler. Furthermore, the constant volume heat addition and rejection processes are made possible by assuming perfect regeneration as the gas is shuttled from hot to cold end (2→3) and vice versa (i.e. 4→1). Following these assumptions, the heat input and output requirements of the engine are only dependent on the expansion and compression processes and consequently, the ideal Stirling efficiency equals that of Carnot. For real Stirling engines, Chen and Griffin (1983) suggest that an optimised engine may optimistically be expected to reach a thermal efficiency equalling between 50 and 70 % of the idealised Carnot cycle thermal efficiency, whereas Martini (1983) suggests at maximum, 58 % of the idealised Carnot efficiency may realistically be reached.

As described in the section that follows, theoretical modelling of the Stirling cycle often starts with a per-cycle based analysis, in which either the assumptions of isothermal or adiabatic expansion and compression are made.

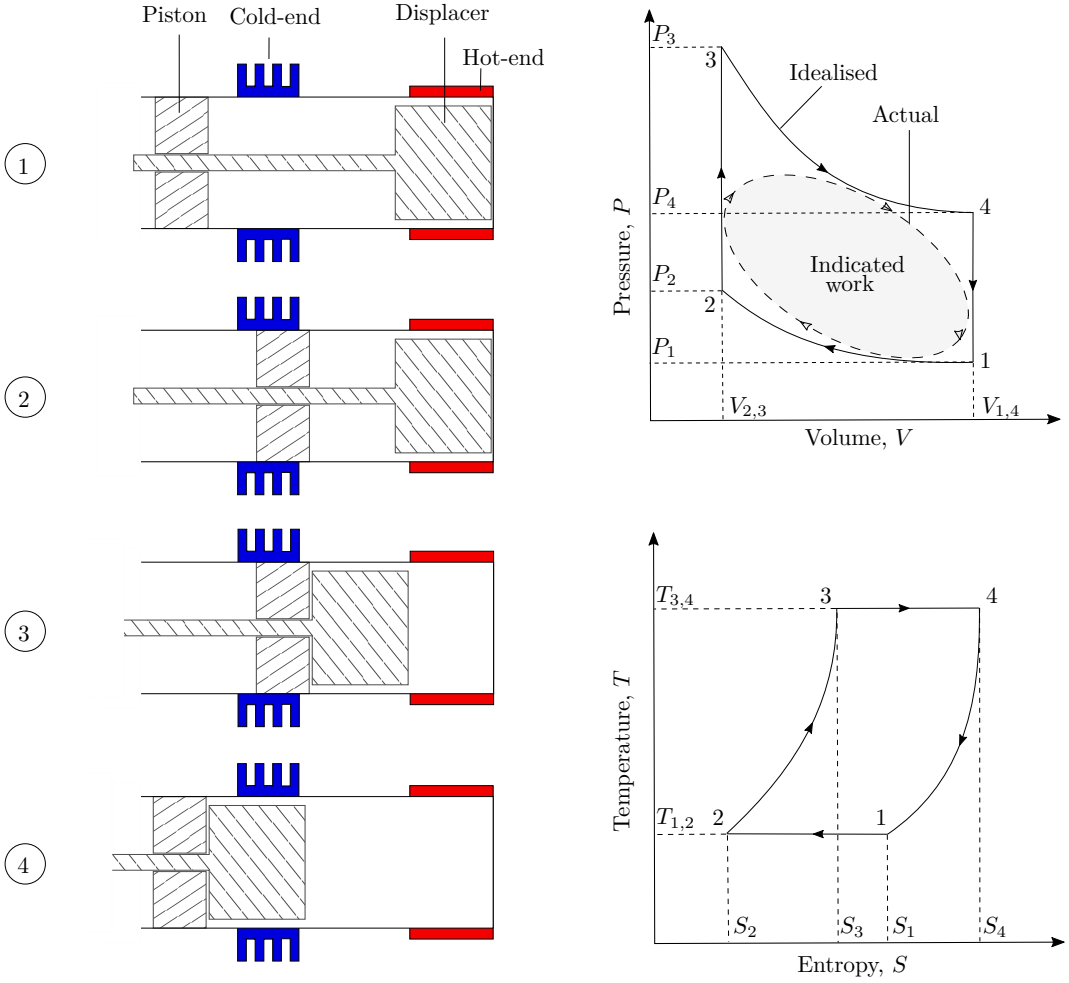

Figure 2.3: Displacer and piston positions at each step of the Stirling engine cycle with the corresponding PV and TS diagrams

2.4. Overview of theoretical modelling approaches

Theoretical modelling approaches regarding the working fluid thermodynamic cycle are generally classified as either being first-, second- or third-order modelling techniques, with the increased order number indicating increased modelling complexity. Chen and Griffin (1983) discuss the different modelling techniques, for which a summary of applicable literature is given below.

2.4.1. First-order or approximate design methods

First-order design methods provide a quick way of estimating a Stirling engine's performance, by relating the estimated efficiency and power output to hot-end and cold-end temperatures, engine operating frequency and cycle swept volume. The calculation of the per-cycle power output starts with the computation of an idealised loss-free analysis using, for example, an ideal-isothermal cycle analysis as is described in Chapter 2.4.2, or the more generalised Beale equation given by Walker (1980):

$$P = Bpf\Delta V \tag{2.1}$$

where the output power P in Watts is estimated based on B the Beale number constant; p, the average charge pressure in MPa; f, the cycle frequency; and ΔV, the swept volume in cubic centimetres. Beale proved Equation (2.1) to remain approximately true for various types and sizes of Stirling engines tested in the 1970s and 1980s, in which the Beale number typically ranged between 0.11 and 0.15 for engines with hot-end temperatures in the range of 650 °C. The engine brake efficiency is then related to the idealised Carnot efficiency through a simple correction factor that accommodates *all* forms of energy losses. Martini (1983) suggests that this correction factors may typically vary from 0.65 to 0.8, although for some engines modelled it may even be as low of 0.5.

It is suggested that, although first-order methods provide a way of estimating engine power output and cycle efficiency, they do not suffice as detailed design tools in the case of a free-piston Stirling engine. Therefore, these methods are traditionally deemed satisfactory only in evaluating the feasibility of employing a Stirling engine for a given temperature range.

2.4.2. Second-order or decoupled design methods

Second-order design methods start with a simplified cycle analysis to determine the basic heat input and boundary work output of the engine. Such cycle analyses are typically classified as being either ideal-isothermal or ideal-adiabatic, distinguishable in the way in which heat transfer is modelled for the expansion and compression space volumes. Significant assumptions regarding these approaches are that the total mass of the working fluid remains constant (i.e. no gas leakage occurs) and that there is no spatial pressure gradient (i.e. the instantaneous pressure is representative of the entire engine). In essence, these assumptions permit solving the system equations as a function of volume variation specified for the expansion and compression spaces. Then, once the idealised engine performance is calculated, in-

dividually identifiable power loss terms are subtracted from the per-cycle estimated power output, and non-idealised heat losses are added to the required heat input to more realistically estimate the engine's net efficiency. According to Martini (1983), significant engine losses may include (but are not limited to) energy dissipation by fluid friction, mechanical contact friction, parasitic heat losses by convection and metal conduction, dead-space and fluid hysteresis losses, heat exchanger inefficiencies and associated shuttling losses, and energy losses by gas leakage[1]. It must be noted that in the absence of additional loss terms, these cycle analyses are classified as being first-order methods.

Ideal-isothermal cycle analysis

Being the simplest of Stirling cycle analyses, the ideal-isothermal analysis is based around the principle assumptions that all the working gas in the expansion space (and heater) are at a constant hot sink temperature T_h, whereas all the working fluid located in the compression space (and cooler) are at a constant cold sink temperature T_k. Furthermore, the assumptions of ideal gas laws are made; perfect heat regeneration is assumed – implying there is a linear temperature profile throughout the regenerator section; that the engine workspace gas mass remains constant (i.e. zero gas leakage to backspace); and that the instantaneous pressure in the engine workspace is constant.

By employing the above mentioned assumption, Walker and Senft (1985) derived the instantaneous workspace pressure P in terms of the temperature T and volume V from the ideal gas law:

$$P = mR\left(\frac{V_c}{T_k} + V_r\frac{\ln(T_h/T_k)}{(T_h - T_k)} + \frac{V_e}{T_h}\right)^{-1} \tag{2.2}$$

in which the expansion and compression space volumes V_e and V_c are linear functions of displacer and piston position. If the displacer and piston are made to move cyclically then the volume variations will be periodic functions of crank angle (or time) and the work done per cycle may be calculated from:

$$W = mR\oint \frac{d(V_c + V_e)}{V_c/T_k + V_e/T_h + V_r\ln(T_h/T_k)/(T_h - T_k)} \tag{2.3}$$

By assuming sinusoidal piston and displacer motions, Schmidt (1871) first derived and integrated Equation (2.3) to obtain a closed-from solution to the ideal-isothermal cycle. Furthermore, Urieli and Berchowitz (1984) have shown how this integral may be computed numerically for more arbitrarily defined volume variations.

Ideal-adiabatic cycle analysis

As a more realistic approximation to modelling the Stirling cycle, the ideal-adiabatic cycle analysis – often referred to as the Finkelstein method, being named after its inventor Theodor Finkelstein (1960) – assumes that the compression and expansion spaces are perfectly insulated and that external heat transfer occurs only in the heater and cooler sections. The working fluid leaving the heater and entering

[1]The interested reader is referred to *Stirling Engine Design Manual* by Martini (1983) for a more in-depth discussion of various second-order power losses.

the regenerator section is assumed to be at the hot-end temperature, whereas the working fluid leaving the cooler section and entering the regenerator is assumed to be at the cold-end temperature. The resulting temperature distribution through the five engine control volumes is depicted in Figure 2.4. The fluid temperature in the compression and expansion spaces vary over the cycle duration following reversible adiabatic compression and expansion, whereas the heater and cooler gas temperatures equal that of the heater and cooler walls. At the interfaces between compression and cooler, and similarly between heater and expansion space, the gas temperature is conditional upon the direction of flow. As a similar approximation to the ideal-isothermal model, it is assumed that no workspace gas leakage occurs and that the instantaneous pressure P varies only with time. To solve the system equations and determine the per-cycle work done and net efficiency, the continuity and energy equations, as well as equation of state, requires numerical solving.

Paul and Engeda (2015) applied the ideal adiabatic model to the GPU-3 Stirling engine and in addition to the five control volumes shown in Figure 2.4, have included two additional volume domains as 'heater-regenerator' and 'cooler-regenerator' manifolds to more accurately represent the engine's actual geometry. Similarly, an 'appendix gap' channel linking the expansion and compression spaces together has been included to estimate power loss by gas leakage. Power losses associated with the external heat transfer mechanism (combustion modelling) and the engine exhaust-gas recuperator are included to arrive at more realistic net thermal efficiency estimations. Although achieving good correlation to experimental data, the authors argue that since the ideal adiabatic assumption does not inherently account for viscous dissipation, the modelled power output and net efficiency are still typically overpredicted and should be corrected using an empirically related correction factor.

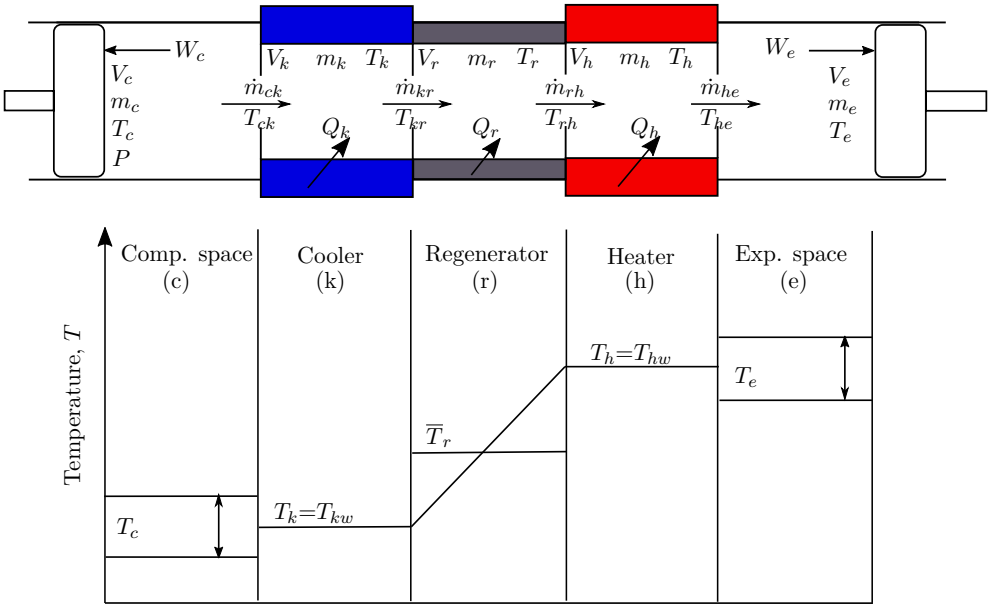

Figure 2.4: Temperature distribution through the five engine volumes, according to the ideal-adiabatic analysis (Adapted from Urieli and Berchowitz, 1984)

Simple analysis

As an extension of ideal-adiabatic cycle analysis, the *simple* analysis considers non-ideal effects on engine performance that were considered negligible in the aforementioned isothermal and adiabatic analyses. The simple analysis extends on the ideal-adiabatic analysis to include the non-ideal performance of the heater, regenerator and cooler by use of empirical relations to define heat exchanger efficiencies and quantify 'pumping losses' by flow friction dissipation. As outlined by Urieli and Berchowitz (1984), the heat exchanger performances are evaluated by following a Number of Transfer Units (NTU) analogy that is defined in terms of a Stanton number. With reference to Figure 2.4, this assumption implies that the actual gas temperature in the heater channel is lower than the heater wall temperature ($T_h < T_{hw}$), and that the gas temperature in the cooler channel is higher than the cooler wall temperature ($T_k > T_{kw}$). Due to the regenerator ineffectiveness, the linear gas temperature distribution previously assumed between hot and cold end shifts either towards the heater and cooler side depending on flow direction, resulting in a net temperature difference ΔT between expansion and compression stroke. Additionally, the frictional pressure drop ΔP through the regenerator may be quantified as a'pumping loss' by using an empirically related coefficient of friction. This flow loss is then used to further degrade the net per-cycle work done.

Both Snyman (2007) and Strauss (2013) have achieved success in applying the simple analysis method to model Stirling engine performance. Snyman discusses second-order models of increased complexity and has shown simulation results from the Simple analysis to correlate fairly well to experimental measurements performed on the Heinrici hot-air engine. However, he ultimately concludes that for a second-order model to capture the performance of a Stirling engine more accurately, model refinement is essential using experimentally determined correction factors (for example wall temperature, fluid friction and heat transfer coefficients). Strauss (2013) has further used the Simple analysis to investigate direct displacement control strategies for free-piston Stirling engines.

Free-piston dynamics

The operation of a free-piston Stirling engine may be simulated using a second-order method by adopting an approach in which the displacer and piston motions are first described as *linearised harmonic motion*. These dynamic analyses are often useful for early engine design optimisation or performance evaluation, as they can be computed analytically or numerically with little difficulty. To describe the engine thermodynamics, the assumptions of the ideal-isothermal model are inferred and it is assumed that the displacer and piston motions are purely sinusoidal (i.e. Schmidt's thermodynamic analysis is assumed). The approach then considers the displacer and piston as a two-degree-of-freedom dynamic mass-damper system, with the equations of motion written in the form (Kankam and Rauch, 1991):

$$[M][\ddot{X}] + [C][\dot{X}] + [K][X] = [F(t)] \tag{2.4}$$

where the matrices $[M]$ represent the coefficients of the mover masses, $[C]$ the coefficients of linearised damping and $[K]$ the coefficients of stiffness external to the thermodynamic cycle. The force vector $[F(t)]$ can be subdivided as being the sum

of the forces due to the thermodynamic cycle pressure, $[F_T(t)]$, and the appropriate time-dependent external forces $[F_E(t)]$ that act on the displacer and piston.

In the linearised dynamic approach, the thermodynamic pressure forces, $[F_T(t)]$, are linearised in terms of the displacer and piston mid-stroke locations. If linear spring stiffness and viscous damping are assumed, the coefficients of the dynamic equations may be rewritten to obtain closed-form expressions for angular frequency and displacer-piston phase difference. This is achieved by first using the method of Laplace transformation to convert the time-dependent linearised equation set to complex space with the nature of the solution of $[X]$ being characterised by the location of its poles in complex space. An important outcome of this approach is that well-established state-space or control-system methods may then be used to study and refine engine design parameters early in the design process (Riofrio *et al.*, 2008; Zare and Tavakolpour-Saleh, 2016). With the relationship between frequency, phase and strokes defined, one of the aforementioned cycle analyses can be performed to more accurately estimate the overall per-cycle work done and efficiency.

Often credited for first proposing the use of a linearised harmonic model, Redlich and Berchowitz (1985) investigated the requirements for steady operation of free-piston Stirling engines. By using the ideal-isothermal modelling approach to present the working fluid thermodynamics, and transforming the linearised equations to complex space, the authors investigated regions of stable and sustainable operation for different FPSE configurations. As a key finding, the authors showed that for sustained engine oscillation, there is a requirement for at least two roots (poles) of the piston solution to have a negative real part. In a physical sense this implies the requirements of some minimum temperature difference and displacer/piston stroke to achieve sustained engine operation. In 1986, Berchowitz (1986) published his dissertation on the design optimisation of Stirling engines in which specific focus was given to second-order approaches and the approximation of linear dynamics by which FPSEs may be modelled. Benvenuto *et al.* (1990) extended on the aforementioned analyses, by performing a linear dynamic analysis in which the pressure drop in the regenerator was also considered. As a key outcome, the pressure drop through the internal heat exchangers was shown to have a stabilising effect on engine oscillation.

As an improvement over linearised dynamic models, non-linearised dynamic models of FPSEs have also been studied (Zare and Tavakolpour-Saleh, 2019); the main difference being that the equations representing the engine pressure forces are not linearised. If the assumptions of the ideal-isothermal cycle analysis are invoked and Eq. (2.2) is substituted into Eq. (2.4) as part of the thermodynamic force term, and additionally the electrodynamic behaviour of the piston linear generator is considered, the non-linear equations of motions may be derived as outlined by Ulusoy (1994). The drawback of employing a non-linearised dynamic model is that the equation set can no longer be converted to complex space, and consequently, a closed-form solution can no longer be derived. Numerical solving of the system equations with temporal integration is thus required. The upside of employing a non-linearised model is that more realistic modelling assumptions may be inferred, such as that outlined for the aforementioned ideal-adiabatic or simple analysis methods.

Karabulut (2011) showed how a non-linear dynamic analysis may be solved as an initial value problem to a hypothesised free-piston Stirling engine. In his paper, Karabulut simplifies the thermodynamic cycle to being ideal-adiabatic. A sensitivity analysis of operational parameters was performed to highlight the narrow margin for stable operation, emphasising the requirement of employing some sort of engine feedback control to ultimately attain a stable limit cycle. Following a similar approach, Formosa (2011) derived a semi-analytical model of a free-piston engine in which the thermodynamic cycle is linked to the displacer and piston dynamics through an iterative solver. Numerical results were verified against experimental results of NASA's RE-1000 FPSE. Tavakolpour-Saleh *et al.* (2016) derived a dynamic model for a FPSE with non-linear springs based on a perturbation method. In their derivation, the authors infer the assumptions of the ideal-isothermal (Schmidt) model. However, in their model, the engine dynamic modelling is coupled to empirical finite-time heat transfer relations of the engine heat exchangers, allowing for more accurate estimates the steady-state internal gas temperatures to be used.

In spite of the reduced modelling complexity that second-order models may have over solving the full transport equations of the gaseous working fluid, it must be emphasised that the influence of real engine transients *cannot* be studied directly. This is the main drawback of *decoupling* the engine thermodynamic cycle from the displacer and piston kinematics. Still, it is worth noting that, due to their low computational requirements, second-order models coupled to linearised dynamic analyses are well suited for preliminary engine optimisation studies (Boucher *et al.*, 2007; Ramos, 2015). Relating to free-piston type engines in particular, if a closed-form solution to the engine dynamics is not required, a non-linearised dynamic model with the assumptions of an ideal-adiabatic thermodynamic cycle may be preferred.

2.4.3. Third-order or nodal design methods

Third-order or nodal design methods model a complex system of working fluid thermodynamics and piston and displacer dynamics, which in reality simultaneously influences one another. According to Chen and Griffin (1983) this method consists of three principal steps, that are: (i) Dividing the workspace into an array of one-dimensional finite control volumes; (ii) deriving finite difference equations by applying the principles of conservation of mass, momentum, energy to the gas control volumes and an applicable equations of state for the working gas; and (iii) solving the resulting finite difference equations numerically.

Third-order models may furthermore be classified as 'rigorous' or 'less rigorous'. In the latter case, the working fluid kinetic energy is neglected. This reduces the momentum equation to a quasi-steady state, i.e. the pressure gradient is only induced by flow friction. If the further simplifying assumption of a negligible spatial pressure gradient is made, as is done with the aforementioned isothermal and adiabatic cycle analyses, the momentum equation becomes redundant. Urieli (1977) notes that elimination of the gas momentum equation vastly decreases the required computational time, by permitting the solving of larger time-steps in contrast to the more time-step sensitive pressure-velocity coupling of more rigorous models. However,

an additional equation is then required to infer the engine temporal pressure variation (Martini, 1983). Deetlefs (2014) showed that to facilitate solving the system equations for pressure, density and temperature, the assumption is made that the workspace gas mass remains constant, i.e. there is no gas leakage to the backspace. The instantaneous but uniform pressure through the working space is then solved by differentiating the ideal gas law with respect to time and reformulating the equation to be solved as a function of temporal volume and temperature variations.

Although Finkelstein (1975) is often credited for first employing a nodal analysis method in his development of a miniature Stirling cryocooler at the University of Calgary in 1969, to date, the dissertation published by Israel Urieli (1977) at the University of Witwatersrand remains arguably the most thoroughly documented third-order model of the Stirling cycle available from published literature. In his dissertation, Urieli solves the complete set of working fluid transport equations, including the gas kinetic energy in the momentum equation, as an initial value problem to a hypothesised kinematic type Stirling engine. Independently from Urieli, Schock (1978) from Fairchild Space and Electronic Company (now Fairchild Corporation) developed a rigorous third-order computer simulation program named *Stirling Engine Nodal Analysis Program* (SNAP). In this model, the transport equations are solved using an explicit forward-marching-in-time solver. In contrast to Urieli's model in which the transport equations have been manipulated to yield relations for gas density, velocity and temperature, Schock retains the conservation equations in integral (conservative) form for mass, momentum and energy. Although Urieli and Schock both made significant contributions to the field of third-order modelling, the displacer and piston motions were defined as input parameters to the numerical model. Azetsu (1982) from the University of Tokyo developed a similar third-order model, which has been validated against experimental results of a 25 kW in-house developed kinematic-type Stirling engine. Azetsu assumes a quasi-static approach by neglecting the gas kinetic term of the momentum equation and estimates frictional pressure drop and engine pumping losses from empirical steady-flow correlations.

Under contract from the United States Department of Energy, NASA's Lewis Research Centre developed a less rigorous third-order numerical model for the Department's Stirling Engine Highway Vehicle Systems Program – that ultimately envisaged using Stirling engines to replace conventional spark-ignition engines (Tew, 1983). In a similar approach to Azetsu, the model assumes a quasi-static approach to omit solving the full gas momentum equation. Using a fully-explicit solver the gas pressure at the centre of the regenerator channel is computed from the ideal gas equation. The energy equation is solved explicitly to determine the new gas temperatures, then the fluid mass distribution through the working space is inferred by assuming that the fluid will redistribute itself in accordance with the new engine volumes and gas temperatures to maintain the uniform pressure throughout the workspace. Mass flow rates are computed from the rate of change in control volume mass and used to infer the gas velocity profile. Accordingly, the model predicts decoupled pressure losses using steady flow correlations related to velocity. Tew's model has been evaluated against experimental data from the GPU-3, United Stirling's P-40 and Sunpower's Re-1000 Stirling engines in a report published by

Sullivan (1989), with the modelled indicated power typically being over-predicted by between −11 to 16 percent due to an over-prediction in gas pressure.

In 1987, Goldberg (1987) from the University of the Witwatersrand extended on both Urieli and Berchowitz' previous studies. In his dissertation, Goldberg derives first a linearised dynamic analysis model of a back-to-back FPSE based on state-space theory, and secondly, a fully-implicit third-order model that includes a turbulence model for the engine heat exchanger sections. Goldberg validated the state-space model against experimental results from the RE-1000 FPSE, and the third-order model against experimental results from the GPU-3 kinematic Stirling engine: both models were found to be in reasonably good agreement with their experiments. Under contract for NASA's Lewis Research Centre, Goldberg (1990) later validated his implicit third-order model against experimental results of NASA's Space Demonstrator Engine. In this follow-up study, Goldberg also considered two-dimensional axisymmetric flow in the heater section, although it was found that the only slight increase in model accuracy above the fully one-dimensional model did not justify the increased model complexity. Despite achieving an overall good agreement with experimental data, it was observed that, due to the infinite rate at which gas thermodynamic information may propagate in his implicit cyclic equilibrium model used, a notable discrepancy between the simulated and measured phase difference between the pressure swing and the power piston resulted. This arguably led to a 30 % over-prediction in the simulated piston indicated power.

In 1992, Yuan and Spradley (1992) from Lockheed Missiles and Space Company (now Lockheed Martin) published a study on the development of a third-order model for split-cycle Stirling refrigerators – with validation having been performed on the Lucas Stirling Refrigerator. Unfortunately, the system equations and modelling procedures were not thoroughly documented. The authors only list the one-dimensional transport equations for mass, momentum and energy and mention that the equations have been solved using a CSSL (Continuous System Simulation Language) computer program. More recently in 2006, Anderson (2006) from the Technical University of Denmark published a dissertation on an in-house developed, semi-implicit, one-dimensional program named MUSSIM (Multipurpose Software for Simulation). In his study, Anderson transforms the ordinary differential equations (ODEs) for mass and energy into ODEs for pressure and temperature, using the ideal gas law and neglecting the gas kinetic energy term in the energy equation. Given the displacer and piston motion as model input parameters, MUSSIM integrates the governing differential equations using either an explicit or implicit Runge-Kutta scheme. A *shooter-predictor* method is then employed to find the dynamic steady-state operating cycle, in contrast to using a more elementary *integrate to convergence* approach. Relating to Stirling engines, Anderson has shown good correlation to experimental results from both the *SM5* Stirling engine and the *Twinbird* free-piston cryocooler.

At Stellenbosch University, Smith (2006) took a different approach in developing an implicit one-dimensional model for a pulse-tube cryocooler. The transport equations were solved as a boundary value problem with linear harmonic analysis (the piston representing a cyclical pressure boundary). Smith employs a backwards-staggered

velocity grid to solve the momentum balance equation; the continuity equation is used in the form of a pressure correction equation. These equations are solved using a tri-diagonal matrix algorithm (TDMA), after which the cell densities and interface node velocities are corrected. The energy equation is then solved implicitly for the working fluid and surrounding environment. Relating to FPSEs, Deetlefs (2014) developed a quasi-static third-order model based mainly on the assumptions made by Urieli (1977). Results have been verified against that of a modified Beale B-10 demonstrator engine from Sunpower Inc. However, simulation and experimental results were not well correlated, arguably due to grossly simplifying assumptions regarding the heat transfer rates and not having taken gas leakage into account.

In spite of the increased computational power over the last decades that have made solving more complicated third-order models considerably quicker, at the time of writing the computer program Sage by Gedeon Associates (2016) remains arguably the only commercially available software package for modelling Stirling cycle machines. Sage is the successor of the computer program *GLIMPS* (Globally-Implicit Stirling Cycle Simulation) and is based on a third-order numerical model that employs a backwards-staggered velocity grid. The program requires that heater and cooler temperatures to be specified along with the piston motion as input parameter. Sage then computes the periodic steady-steady operation by solving conservation of mass, momentum and energy equations implicitly over a discretised spatial domain. Both Sunpower (2016) and the late Infinia Corporation have extensively used Sage in their efforts to develop FPSEs fit for space application (Wood *et al.*, 2010), contributing to the widely accepted confidence in the model's fidelity. More recently, Qiu *et al.* (2019) employed Sage in the development of their one kilowatt electrical FPSE for micro CHP application. However, due to program licensing costs being expensive and solver algorithms being protected under intellectual property legislature, limited published literature is available on the program aside from its user manual. More sophisticated and accurate solutions than Sage are attainable using two- and three-dimensional computational fluid dynamic (CFD) models (Mahkamov, 2006; Dyson *et al.*, 2008; Mohammadi and Jafarian, 2018), but since these higher-order models are timely to construct for changing engine design parameters, they have not been considered in the context of this study.

To conclude the discussion relating to third-order models, it should be emphasised that third-order methods are the most capable of simulating the intrinsically linked thermodynamic and kinematic behaviour of a real Stirling engine. However, due to the significant computational resources that have traditionally been required to solve such models, rigorous third-order approaches still remain largely understudied in the literature today. Most published third-order models date back to the 1980s, followed by a period of decreased research interest during the '90s and early 2000s, arguably as funding on NASA's FPSE program was reduced. To the author's best knowledge, no transient third-order model in published literature considers the inherent coupling between the working fluid thermodynamics and generator electromechanical behaviour. This is especially important for free-piston type engines, as the actual non-linear displacer and piston motions are highly dependent on the coupled working fluid thermodynamic and linear generator electromechanical interaction.

2.5. Summary

This chapter has presented a brief history of Stirling engines with emphasis on the free-piston variant. The idealised working cycle of a Stirling engine has been discussed with the aid of PV and TS diagrams, and an overview of prevalent theoretical modelling approaches found in the published literature have been presented. These may be classified as first-, second- and third-order modelling approaches with the increased numbering indicating increased model complexity.

From the available literature it is postulated that the first- and second-order modelling methodologies are not well suited to act as comprehensive design tools for the development of a free-piston Stirling engine, since these models do not consider the intrinsically linked thermodynamic, kinematic and electrodynamic behaviour. Although second-order ideal-adiabatic or simple analysis methods are satisfactory to studying and improving existing engines, it is argued that they can only provide limited insight into the ground-up development efforts of a FPSE, as these analyses traditionally consider the displacer or piston motions as input parameters to the thermodynamic model with the assumptions of linearised movement. In employing these methods the inherent 'coupling' between working fluid thermodynamics, the displacer and piston kinematics, and the generator electrodynamics is sacrificed for the convenience in solving and optimising these constituents separately.

Third-order models may offer a considerable improvement over second-order methods as the working fluid transport equations are considered. However, in the existing published literature, simplifying assumptions regarding the piston and displacer motion are still generally made. Such assumptions range form specifying both the piston and displacer motions (and phase difference) as input parameters, to linearising the acting engine load and pressure forces, to neglecting the gas momentum equation and using a quasi-static approach. To reduce computational time, 'less rigorous' analyses are traditionally employed that omit solving the gas momentum equation completely. As with second-order models, there has been a preference to studying the engine thermodynamics separately from the piston and displacer linked kinematics and generator electrodynamics (e.g. the engine dynamics are partially constrained by specifying the piston motion as a boundary condition in Sage).

With reference to the study's research objectives that have been outlined in Chapter 1.2, it is hypothesised that a rigorous third-order model that is directly coupled to non-linearised displacer and piston dynamics would be best suited as a detailed design tool for the ground-up development of a working FPSE prototype which, in turn, could be used to validate its underlying theoretical basis. It is to the author's best knowledge that in all the published literature surveyed, there existed no available third-order model that considers the intrinsically linked thermodynamic, kinematic and electrodynamic behaviour of a FPSE that is *also* capable of solving and emulating *real* engine transients (this includes the fluid stress waves induced by a piston or displacer collision). A numerical simulation tool fit for FPSE should be capable of predicting the non-linear motions of the displacer and piston as simulation outputs, as in free-piston engines, these parameters are in fact unknown.

3. Derivation of a third-order theoretical model

In this chapter, the derivation of a *rigorous third-order* theoretical model of a free-piston Stirling engine prototype is presented. The derivation starts with a schematic illustration of the prototype under consideration, which is subsequently discretised into sequential arrays of one-dimensional control volumes representative of the engine gas and metal sections. The governing transport equations are derived in a fully-explicit form by applying the conservation of mass, momentum and energy to the gas control volumes. Modelling assumptions pertaining to the main engine control volumes are discussed and thermal networks representative of heat transfer for the heater, regenerator and cooler channels are derived. The chapter is concluded with a derivation of the non-linearised equations governing the free-running displacer and power piston motions.

3.1. Overview of an engine prototype

An illustrative drawing of the novel, single-cylinder engine prototype considered throughout this study is given in Figure 3.1. The principal model dimensions (or naming of the model variables) are depicted in Figure 3.2. The engine is sealed within a pressure-retaining engine casing that is charged with helium gas as the working fluid. A ceramic band electrical heater and a water cooling jacket are attached to the outside of the casing, to supply the heating and cooling loads during experimental operation. Inside the engine casing, axially aligned copper fins transfer the heating and cooling loads to the gas working fluid. Located between the heater and cooler fins is a copper mesh-screen regenerator that functions as a gas recuperator to pre-heat and pre-cool the working fluid during its respective expansion and compression blows. According to Ibrahim and Tew (2012), this unique application to Stirling

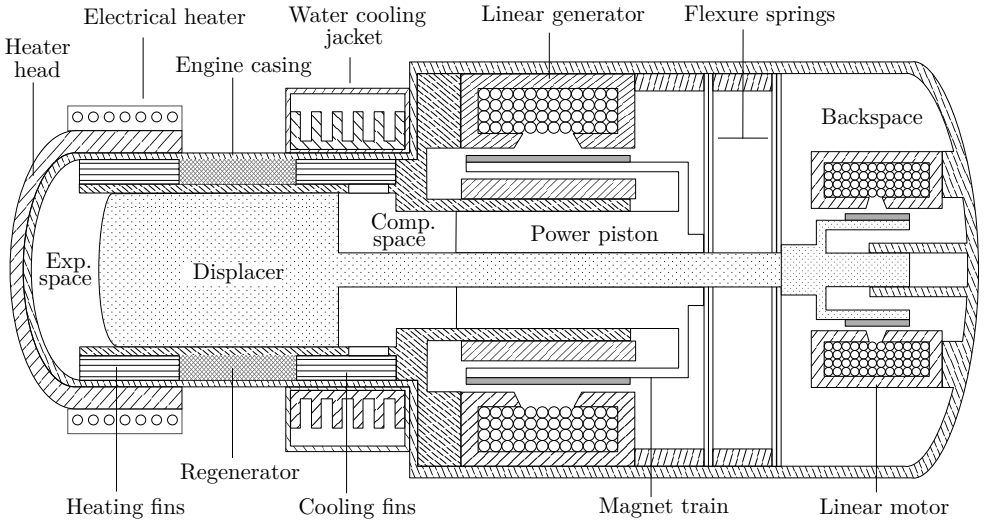

Figure 3.1: Cross-sectional drawing of the free-piston Stirling engine prototype

engines reduces the thermal requirements of the heater and cooler, consequently allowing these engines to approach thermal efficiencies of Carnot.

Traditionally, free-piston Stirling engines have only two moving components: the displacer and the power piston. The displacer shuttles the working fluid from the expansion space to the compression space and vice versa. As the working fluid moves from the compression space and into the expansion space it is heated by the electrical heater. This thermally expands the working fluid; the working fluid pressure builds up and forces the power piston outwards, through its *expansion stroke* and into the backspace. In turn, when the gas is shuttled in the opposite direction and passes into the compression space, it is thermally contracted by the cooler. In this engine layout both the power piston and displacer are attached to respective flexure springs – to provide the required restoring forces of the Stirling cycle and additionally provide mechanical stroke centring. Due in part to the generator load forces acting on the power piston (and sometimes lower natural frequency of the power piston assembly) its motion lags behind that of the displacer as the piston, in fact, resonates with the thermally induced workspace pressure swing. The difference in phase between the displacer and power piston induces a secondary pressure variation in the working space as the gas is expanded or compressed by the moving piston, which in turn, acts as a differential driving force on the displacer shaft. When this induced differential gas pressure force acting on the displacer shaft (including the gas force from the backspace) is sufficient to overcome fluid and mechanical friction losses, both the displacer and piston resonate (reciprocate) indefinitely in a self-sustained fashion.

To extract usable work from the engine, the power piston is attached to a magnet train which, together with a stationary toroidally wound copper coil and soft-iron stator assembly, forms a linear electric generator. The generator voltage is traditionally controlled by use of power electronics modulation that limits the power piston

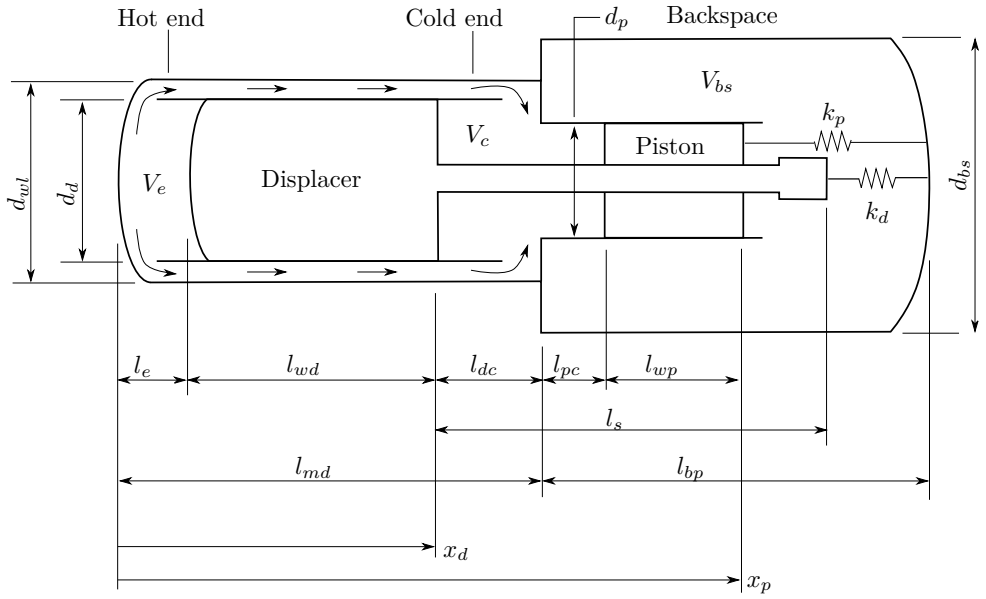

Figure 3.2: Illustration of FPSE showing the principal modelling dimensions

motion (and overall engine operation) around a pre-defined nominal stroke. However, in the scope of this work, the development of a generator controller has been omitted. Instead, as seen from the engine design-layout in Figure 3.1, the displacer shaft has been attached to a linear electric motor of a similar design located in the engine backspace. During experimental testing the motor was predominantly used to induce engine operation, and by doing so, validation of the numerical model could be extended to low charge pressures and moderate hot-end temperatures where self-sustained operation could not otherwise be achieved. The displacer motor is further envisaged as a possible means for providing direct control over the displacer motion in a future study, as was previously suggested by Strauss (2013).

The modelling dimensions depicted in Figure 3.2 are defined as input parameters to the theoretical model under consideration, and can readily be modified to perform a parametric investigation on the engine design layout. The model also accounts for a piston and displacer of differing diameters, as for the case of the considered prototype. Throughout the model derivation, the convention has been adopted that the displacer and power piston are moving in a *positive stroke* when moving from the *left* to the *right*. Both the power piston and displacer are 'sprung' to the stationary engine casing by flexure springs, having stiffnesses of k_p and k_d respectively. Positive fluid flow has been defined from the expansion space V_e through the heat exchanger channel and into the compression space V_c, as indicated by the arrows.

In the section that follows, the working fluid and engine metal sections are discretised into respective arrays of one-dimensional control volumes – to which the principles of conservation of mass, momentum and energy are applied.

3.2. Derivation of the governing fluid-dynamic equations

The approach adopted to modelling the working fluid thermodynamics is based on applying the principles of conservation of mass, momentum and energy sequentially to arrays of discretised one-dimensional finite control volumes (cells), as is illustrated in Figure 3.3. The heater, regenerator and cooler sections were each subdivided into N_h, N_r and N_k number of control volumes respectively, whereas the expansion, compression and backspace chambers were modelled as being fixed Eulerian control volumes with moving boundaries. The electrical heating jacket may either be defined as a constant temperature heat source T_h (or the temperature profile specified along the heater wall), or a heater flux $\dot{Q}''_{heat}$ may be specified and the heater wall temperature calculated as a model output. At the engine cold-end, the water cooling jacket was subdivided into a corresponding number of control volumes to model the gradual increase in water temperature, from inlet temperature $T_{w,i}$ to outlet $T_{w,o}$.

The working fluid control volumes, also referred to as *scalar* elements or cells, were defined as containing a finite amount of mass with uniform thermodynamic properties (such as density, pressure and temperature). Referring to Figure 3.3, these scalar control volumes are denoted by the subscript 'i' and have cell centres depicted by '$\bullet$'. The principles of conservation of mass and energy were applied to each scalar control volume to compute its mass and thermal energy (temperature). At the in-

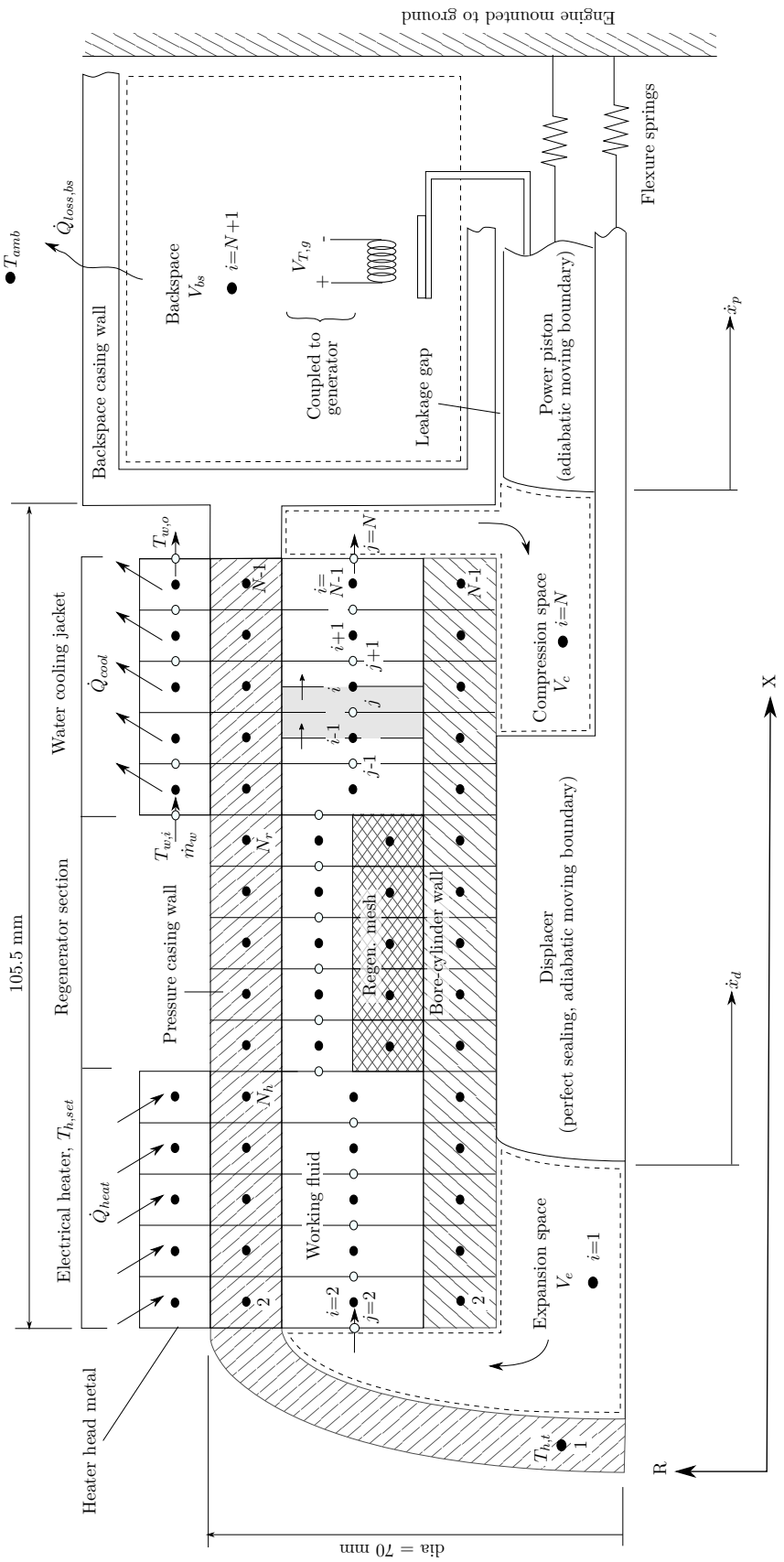

Figure 3.3: Discretisation scheme as applied to the engine working fluid and metal, illustrating external heat transfer of the heater, cooler and backspace, and also showing the positive direction of movement adopted by the model

terface between two consecutive control volumes where convective transport occurs, a boundary node was defined. Boundary nodes are denoted by the subscript 'j' and depicted by '$\circ$', and are employed to define the magnitude and direction of convective fluid flow that results due to an imbalance in pressure between neighbouring scaler cells. As is further illustrated by the shaded control volume in Figure 3.3, *vector* control volumes were staggered-stacked about the boundary nodes j – over half the upstream and downstream scalar control volumes. The principle of conservation of momentum was applied to each vector control volume to compute the fluid velocity at the boundary node. Patankar and Spalding (1972) note that by this *backwards staggering* of the vector control volumes, the pressure and velocity fields are coupled and the so-called *checker board* pressure-field phenomenon is avoided.

The governing differential equations for mass, momentum and energy were derived from first principles as is detailed in Appendix A, and spatially integrated by Gauss's Divergence Theorem to control volumes numbered 1 to $N+1$ as described in Appendix B. Euler's method was used to integrate the differential equations temporally to solvable finite difference equations of a fully-explicit form, to ultimately represent the control volume mass, momentum and thermal energy at a following time-step $t+\Delta t$. By using the ideal gas law as an equation of state, the working fluid volume V_i, mass m_i and temperature T_i were related to pressure P_i for each control volume i. The governing finite difference equations of a generalised scalar control volume i and vector control volume j are repeated in this chapter for convenience.

The finite rate of change in mass, as applied to the generalised scalar control volume i, is given in integral form by:

$$\frac{\Delta m_i}{\Delta t} = \left[\rho_j v_j A_j - \rho_{j+1} v_{j+1} A_{j+1}\right] \tag{3.1}$$

and the following time-step mass may be expressed in fully-explicit form by:

$${m_i}^{t+\Delta t} = m_i^t + \Delta t\left[\rho_j v_j A_j - \rho_{j+1} v_{j+1} A_{j+1}\right]^t \tag{3.2}$$

where the density ρ_j is obtained from first-order upwind differencing, velocity v_j is determined from the momentum balance equation, and the fluid-to-fluid interface area perpendicular to velocity is used for A_j.

The finite rate of change of momentum, as applied to the generalised vector control volume j depicted in Figure B.1 on page B-3, is given in integral form by:

$$\begin{aligned}\frac{\Delta}{\Delta t}(m_j v_j) = &\left[\rho_{i-1} v_{i-1}|v_{i-1}|A_{x_{i-1}} - \rho_i v_i|v_i|A_{x_i}\right] + \left[P_{i-1} - P_i\right]A_j \\ &-\left[\tau_{s_{i-1}}\frac{A_{z_{i-1}}}{2} + \tau_{s_i}\frac{A_{z_i}}{2}\right] - \left[\frac{1}{2}K_L \rho_j {v_j}^2 A_{x_j}\right]\end{aligned} \tag{3.3}$$

where the absolute velocity term is used to retain the scalar velocity direction. Furthermore, the vector cell mass m_j is defined as the sum of half the adjacent cell masses over which the vector volumes were staggered, A_x represents the cross-sectional flow area perpendicular to velocity, A_z is the wetted flow area parallel to velocity and A_j is the fluid-to-fluid interface area at node j. Urieli (1977) notes that by employing a backwards-staggered velocity grid, the cell centre velocity v_i

can be inferred from a volumetric flow interpolation between neighbouring interface (node) velocities v_j as acting over different cross-sectional flow areas. Additionally, the average fluid stress experienced by a finite cell is simplified to an empirically related shear stresses τ_s that is defined in terms of the cell centre velocity by means of an empirical steady flow coefficient of friction C_f. However, for the case of the expansion and compression space volumes – where rapid expansion or contraction occurs – an additional minor-loss body force that opposes the direction of flow is included, given by the loss coefficient K_L. No minor loss has been modelled at the interfaces on either side of the regenerator channel, as the fluid friction factor C_f is already encapsulating of this loss. Then, with rearrangement of Equation (3.3), the following time-step nodal velocity is given in a fully-explicit form by:

$$v_j{}^{t+\Delta t} = \frac{(m_j v_j)^t + \Delta t\big[DM + DP + DF\big]^t}{m_j^{t+\Delta t}} \tag{3.4}$$

where DM and DP represent the first and second terms of Equation (3.3) respectively, and DF the body forces of the third and fourth terms.

The finite rate of change in internal energy of the generalised scalar control volume i, depicted in Figure B.2 on page B-4, is given by the thermal energy equation:

$$\begin{aligned}\frac{\Delta}{\Delta t}(m_i u_i) = &\big[\rho_j v_j A_j u_j - \rho_{j+1} v_{j+1} A_{j+1} u_{j+1}\big] + \dot{Q}_{net} \\ &+ P_i\big[v_j A_j - v_{j+1} A_{j+1}\big] + \dot{W}_b + \tau_{f_i} A_{z_i} |v_i|\end{aligned} \tag{3.5}$$

where the specific internal energy u_j is obtained from first-order upwind differencing. To simplify the thermal energy equation, the work done on the working fluid by a moving boundary has been decoupled from the reversible compression or expansion work term and is represented by $\dot{W}_b$. The heat generated irreversibly by viscous dissipation is encapsulated by the surface friction term, where the absolute velocity $|\bar{v}_i|$ is indicative of the increase in thermal energy regardless of flow direction. The following time-step internal energy is given in fully-explicit form by:

$$(m_i u_i)^{t+\Delta t} = (m_i u_i)^t + \Delta t\big[DM_e + \dot{Q}_{net} + DP_e + \dot{W}_b + DF_e\big]^t \tag{3.6}$$

where DM_e, DP_e and DF_e represent the first, third and fifth terms of Equation (3.5) respectively. Accordingly, the new time-step specific internal energy $u_i{}^{t+\Delta t}$ is then calculated by dividing Equation (3.6) with the new time-step cell mass computed from Equation (3.2). The new time-step working fluid temperature is then related to specific internal energy in fully-explicit form, by:

$$T_i^{t+\Delta t} = T_i^t + \big(u_i{}^{t+\Delta t} - u_i{}^t\big)/c_v \tag{3.7}$$

in which c_v is the specific heat at constant volume, which has been assumed to remain constant over the range of temperatures, pressures and densities considered. From the ideal gas law, the control volume pressure is calculated according to:

$$P_i = \rho_i R_g T_i \tag{3.8}$$

where the density ρ_i is determined from the continuity equation and R_g is the specific gas constant for the helium working fluid.

3.2.1. Expansion space chamber

Figure 3.4 depicts the expansion space control volume as a scalar cell $i = 1$ that is connected to the heater channel with cell numbering $i = 2 \rightarrow N_h$. The illustration shows the defined positive movement direction of the displacer $\dot{x}_d$ as well as the defined positive direction of heat flow in the heater section. Furthermore, it shows a backwards-staggered momentum control volume with cell number $j = 2$ that is projected *into* the expansion space, forming a boundary condition to solving the gas momentum and fluid velocity using Equations (3.3) and (3.4), respectively. To simplify modelling, it has been assumed that the bulk of the working fluid located in the expansion volume is stationary, well mixed and may be represented by uniform thermodynamic properties such as temperature, pressure and density. Additionally, due to the low expected pressure difference between the expansion and compression spaces (i.e. across the displacer), gas leakage between the displacer dome and bore-cylinder wall has been assumed to be negligible.

The aforementioned simplifications imply that the expansion space has been modelled as a *fixed Eulerian control volume* with an adiabatic moving boundary (being the displacer dome) and that the volume of gas inside the expansion space can at any time be calculated given the displacer's position. Additionally, the figure illustrates the thermal resistance analogy that must be solved to compute $\dot{Q}_{net}$ in Equation (3.6). Heat is conducted axially from the casing cylinder top wall $T_{h,t}$ towards the heater channel wall $T_{wl,2}$ at $i = 2$ and so on in the direction of the regenerator. As depicted, convective and radiative heat transfer between the ex-

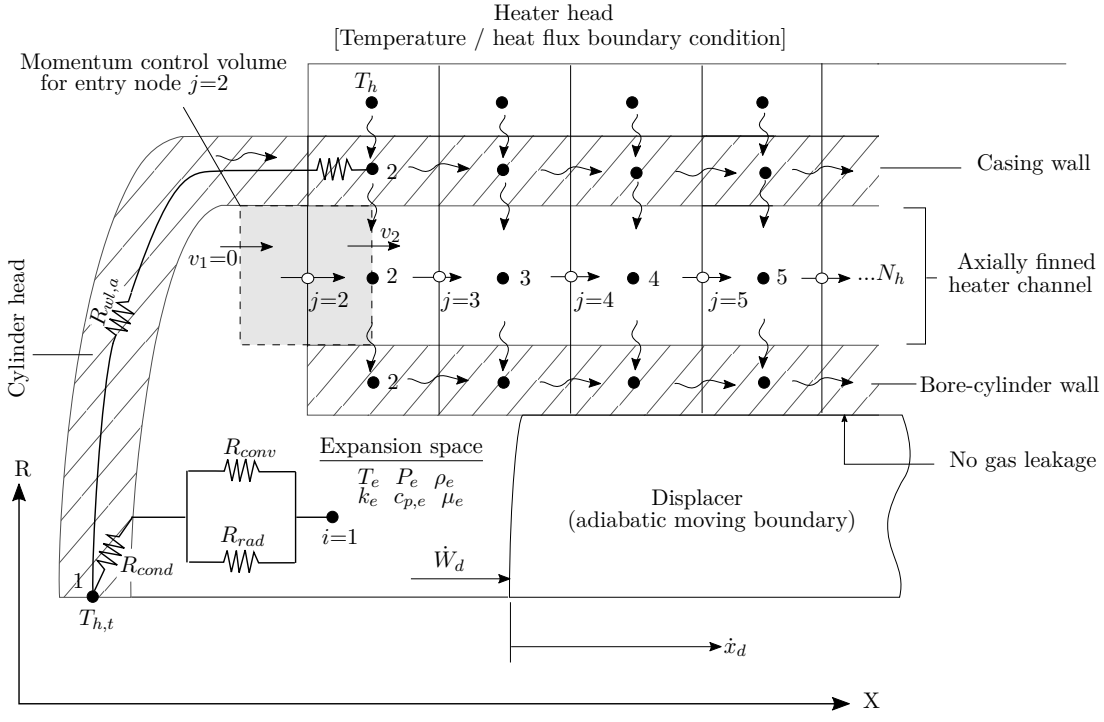

Figure 3.4: Illustration of the expansion space linking to the heater channel

pansion space wall and working fluid is considered, although heat transfer between bore-cylinder wall and the expansion space gas has been assumed negligible.

With reference to Equation (3.6), the rate of boundary work done by the working fluid *onto* the moving displacer dome is given by:

$$\dot{W}_d = -P_e \frac{dV_e}{dt} \tag{3.9}$$

where the negative sign is indicative of an expanding volume. The rate of change in volume for the expansion space is given by:

$$\frac{dV_e}{dt} = A_d v_d \tag{3.10}$$

for which a positive velocity is defined in the positive x-direction. The finite rate of change in volume, as defined in terms of the fully-explicit forwards differencing scheme, is given by:

$$\begin{aligned} \frac{\Delta V_e}{\Delta t} &= \frac{1}{\Delta t} \int_t^{t+\Delta t} (A_d \frac{dx_d}{dt}) dt \\ &= A_d \frac{{x_d}^{t+\Delta t} - {x_d}^t}{\Delta t} \end{aligned} \tag{3.11}$$

To calculate the gas inflow/outflow velocity at the interface node $j = 2$, an approach similar to that employed by Urieli (1977) has been adopted in which a shaded *vector* control volume is projected *into* the expansion space. As a boundary condition to the momentum equations in Equation (3.5), the velocity term v_1 at the left side of the shaded volume is set to zero, implying that the working fluid either supplies or dissipates the gas momentum nearly instantaneously upon exiting or entering the volume. The total minor loss coefficient K_L is considered the sum of a ninety-degree 'sharp bend' coefficient and the turbulent loss coefficient of either suddenly expanding or contracting flow:

$$K_L = 1.1 + 0.5 \qquad (v_j \geq 0); \qquad\qquad K_L = -(1.1 + 1.05) \qquad (v_j < 0) \tag{3.12}$$

where in the first instance, flow is contracting, and in the second instance, is rapidly expanding. Furthermore, the negative sign in the second instance is indicative that the loss term given in Equation (3.3) is always acting against the direction of flow.

The convective heat transfer coefficient in the expansion space is estimated from Equations (3.25) to (3.29) using the gas velocity v_2 at entry/exit to the expansion space to define the Reynolds number, whereas the radiation heat rate is calculated from:

$$\dot{Q}_{rad} = \sigma A_{wl} F (T_{wl}^4 - T_g^4) \tag{3.13}$$

in which σ is the Stefan-Boltzmann constant, A_{wl} is the dome surface area, and F is the product of emissivity and view factor – assumed to be 0.7, as has been suggested by Tew (1983). These heat transfer equations may further be rewritten

as equivalent thermal resistances:

$$R_{wl,conv} = \frac{1}{h_{conv}A} \; ; \qquad R_{wl,rad} = \frac{1}{\sigma AF(T_{wl}+T_g)(T_{wl}^2+T_g^2)} \tag{3.14}$$

which are solved explicitly as part of the gas and metal energy equations to ultimately calculate the new time-step metal and gas temperatures.

Upon a critical review of the modelling assumptions made, it must be noted that in reality, the displacer subjects the engine to some additional parasitic energy losses between hot and cold ends. When, for example, the displacer is located near the hot end, its average temperature increases. The opposite occurs when the displacer is nearer to the cold side. By this cyclic heating and cooling of the displacer dome a physical 'heat shuttling loss' is induced. Rinker *et al.* (2018) notes that in high-efficiency Stirling engines, the transport of energy by radiation occurring within the hollow displacer dome between hot and cold ends may be of significance – prompting engine designers to include axially stacked radiation shielding discs within the displacer dome to mitigate this effect. To simulate such displacer loss mechanisms accurately – and in a coupled fashion to solving the gas thermodynamics – the model could be expanded to also consider the displacer dome metal temperature. Additionally, this expanded model could then also be made to consider the thin gas channel (or displacer gas cushion) that exists between the displacer dome and bore-cylinder wall (often referred to as the displacer appendix gap). This would allow for more accurate modelling of the displacer temperature distribution and gas enthalpy leakage, which has otherwise been omitted in the scope of this study.

Instead of increasing the model complexity to this point, additional loss terms traditionally used in second-order analyses may be used to increase the third-order model's accuracy (Sayyaadi and Ghasemi, 2018). Such losses are, however, deemed *decoupled* from the working fluid dynamics as they are computed (or estimated) only at the end of the engine cycle and require the use of variables calculated during the cycle. To estimate the displacer shuttling loss, the equation by Tew (1983) is used:

$$\dot{Q}_{shuttle} = \frac{\pi}{8}\frac{k_g D_d S_d^2(\overline{T}_h - \overline{T}_k)}{\delta_{gap} L_d} \tag{3.15}$$

in which k_g is the working fluid thermal conductivity, D_d the displacer diameter, S_d the displacer stroke, δ_{gap} the clearance gap distance between displacer wall and bore cylinder, and L_d the displacer length. The overlines denote that the average hot and cold end gas temperatures were used to approximate the temperatures at either side of the displacer. Additionally, the rate of heat conducted axially within the displacer wall may be calculated from:

$$\dot{Q}_{wll} = \frac{k_d L_d}{A_{x,wll}}(\overline{T}_h - \overline{T}_k) \tag{3.16}$$

in which k_d is the thermal conductivity of the displacer metal and $A_{x,wll}$ the cross-sectional area of its wall. Then, to calculate a more realistic thermal efficiency, these additional losses must be added to the heater input requirement.

3.2.2. Compression and backspace chambers

The one-dimensional control volume layout of the compression space with its interconnecting cooler channel and engine backspace chamber is illustrated in Figure 3.5. Analogous to the expansion space, the working fluid is thermally contracted as it moves through the cooling channel and into the compression space. Heat is conducted axially along the casing and bore-cylinder walls in the direction of the compression space (cell number N). An insulated boundary has been assumed between the casing and backspace walls. As shown by the thermal resistance diagram, the backspace gas loses heat at a rate $\dot{Q}_{loss}$ to the ambient surroundings through the uninsulated backspace casing wall.

Modelling simplifications similar to that of the expansion space have been invoked. This includes inferring a momentum control volume into the compression space with a zero velocity boundary and the addition of a sudden compression/expansion minor loss term in the momentum equation at this inflow/outflow interface, with the sign of K_L given in Equation (3.12) reversed. In contrast to the expansion space, however, no convective or radiative heat transfer is modelled between the casing wall and the working fluid, thus the compression space may be viewed as being analogous to an adiabatic control volume with two moving boundaries. The compression space volume is computed from the instantaneous power piston and displacer positions, wherein this instance, both the displacer and power piston are depicted as moving in the positive x-direction (from left to right).

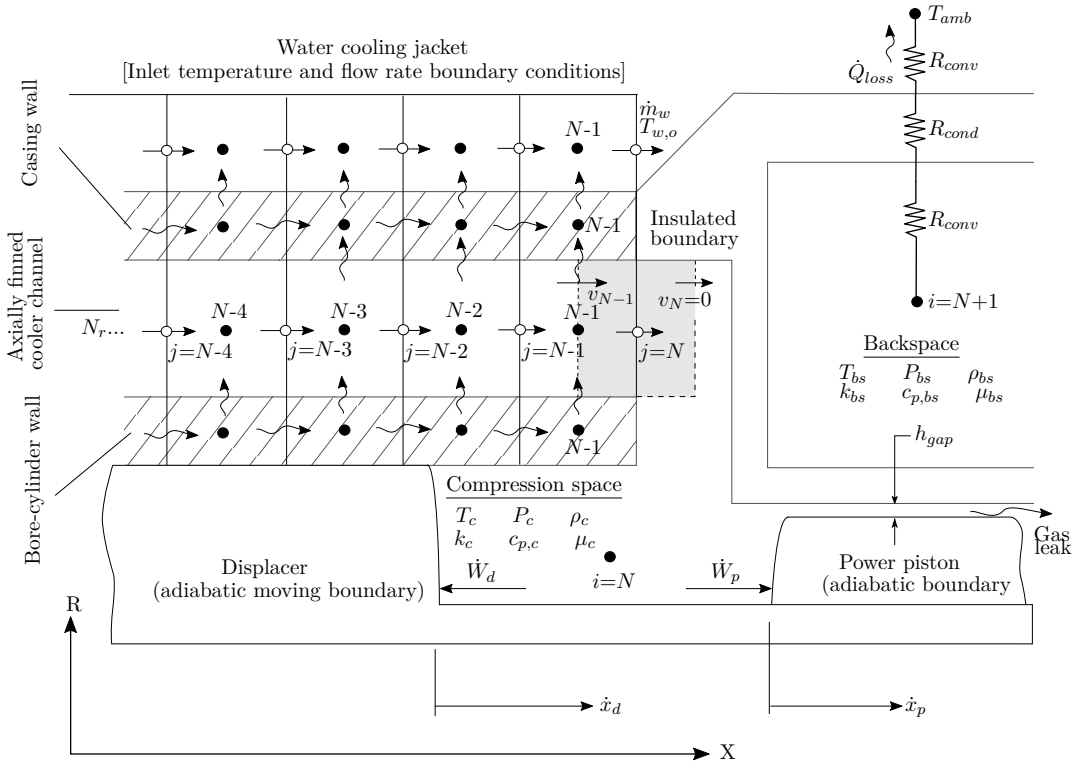

Figure 3.5: Illustration of the compression and backspace volumes

The net rate of boundary work done by the displacer and piston onto the working fluid is given by:

$$\dot{W}_b = -P_c \frac{dV_c}{dt} \tag{3.17}$$

The net rate of change in volume for the compression space is given in terms of piston and displacer motion as:

$$\frac{dV_c}{dt} = v_p(A_p - A_s) - v_d(A_d - A_s) \tag{3.18}$$

where A_s represents the cross-sectional area of the displacer shaft. The finite rate of change in volume may be rewritten in explicit form as:

$$\begin{aligned} \frac{\Delta V_c}{\Delta t} &= \frac{1}{\Delta t}\int_t^{t+\Delta t} ((A_p - A_s)\frac{dx_p}{dt} - (A_d - A_s)\frac{dx_d}{dt})dt \\ &= (A_p - A_s)\frac{x_p^{t+\Delta t} - x_p^t}{\Delta t} - (A_d - A_s)\frac{x_d^{t+\Delta t} - x_d^t}{\Delta t} \end{aligned} \tag{3.19}$$

Figure 3.5 showed that a small amount of gas leakage occurs through the thin annular passage that exists between the piston wall and bore cylinder. By considering this gas leakage, the piston's tendency to *drift* or *creep* from its mechanical mid-stroke location can be simulated more accurately; a phenomenon that Walker and Senft (1985) ascribe to occur as a net amount of gas leaks to the backspace during operation. Grinnell (1956) has theoretically and experimentally evaluated compressible flow phenomena through thin annular passages of non-contact seals with excellent correlation. Modelling of the leakage channel has been simplified as being zero dimensional, with mass transport across this 'boundary' being isothermal (i.e. temperature dependent on flow direction). If the assumptions of isothermal, fully-developed laminar flow are inferred, the mass flow rate and thermal energy transport by gas leakage may be estimated analytically by:

$$\dot{m}_{leak} = \frac{\pi D h^3}{24 \mu R_g T L}({P_c}^2 - {P_{bs}}^2); \quad \text{and} \quad \dot{U}_{leak} = \dot{m}_{leak} u \tag{3.20}$$

in which the flow is defined as being positive if leakage occurs from the compression space P_c towards the backspace P_{bs}, with D being the diameter of the cylinder bore, h the gap height between the cylinder bore and piston wall and L the length of the leakage gap. By employing linear upwind differencing, thermodynamic properties such as temperature, density and specific internal energy are defined conditionally upon the flow direction.

The reversible rate of boundary work done *by* the compression space *onto* the leakage channel is given by:

$$\begin{aligned} P dV_l &= (PvA)_l \qquad \text{where} \quad v = \dot{m}/\rho A \\ &= P(\frac{\dot{m}}{\rho A})_l \qquad \text{where} \quad \rho = P/R_g T \\ &= (\dot{m}_l R_g T)_l \end{aligned} \tag{3.21}$$

If the heat transfer associated with thermal expansion/contraction of the gas passing

from one reserve to the other is assumed negligibly small (i.e. the net rate of heat transfer to the zero-dimensional leakage node denoted '$_l$' is zero) the rate of boundary work that is exerted *by* the backspace *onto* the leakage channel equals $-PdV_l$.

3.2.3. Heater thermal resistance network

To increase the heat transfer surface area, the internal heater channel consists of 135 axially aligned copper fins. As illustrated by the thermal resistance analogy in Figure 3.6 (a), the direction of heat flow has been modelled as being positive from the outside of the engine casing wall T_h, through the pressure casing wall and towards the entrapped working gas channel at temperature T_g. In addition to transmitting heat from the hot-end to the working fluid, the internal fins conduct heat radially from the fin base temperature T_b across the breadth of the fins and into the displacer bore-cylinder wall, which is then conducted axially towards the regenerator side. To simplify modelling, radiation heat transfer between metal and gas is not considered within the finned duct and the displacer wall is treated as an insulated boundary.

In Figure 3.6 (b) the thermal resistance network is given with the inclusion of axial conduction and advection. The resistance network is solved explicitly to compute the following time-step cell temperatures $T^{t+\Delta t}$. The model considers axial conductive heat transfer in the engine metal (casing wall, heater fin and bore-cylinder) with thermal resistances of $R_{wl,a}$, $R_{f,a}$ and $R_{cw,a}$ respectively. As will be discussed in Chapter 5, this axial conductive heat transfer in the casing and bore-cylinder walls significantly reduces the performance and thermal efficiency of the prototype, and is therefore important to take into account. Furthermore, axial conductive heat transfer is also considered within the working fluid (with a thermal resistance of $R_{g,a}$), despite energy transfer between adjacent fluid cells being dominated by advection.

To simplify modelling of the internally located fins, the heater channel is approximated as a smooth duct with equivalent hydraulic diameter d_h, given by:

$$d_h = \frac{4A_{x_f}}{p_w} \tag{3.22}$$

in which A_{x_f} is the cross-sectional fluid area within the finned duct and p_w is the wetted perimeter. This flow area, being perpendicular to the fluid velocity, is calculated by:

$$A_{x_f} = \pi[r_b^2 - (r_b - l_f)^2] - (N_f l_f t_f) \tag{3.23}$$

in which r_b is the radius at the fin base, l_f the fin length, t_f the constant fin thickness and N_f the total number of square fins.

The fin wetted perimeter p_w is given by:

$$p_w = N_f(2l_f + r_b\theta_f) \tag{3.24}$$

where θ_f is the angle of opening between two adjacent fins.

The calculation of heat transfer and fluid friction relations have been based on empirical correlations of steady flow conditions, as is often done in literature. For

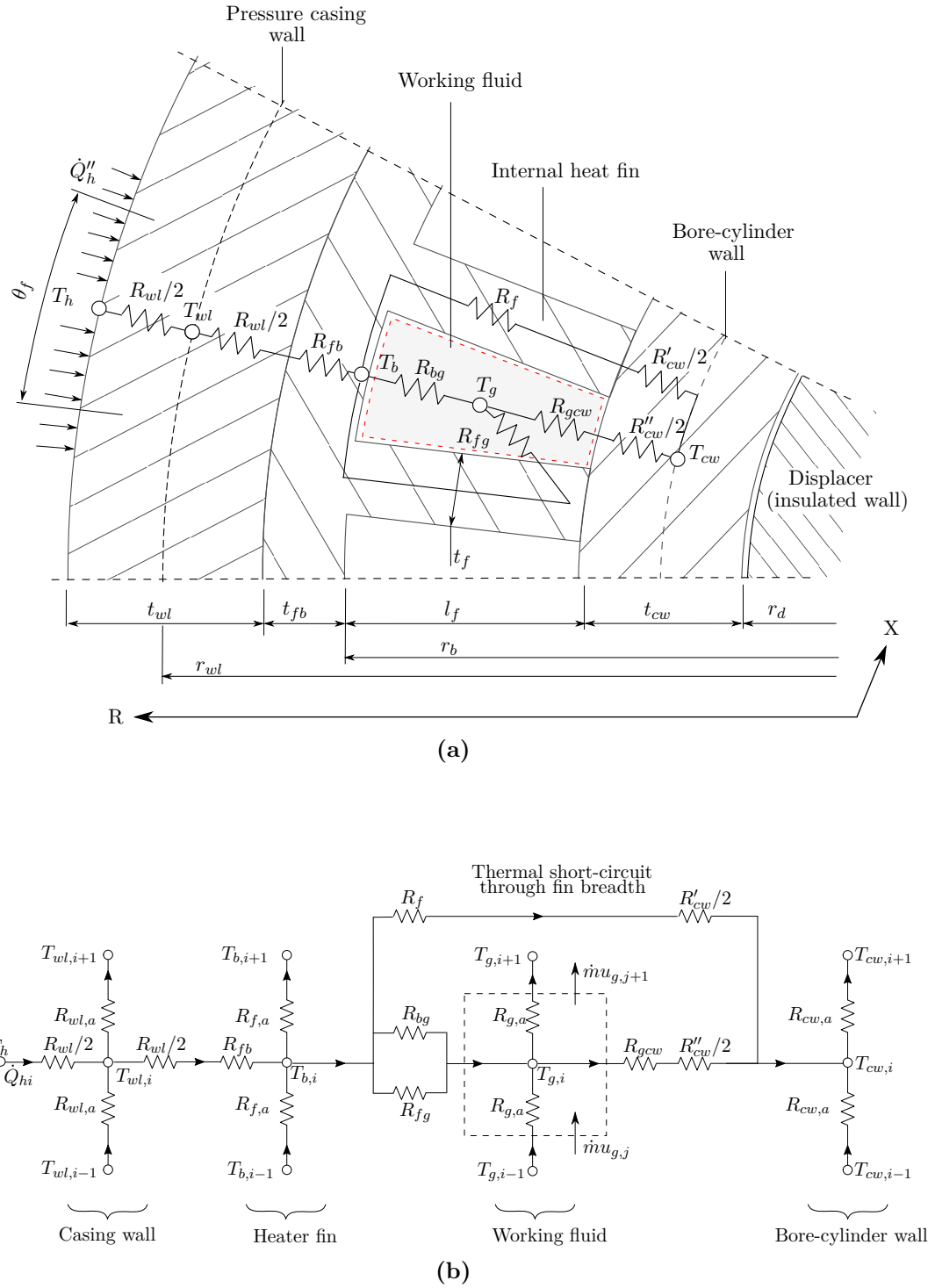

Figure 3.6: (a) Thermal resistance analogy as seen between casing wall, heater fin, working fluid and bore-cylinder wall when viewed from above, (b) thermal resistance network as seen from the side with the addition of axial heat flow

Reynolds numbers less than or equal to unity, the skin coefficient of friction was set to 16. For laminar fluid flow the coefficient of friction is proposed to vary hyperbolically with Reynolds number:

$$C_f = \frac{16}{Re} \qquad (1 < Re \leq 2300) \tag{3.25}$$

and for the transitional to turbulent flow regimes, the skin coefficient of friction was simplified to the Petukhov power law correlation (Mikalsen and Roskilly, 2007):

$$C_f = 0.25(0.79 \ln Re - 1.64)^{-2} \qquad (Re > 2300) \tag{3.26}$$

For fully-developed laminar flow, the gas Nusselt number is approximated by:

$$Nu = \frac{4.66 + 3.67}{2} \qquad (Re \leq 2300) \tag{3.27}$$

which represents the linear average value between constant wall heat flux and constant wall temperature boundaries of fully-developed smooth duct flow (Mills and Ganesan, 1999). For transitional to fully-developed smooth duct flow the Gnielinski equation is used:

$$Nu = \frac{(4C_f/8)(Re - 1000)Pr}{1 + 12.7(4C_f/8)^{1/2}(Pr^{2/3} - 1)} \qquad (3000 \leq Re \leq 5 \times 10^6) \tag{3.28}$$

and for Reynolds numbers in between these values, i.e. 2,300<Re<3,000, a linear interpolation is proposed to approximate the Nusselt number, as suggested in the VDI Heat Atlas (2015). The gas convective heat transfer coefficient h is then related to Nusselt number using the heater fin hydraulic diameter:

$$h = \frac{kNu}{d_h} \tag{3.29}$$

The casing wall, fin base and bore cylinder walls can be simplified as being thin-walled vessels, having radii to thickness ratio's greater than 10. Therefore, the calculation of their thermal resistances was simplified to the conduction analogy across equispaced flat walls. Referring to Figure 3.6 (b), the heater fins were modelled as being at a uniform base temperature T_b by employing a fin-efficiency analogy. According to Çengel and Ghajar (2011), the fin efficiency for a straight rectangular fin is given by:

$$\eta_f = \tanh\left(\sqrt{\frac{2h}{kt_f}} l_f\right) \Big/ \left(\sqrt{\frac{2h}{kt_f}} l_f\right) \tag{3.30}$$

so that the thermal resistance from the fin base to the entrapped working fluid control volume of length Δx may be calculated according to:

$$R_{b-g} = \left(h(r_b \theta_f N_f \Delta x) + \eta_f h(2 l_f N_f \Delta x)\right)^{-1} \tag{3.31}$$

The conductive resistance between the casing wall and fin base is calculated by:

$$R_{wl-b} = \frac{t_{wl}/2}{k_{wl}(\pi d_{wl} \Delta x)} + \frac{t_{fb}}{k_f(\pi d_b \Delta x)} \tag{3.32}$$

and assuming that the heater fins have a uniform thickness t_f, the thermal resistance from the fin base to the centre of the bore-cylinder wall is given:

$$R_{b-cw} = \frac{l_f}{k_f(t_f \Delta x N_f)} + \frac{t_{cw}/2}{k_{cw}(t_f \Delta x N_f)} \tag{3.33}$$

The thermal resistance from the working fluid to the centre of the bore-cylinder wall is given by:

$$R_{g-cw} = \frac{1}{h(r_{cw}\theta_f N_f \Delta x)} + \frac{t_{cw}/2}{k_{cw}((d_{cw}\pi - t_f N_f)\Delta x)} \tag{3.34}$$

Furthermore, the thermal resistance of any form of axial conductive heat transfer considered may be written as:

$$R_a = \frac{\Delta x}{k A_x} \tag{3.35}$$

in which k is the cell's thermal conductivity and A_x is the cross-sectional area of either the fluid or metal under consideration. Once all thermal resistances have been calculated, the engine metal temperatures are computed by solving the thermal energy balance equation explicitly:

$$T^{t+\Delta t} = T^t + \frac{1}{mc}\Delta t\left(\frac{\Delta Q_{net}}{\Delta t}\right)^t \tag{3.36}$$

in which $\Delta Q_{net}/\Delta t$ is net heat transfer rate defined *into* the metal cell as calculated from the thermal resistance analogy using the previous time-step temperatures, m is the metal cell's mass and c is the metal specific heat.

3.2.4. Cooler thermal resistance network

Similarly to the heater channel, the cooler heat exchanger consists of 135 axially aligned internal fins machined from copper to maximise the heat transfer surface area with the working fluid. In contrast to the heater modelling, the heat transfer direction has been defined as positive from the gas to the cooling fins. Moreover, as shown in Figure 6.6 on page 89, heat is rejected to an externally located, radially-finned water cooling jacket. The water-side fins are spirally machined channels having a fin pitch $p_{f,w}$ as shown in the figure. Similar empirical relations for convective heat transfer and fluid friction have been applied to the internal cooling fins as was outlined for the heater channel. In addition to the equations derived throughout Chapter 3.2.3, in this section, the thermal resistance analogy is extended to model heat transfer from the casing wall to the cooling water channel.

Figure 3.7 (a) gives a schematic cross-section of the radially finned cooling jacket, the casing wall, the internal cooling fins, and the bore-cylinder wall as seen from the side. The water channel is subdivided into N_k control volumes along with the height of the cooling jacket, coinciding with the number of gas control volumes modelled. However, depending on the number of control volumes considered, the radial fins do *not* necessarily coincide with the gas control volumes as depicted in the figure. It is assumed that as the fin gap l_g is small, the bulk of the cooling water flows perpendicular through the 'T'-shaped (shaded) cooling channel, progressing axially

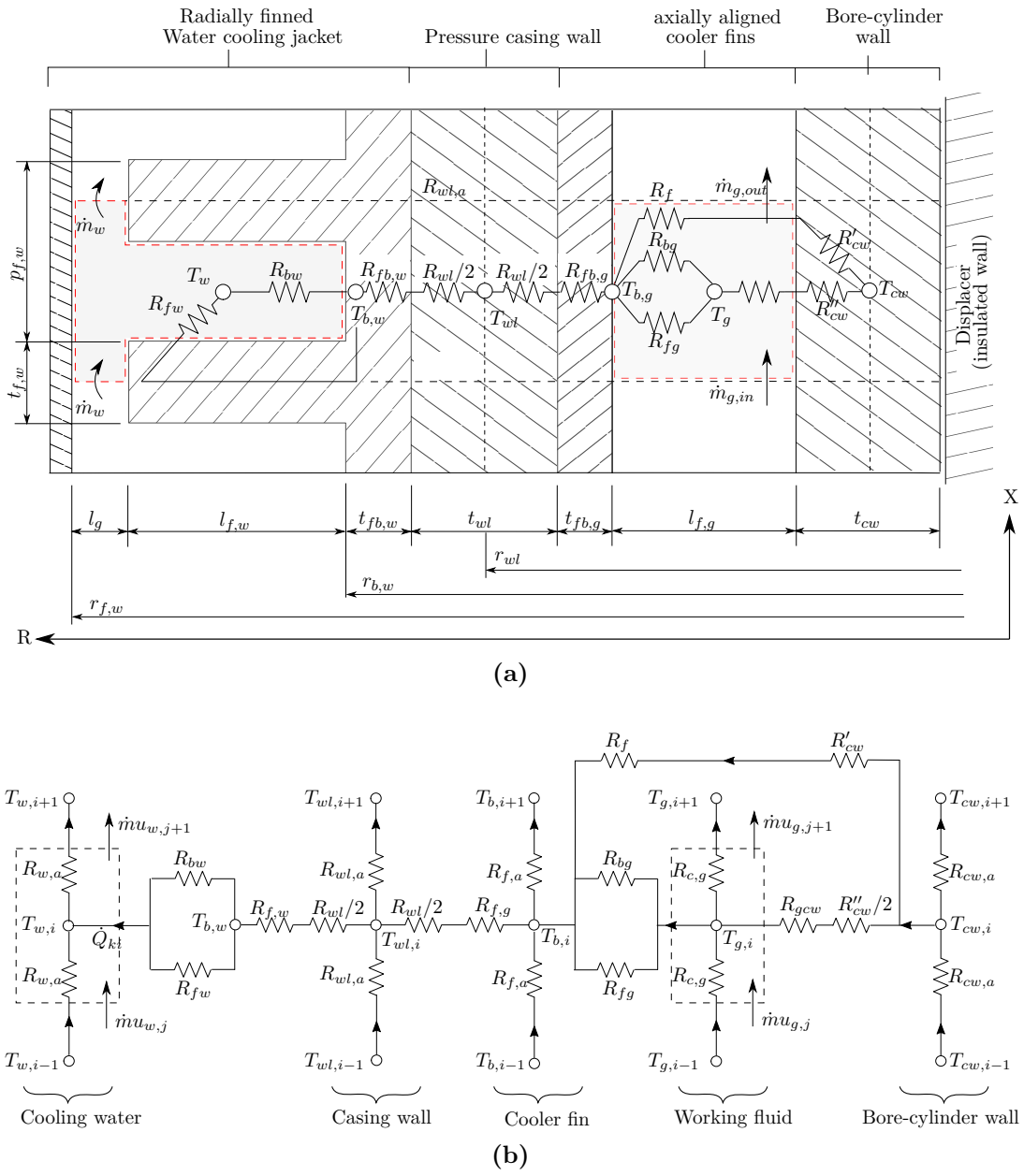

Figure 3.7: (a) Thermal resistance analogy between the radially finned cooling jacket, the casing wall, cooler fin, working fluid and bore-cylinder wall when viewed from the side, (b) thermal resistance network with the addition of axial heat flow

(in direction X) *only* with the fin pitch p_f at a mass flow rate of $\dot{m}_w$. The tangential water flow velocity in this spirally finned water channel is used to infer the water-side Nusselt number and convective heat transfer coefficient to the cooler fins and base. Then, by applying the principle of conservation of energy to each water cell, the gradual increase in coolant temperature is computed. In Figure 3.7 (b) the thermal resistance analogy of the cooling jacket with the inclusion of axial heat conduction and advection is depicted. It must be noted that heat transfer modelling between the

casing wall temperature at temperature T_{wll}, and bore-cylinder wall at temperature T_{cw}, may be treated identically to that of the heater channel given by Figure 3.6.

The water-side Reynolds number and heat transfer coefficient are defined in terms of the tangential flow velocity and hydraulic diameter d_{h_t}, given by:

$$d_{h_t} = \frac{4A_{t_f}}{2(h_f + t_f)} \tag{3.37}$$

in which A_{t_f} is the tangential water flow area of the T-shaped channel, defined by:

$$A_{t_f} = (p_{f,w} - t_{f,w})l_{f,w} + p_{f,w}l_g \tag{3.38}$$

where $t_{f,w}$ is the fin thickness, $l_{f,w}$ is the fin length and l_g the distance between fin edge and outer jacket wall. The convective heat transfer coefficient h_w is then related to Nusselt number using the above-mentioned hydraulic diameter by:

$$h_w = \frac{k_w Nu_w}{d_{h,t}} \tag{3.39}$$

in which the water flow Nusselt number Nu_w is determined from either Equation (3.27) or Equation (3.28) depending on the tangential flow Reynolds number. Furthermore, the water-side fins were modelled as square-shaped annular fins with uniform thickness. Similarly to modelling the internal fins, a fin efficiency has been used to permit modelling the fin at a uniform base temperature. Kröger (1998) gives the fin efficiency by:

$$\eta_{fw} = \frac{\tanh(bd_b\phi/2)}{d_b\phi/2} \tag{3.40}$$

where d_b is the fin base diameter. Parameters b and ϕ are given by:

$$\begin{aligned} b &= \Big(\frac{2h_w}{t_{f,w}k_{f,w}}\Big)^{1/2} \\ \phi &= (d_{f,w}/d_0 - 1)[1 + 0.35\ln(d_{f,w}/d_0)] \end{aligned} \tag{3.41}$$

in which $d_{f,w}$ is the fin outside diameter. Using the fin efficiency analogy, the total thermal resistance from the cooling water to the casing wall may be expressed as:

$$R_{w-wl} = (h_w A_{bw} + \eta_{fw} h_w A_{fw})^{-1} + \frac{t_{fb,w}}{k_{f,w}(\pi d_b \Delta x)} + \frac{t_{wl}/2}{k_{wl}(\pi d_{wl}\Delta x)} \tag{3.42}$$

The heat transfer surface area to the fin base is given by:

$$A_{bw} = \Big[N_{f,w}(2\pi r_{b,w}(p_{f,w} - t_{f,w}))\Big]/N_{cells,k} \tag{3.43}$$

and the heat transfer surface area of the fin side walls is given by:

$$A_{bf} = \Big[N_{f,w}\Big(2\pi(r_{f,w}^2 - r_{b,w}^2)\Big)\Big]/N_{cells,k} \tag{3.44}$$

in which $N_{f,w}$ is the total number of radial cooling fins in the cooling jacket and $N_{cells,k}$ the total number of cooler control volumes modelled. Finally, the thermal resistance network of the cooler channel is applied and solved in a fully-explicit fashion as for the heater channel and the new time-step metal and water temperatures computed from an energy balance.

3.2.5. Regenerator thermal resistance network

The regenerator canister is made up of a radially wound copper 60-mesh wire screen, having an overall volume void fraction of approximately 78 %. As shown in Figure 6.6 on page 89, the regenerator canister is located between the heater and cooler fins, serving to improve the overall thermal efficiency of the engine by acting as a heat recuperator. Modelling of the regenerator is typically simplified to defining a regenerator effectiveness – representing the amount heat released from the regenerator as a fraction of the amount of heat absorbed by the regenerator. Often in literature, the regenerator effectiveness is determined from a 'Number of Transfer Units' methodology, as first outlined by Berchowitz (1986). Using the GPU-3 engine as a case study, Urieli and Berchowitz (1984) highlighted the significant influence the regenerator effectiveness holds over engine indicated efficiency. As an illustrative example, the authors have shown how a mere 1 % reduction in regenerator effectiveness results in a 4 % reduction in indicated efficiency.

In this study, however, the regenerator has been modelled from first principles, by subdividing the mesh metal and void volume into a corresponding number of one-dimensional finite control volumes. Heat transfer and fluid friction relations have been simplified to empirical steady-flow correlations, as done by Smith (2006), and are related to local Reynolds number and the regenerator void fraction. Figure 3.8 (a) illustrates the thermal resistance analogy adopted to model heat transfer between the pressure casing wall, regenerator mesh, working fluid (gas) and bore-cylinder wall. To simplify modelling, only convective heat transfer is considered between the metal mesh and working fluid, with conductive heat transfer between the mesh and casing walls being assumed negligible. In Figure 3.8 (b) the thermal resistance network is illustrated with the addition of axial heat flow. As in the case of the heater and cooler, axial conductive heat transfer is modelled in the engine casing and bore-cylinder walls. Additionally, axial conduction in the regenerator mesh and working fluid is considered, although heat transfer by convection and advection is expected to dominate heat transfer to the fluid.

The regenerator void fraction is defined as the ratio between the void volume V_v and the total volume V_0, whereas the void volume is expressed as the difference between the total volume and the volume occupied by the mesh V_m, given by:

$$\varepsilon_r = \frac{V_0 - V_m}{V_0} \tag{3.45}$$

In terms of the total canister volume, the fluid void volume is expressed as:

$$V_v = \varepsilon_r V_0 \tag{3.46}$$

and the mesh volume is expressed as:

$$V_m = (1 - \varepsilon_r) V_0 \tag{3.47}$$

The volume occupied by the mesh can also be expressed as the product of the wire cross-sectional area A_w and the total length of wire making up the mesh, l_w, as

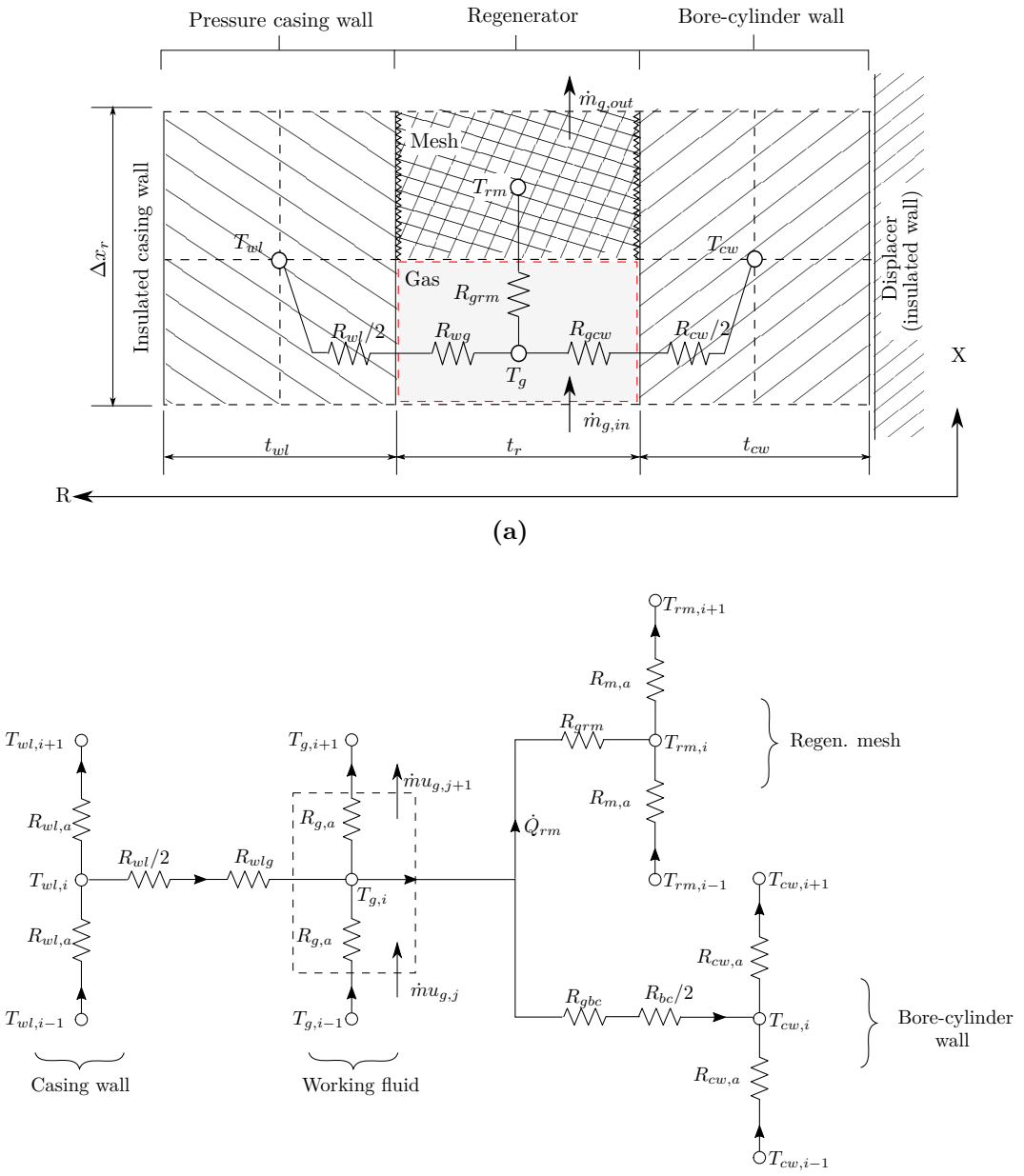

Figure 3.8: (a) Thermal resistance analogy between the casing wall, working fluid, regenerator mesh and bore-cylinder wall when viewed from the side, (b) thermal resistance network with the addition of axial heat flow

given by:

$$V_m = \left(\frac{\pi d_w^2}{4}\right) l_w \tag{3.48}$$

In terms of the wire length, the total wetted area of the mesh is:

$$A_w = \pi d_w l_w \tag{3.49}$$

Rearrangement of the above three equations to eliminate the wire length l_w yields a more practical form of the model for the wetted area, expressed by:

$$A_w = \frac{4V_0(1-\varepsilon_r)}{d_w} \tag{3.50}$$

The cross-sectional area of the regenerator can be expressed as the total volume divided by the length of the regenerator l_r:

$$A_{x_0} = \frac{V_0}{l_r} \tag{3.51}$$

The cross-sectional flow area (void area) is expressed in terms of the void fraction and the cross-section area:

$$A_{x_f} = \varepsilon_r A_{x_0} \tag{3.52}$$

assuming that the void fraction remains constant throughout the regenerator and therefore neglecting anisotropic mesh characteristics.

The wetted perimeter p_w is defined as the total wetted area divided by the regenerator length:

$$p_w = \frac{A_w}{l_r} \tag{3.53}$$

which may be arranged in terms of total cross-sectional area by substituting the definitions of the wetted area and total cross-sectional area:

$$p_w = \frac{4A_{x_0}(1-\varepsilon_r)}{d_w} \tag{3.54}$$

The hydraulic diameter d_h is defined as four times the wetted area divided by the wetted perimeter:

$$d_h = \frac{4A_w}{p_w} \tag{3.55}$$

which may be rearranged in terms of the void fraction to yield:

$$d_h = \frac{\varepsilon_r d_w}{1-\varepsilon_r} \tag{3.56}$$

Finally the flow Reynolds number is defined in terms of the hydraulic diameter and mesh flow velocity v_m, as given by:

$$Re = \frac{\rho v_m d_h}{\mu} \tag{3.57}$$

Gedeon and Wood (1996) have extensively studied the frictional pressure drop and heat transfer aspects of wire-mesh and metal-felt regenerators for Stirling engine application. They have derived a set of Darcy friction and Nusselt number correlations that are widely used in literature. Their correlations have been derived from an experimental oscillating-flow regenerator test rig developed at Ohio University. The authors suggest that for a generic woven-screen regenerator mesh with random stacking the coefficient of friction can be given by a three-parameter 'modified'

Ergun equation, given as a skin coefficient of friction by:

$$C_f = \Big[129/Re + 2.91Re^{-0.103}\Big]/4 \tag{3.58}$$

The Nusselt number may be given by:

$$Nu = (1.0 + 0.99P_e^{0.66})\varepsilon_r^{1.79} \tag{3.59}$$

in which P_e is the local cell Peclet number, taken as the product of the local Reynolds and Prandtl numbers. These equations hold for mesh porosities ranging from 0.62 to 0.78 and for Reynolds numbers varying between unity and $3,400$. An interesting outcome of their study has been that the mesh friction factor exhibits no clear trend with changing porosity, and have been shown to correlate well with the widely-used steady-flow correlations presented by Kays and London (1984).

More recently, Costa *et al.* (2013) and Costa *et al.* (2015) performed a series of numerical investigations into randomly orientated wound-mesh Stirling regenerators in the laminar flow region with $Re < 400$. Their model shows excellent correlation with that of Gedeon and Wood (1996) and Tanaka *et al.* (1990) for axially stacked regenerator meshes with misaligned fibre orientations. In these studies they have numerically characterised the flow friction and heat transfer correlations of a wound wire-mesh regenerator having a wire diameter of 110 µm and volumetric porosity of 0.63, correlating to a skin coefficient of friction:

$$C_f = \Big[165.5/Re + 2.04\Big]/4 \tag{3.60}$$

The authors argue that there exists an increased frictional pressure drop for wound -wire-mesh regenerators over their axially-stacked counterparts, which may be attributed to these regenerator having smaller cross-sectional flow opening area. However, since the findings of both studies were limited to volumetric porosities smaller than 0.64 and mesh wire diameters between 80 and 110 µm, the more generalised and widely accepted experimental correlations of Equation (3.58) and Equation (3.59) have been retained in this study.

Referring to Figure 3.8, the convective thermal resistance R_{grm} between working fluid and mesh metal is related to mesh Nusselt number by:

$$R_{grm} = \frac{1}{h_{grm}(A_w/Nr)} \tag{3.61}$$

where $h_{rgm} = Nu/k_g d_h$ and N_r represent the total number of regenerator control volumes modelled. The thermal resistance from the casing wall to working fluid is given by:

$$R_{wl-r} = \frac{t_{wl}/2}{k_{wll}(\pi d_{wll}\Delta x)} + \frac{1}{h_{wg}A_{wg}} \tag{3.62}$$

and from working fluid to bore-cylinder wall by:

$$R_{g-cw} = \frac{1}{h_{gwc}A_{gwc}} + \frac{t_{cw}/2}{k_{cw}(\pi d_{cw}\Delta x)} \tag{3.63}$$

where the convective heat transfer coefficients h_{wg} and h_{gwc} are related to the smooth

duct-flow Nusselt numbers, calculated using Equation (3.28).

In addition to the convective heat transfer mechanism, Figure 3.8 (b) shows the inclusion of axial conduction between adjacent gas and mesh metal control volumes. Gedeon (2016) notes that the total gas conduction through a regenerator canister is typically *less* than the sum of the static gas and mesh conduction through the canister, and consequently modifies the gas conduction through the mesh medium by a *tortuosity* factor f_{rm}, defined as:

$$f_{rm} \equiv \frac{Q_t - Q_g}{Q_{rm}} \equiv \frac{k_{av} - k_g \varepsilon_r}{k_{rm}(1 - \varepsilon_r)} \tag{3.64}$$

in which Q_t is the total axial heat conducted, Q_g the axial heat conducted by the working fluid and Q_{rm} the heat conducted by the solid mesh. Similarly k_g represents the thermal conductivity of the working fluid, k_s of the solid mesh and k_{av} the average regenerator conductivity. Gedeon (2016) recommends using a calibrated form of the tortuous function f_{rm}, given by:

$$f_{rm} = \left(\frac{k_{rm}}{k_g}\right)^{m-1} \left[\frac{3(k_{rm}/k_g - \varepsilon_r) + (2 + k_s/k_g)\varepsilon_r}{3(1 - \varepsilon_r) + (2 + k_{rm}/k_g)\epsilon_r}\right] \tag{3.65}$$

for which the calibration exponent m is correlated to experimental test data conducted by Lewis and Radebaugh (2011) on packed-sphere and woven mesh screen heat exchangers. For a woven screen matrix, a calibration coefficient of $m = 0.165$ is derived based on a curve-fitting to the experimental data of stainless-steel and phosphorous bronze stacked mesh media with volumetric porosities ranging from 0.62 to 0.78. Gedeon further recommends using an axial gas conduction enhancement factor N_k to capture some of the intricate gas flow heat transfer characteristics one-dimensional models are unable to resolve. This gas conduction enhancement factor may be defined as:

$$N_k \equiv k_e/k_g \tag{3.66}$$

where k_e is representative of the effective working fluid conductively and k_g the molecular conductivity. Gedeon and Wood (1996) give the enhancement factor as:

$$N_k = 1.0 + 0.5 Pe^{0.66} \varepsilon_r^{-2.91} \tag{3.67}$$

Then, using the tortuosity factor the axial conductive resistance between adjacent mesh metal cells is given by:

$$R_{rm,a} = \frac{\Delta x}{(f_{rm} k_{rm})(1 - \varepsilon_r) A_{x_0}} \tag{3.68}$$

and using gas conduction enhancement factor the axial conductive resistance between adjacent fluid cells is given yb:

$$R_{g,a} = \frac{\Delta x}{(N_k k_g)(\varepsilon_r) A_{x_0}} \tag{3.69}$$

where axial heat transfer in the pressure casing and bore-cylinder wall have been formulated from Equation (3.35).

3.3. Dynamic equations of motion

The governing equations of motion of the displacer and power piston were derived by application of Newton's second law of motion. Figure 3.9 shows the respective free body diagrams of the rigid displacer and power piston as being 'sprung to ground', depicting the forces acting on them if both are moving from right to left. The net force acting on the displacer is comprised of the compression and expansion space working fluid pressure forces, denoted by $P_c(A_d - A_s)$ and $P_e A_d$ respectively, the backspace (bounce space) pressure force acting on the displacer shaft $P_{bs}A_s$, and the flexure spring force $k_{fd}(x_d - {x_d}^0)$. An electromagnetic force F_{md} is exerted on the displacer by the linear electric motor with terminal voltage $V_{T,m}$. There is also fluid shear friction between the displacer shaft and the piston, denoted by $\tau_{dp}A_{zs}$, and between the displacer and bore, $\tau_d A_{zd}$. Coulomb or dry-sliding contact friction $F_{f,d}$ acts on the displacer dome against the direction of movement, as was determined experimentally in Chapter 7.1.

The power piston is also subject to the working fluid pressure and flexure spring forces as shown, and in addition, is subject to the generator load force F_{mp} with terminal voltage $V_{T,g}$. This force is a function of piston velocity and magnet train displacement from its mid-stroke position, furthermore being comprised of both open-circuit magnetic and closed-circuit electromagnetic force constituents, as determined by the electromagnetic finite element analysis presented in Chapter 4. As

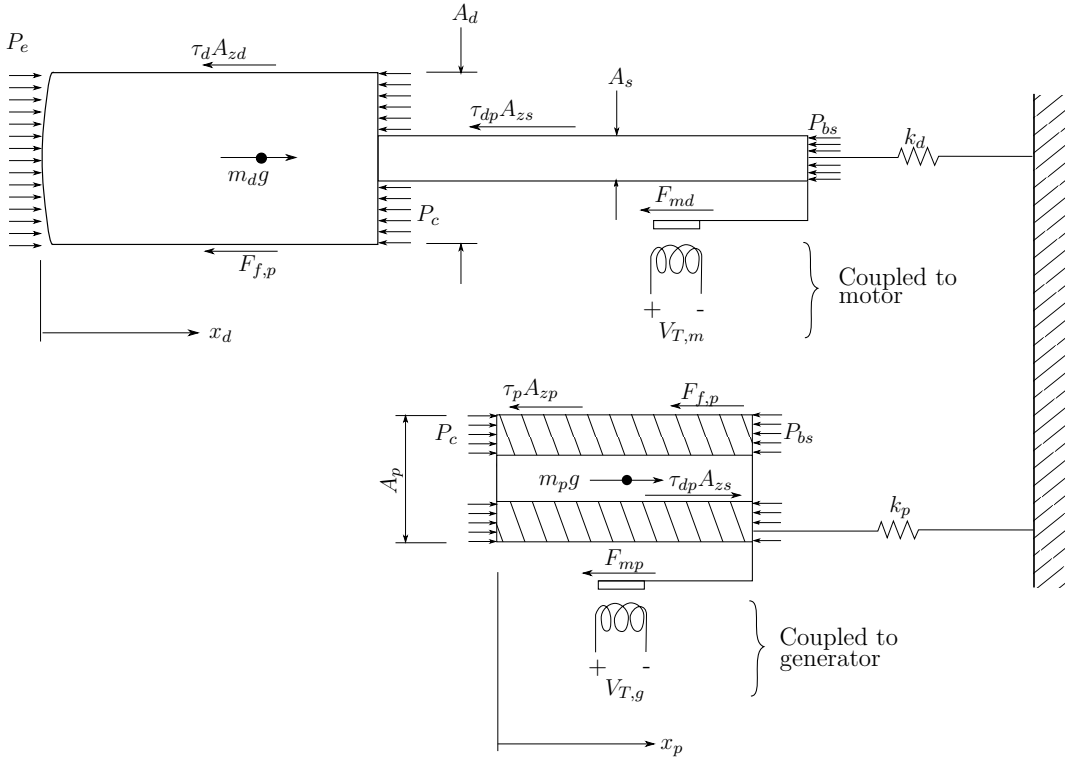

Figure 3.9: Free body diagrams of the displacer (top) and the power piston (bottom) which are both sprung to the engine casing

was determined from the experiment in Chapter 7.1, due to the presence of magnetic side load forces on the piston magnet train, the piston mechanical contact-friction $F_{f,p}$ is given as a form of viscous damping.

The net body forces acting on the displacer and piston in the positive x-direction (from left to right) are given by:

$$\sum F_d = P_e A_d - P_c(A_d - A_s) - P_{bs}A_s - k_d(x_d - {x_d}^0) - F_{md} \\ -\tau_{dp}A_{zs} - \tau_d A_{zd} - F_{f,d} + m_d g \tag{3.70}$$

$$\sum F_p = (P_c - P_{bs})(A_p - A_s) - k_p(x_p - x_p^0) - F_{mp} + \tau_{dp}A_{zs} \\ -\tau_p A_{zp} - F_{f,p} + m_p g \tag{3.71}$$

Applying Newton's second law and rearranging for the acceleration term yields:

$$\left(\frac{d^2x_d}{dt^2}\right) = \frac{\sum F_d}{m_d} \tag{3.72}$$

$$\left(\frac{d^2x_p}{dt^2}\right) = \frac{\sum F_p}{m_p} \tag{3.73}$$

Over the duration of a finite time-step Δt, constant body acceleration was assumed. The fully-explicit method was used to integrate Equations (3.72) and (3.73) temporally, by using the rates of change from the current time-step to determine the following time-step velocities. The displacer and piston velocities are given by:

$${v_d}^{t+\Delta t} = {v_d}^t + \Delta t\left(\frac{\sum F_d}{m_d}\right)^t \tag{3.74}$$

$${v_p}^{t+\Delta t} = {v_p}^t + \Delta t\left(\frac{\sum F_p}{m_p}\right)^t \tag{3.75}$$

By following this same approach and integrating the velocity profile with respect to time, the displacer and piston displacements are given by:

$${x_d}^{t+\Delta t} = {x_d}^t + (\Delta t){v_d}^t + \frac{(\Delta t)^2}{2}\left(\frac{\sum F_d}{m_d}\right)^t \tag{3.76}$$

$${x_p}^{t+\Delta t} = {x_p}^t + (\Delta t){v_p}^t + \frac{(\Delta t)^2}{2}\left(\frac{\sum F_p}{m_p}\right)^t \tag{3.77}$$

As shown by the program flow diagram in Figure 5.1 on page 60, if the newly determined velocities would lead either to the displacer or piston colliding with the engine casing, the new time-step velocity is set equal to zero before integrating to displacement. Furthermore, should the displacer collide with the power piston, the displacer is given a velocity profile identical to that of the heavier power piston before their velocities are integrated to displacements. This approach ensures that neither negative nor zero expansion or compression space volumes can be induced within the numerical model, which would otherwise lead to numerical instability.

3.4. Concluding remarks

Throughout this chapter, the derivation of a 'third-order' theoretical model of a free-piston Stirling engine has been discussed. The chapter has presented a schematic of a novel experimental FPSE prototype that includes a linear motor attached to the displacer shaft. The working fluid (gas) and engine metal sections have been discretised into arrays of finite control volumes to which the governing transport equations are applied and computed sequentially. The principles of conservation of mass and energy have been applied to arrays of scalar control volumes numbered i, whereas the principle of conservation of momentum has been applied to vector control volumes numbered j using a backwards-staggered velocity grid. The governing fluid dynamic transport equations have been retained in integral form and discretised to solvable finite difference equations of mass, momentum and thermal energy, which were subsequently solved using a fully-explicit numerical method. Application of the governing transport equations to the expansion and compression space chambers and heater, cooler and regenerator channels has been outlined. Steady-flow empirical correlations were used accordingly to relate relations for convective heat transfer and fluid friction to the engine heat exchanger sections.

The modelling steps taken may be summarised as follows:

- Applying the principle of conservation of mass to an array of discretised scalar control volumes i to compute the following time-step mass m_i, and consequently relate the mass to density ρ_i.
- Applying the principle of conservation of momentum to an array of backwards-staggered vector control volumes j to compute the following time-step cell-interface momentum $m_j v_j$, and consequently, by using the continuity equation, relate the momentum to nodal velocity v_j.
- Applying the principle of conservation of energy to arrays of metal and gas scalar control volumes i to compute the following time-step specific internal energy u_i. For each gas and metal control volume, relating the rate of change in its internal thermal energy to a rate of change in its temperature so as to compute the new time-step gas and metal temperatures T_i.
- For each control volume i, relating its new time-step gas mass, volume and temperature to pressure P_i using the ideal gas law as an equation of state.

The chapter has furthermore discussed the derivation of the non-linearised equations governing the motions of the free-running displacer and power piston. The power piston has been shown to be coupled to the working fluid dynamics by the acting pressure forces, and to the linear generator electrodynamics by the electromagnetic force interaction of its magnet train. However, in order to emulate the generator performance in the numerical model, characterising functions are required to map the expected magnetic force and generator output power to piston motion. The derivation of these so-called *generator characteristic functions* will be discussed in the chapter that follows, before a sample simulation case study of the engine's envisaged operation will be presented to illustrate this *linked* model's capability.

4. Numerical modelling of the linear generator

In this chapter, a theoretical model of the linear electric generator is derived and simulated using transient Finite Element Analysis (FEA). Firstly, the operating mechanism of the generator is discussed and an electrical circuit analogy is presented. Thereafter the open-circuit and closed-circuit operation of the generator is simulated over the range of anticipated piston strokes. These simulation results are used to infer generator characteristic functions in terms of magnet train displacement and velocity – representing the magnetic force interaction with the power piston in the overarching numerical model. The chapter concludes with an investigation into the linear generator performance at the envisaged operating frequency and piston stroke.

4.1. Overview of working principle

The geometry of the linear electric generator is based on work done by Mechanical Technology Incorporated (Dhar, 1999), incorporating a magnet *train* that reciprocates through a stationary soft-iron stator assembly, as illustrated in Figure 4.1. The as-modelled magnet train consists of four rings of radially polarised magnets that induces one of three flux paths through the generator core. When the magnet train is located to the far right, the flux path forms clockwise around the coil from stator end-to-end. A counter-clockwise flux path is induced when the magnet is located to the far left. When the magnet train is located in the centre, the coil flux linkage is short-circuited by two smaller flux paths that drive the flux linkage to zero. If nearly sinusoidal piston motion is assumed, it is at this instance that the rate of change in magnetic flux is greatest and the maximum amount of power is generated.

According to Faraday's law of induction, if a change in flux linkage is presented, an opposing electromotive force (emf) will be induced in the coil that is directly proportional to the rate of change of the encapsulating flux (Boldea and Nasar, 1997). In the case of having a coil made up of N identical windings, this induced emf is given by:

$$emf = -N\frac{d\phi}{dt} = -\frac{d\lambda}{dt} \tag{4.1}$$

where $\lambda = N\phi$ is known as the flux linkage. When a load is attached to the coil terminals, the electrical circuit is complete and current flows. This current interacts with the magnetic field and induces the Lorentz electromagnetic force, given by the cross product:

$$F = \boldsymbol{i}\ell \times \boldsymbol{B} \tag{4.2}$$

where $\boldsymbol{i}$ represents the magnitude and direction of current flowing, ℓ the total length of the conducting coil and $\boldsymbol{B}$ the vector magnetic field (also called flux density). If the right-hand rule is followed and the magnetic field perpendicular to the current flow is used, the electromagnetic force is seen to oppose the movement of the magnet train. This electromagnetic load force, together with the magnetic force

exerted by the moving magnets onto the stationary iron stators, is primarily responsible for the engine damping force exerted onto the power piston (if mechanical friction is assumed negligible). It is *this* magnetically induced force that couples the generator electrodynamic behaviour via the power piston kinematics to the engines thermodynamic behaviour.

It is well established from the literature that free-piston Stirling engines, in contrast to their kinematic counterparts, are easily subject to unstable operation that can lead to over-stroking (with piston-displacer collisions) or even engine stalling. Berchowitz (1988) discusses the operational response of FPSEs to changes in hot-end temperature, pressure and engine load. According to Berchowitz, control strategies can be focussed on influencing either displacer or piston stroke by means of a linear motor, or influencing the generator current by feedback control (either changing

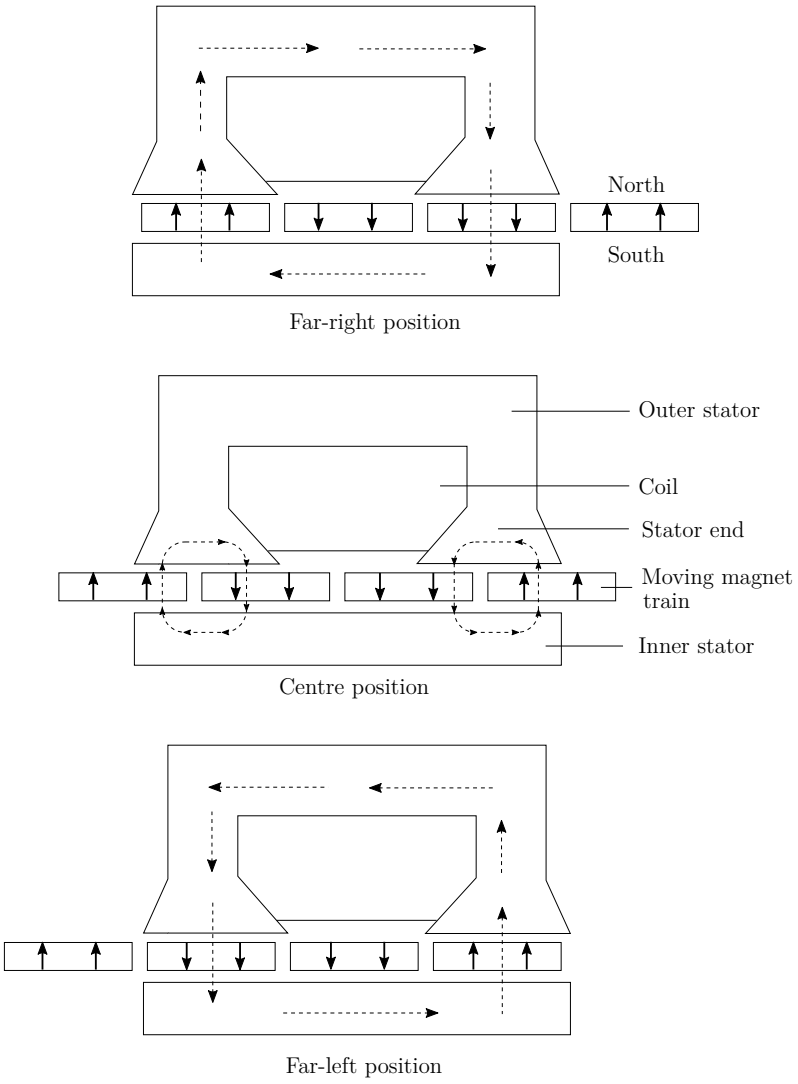

Figure 4.1: Schematic cross-section of the linear generator, depicting the flux path when the magnet train is located at three positions relative to the stator

the circuit resistance or voltage-current phase difference). For engine compactness, the latter control strategy is often preferred, with state-of-the-art engine controllers making use of Power Electronic (PE) modulation to control the piston generator voltage, current and phase – thereby influencing its motion (Lenand *et al.*, 2008). Furthermore the real-time control of the piston and displacer has also been suggested (Strauss, 2013) to ensure optimal engine efficiency, or as discussed by Briggs (2015), to infer a more square-like motion for the displacer so that the engine's pressure-volume diagram can be made closer to that of the idealised Stirling cycle – thereby increasing per-cycle indicated power and thus power density of the engine.

But in spite of the obvious advantages that an engine controller might have for the functioning of a task-suited and working free-piston Stirling engine, the development thereof has remained outside the scope of this study. Consequently in this work, the displacer motor has been used *only* to experimentally investigate engine performance – and validate the numerical model – under charge pressures and temperatures where self-sustained engine operation could otherwise not be achieved, with generator load adjustment being performed manually.

4.2. Electrical circuit analogy

Figure 4.2 depicts an electrical circuit diagram of the linear generator with its terminal leads V_T attached to an adjustable load circuit with resistor bank R_{load}. The internal circuit represents the generator stator, showing the induced emf as a voltage source e with a coil inductance L_{coil} and internal resistance R_{coil}. The coil inductance not only induces a drop in voltage due to its reactance but more significantly, shifts the phase of induced current and Lorentz load to lag behind that of the induced emf. This phase shift may be reduced passively by including a tuning capacitor in series with the inductance and load (Boldea and Nasar, 1997). For example, the circuit diagram shows how two electrolytic tuning capacitors C_1 and C_2

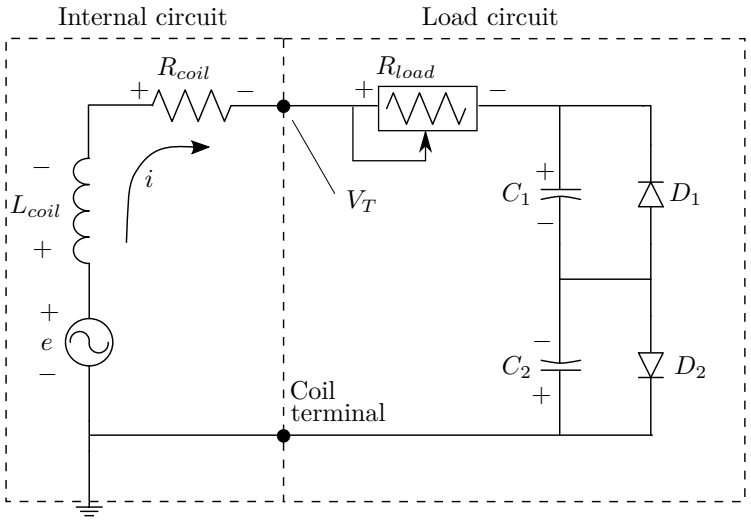

Figure 4.2: Electrical circuit diagram of the generator and load circuit

may be connected in parallel with two diodes D_1 and D_2 in a circuit arrangement that allows the circuit to be switched on in reverse-bias as well. In theory, when the circuit's resonant frequency matches the operating frequency of the power piston, the current phase lag is eliminated and maximum electrical power is extracted.

To derive a differential equation for the current i, the diodes were neglected for steady-state operation and the two capacitors were modelled as a single equivalent capacitor in series, C_t. Applying Kirchoff's voltage law yields:

$$L\frac{di}{dt} + R_t i + \frac{1}{C_t}Q = e \tag{4.3}$$

where e is the induced *emf* taken as a voltage source, R_t is the combined coil and load resistance, $i = dQ/dt$ and Q is the electrical charge stored in the capacitor. Differentiating with respect to time and substituting for the term dQ/dt yields:

$$L\frac{d^2i}{dt^2} + R_t\frac{di}{dt} + \frac{1}{C_t}i = \frac{de}{dt} \tag{4.4}$$

which is a second-order ordinary differential equation in time. When the inductance and resistance values are known, the capacitance is chosen to match the circuit's resonant frequency. From Equation (4.4) the current may be expressed in a fully-explicit form, by use of forward and central differencing schemes, as:

$$i^{t+\Delta t} = \frac{\Delta t^2\Big[(\dfrac{e^{t+\Delta t} - e^t}{\Delta t}) - \dfrac{i^t}{C_t} + \dfrac{R_t i^t}{\Delta t}\Big] + 2Li^t - Li^{t-\Delta t}}{L + \Delta t/R_t} \tag{4.5}$$

To solve Equation (4.1), (4.2) and (4.5) so-called *generator characteristic functions* for flux linkage, magnetic force and magnetic flux density were inferred from an electromagnetic finite element analysis, as will be detailed in the following section.

4.3. Generator characteristic functions

The nominal 30 Hz operation of the linear electric generator was simulated using the finite element analysis (FEA) software *ANSYS Maxwell 16.0* (ANSYS, 2017). Derivation of the FEA model is discussed in Appendix C. Refer to Figure 6.7 on page 90 for an illustration of the prototype linear electric generator.

The power piston's oscillatory motion was emulated by subjecting the magnet train to a sinusoidal velocity boundary condition with a fixed design-point operating frequency of 30 Hz. The simulated displacement amplitude was varied between 2.5 and 15 mm. Two generator load conditions were simulated: open-circuit and purely resistive closed-circuit operation. In the open-circuit simulation, the generator coil was subject to a zero-current boundary condition and the induced flux linkage, electromotive force and magnetic force were subsequently computed. To simulate closed-circuit operation, a purely resistive load was modelled as being attached across the coil terminals and the resultant load voltage, current and electromagnetic load force were computed. By mapping the flux linkage, magnetic force, load current and inferred flux density to magnet train displacement, and curve fitting relations to each of

these variables, a set of *generator characteristic functions* were derived. The generator characteristic functions represent the electromagnetic FEA in the overarching numerical model as simplified analytical relations, linking to the thermodynamic model derived in the previous chapter to the piston kinematic behaviour.

4.3.1. Open-circuit simulation results

The open-circuit coil flux linkage as a function of magnet train displacement is shown in Figure 4.3. It is seen that the flux linkage varies approximately linearly with magnet train displacement, although flattening out at the stroke limits. With an increase in magnet train displacement (and velocity) the flux linkage curves are widened due to magnetic hysteresis in the stator core. Nevertheless, for the range of magnet train displacements simulated, there is a strong correlation between the flux linkage results and the magnet train displacement. With the influence of magnetic hysteresis neglected, the average relation between flux linkage and displacement can be approximated by the fifth-order polynomial:

$$\begin{aligned}\lambda(x) = &-3.24\times10^{-8}{x_p}^5 + 1.21\times10^{-8}{x_p}^4 + 2.69\times10^{-5}{x_p}^3 \\ &-3.93\times10^{-6}{x_p}^2 - 8.94\times10^{-3}x_p + 2.27\times10^{-4}\end{aligned} \tag{4.6}$$

where flux linkage λ is in Weber and x_p the magnet displacement in millimetres.

Figure 4.4 shows the open-circuit magnetic force exerted by the magnet train onto the generator stators as a function of magnet train displacement. This force significantly influences the resonant frequency of the power piston assembly, by acting as a non-linear magnetic spring to the magnet train. Between displacements of -4 and $+4$ mm, the magnetic force exhibits a nearly linear behaviour with an effective spring stiffness of approximately 10.35 N/mm. Between piston displacements of 5 mm and 10 mm, the effective magnetic spring stiffness weakens until crossing the

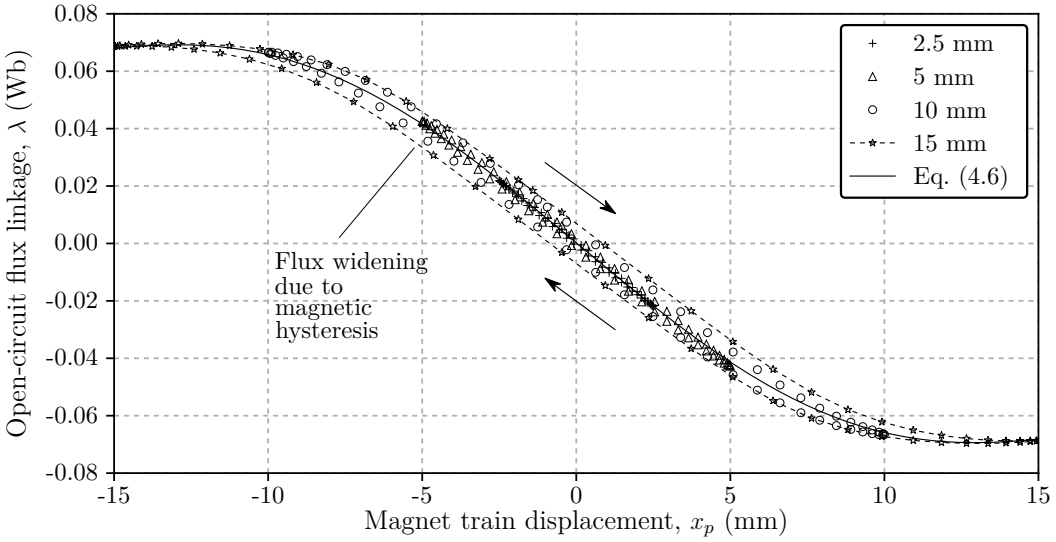

Figure 4.3: Open-circuit flux linkage as a function of magnet train displacement

zero-axis magnetic force around 10 mm. When the magnet train exceeds its design-point displacement of 10 mm, the magnets again act to oppose the piston's motion. In a technical report published by Wood *et al.* (2010) under contract from NASA, it is shown that for an optimised FPSE, the open-circuit magnetic force may be sufficient to support the power piston entirely – eliminating the requirement of a power piston flexure spring and simplifying the overall design. It is also apparent that at increased piston displacements, the open-circuit magnetic force path widens about the magnetostatic force depicted. The enclosed area within the force-displacement path represents the total per-cycle energy dissipated by magnetic hysteresis and eddy currents in the generator stators, known as *core losses*. These core loss effects become more significant as magnet train velocity increases.

Figure 4.5 shows a surface plot of the open-circuit magnetic force as a function of both magnet train displacement and velocity. The open-circuit force moves in a clockwise 'path' with regards to displacement and velocity; the 10 mm displacement path shows the design-operating point and the force profile experienced along this path. This *force map* was generated from a bi-cubic interpolation of the FEA simulation results (by using MATLAB's curve-fitting toolbox). The surface geometry was then resampled and stored as a three-dimensional array data-set. Then, in the numerical simulation model, the piston's displacement and velocity profiles were cross-referenced to the open-circuit force map using a binary search algorithm with bilinear interpolation, to ultimately reproduce the force-displacement paths shown in Figure 4.4. The use of such a force characterising map within the overarching numerical model allows for the simulation of the complete non-linearised piston motion in a simplified manner, as opposed to iteratively switching between a thermodynamic and finite element solver.

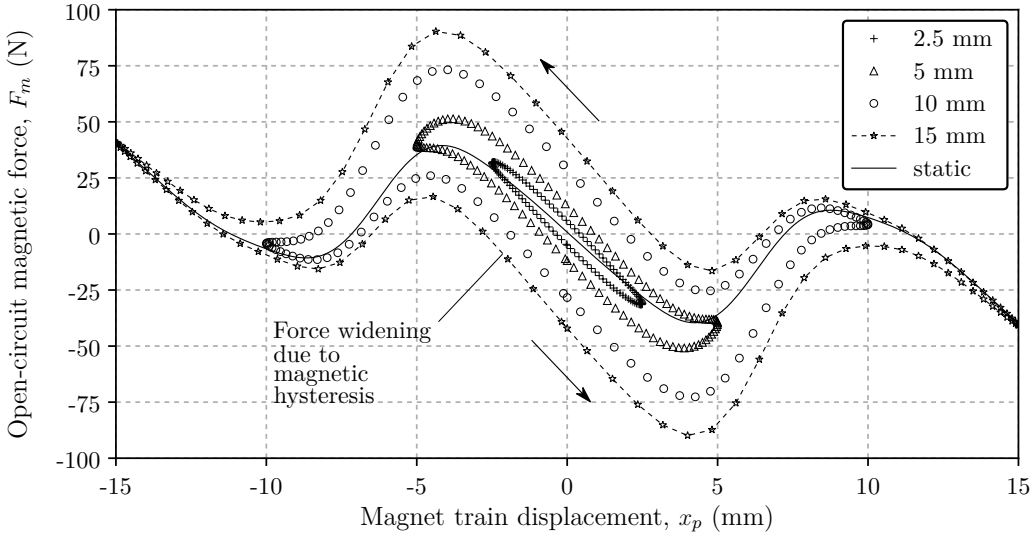

Figure 4.4: Open-circuit magnetic force as a function of magnet train displacement

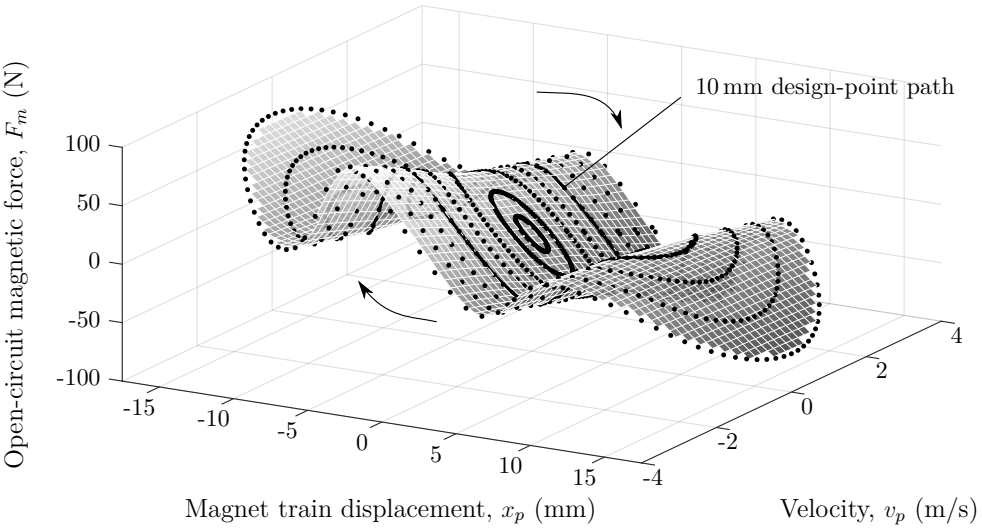

Figure 4.5: Open-circuit magnetic force as a function of magnet train displacement and velocity

4.3.2. Closed-circuit simulation results

To investigate the effect of large current flows on generator performance, a purely resistive 1 Ω load was simulated as being attached across the coil terminals. The load was simulated by defining an external circuit in Maxwell's *Circuit Editor* and imposing the circuit as a *coil boundary condition*. From experimental investigation, and as listed in Table 6.2 on page 91, it was determined that the coil has an internal resistance of 0.4 Ω, which is also accounted for by this boundary condition.

In Figure 4.6 the closed-circuit coil flux linkage is given as a function of magnet train displacement. In contrast to the open-circuit model results, the closed-circuit induced flux linkage paths are considerably more spread out. In addition to the magnetic hysteresis of open-circuit operation, this widening in flux linkage about the static case is attributed to the electrical field induced by the current-flow that acts to oppose the rate of change in flux linkage. But despite the widening of the flux linkage curve at increased displacements, the average gradient in flux linkage between displacements of −10 mm and 10 mm remain approximately similar to that of Equation (4.6). For this reason the assumption of an approximated static coil flux linkage represented by Equation (4.6) is retained.

In Figure 4.7, the load current is given for different piston strokes at the design-point operating frequency of 30 Hz. As shown, the current delivered to the 1 Ω load is asymmetrical about the zero displacement Y-axis, primarily due to magnetic hysteresis and internal coil inductance. This induced phase lag in the current, that becomes more significant at larger piston strokes, may be minimised by employing a series tuning capacitor in the load circuit, as was shown in Figure 4.2. According to Equation (4.2), the current flow through the generator coil induces an electromag-

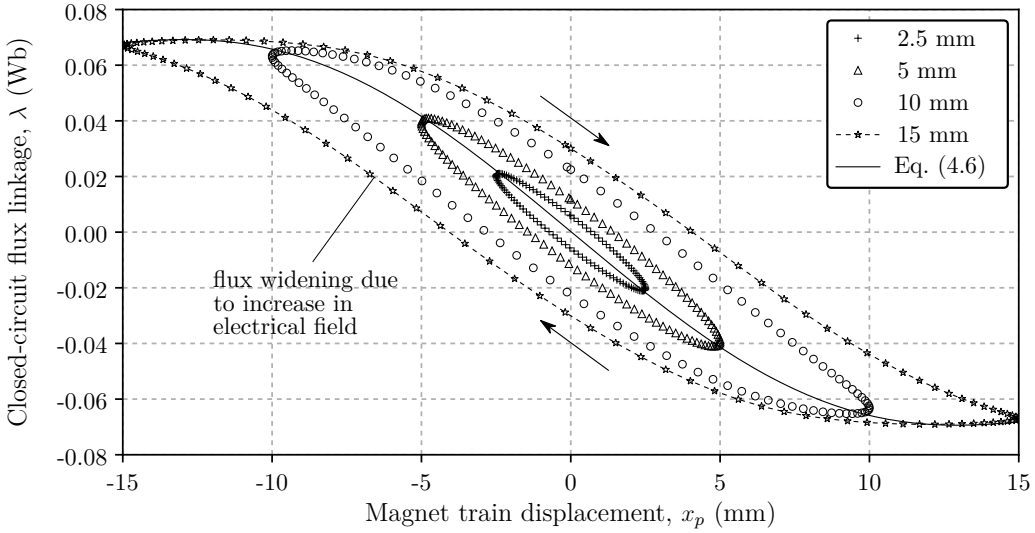

Figure 4.6: Closed-circuit coil flux linkage as a function of magnet train displacement for different piston strokes

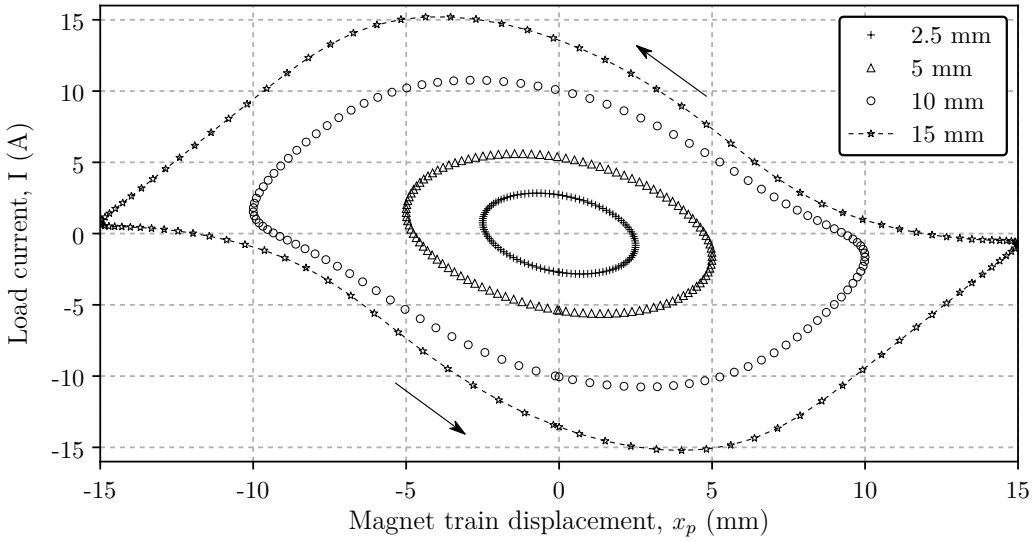

Figure 4.7: Load current as a function of magnet train displacement

netic force that, in turn, opposes the movement of the magnet train. When added to the open-circuit magnetic force F_m, the *total* electromagnetic force F_{mp} exerted on the magnet train is determined.

Figure 4.8 shows the electromagnetic load force divided by load current as a function of magnet train displacement. The load force was determined by subtracting the magnetic force computed from the open-circuit simulation from the *total* magnetic force computed from the closed-circuit simulation – representing only the force con-

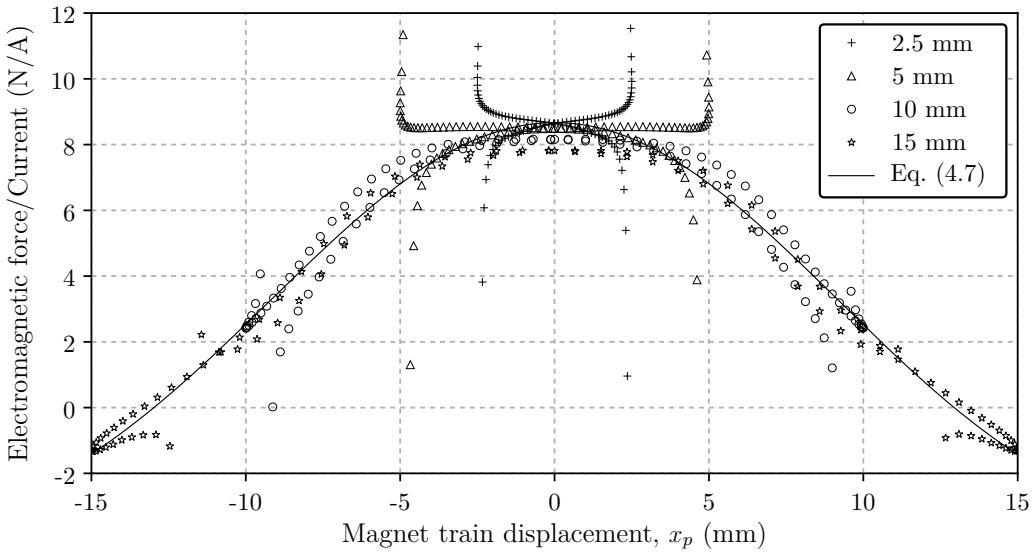

Figure 4.8: Load force divided by current as a function of magnet displacement

stituent induced by current flow. Further dividing the electromagnetic load force by induced current normalises the results obtained from simulating different magnet train displacements, as shown in Figure 4.8. The normalised load-force curve can then be approximated by the sixth-order polynomial as:

$$F/i(x) = -1.91 \times 10^{-7} {x_p}^6 + 9.92 \times 10^{-8} {x_p}^5 + 1.84 \times 10^{-4} {x_p}^4 - 3.14 \times 10^{-5} {x_p}^3 - 7.33 \times 10^{-2} {x_p}^2 + 1.59 \times 10^{-3} x_p + 8.012 \tag{4.7}$$

It is seen that the simulated data deviates considerably from the fitted polynomial curve at small displacement amplitudes. This is attributed to the magnetic field not sufficiently penetrating the outer stator ends and thereby inducing only a small magnetic flux path around the outer stator – resulting in the straying of the force per current curve at the peak displacements. Nevertheless, nearer to the design-specified stroke of 10 mm the analytical relation appears to emulate the simulation data sufficiently well. Dividing Equation (4.7) by the generator coil length ℓ yields the average magnetic flux density $\boldsymbol{B}$ as a function of magnet train displacement, which is used to determine the Lorentz electromagnetic force given by Equation (4.2).

4.4. Performance investigation

Following the derivation of analytical equations for generator flux linkage, magnetic force and flux density, the simulated performance of the prototype generator was investigated and the idealised mechanical-to-electrical efficiency determined. Since the piston's stroke is variable under changing operational conditions (most prominently the hot-end temperature and generator load), the generator overall efficiency was investigated first for different piston strokes up to a peak displacement amplitude of 15 mm, and secondly for generator loads varying between 0.5 to 10 Ω whilst keeping the piston displacement amplitude constant at 10 mm.

For a single piston stroke with a reciprocation period Δt, the mechanical power required to overcome the total magnetic and electromagnetic load force is given by the temporal integral of its encapsulating force-velocity profile:

$$P_{mech,in} = -1/\Delta t \int_{t_1}^{t_1+\Delta t} v_p F_{mp}\, dt \tag{4.8}$$

where the negative sign indicates that the magnetic force opposes the piston movement. The electrical power extracted by the purely resistive load is given by:

$$P_{load,out} = 1/\Delta t \int_{t_1}^{t_1+\Delta t} i^2 R_{load}\, dt \tag{4.9}$$

so that the total power loss P_{loss} can be calculated as the difference between the input mechanical power and the electrical power extracted by the load. This total energy loss includes magnetic hysteresis and eddy current losses in the generator stators (the core losses) and ohmic losses in the generator coil. Internal core losses were also computed using Maxwell's built-in *solid loss* solver. The overall mechanical-to-electrical efficiency represents the fraction of usable load power to required mechanical input power, given by:

$$\eta_{ME} = P_{load,out}/P_{mech,in} \times \frac{100}{1} \qquad (\%) \tag{4.10}$$

Figure 4.9 shows the average rate of mechanical input, loss and power extracted by a 1 Ω electrical load when the magnet train is reciprocated with different displacements amplitudes. From the figure it is noted that the generator is subject to considerable power losses, with core losses being almost equal in amplitude to that extracted by the load. The difference in total loss and core loss is attributed mainly to large ohmic losses in the generator coil, which are significant if the generator is operated with a low external load of 1 Ω. As the displacement amplitude is increased, the mechanical-to-electrical efficiency decreases from 60 to 52 %. The generator is predicted to deliver between 30 to 60 W_e with a conversion efficiency between 56 to 53 % when operated in the design-specified range shown. Figure 4.10 shows the average power delivery as the load is varied from 0.5 to 10 Ω whilst retaining a displacement amplitude of 10 mm. As the load is increased, the required mechanical input power, load power and overall power losses decrease exponentially. The core loss and the total power loss asymptotically approach the open-circuit core loss of 22.4 W (computed as the encapsulating area within the magnetic force-displacement path of Figure 4.4). These significant core losses contribute to the overall poor mechanical-to-electrical efficiency. Only when the generator is operated with a load between 1 and 3 Ω is a mechanical-to-electrical efficiency greater than 50 % achieved. It is seen that operating the generator with loads smaller than 2 Ω lead to large ohmic losses, thereby giving rise to the sharp increase in overall power loss and the mechanical power required to overcome it.

From both Figure 4.9 and Figure 4.10, it is deduced that the generator efficiency can greatly be improved by decreasing the generator core loss. To further investigate why these significant core losses occur, Figure 4.11 shows the magnet-induced magnetic flux density B when (a) the magnet train velocity is reversing and a maximum flux linkage λ is induced in the stators and (b), a peak electrical current of approximately

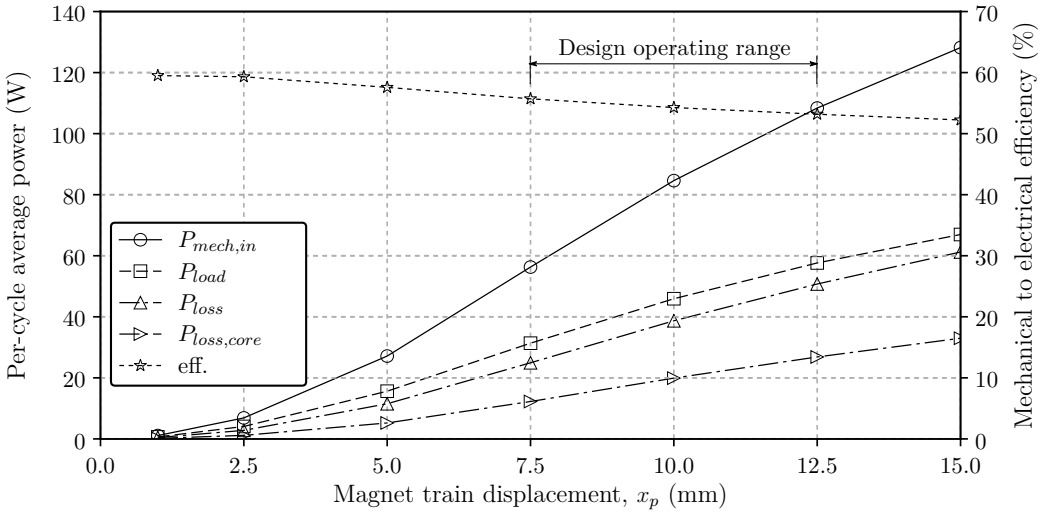

Figure 4.9: Per-cycle mechanical power, power loss and power delivery to the 1 Ω electrical load at different magnet train displacements

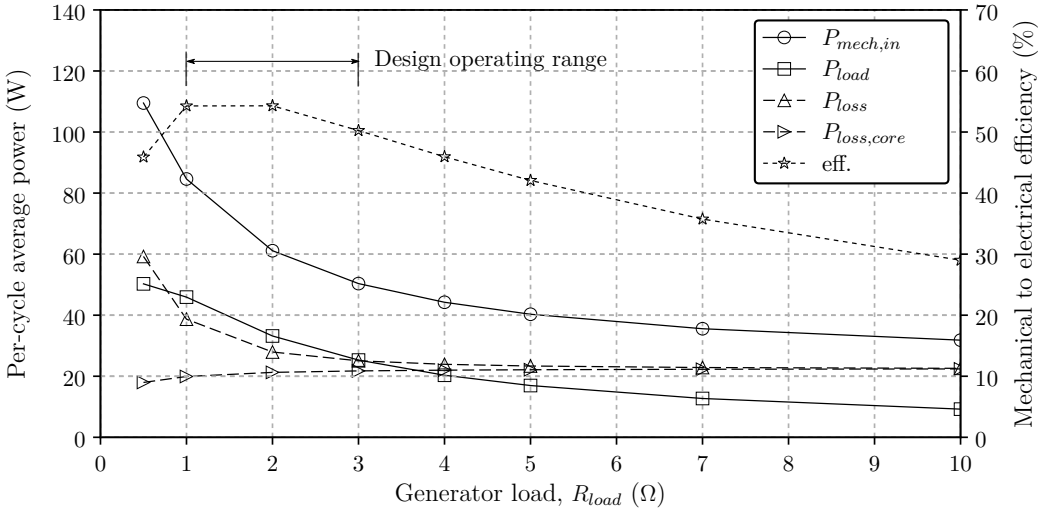

Figure 4.10: Per-cycle mechanical power, power loss and power delivery to different loads when operated at a constant 10 mm magnet train displacement

10 A is delivered to a 1 Ω load. Upon closer inspection of (a), it is postulated that the inner soft-iron stator quickly becomes magnetically saturated around 2.0 T. This saturation leads to especially large hysteresis losses in the inner stator which contributes greatly to the approximately 22 W of core losses simulated under a 10 mm displacement amplitude. The apparent 'widening' of the magnetic force profile that was shown in Figure 4.4 is also attributed to the inner stator becoming magnetically saturated. In contrast, (b) shows a less saturated inner core when the peak electrical current is delivered and the flux linkage is induced towards zero by the magnets.

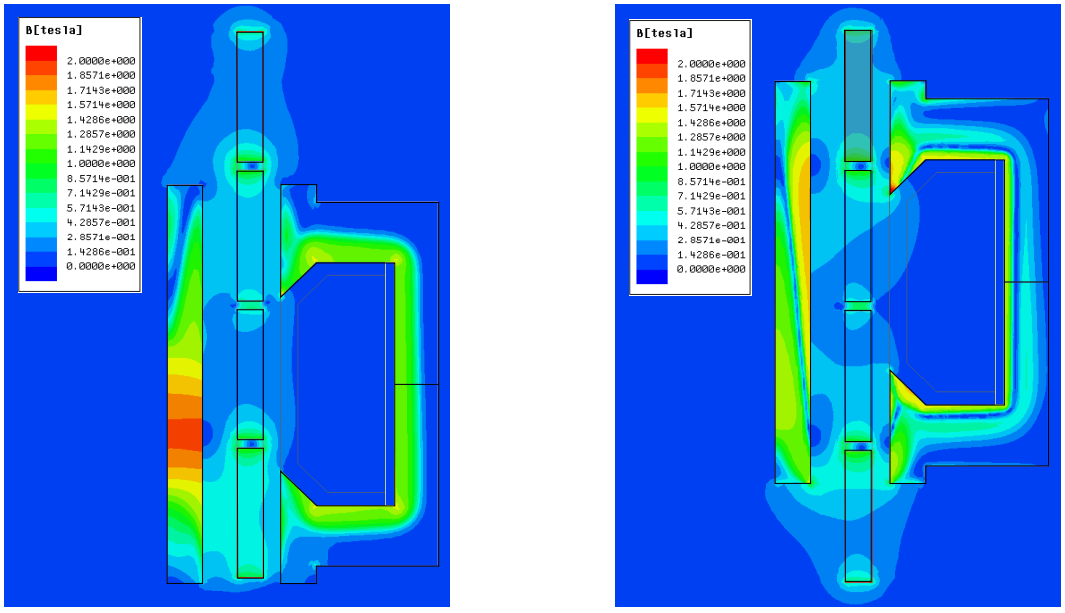

(a) **(b)**

Figure 4.11: Magnitude of flux density when (a) the peak magnet-induced flux is achieved, (b) the peak electrical current is delivered

4.5. Concluding remarks

In this chapter, a numerical model of the linear generator prototype was derived using transient electromagnetic finite element software (ANSYS Maxwell 16.0). Operation of the generator was simulated by reciprocating the magnet at its design-point specified frequency of 30 Hz and varying the generator load and piston stroke. From the FEA results, analytical relations for flux linkage, magnetic force experienced by the magnet train and magnetic flux density were inferred to characterise the linear generator. Using these simplifying generator characteristic functions, the linear generator may be represented and coupled to the power piston dynamical modelling in the overarching numerical model. The chapter also investigated the theoretical performance and expected conversion efficiency of the linear generator. It was shown that a significant amount of usable power is lost to generator core losses, most prominently to magnetic hysteresis in the inner stator core. It is postulated that, should the generator core losses be eliminated completely, the generator would theoretically be capable of delivering 22 W electrical power more per cycle at a 10 mm design amplitude. This would increase the overall generator efficiency from 50 to nearly 80 % if operated with a 1 Ω electrical load. Nevertheless, under the scope limitations of this study, the linear generator has remained unoptimised.

Following the derivation of the governing equations in Chapter 3 and generator characteristic equations outlined in this chapter, a fully-explicit numerical simulation was programmed in Fortran to simulate linked thermodynamic and kinematic operation of the assembled engine prototype, as is outlined in the chapter that follows.

5. Simulation results: a hypothetical case study

In this chapter, simulation results of the prototype FPSE shown in Figure 6.1 on page 83 is presented as an illustrative modelling case study. Firstly, the program methodology is presented with a top-level flow diagram, the model parameters are defined and a temperature adjusting scheme that accelerates model convergence towards thermodynamic steady-state is discussed. Secondly, simulation results are presented as a case study of envisaged steady-state operation of the prototype with an attached $1\,\Omega$ load and using passive current phase correction. The chapter is concluded with an investigation into grid independence and numerical stability.

5.1. Introduction

As discussed throughout Chapter 3, transient numerical simulation of the theoretical model is based on applying the governing equations for the conservation of mass, momentum, energy and equation of state for pressure sequentially to a one-dimensional array of finite control volumes. The model essentially computes 'new' time-step variables by marching forward in time using a fully-explicit numerical method programmed in Fortran 95. This implies that the working fluid state variables such as density, velocity, temperature and pressure at 'new' time-steps $t + \Delta t$ are computed from readily available variables of the current time-step t. The working fluid transport equations were applied by numerically 'sweeping' from control volume 1 to N+1, with each control volume being able to influence only its direct neighbouring control volumes once per time-step. This is in contrast to the commercial Stirling simulation program Sage (2016), which solves the transport equations simultaneously as a boundary value problem using an implicit method, but requiring as an input boundary condition either the piston or displacer motion to be specified. In considering the system equations as an 'initial value problem', this study allows the engine dynamics to evolve naturally over time as simulation outcomes.

The motivation for developing a fully-explicit solver lies in the inherent transparency by which the thermodynamic, kinematic and electrodynamic modelling constituents could be coupled; the ease by which growing model complexity could be accommodated for; and the requirement of a time-integrating solver that can accurately simulate engine transients. Considering that 'third-order' Stirling engine models traditionally solve one-dimensional computational meshes in the order of only tens to a few hundred cells (Anderson, 2006), the additional effort of developing a transient implicit method that can accurately simulate the finite rate of information propagation through the engine workspace was not justified. However, depending on the number of control volumes simulated, micro- to nano-scale time-steps are required for the conditional stability of the gas momentum-balance equation. The backwards-staggered nodal velocities were found to be highly sensitive to changing control volume differential forces. This is especially true when the flow direction reverses and the empirically related fluid friction factor becomes large.

5.2. Methodology and setup

In this section an overview of the program algorithm is given and the setup parameters of a simulated case study are defined. A temperature adjusting scheme that accelerates the numerical model towards thermodynamic steady-state is outlined.

5.2.1. Program flow diagram

The program flow diagram shown in Figure 5.1 gives an overview of the principal sequence of events encompassed by the numerical model. The program starts by importing the simulation operating parameters and modelling dimensions. Then the working fluid, casing wall, regenerator mesh and water cooling channel are discretised into arrays of one-dimensional control volumes as was shown by way of Figure 3.3. These control volumes are subsequently initialised with thermodynamic properties from either a *cold start-up* or guessed *dynamic steady-state* condition, or may even be initialised with properties obtained from a previous simulation run.

After setting the initial conditions for the discretised control volumes, the *main loop* of the program is entered. Within the main loop, the program first considers the 'electrodynamic part' of the model – by using the generator characteristic functions described throughout Chapter 4.3 to compute the induced flux linkage λ, flux density $\boldsymbol{B}$ and magnetic forces F_m acting on the power piston. With the new time-step electromagnetic forces determined, the 'displacer and piston kinematic part' is computed, as represented by Equations (3.74) through (3.77). A conditional subroutine evaluates whether the piston and displacer velocities computed for the 'new' time-step would lead to any collisions with the engine casing. If a collision is predicted, it is assumed that the smallest distance before an impending collision has been realised and the displacer or piston velocity is set to zero before the 'new' displacements are computed. This subroutine is followed by the calculation of the new time-step volumes representative of the expansion, compression and backspace chambers, concluding the model kinematic part.

The 'gas thermodynamic part' of the model is computed in four subroutines that are: heat transfer and fluid friction relations, and the conservation equations of mass, momentum and energy. Firstly, in the heat transfer and fluid friction subroutine, the local Reynolds numbers for control volumes numbered i to N are computed and related to Fanning friction factor, Nusselt number and convective heat transfer rates accordingly using the empirical correlations described throughout Chapter 3.2. Secondly, the conservation of mass is applied to each scalar control volume numbered i through $N+1$ to compute the 'new' time-step cell mass and densities. This step includes adjusting the workspace and backspace gas mass for gas leakages. Thirdly, the gas momentum-balance equation is applied to each vector control volume j to compute the following time-step nodal velocity v_j. Lastly, the conservation of energy is applied to the scaler control volumes denoted i and the 'new' time-step gas, metal and cooling water temperatures are computed accordingly. This is achieved by employing and solving the thermal resistance analogies that were derived throughout Chapter 3.2 to model heat transfer.

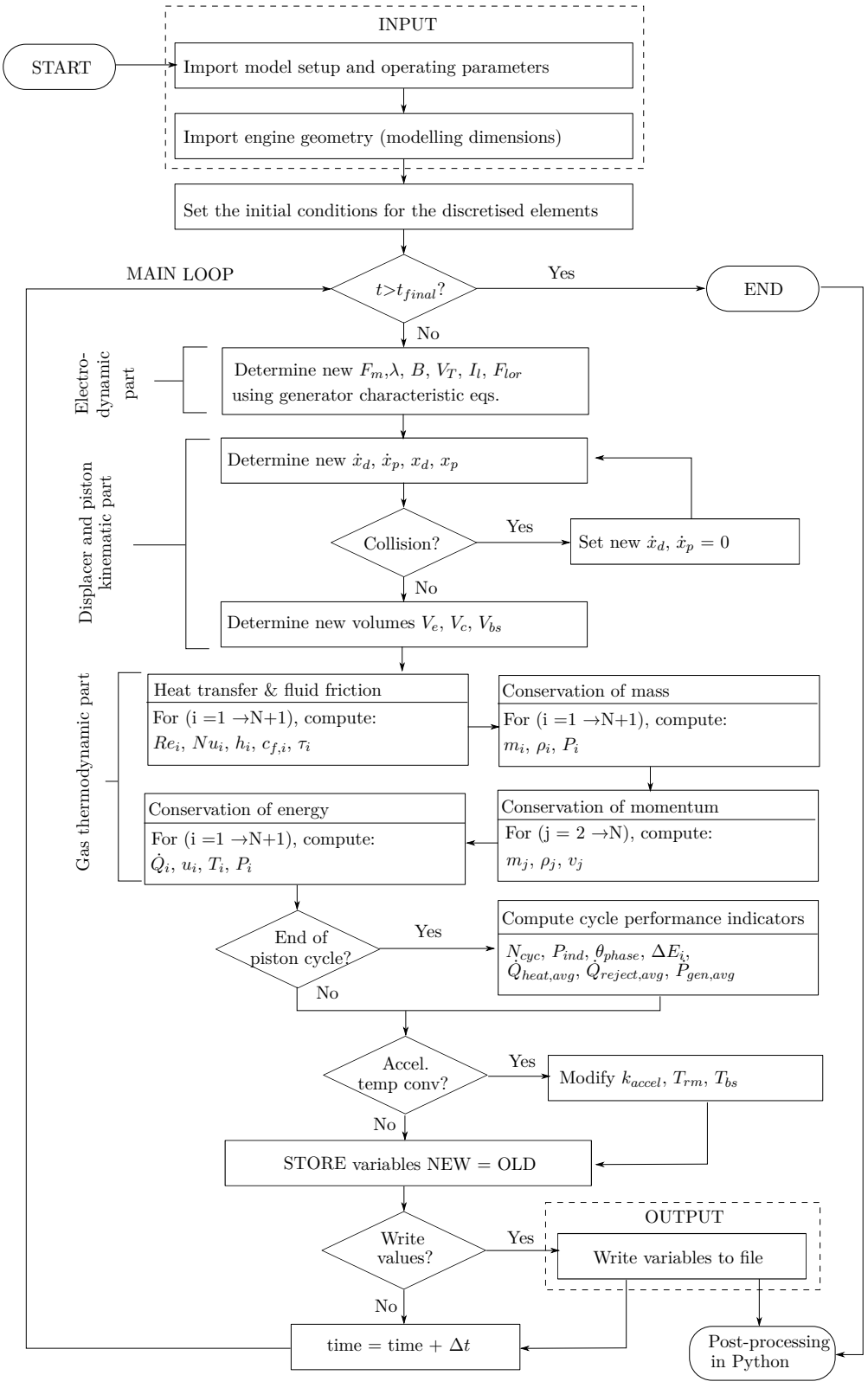

Figure 5.1: Top-level flow diagram of the computer simulation program

From trial-and-error it was deduced that the gas momentum equation is most stable when the working fluid pressure field P_i is computed and updated twice per solver cycle. The pressure field is first solved and updated after the 'new' cell densities and volumes have been computed from the continuity equation. The momentum-balance equation is then applied and the gas velocity profile computed using this newly updated pressure field. After computing the 'new' cell temperatures from the energy equation, the gas pressure field is recalculated and updated for a second time. It is postulated that solving the pressure field twice per solver iteration leads to improved 'coupling' between the otherwise sequentially-computed transport equations.

After computing the 'gas thermodynamic part', a conditional function evaluates whether an engine cycle (based on piston motion) has been completed. If this is the case, the model computes the 'per-cycle performance indicators'. This includes the total number of engine cycles since simulation start N_{cyc}, the engine indicated power P_{ind}, the piston-displacer phase difference θ_{phase}, the average heat input $\dot{Q}_{heat,avg}$, the cooler heat rejection rate $\dot{Q}_{reject,avg}$, the generator output power $P_{gen,avg}$, etc. It is during this step that the integrated per-cycle change in internal energy (ΔE_i) of the working fluid and metal elements are investigated as a measure of dynamic steady-state convergence. Thereafter a temperature-adjusting scheme is applied to accelerate the evolution of the numerical solution towards a state of thermodynamic steady-state operation. When the solver comes to the completion of a time-step Δt, the program stores the 'new' time-step variables in place of previous. The program then evaluates whether it is required to write the output variables to hard disk storage before subsequently progressing to the following time-step. Results post-processing was accomplished using a separate program coded in *Python 3.6*.

5.2.2. Setup parameters for a case study

The main setup and operating parameters are listed in Table 5.1 for a sample simulated case study of envisaged engine operation. The simulation settings (switches) and operational parameters are imported from user-defined text files, whereas the complete set of engine design parameters have been defined in a separate Fortran module to be representative of the as-manufactured and assembled prototype. Refer to Table D.1 in Appendix D for an extended list of the engine design geometry.

The program facilitates two boundary conditions that may be employed to emulate the power input from the electrical heater head: either a temperature profile may be specified along the outer casing wall, or the heat input flux may be specified. In the case of the latter, a binary-state (on/off) heat input is simulated to emulate the characteristics of a simple electrical heater controller and in so doing limit the hot-end temperature to a predefined set-point temperature $T_{h,set}$ (as was performed in the experimental setup). Depending on the heater input power and controller switching frequency, the average wall temperature profile (also coupled to the engine's kinematic and electrodynamic behaviour) may be expected to fluctuate around this set-point in dynamic steady-state operation. Conversely, if the power input is insufficient, the engine may fail to reach the specified set-point temperature.

Table 5.1: Simulation setup and operating parameters

	Value	[Unit]
Simulation settings (switches)		
Enable piston gas leakage	YES	–
Enable solving temperature profile in casing wall	YES	–
Enable solving temperature profile in bore-cylinder wall	YES	–
Enable temperature acceleration scheme	YES	–
Simulate heater head as heat flux profile	YES	–
Simulation setup parameters		
Time-step	170	ns
No. of heater cells	72	–
No. of regenerator cells	72	–
No. of cooler cells	72	–
Operational parameters		
Working fluid	He	
Charge pressure (abs.) at t_0	1.50	MPa
Total engine gas mass	4.799	g
Heater set-point temperature, $T_{h,set}$	550	°C
Heater power delivery, $\dot{Q}_{h,in}$	1 000	W_{th}
Coolant inlet temperature	20	°C
Coolant volume flow rate	5.5	L/min
Ambient temperature	30	°C
Generator load, R_{load}	1.0	Ω
Tuning capacitor, C_t	12.3	mF
Principal design parameters[1]		
Heater length	35	mm
Regenerator length	34.5	mm
Cooler length	36	mm
Heater-fin heat transfer area (135 fins)	412.08	cm^2
Regenerator void fraction	77.8	%
Regenerator mesh heat transfer area	1 251.34	cm^2
Cooler-fin heat transfer area (135 fins)	326.66	cm^2
Heater channel void volume	13.63	cm^3
Regenerator void volume	17.57	cm^3
Cooler channel void volume	10.52	cm^3
Expansion manifold dead volume	11.81	cm^3
Compression manifold dead volume	7.61	cm^3
Backspace volume	1 970	cm^3
Displacer bore	48	mm
Displacer shaft diameter	10	mm
Piston bore	30	mm
Piston leakage gap (wall-to-wall)	30	µm
Displacer mass, m_d	0.526	kg
Piston mass, m_p	0.952	kg
Displacer spring stiffness, k_d	20 019	N/m
Piston spring stiffness, k_p	24 610	N/m
Piston viscous friction[2], c_p	30	N s/m
Displacer sliding friction, F_d	(±) 1.74	N

[1] The design parameters listed here are representative of the as-assembled prototype.

[2] Although the experimental evaluation in Chapter 7 suggest a piston viscous damping coefficient of between 40 and 77.4 N s/m, the lower value of 30 N s/m was simulated to show the more idealised operation of the prototype engine, as was originally intended.

5.2.3. Accelerated convergence to steady-state

To accelerate the evolution of the numerical solution to reaching thermodynamic equilibrium (in which the engine operates in dynamic steady-state), a *temperature acceleration scheme* has been employed. Analogous to the method first adopted by Schock (1978), the acceleration scheme divides the engine metal (casing wall and bore cylinder) specific heat and internal energy by an 'acceleration factor' k_{accel} to increase the metal's sensitivity to changes in temperature. Then, during the first N_{accel} engine cycles simulated, these reduced specific heats are linearly increased until reaching a factor of unity – consequently damping out any artificially induced temperature oscillations over time. Additionally, at the end of each engine cycle, the backspace gas and regenerator mesh metal temperatures are adjusted as step changes to ultimately minimise their per-cycle rate of change in temperature. More advanced convergence acceleration methods such as the 'shooter-and-predictor' algorithm proposed by Anderson (2006) may be able to accelerate convergence even more, but for its added modelling complexity, has not been considered in the scope of this study.

Figure 5.2 shows the absolute per-cycle rates of change in internal energy of the engine casing wall, bore-cylinder wall and backspace gas as the simulation approaches thermodynamic equilibrium. During the first five seconds, the rates of change in energy are seen to oscillate rapidly as the transient engine start-up induces overshoots and under-shoots in displacer and piston stroke, being intrinsically coupled to the engine thermodynamics and generator electrodynamics. As the simulation time increases towards 10 seconds (and engine cycle count towards 300) the acceleration factor is decreased towards unity. Consequently, the oscillations in metal temperature are damped out. The erratic behaviour exhibited by the backspace gas (especially visible between eight and ten seconds) is attributed to the finite 'step-change' algorithm employed to minimise the per-cycle change in backspace temperature, but has nearly any influence on overall engine dynamics as the rate

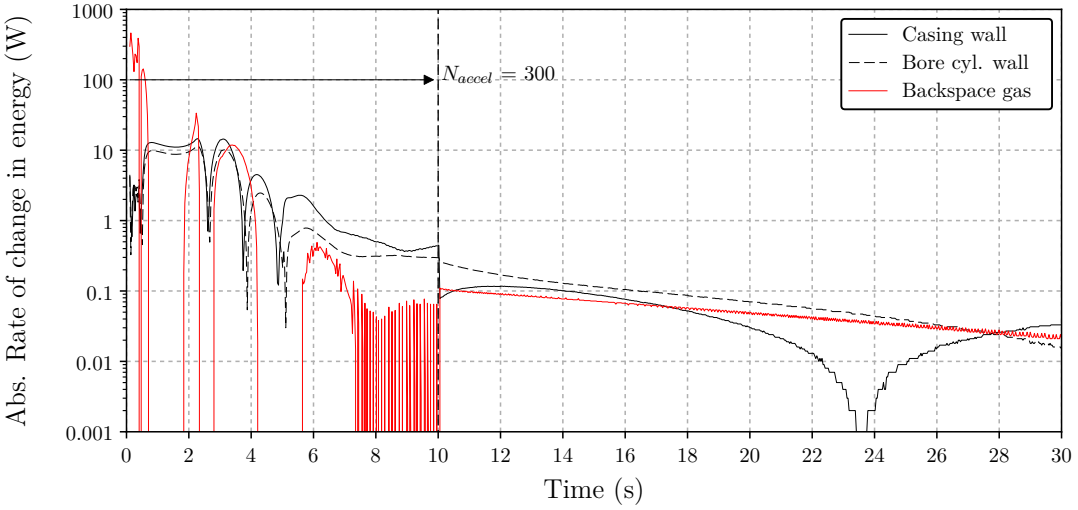

Figure 5.2: Absolute per-cycle rates of change in internal energy

of change is already below 0.1 W. From ten seconds onward, engine operation is simulated without any temperature adjusting scheme. The rates of change converge to below 0.1 W by approximately seventeen seconds and to below 0.04 W after simulating thirty seconds.

5.3. Steady-state simulation results

The simulation results presented in this section are of self-sustained, 1 Ω loaded operation, once dynamic steady-state has been observed to an acceptable degree of accuracy (i.e. the per-cycle rate of change in casing wall thermal energy being less than 0.05 W). The setup parameters listed in Table 5.1 have been used along with a constant heat input of 1.0 kW_{th} being applied as a boundary condition to the hot-end casing wall.

Engine metal temperature profile

Figure 5.3 depicts the engine casing wall T_{wall}, the bore cylinder wall T_{cyl} and the regenerator mesh temperatures T_{rm} as functions of distance x from the top of the heater fins. The figure gives both the initialised (estimated) temperature profile at simulation start-up and the final converged metal temperatures at dynamic steady-state, after simulating in total thirty seconds of engine operation. The temperature profile indicates that the 1 kW thermal heat input from the heater is insufficient to elevate the wall temperature to the design-specified 550 °C. In fact, the temperature profile in the heater section is seen to decrease exponentially towards the regenerator section, varying nearly linearly across the regenerator section towards the cold end. As given by Figure 5.15 on page 75, the simulation results suggest that nearly 210 W of heat flows from the heater wall to the cooler wall via the engine casing and 190 W via the displacer bore cylinder. These profound axial conductive heat flows – often referred to as parasitic heat losses – induce the gradual decrease in hot-end temperature that is nearly 100 °C lower at the interface with the regenerator than at

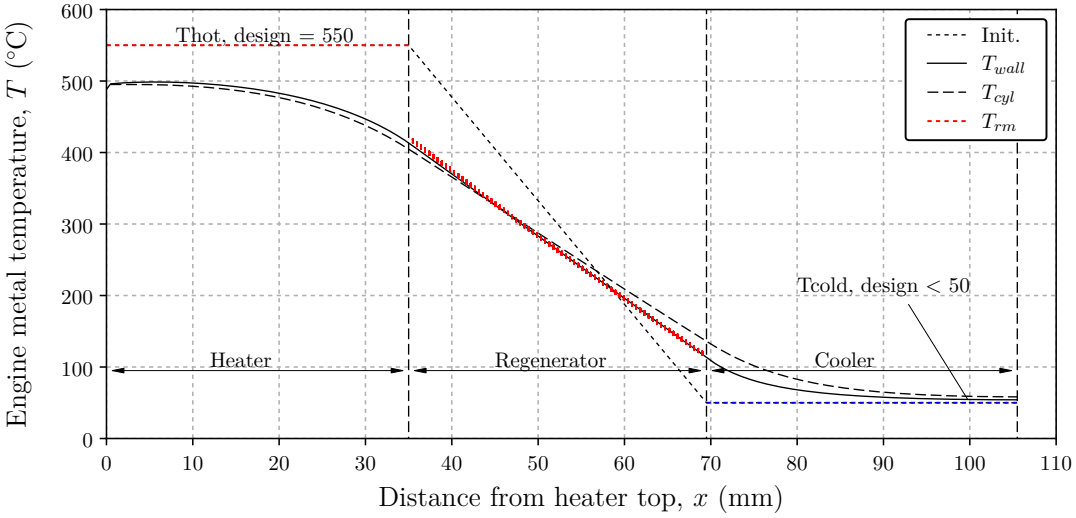

Figure 5.3: Casing wall temperature distribution

the heater top-end. The regenerator mesh temperature is depicted in red, fluctuating by approximately 5 °C along an otherwise linear temperature profile between hot and cold ends, despite being nearly indistinguishable from the casing wall temperature profile on the scale of the figure. These fluctuations result from convective heat transfer with the working fluid as the gas is shuttled between the hot and cold ends.

Displacement and volume variation

In Figure 5.4 the engine's physical motion, and the chamber space volumes induced thereby, is visually illustrated over nearly two complete engine cycles. Due to the phase shift between the displacer and piston motion, the displacer is limited to a minimum distance of 10.3 mm from the piston, being closest at a cycle angle of 330° and coinciding to when the peak in working space pressure P_{max} is induced. In Figure 5.5 the displacer and piston displacements are shown relative to their mid-stroke locations over two complete engine cycle, with the direction of positive displacement being defined *into* the backspace, as was shown in Figure 3.3. Under the operating parameters listed in Table 5.1, the model indicates self-sustained operation at a damped natural frequency of 29.94 Hz with peak-to-peak displacer and piston strokes of 24.93 mm and 22.58 mm respectively, and a piston-displacer phase difference θ of 76.3°. The workspace pressure swing is seen to lead the displacer and piston's peak expansion strokes (downward motion) by 48.9° and 125.2° respectively, denoted by α and β. The piston reciprocates with a positive offset of 1.08 mm, which has resulted as a natural model outcome as the engine operates at a state of thermodynamic equilibrium. As noted by Karabulut (2011), the piston offset can be decreased by allowing for the controlled leakage of gas from either the workspace to the backspace or vice versa via a connecting port that opens when the piston exceeds some design-specified displacement range.

Figure 5.6 shows the volume variations in the expansion (e) and compression (c)

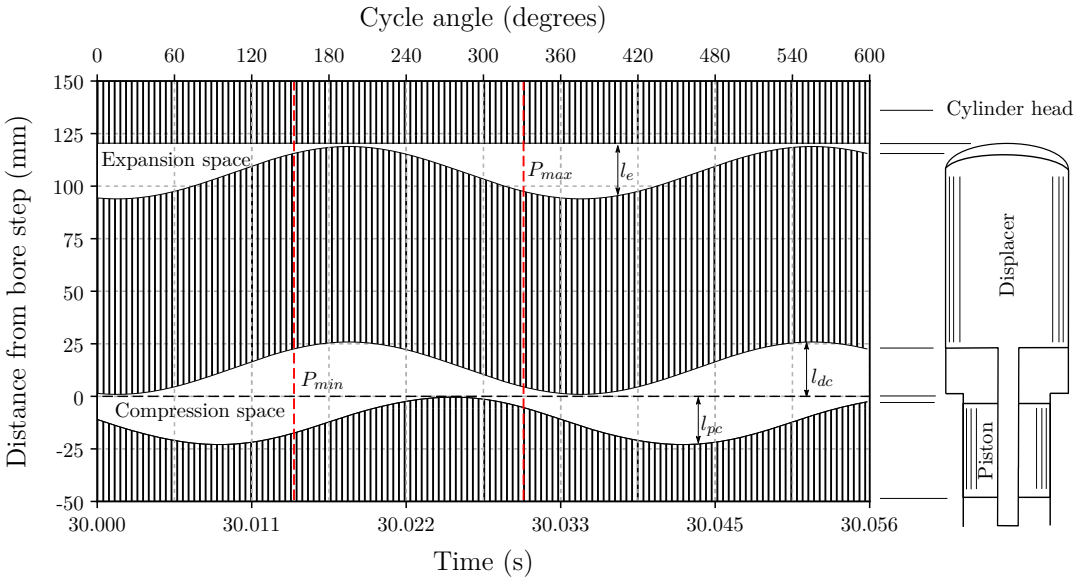

Figure 5.4: Displacer and piston distances from cylinder bore step over time

spaces (including their respective manifold dead volumes) together with the variation in *total* working space volume (ws) as induced by the moving displacer and piston. The addition of the heat exchanger dead-volume is also depicted. The figure should highlight that, in comparison to total working space volume, the 14.5 cm^3 variation thereof is small, consequently resulting in a small volumetric compression ratio (V_{max}/V_{min}) of 1.13. It is well known from the literature that Stirling engines generally achieve low compression ratios (and power densities), with an upper limit of 2.5 proposed by Walker (1980). This is due to the requirement of large internal

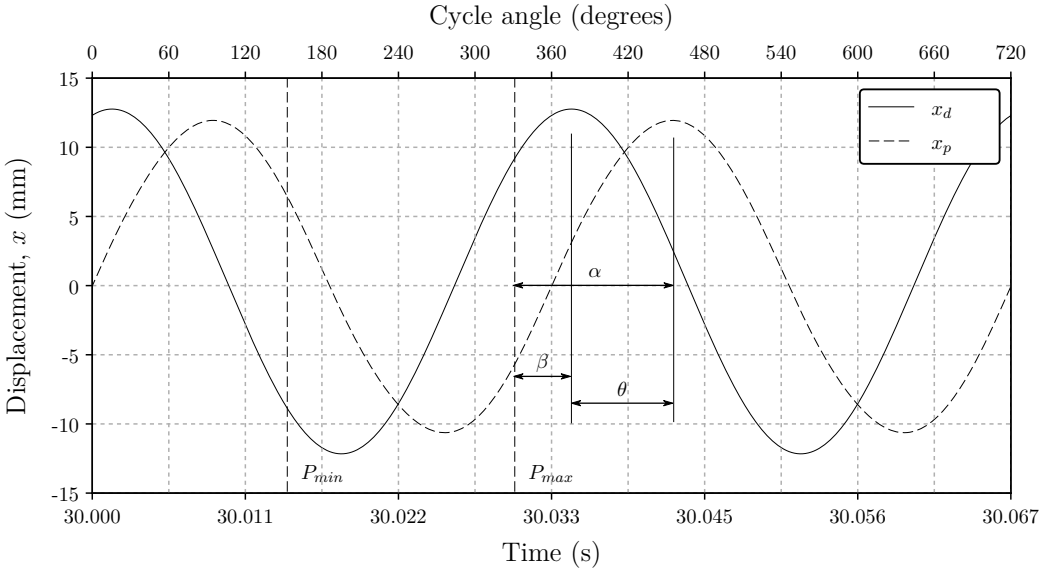

Figure 5.5: Displacer and piston displacements over time

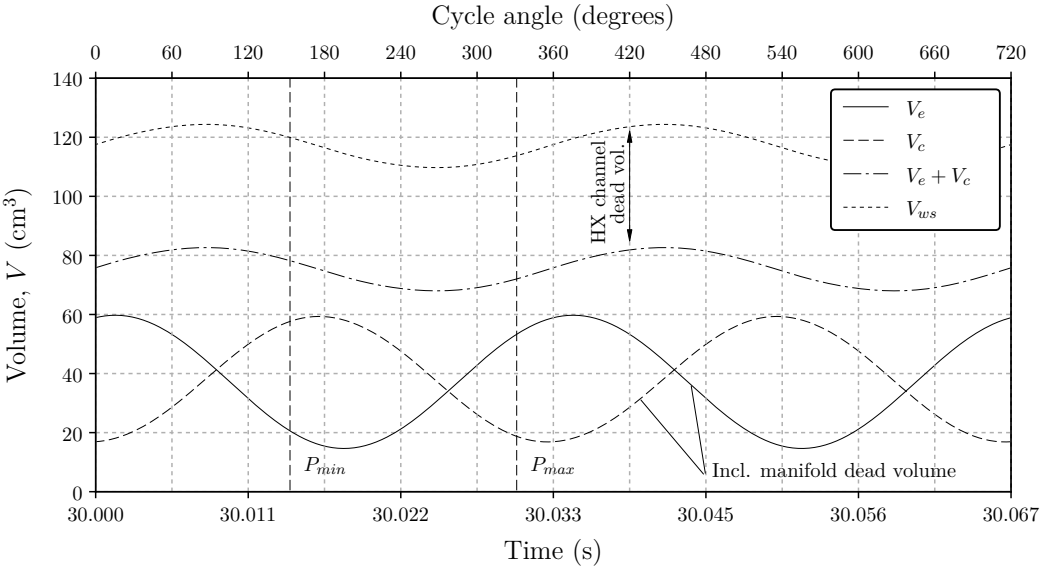

Figure 5.6: Volume variation of the engine working spaces over time

heat exchange surfaces for sufficient heat transfer. It is worthwhile to note that in this study, the especially low compression ratio simulated for the prototype is a result of the small piston swept volume relative to the internal engine dead volume.

Pressure, velocity and mass flow rate profiles

Figure 5.7 shows the variation in gas pressure of each i^{th} control volume and the gas velocity distribution at fifteen equispaced locations along the interface nodes j. The engine cell pressures and nodal velocities are coupled by the backwards-staggered vector control volume grid used, with positive interface velocities indicating flow from the expansion to compression space and vice versa. The distribution of the velocity profile suggests continuous flow through the heater, regenerator and cooler sections for which the cross-sectional flow area remains uniform. However, at the interface where differing flow boundaries are connected, for example, where the regenerator interfaces with the heater and cooler sections (N_h and N_r), this distribution becomes discontinuous. Consequently, a sudden 'step change' in velocity distribution is seen despite the mass flow rate distribution remaining continuous. The steepest velocity gradient is seen to occur through the regenerator section, where fluid friction is also most prominent. As the gas passes through the regenerator in the direction of the compression space, it essentially 'deposits' heat into the regenerator mesh and is thermally contracted. The opposite occurs when the gas is flowing towards the expansion space, thereby inducing the steep gradient in nodal velocity. At a cycle angle of approximately 90°, when the gas is being shuttled at its peak velocity towards the compression space, a slight gradient in heater velocity profile is noted. This occurs as the gas is in fact *expanded* by the heater and consequently accelerated into the regenerator channel, flowing from node N_2 towards N_h. Similarly, at a cycle angle of 270° when the gas is shuttled towards the expansion space, the cooler *contracts* and slows down the gas flow, resulting in a slight velocity gradient as gas flows from node N towards N_r.

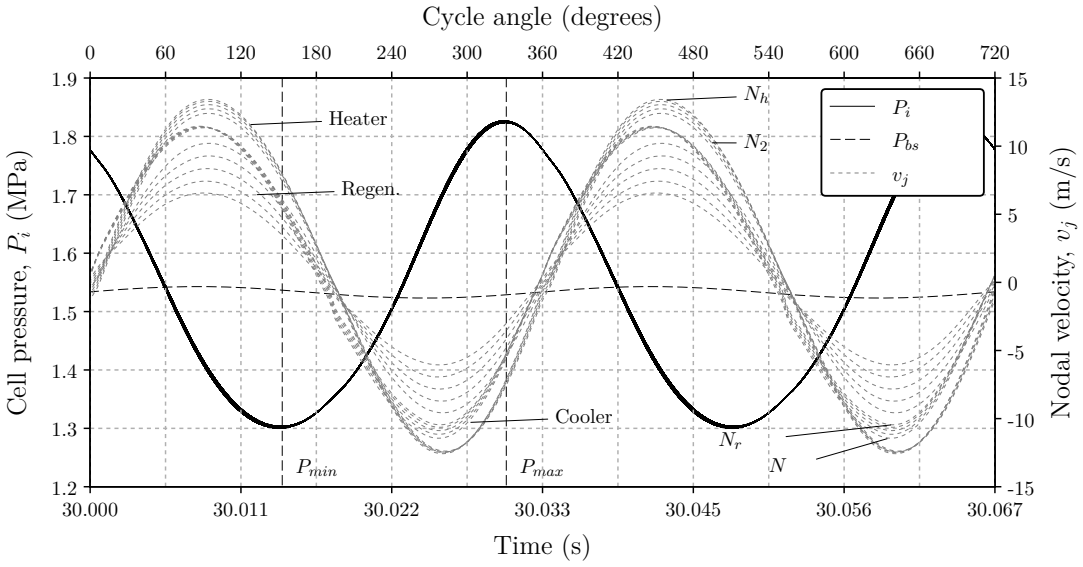

Figure 5.7: Cell pressure and interface node velocity variations over time

The pressure curves P_i shown in Figure 5.7 are distributed so close to one another that they appear visually indistinguishable on the scale of the figure. Between the expansion and compression space volumes, there is a maximum pressure difference of approximately 10 kPa. This pressure difference is induced mainly by flow friction in the regenerator mesh, as will be further highlighted in Figure 5.16 (c). Additionally, due to the finite-speed propagation of information through the system that occurs at the speed of sound in the gas medium, there is a slight shift in phase between the expansion and compression pressure swings. Moreover, as a consequence of the low volumetric compression ratio, a low pressure ratio (P_{max}/P_{min}) of 1.4 is expected from the prototype. It is also noted that the workspace pressure swing P_i is positively offset about the backspace pressure P_{bs}, and that the rate of change in peak pressure swing is slightly larger than the rate of change during the low pressure swing. As described by Walker and Senft (1985), this phenomenon is induced by nearly adiabatic nature by which the working fluid is compressed and expanded by the moving power piston. The more 'peaky' nature of the workspace pressure swing induces a net amount of enthalpy leakage to the backspace, often resulting in the piston to drift towards the expansion space. However, as the workspace pressure swing is in this model predicted to be positively offset from the more uniform backspace pressure, the piston has drifted into the backspace, as is seen from Figure 5.5.

Figure 5.8 shows the cyclical variation in node mass flow rate $\dot{m}_j$ to be non-uniform. At a cycle angle of approximately 200°, the displacer is brought to a brief standstill whilst the piston is compressing the gas. This results in the sudden (negative) acceleration of the mass flow rate in the cooler side. This phenomenon gives rise to the appearance of a travelling 'density wave' in the working fluid that propagates from the compression space towards the expansion space, as will be shown by way of Figure 5.16 (b). A similar phenomenon occurs in the heater gas channel

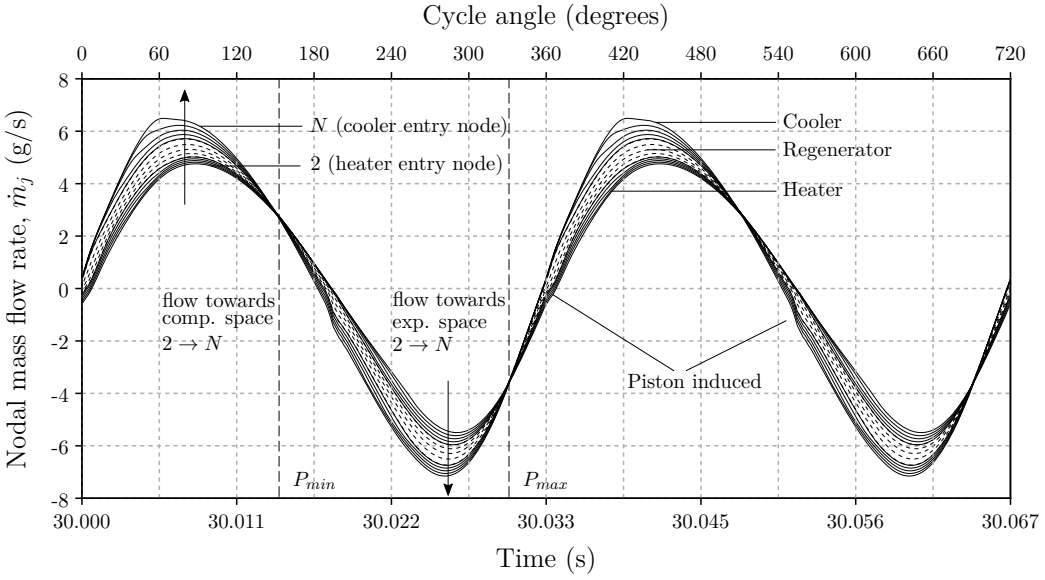

Figure 5.8: Variation in nodal mass flow rate over time

around a cycle angle of 360° when the working fluid is being expanded by the piston. Only when the pressure swing is at a maximum or minimum is the mass flow rate approximately uniform, being in accordance with the gas density distribution becoming nearly uniform. Furthermore, at cycle angles of approximately 60 and 420° the appearance of a local peak in positive mass flow rate is noted at the interface between the cooler and compression space (at node $j = N$). This peak coincides to when the compression space and backspace pressure curves intersect one another and subsequently, the direction of workspace-backspace gas leakage changes. In this particular instance, the piston is still expanding the working space whilst gas has started flowing from the backspace towards the compression space (node N), resulting in the sudden reduction and flattening of the positive nodal mass flow rate in the direction of the compression space. Although barely noticeable, around 240° the opposite occurs, as gas starts leaking from the compression space towards the backspace.

Mechanical and electrical power delivery

The net gas forces acting on the displacer and power piston are depicted in Figure 5.9 in relation to their displacements, with the arrows denoting how the force profiles revolve around the direction of movement. Correlating to the positive offset in piston mid-stroke, the net gas force acting on the piston is also seen to be offset in the positive force direction. Consequently, the net pressure force acting on the piston reaches a peak value of nearly 200 N at a displacement of approximately −6 mm when the piston is travelling in the positive displacement direction. In contrast, a peak gas force of −150 N at a displacement of 7.5 mm is induced when the piston is moving in the negative direction. The encapsulating area within the piston force-displacement diagram represents the net per-cycle indicated work done *onto* the power piston *by* both the workspace and backspace gas, relating to a net indicated power of 148.7 W. Of this piston indicated power, 68.4 W is dissipated by mechanical friction, which has for reading clarity been omitted from this figure. As shown by the displacer force-displacement diagram, the displacer extracts a nearly negligible indicated power of

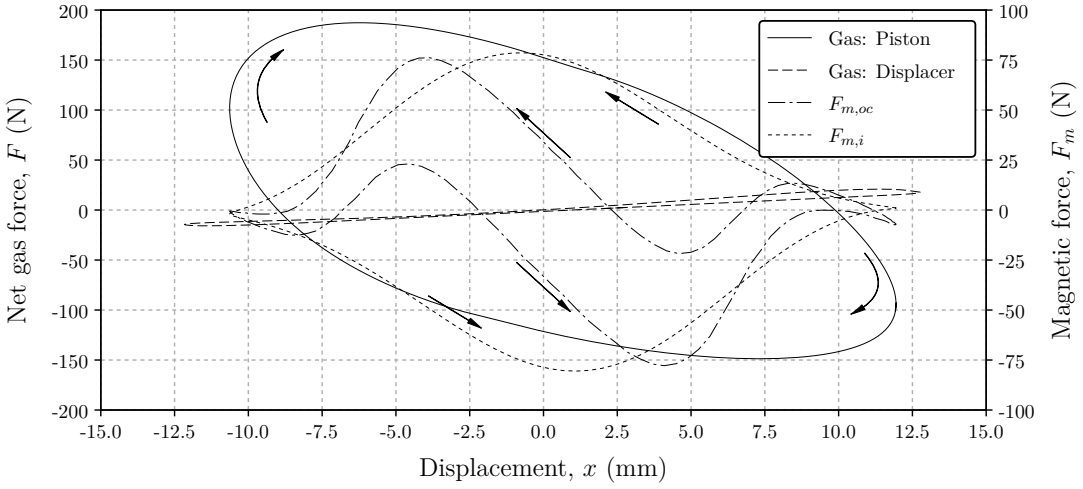

Figure 5.9: Gas and electromagnetic force-displacement diagram

2.6 W from the combined working space and backspace gas to overcome displacer friction. Furthermore, the figure shows the generator magnetostatic force constituent $F_{m,oc}$ and the current-induced Lorentz load force $F_{m,i}$, as being inferred from the generator characteristic equations. The electromagnetic load force is slightly offset from the zero-displacement location due to emf-current phase lag, as is more clearly illustrated by Figure 5.12 for example. The encapsulating area within the open-circuit magnetic force-displacement diagram relates to 27.5 W of power being lost irreversibly to heat generation by core losses. Of the piston indicated power, 52.8 W of power is being extracted by the electromagnetic load force (excluding core losses), of which 14.3 W is irreversibly dissipated to ohmic losses in the generator coil so that the generator ultimately delivers 38.5 W usable electric power to the external load.

In Figure 5.10 a pressure-volume (PV) diagram is given, depicting the per-cycle variation in expansion and compression space pressures to their respective chamber volumes. The PV curves evolve in opposing directions with volume as depicted by the arrows. By integrating the area encapsulated by these PV curves, it is calculated that during a single engine cycle, the gas working fluid has a net 7.15 J of work done *onto* it in the compression space, whilst the gas delivers a net 12.21 J of positive work in the expansion space. This relates to 214.27 W and 365.68 W of compression and expansion space boundary work rates, with the workspace delivering a net positive indicated power of 151.41 W. Not shown here is that 0.11 W of net work is being done *onto* the backspace gas by the reciprocating piston and displacer, which is virtually negligible. Neither the expansion nor compression space chambers reach volumes smaller than 15 cm^3, indicating the remainder of unswept dead volume. This chamber dead volume is most prominently attributed to the additional volume of the heater and cooler manifolds that cannot be 'swept' by the piston or displacer.

Figure 5.11 shows the expansion and compression space pressures in relation to the *total* working space volume. It is seen the expansion and compression space pressures

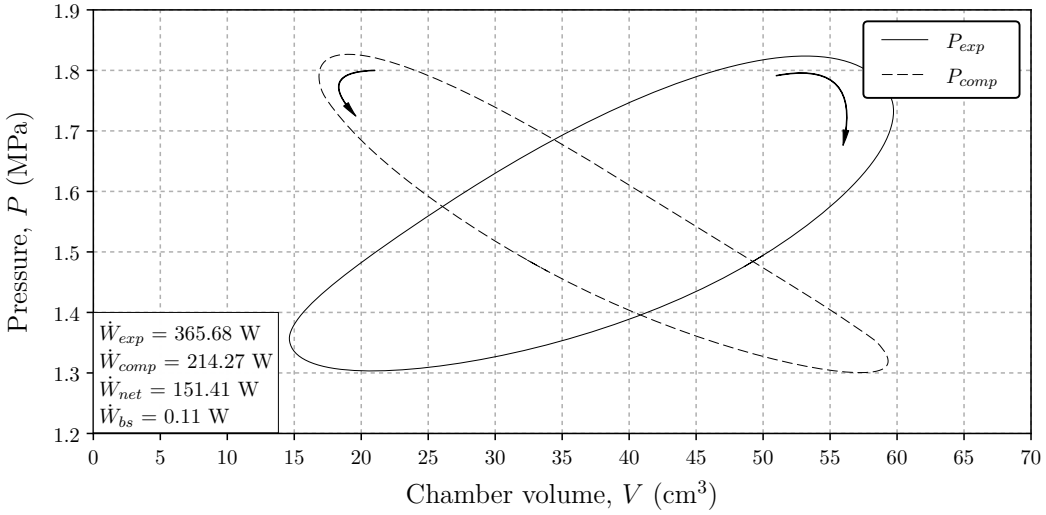

Figure 5.10: Expansion and compression space pressure versus chamber volume

are nearly indistinguishable, apart from the viscous dissipation pressure loss and a small pressure phase shift that results from the finite-time thermodynamics. The encapsulating area within the expansion space curve indicates a net work rate of 165.72 W whereas the compression space curve yields 166.26 W, resulting in a net difference of 0.54 W which is attributed to the very slight phase difference between the gas pressures within the chambers. When compared to the net indicated power calculated from Figure 5.10, it must be noted that the average encapsulating area of Figure 5.11 suggests the net indicated power to be larger by 14.5 W as opposed to what was previously calculated. This difference arises as the indicated power calculated using the *total engine volume* of Figure 5.11 does not take into account the work being dissipated to overcome internal flow friction. Furthermore, this finding identifies a limitation of the experimental test setup presented in Chapter 6.5, – in which only the expansion space pressure is measured and used to calculate the engine's net indicated power. Consequently, the experimentally calculated indicated power will be inclusive of regenerator friction flow losses and thus be slightly over-predictive of the actual engine's performance.

The generator induced emf, load voltage and current is shown in Figure 5.12. As seen, the induced emf and load voltage have the approximated shapes of elongated sinusoids with distinctive inflexion points at the zero voltage crossover. These inflexion points arise from the flattening of the flux linkage curve, shown in Figure 4.3 on page 50, that occurs as the piston displacement approaches its design-specified stroke limits. This effect is especially noticeable at a cycle angle of 120°, when the piston reaches a peak displacement of approximately 12.5 mm. Additionally, the emf and load voltage profiles are seen to be slightly asymmetrical due to the offset in piston stroke. But despite the simulation predicting an induced emf with an amplitude in the range of 15 V, a load voltage with an amplitude of only 10 V is produced, as some electrical power is dissipated by the coil's inductance and 0.4 Ω internal resistance. The current flow direction has been defined as being negative

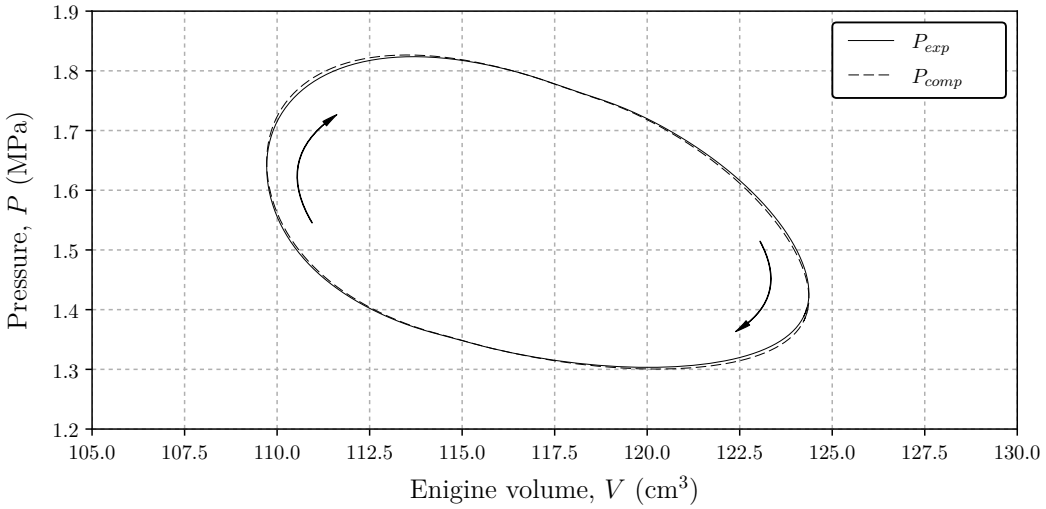

Figure 5.11: Expansion and compression pressure versus engine workspace volume

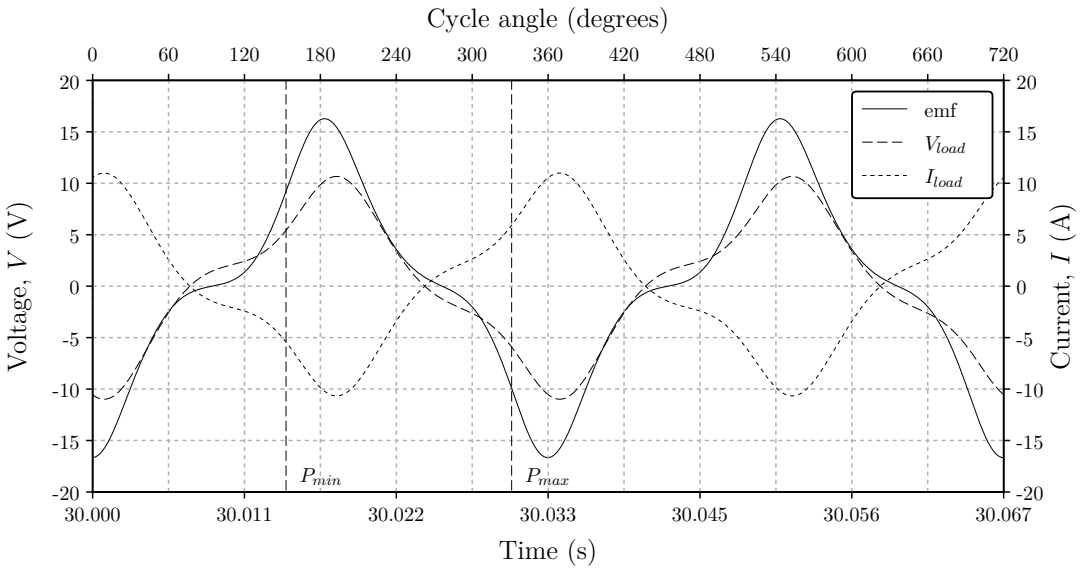

Figure 5.12: Induced emf, load voltage and current for the linear generator

in relation to the induced emf and load voltage, since it acts to oppose the induced emf. By introducing a tuning capacitor in the load circuit, the load voltage and current have been made nearly in phase with the induced emf. However, since the emf is not a perfect sinusoid, the phase lag is not entirely eliminated. This has resulted in the slight force-displacement shift from the zero displacement axis that was observed for the electromagnetic load force in Figure 5.9.

Energy transferred and heat rates

To investigate the engine's expected thermal performance, Figure 5.13 gives the net heat transfer rates from heater and cooler jacket to the engine casing wall ($\dot{Q}_{heat}$ and $\dot{Q}_{cool}$), along with the net heat transfer rates to and from the working fluid ($\dot{Q}_{h-g}$ and $\dot{Q}_{g-k}$) within these heat exchanger sections. Additionally, the figure illustrates the net electrical power delivered to the generator load, P_{gen}. The heater delivers power at a constant rate of 1000 W, whereas at the cold-end, the engine rejects 835.56 W of thermal energy to the cooling water. Additionally, 13.14 W is convected to the ambient surrounding by the backspace casing. The net rate of heat input to the engine may be calculated to be 151.30 W, which equals the per-cycle average mechanical power delivered to the piston and displacer. This proves that the model is conserving energy (as is further illustrated by Figure 5.15). Moreover, the figure shows that the generator delivers power to the electrical load during two peaks of 115 and 120 W respectively, which, when integrated over the engine cycle, leads to an average electrical power output of 38.5 W.

From Figure 5.13, the cyclical variation in net heat absorption rate by the hot gas and net heat rejection rate by the gas in the cooler section should be noted. The two distinctive peaks in both heater-to-gas and gas-to-cooler heat rates are induced when the bulk of the working fluid is being shuttled through the heat exchanger channel (in either direction). The first peak, seen around a cycle angle of 120°,

occurs as the fluid is being shuttled towards the compression space, also coinciding with the thermal charging of the regenerator mesh as seen from Figure 5.14. During this motion the gas is being pre-cooled by the regenerator, resulting in a flatter but more uniform heat rejection rate in the cooler section. Similarly, at around 300°, when the bulk of fluid is being shuttled to the expansion space, a second peak is noticed, coinciding to the discharge of regenerator mesh. The pre-charging of the working fluid by the mesh results in a slightly flatter but more uniform heat transfer rate from the heater. On a per-cycle basis, the net difference of the integrated area under the heater and cooler rates is representative of the net indicated work done

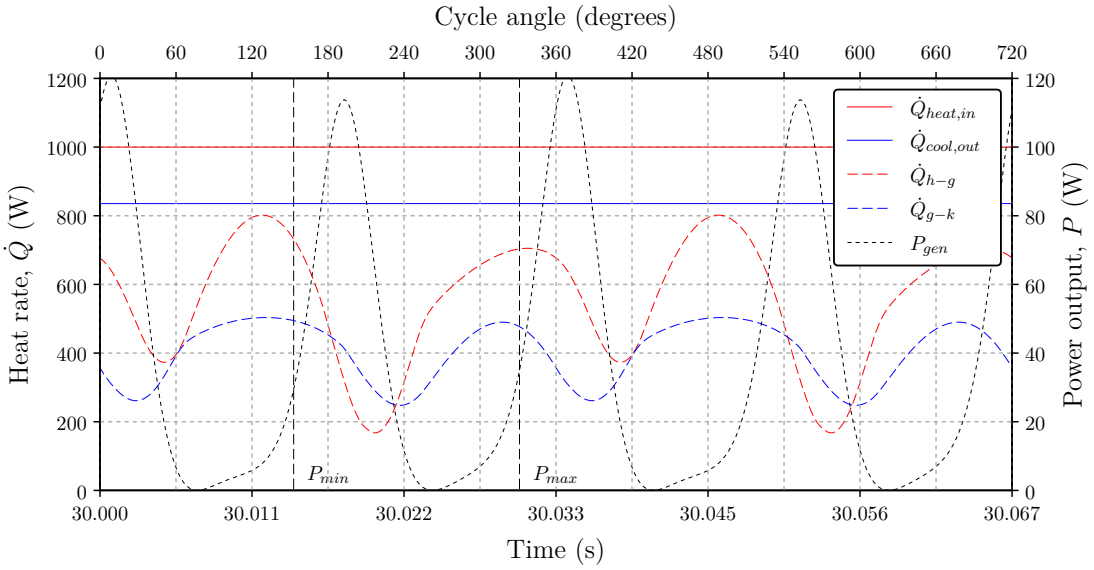

Figure 5.13: Electrical power generated and heat delivery and rejection rates

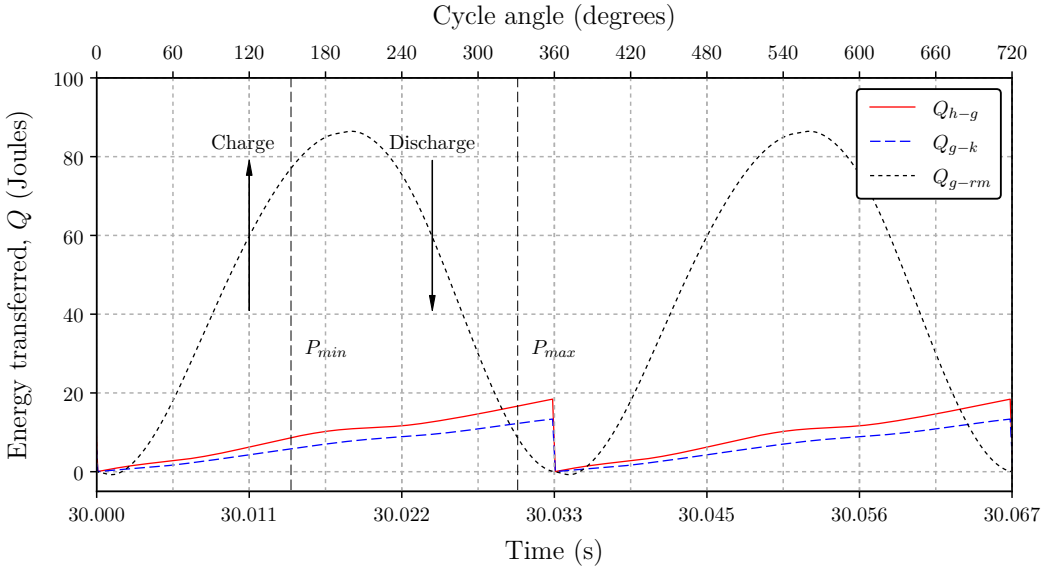

Figure 5.14: Net heat transferred in Joules

by the engine minus the heat rejected by the backspace casing.

In Figure 5.14 the net heat transferred to the hot gas, Q_{h-g}, and net heat rejected by the cold gas, Q_{g-k}, is shown to highlight the scale of heat transfer occurring within the heater and cooler relative to the regenerator. When thermodynamic steady-state is reached, the net amount of heat transferred from the working fluid to the regenerator mesh metal during a single engine cycle is zero. The sinusoidal appearance of Q_{g-rm} illustrates the thermal charging and discharging of the regenerator mesh as mentioned previously. It must be noticed that the regenerator mesh stores and delivers *nearly four times* the thermal energy that is being delivered by the hot-end. As the regenerator surface area and volume are increased, this ratio will increase further and so will the thermodynamic efficiency, but at the expense of larger regenerator frictional pressure losses and dead volume. Consequently, the development of an optimised regenerator presents itself as a trade-off study between increasing the regenerator thermal capacity (and dead volume) and minimising frictional pressure drop (Ibrahim and Tew, 2012). The significantly large amount of heat being rejected to the cold-end (i.e. wasted heat) should also be noted. This could be decreased by further expanding the working fluid, for example, by increasing the piston swept volume.

Energy balance diagram

In Figure 5.15 an energy balance diagram is given to aid in visualising the flow of energy through the engine. It is immediately noticeable that a significant percentage of the thermal heat input is rejected by the cooling jacket. In fact, 83.5 % of the heater input power, or nearly 5.5 times the energy converted to mechanical power, is rejected to the cooler. This poor thermal performance is attributed to the considerably large axial conductive heat transfer that occurs through the casing and bore cylinder walls, making up approximately 50 % the heat rejected to the cooling jacket. The figure indicates that 210.74 W of heat is being conducted axially from the heater towards the regenerator in the casing wall. Since there is nearly any heat transfer between the regenerator wall and working gas, this heat is rejected by the cooling jacket. If the internally located heating and cooling fins are both in contact with the casing and bore-cylinder walls, a thermal-short circuit is created (as has been simulated). This results in a further 234.69 W of heat being conducted from the heater through the fins and into the displacer bore cylinder, of which 220.8 W is then rejected to the cooling jacket. Moreover, from Equations (3.15) and (3.16), 21.4 W and 18.7 W of displacer shuttling and wall conductive losses are estimated to occur between the hot and cold ends. These losses have been omitted from the energy balance diagram as they are classified as being 'decoupled' from the engine thermodynamic model.

Figure 5.15 also shows how the workspace and backspace gas reserves are interlinked via gas leakage and boundary work. By gas enthalpy leakage, energy is transported at a net rate of 13.05 W from the compression space towards the backspace. The working space exerts boundary work at a rate of 149.67 W onto the power piston and 1.74 W onto the displacer. In turn, the free-running power piston exerts 0.97 W of boundary work onto backspace, of which 0.86 W is exerted back onto the displacer

shaft. The displacer dissipates mechanical energy at a net rate of 2.60 W to contact-sliding friction. Due to the large piston mechanical friction simulated under the input parameters of Table 5.1, a considerable 68.37 W of power is expended to piston-sliding friction. Due to the relatively poor electrical efficiency of the linear generator, 41.82 W is irreversibly dissipated by generator core and ohmic losses, so that only 38.51 W is converted to usable electrical power. The irreversible heat generated by mechanical friction and generator core losses has, in this case study, not been added back to the working fluid as a heat-generating source term. If this heat is added back the engine would require a further 112.79 W of heat to be rejected to the water cooling jacket.

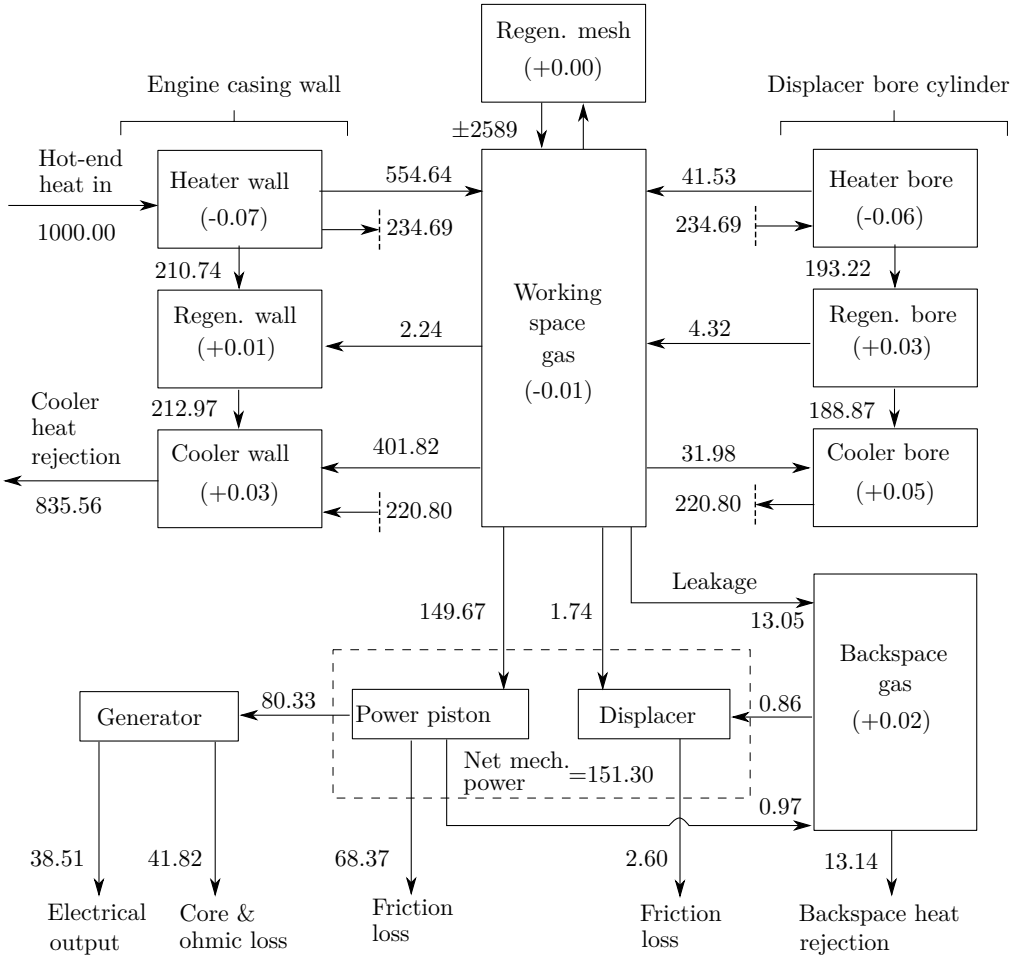

Key performance indicators

Net heat in = 1000.00 W	Indicated power = 151.30 W	Thermal eff. = 15.13 %
Net heat reject = 848.70 W	Irreversible loss = 112.79 W	Mechanical eff. = 53.67 %
Usable power out = 38.51 W	Axial heat loss = 433.77 W	Electrical eff. = 47.94 %

Figure 5.15: Energy balance diagram depicting the per-cycle averaged rates of energy transport and rates of change in internal energy in Watts

From the energy balance diagram the net thermal efficiency may be calculated as 15.13 %; the mechanical efficiency as 53.67 %; and the electrical efficiency as 47.97 %. This leads to a considerably low net thermal-to-electrical efficiency of only 3.89 %. It is suggested that the low net efficiency is attributed to significant axial conductive heat losses in the casing and bore cylinder walls that, in effect, limits the available heat input to expanding the workspace gas. Additionally, large mechanical friction dissipates nearly half of the indicated power being produced. Should a more idealised case study be presented, one in which the axial heat losses are neglected, the thermal efficiency could theoretically be increased to $151.3/(1000-433.77) = 26.7\,\%$. Furthermore, should the combined mechanical and electrical efficiencies be assumed as 90 %, which would entail a more optimised laminated generator core with reduced ohmic losses (and possibly incorporating dynamic gas bearings to reduce piston friction and improve the alignment), the still-unoptimised prototype could be expected to deliver a net efficiency of nearly 24 %.

Spatial and temporal variation in gas properties

The spatial and temporal distribution in gas temperature over a single engine cycle is shown in Figure 5.16 (a), along with the arrows depicting the gas flow direction. The influence of the respective heating and cooling channels on the working fluid is noticeable by the grouping of the gas temperatures around two common sink temperatures, being that of 450 and 80 °C. Between the heater and cooler sections a nearly linear gas temperature distribution in the regenerator section is noted. The spatial 'fold' in the gas temperature, especially noticeable in the heater channel at a cycle angle of 200°, is induced when the gas flow reverses – allowing more time for heat transfer to occur. This induced temperature peak is then propagated in the new direction of gas flow (for example towards the expansion space after 200°). In comparison to the heater and cooler channels, the larger expansion and compression spaces act as thermal reserves. The cyclical temperature variation within these spaces highlights the reversible (nearly adiabatic) boundary work done by the power piston in compression and expanding the fluid, with the peaks in gas temperature being in accordance to the peaks in workspace pressure swing.

The spatial and temporal gas density distribution is given in Figure 5.16 (b). The temporal variation in density is predominantly caused by the thermal expansion and contraction as the working fluid is displaced between the heater and cooler sections, being intrinsically coupled to both temperature and pressure. For example, the density distribution through the heater, regenerator and cooler sections is seen to vary approximately sinusoidally with cycle angle, correlating to the temporal pressure variation shown in Figure 5.7. As the working fluid is displaced from the hot end towards the cold end it is thermally contracted – with an approximately linear density distribution existing between the hot and cold ends. It is partially due to this increase in gas density that the cooler velocity profile, shown in Figure 5.7, is lower than that of the heater channel. Furthermore, with reference to the discussion on mass flow rates, the 'travelling density wave' is also depicted, as seen moving from the compression space towards the regenerator.

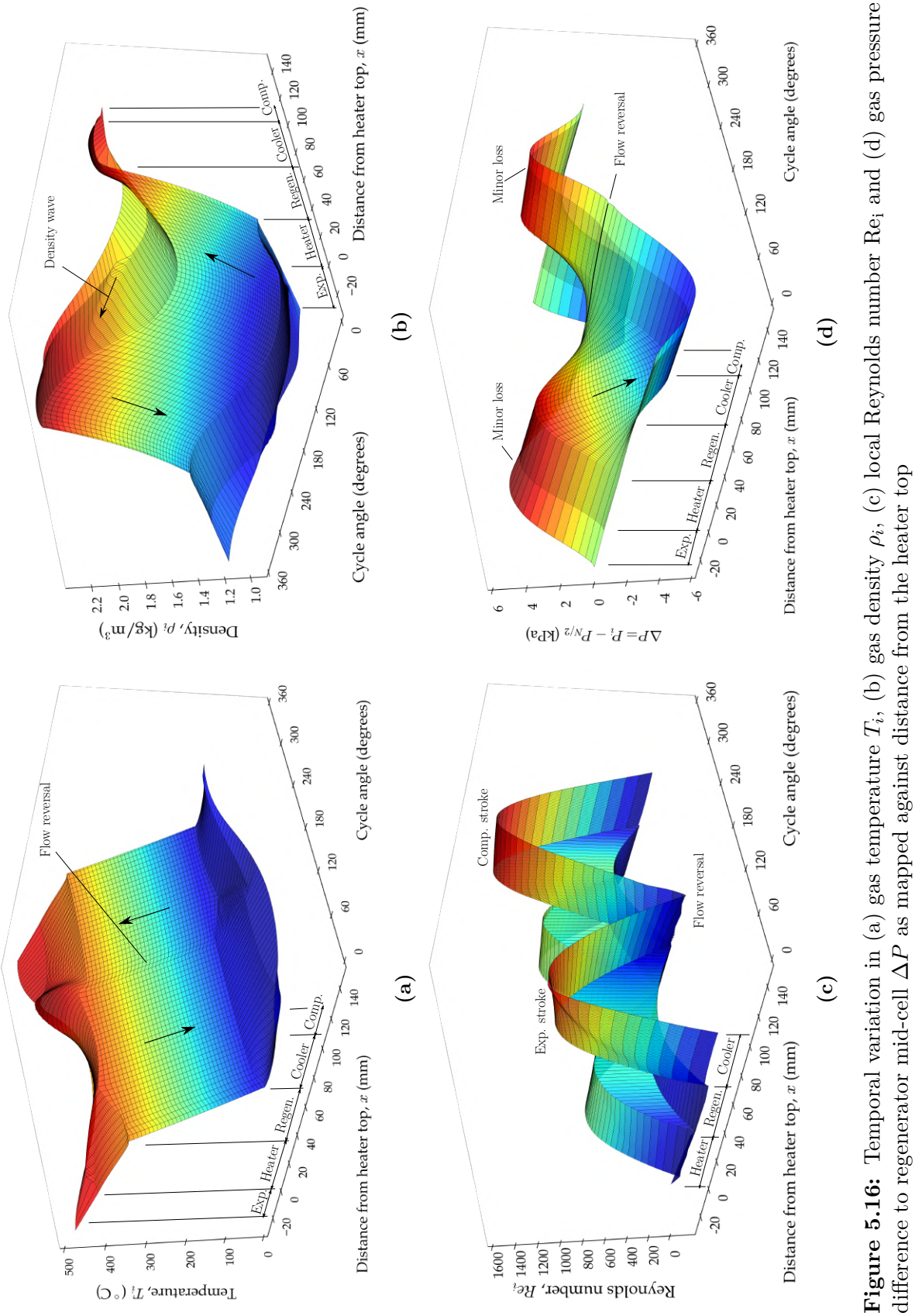

Figure 5.16: Temporal variation in (a) gas temperature T_i, (b) gas density ρ_i, (c) local Reynolds number $\mathrm{Re_i}$ and (d) gas pressure difference to regenerator mid-cell ΔP as mapped against distance from the heater top

In Fig. 5.16 (c) the variation in local Reynolds numbers Re_i along the heater, regenerator and cooler channel is illustrated. The temporal (cycle angle) variation in Reynolds number is induced by the oscillating velocity profile as the gas is shuttled back-and-forth by the displacer. For the design-specified engine geometry and 30 Hz operating speed, the Reynolds numbers appear to be established well below 2,300 and thus indicative of laminar flow throughout all the heat exchanger sections. Interestingly, the Reynolds numbers appear to be the largest in the cooler channel. This may be partially attributed to the gas being most dense in the cooler section, but also the cooler void (flow) channel being smaller than that of the heater. Due to the significantly small hydraulic diameter of the mesh-screen, fluid flow is especially laminar in the regenerator section. This might explain why studies in literature, for example the experimental and numerical investigation by Costa *et al.* (2014), typically limit their findings to low Reynolds numbers (often below 400). Furthermore, a noticeable 'fold' in Reynolds distribution is seen at a cycle angle of about 60°, correlating to the sudden flattening of the nodal mass flow rate in the cooler channel seen from Figure 5.8.

In Figure 5.16 (d) the pressure gradient throughout the heat exchanger channel is depicted as the difference in local cell pressure to the regenerator mid-cell pressure over time, $\Delta P = P_i - P_{N/2}$. It is seen that throughout the heater and cooler channels there appears to be virtually no pressure gradient (drop), leading to the nearly uniform pressure field. In contrast, cyclical pressure differences of approximately ± 5 kPa is seen throughout the regenerator section, varying nearly sinusoidally over time as the working fluid is shuttled back-and-forth by the displacer. It is therefore noted that the only significant pressure drop occurs through the regenerator section, which, together with displacer mechanical friction, must be overcome by the differential pressure forces acting on the displacer shaft if the engine is to operate in a self-sustaining manner. The figure also depicts a slight pressure drop towards the expansion and compression space volumes that results from minor entry-loss effects. These losses are negligible in relation to the pressure drop in the regenerator.

5.4. Grid independence study

Model discretisation accuracy was investigated by performing a grid independence study in which the heater, regenerator and cooler sections were each refined from 10 to 550 control volumes respectively using a grid refinement ratio of 1.5. Since the model considers the *free*-running displacer and piston dynamics, their strokes and the net thermal-to-electrical efficiency were investigated as performance measures to convergence (once sufficient dynamic steady-state operation is reached). As linear upwind differencing was predominantly used throughout the model, the discretised model may be expected to converge with a first-order accuracy to decreasing mesh size (Versteeg and Malalasekera, 2007).

Fig. 5.17 shows the convergence of the displacer and piston strokes to an increasing number of control volumes. The strokes asymptotically approach values of 25.91 and 23.83 mm respectively, which may be noted as the *true* solution to the mathematical model. Simulating only 73 control volumes in the heater, regenerator and cooler sec-

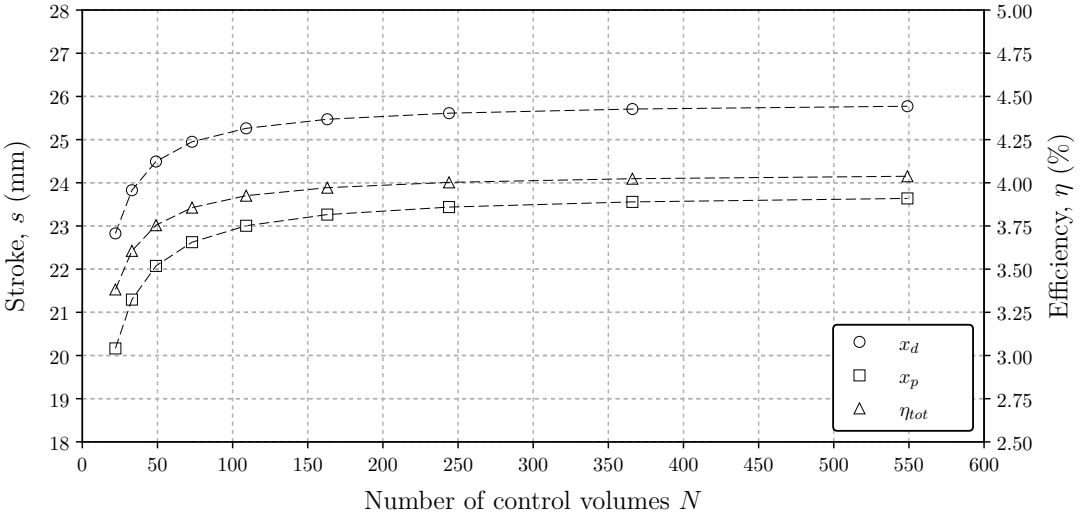

Figure 5.17: Engine stroke and net efficiency versus the number of control volumes simulated in each heat exchanger channel

tions (or 222 control volumes in total if the expansion, compression and backspace volumes are also included) resulted in 3.7 and 5.1 % under-predictions in displacer and piston stroke, respectively. The net thermal-to-electrical efficiency converges towards 4.1 % and although not depicted, the average load power to 40.7 W. Consequent, by simulating 73 control volumes, the net engine efficiency is under-predicted by 5.3 percentage points and the net electrical output power by 5.2 %. But as the number of control volumes and the number of equations to be solved are increased, the time-step size must be decreased to ensure that the momentum equation does not induce numerical instability. This has the profound effect of increasing the computational resource requirement nearly quadratically with an increase in total cell count. It was found that simulating 163 control volumes reduces the displacer and piston stroke error down to 1.69 and 2.37 % respectively, whilst requiring 66.6 seconds of processor time per simulated cycle, compared to 15.1 seconds per cycle with 73 cells, when performed on a 2.10 GHz Intel i7-4600U processor.

It is postulated that the most significant advancement to decreasing the *total* processor time required can be made by accelerating the model's evolution towards reaching thermodynamic steady-state. In a further effort to decrease the required simulation time, it was found that by reducing the number of control volumes in the respective heater and cooler sections down to thirty had a negligible effect on the solution performance indicators (i.e. displacement, power and net efficiency). In contrast, as the regenerator is subject to large temperature, pressure, density and velocity gradients, model convergence is especially sensitive to the number of regenerator cells employed. This model accuracy dependence on regenerator mesh fineness has independently been confirmed by Urieli and Rallis (1976) and Yuan and Spradley (1992), and partially motivates why often in literature a regenerator effectiveness method is adopted. Another consequence of solving the coupled thermodynamic and kinematic engine cycle is that any under- or over-shoot in the gas

thermodynamic properties (pressure and temperature) induce either an under- or over-shoot in the displacer and piston displacement, which in turn, influences the thermodynamic cycle one more. Nevertheless, it is argued that for quick comparative case studies of different engine design considerations, as little as 73 control volumes in the respective heat exchanger sections are sufficient, although resulting in stroke and net efficiency under-predictions in the range of five to seven percent.

5.5. Numerical stability

An investigation into time-step dependence and numerical stability was performed according to the *Courant Friedrichs Lewy* (CFL) stability criterion for fully-explicit numerical methods comprising of advection (Courant *et al.*, 1928). For the one-dimensional control volume i, the local Courant number C_i is given:

$$C_i = \frac{v_i \Delta t}{\Delta x} \tag{5.1}$$

and since the model takes into consideration one-dimensional sonic stress-wave propagation through the working fluid, v_i represents the local speed of sound in the control volume i. If the assumptions the ideal gas law are evoked, the local speed of sound is dependent on temperature only. Then the speed of sound in the medium may be estimated from the Newton-Laplace equation as:

$$v_i = \sqrt{\gamma R_g T_i} \tag{5.2}$$

in which γ is the adiabatic index, R_g is the specific gas constant and T_i the absolute cell temperature. Moreover, according to the CFL stability condition, the local Courant number must remain below unity to ensure that thermodynamic information cannot propagate further downstream of a cell i than its nearest neighbour $i+1$, being located away at a distance Δx. This, as Urieli and Berchowitz (1984) also pointed out, places a significant constraint on the maximum time-step to be used in solving the momentum equation without the occurrence of numerical instabilities and is arguably one of the principal motivations why the assumption of quasi-static flow is typically invoked in the published literature (Deetlefs, 2014).

From trial-and-error it was observed that the model remains numerically stable for $C_i \leq 0.6$ in all the simulations performed during the grid-dependence study. This stability constraint agrees well with results shown by (Schock, 1978), who also employed an explicit third-order model, and to findings by Konangi *et al.* (2018), who presented an investigation on the stability criteria of more general first-order accurate fluid flow equations. From Equation (5.1) and Equation (5.2), this limitation on Courant number translates to a maximum simulation time-step of:

$$\Delta t = 0.6 \frac{\Delta x}{\sqrt{\gamma R_g T_i}} \tag{5.3}$$

Practically, the Courant limitation relates to a minimum time-step requirement of $\Delta t \leq 170 \times 10^{-9}$ seconds when 72 control volumes are simulated in each of the heat exchanger sections (as in the preceding case study) and 20×10^{-9} when simulation 550 control volumes in each section. Although being in the range of nanoseconds,

the time-step requirement is still a few orders of magnitude above machine round-off error associated with the *double precision* variables used. Furthermore, it postulated that by computing the momentum and energy equations sequentially using variables from the previous time-step results in the Courant stability constraint being 40 % less than unity. For example, when external heat transfer is not considered (the heater and cooler are in effect *switched-off*) and the piston and displacer are enforced sinusoidal velocity profiles, the model remains stable for Courant numbers up to 0.96. This suggests the inception of numerical instability in the momentum equation is likely the result of a change in gas density and pressure, being in turn induced by thermal expansion or contraction that leads to the local acceleration or deceleration of the working fluid. Nevertheless, when the constraint of Equation (5.3) was imposed, neither piston collisions nor the thermal shock induced by hot or cold start-up conditions would induce any form of numerical instability.

5.6. Concluding remarks

In this chapter the numerical simulation results of a prototype FPSE has been presented as a case study of envisaged engine operation. Based on the theory derived throughout Chapter 3 and Chapter 4, a fully-explicit numerical program has been developed in Fortran. The use of a fully-explicit method has been motivated for its inherent simplicity by which growing model complexity could be accommodated. The chapter discussed the methodology and program flow of the numerical program. A simple temperature-adjusting scheme has been employed to accelerate model convergence to thermodynamic steady-state.

Simulation results of steady-state 1 Ω loaded operation have been discussed in detail. The simulation predicts a low thermal efficiency of 15 %, mechanical efficiency of 54 % and an electrical efficiency of 48 %. The especially poor thermal efficiency has been attributed to significant parasitic heat losses that occur through the engine casing and bore-cylinder walls, also limiting the hot-end casing wall to reaching a maximum temperature gradient of between 400 and 500 °C. The low mechanical efficiency has been attributed to large mechanical friction on the power piston, which from Chapter 7, are estimated to be even larger than was simulated in this case study. The poor electrical efficiency is primarily a result of the large generator core and ohmic losses, which have been estimated and discussed from the finite element analysis in Chapter 4.4. But despite the overall poor engine performance and low net efficiency prediction, the simulation appears to succeed in capturing the working mechanism from first principle theory. The model has been shown to be well behaved to increasing grid refinement. The numerical solver was found to remain conditionally stable for Courant numbers smaller than or equal to 0.6.

Under the operating parameters simulated, the simulation results have indicated that the principal engine design parameters should yield a self-sustaining and steady-operating FPSE. In order to verify these statements and validate the theoretical simulation model, a testable engine prototype was designed, manufactured and assembled, as is discussed throughout Chapter 6.

6. Overview of the prototype engine

In this chapter, an overview of the manufacture and assembly of a 100 W_e (peak) free-piston Stirling engine electric generator prototype is given. Firstly, the main engine design and operating parameters are given, followed by a descriptive overview of the assembled engine. Secondly, the design and fabrication of principal engine components are discussed: this includes the displacer and power piston, flexure springs and the heater controller. Thereafter, the design and manufacture of the linear generator and displacer motor are discussed. The chapter concludes by presenting the experimental test setup of the fully-assembled prototype.

6.1. Engine description

To validate the numerical model, and to further investigate the free-piston Stirling engine operating mechanics, a 100 W_e (peak) FPSE prototype was designed and manufactured. This *first-generation* prototype has remained unoptimised for the scope of this study and serves primarily to evaluate the numerical model's capability of emulating its underlying operating mechanism. The geometric layout of the prototype is similar to Sunpower Inc.'s P2A FPSE, formally known as the EG-100 (Geng *et al.*, 2008), and Microgen's (2018) commercially available 1.0 kW_e FPSE – but with the unique addition of a linear motor that attaches to the displacer shaft. A trial-and-error design-methodology was ensued using the numerical simulation model to identify design-specific considerations relating to the engine geometry, mover masses, spring stiffnesses and heat exchanger sizing, with the ultimate objective being the manufacture of an inexpensive, lab-based prototype using general engineering materials and machining processes. In Table 6.1 the nominal design and operating parameters of this in-house developed engine prototype are given.

A quarter-section view of the assembled FPSE is illustrated in Figure 6.1 with the principal components labelled. The engine casing consists of three separate sections that seal at the flanges using high-temperature silicone gaskets and is pressurised with helium as the working fluid. Although similar FPSEs of this size typically have operating pressures in the range of 3.0 MPa, the prototype engine is limited to a maximum charge pressure of 2.0 MPa (gauge) so as to fall under the Sound

Table 6.1: Nominal design and operating parameters

Description	Value	[Unit]
Hot-end temperature	500 – 600	°C
Cold-end temperature	<50	°C
Absolute charge pressure	1.5 (<2.0)	MPa
Nominal operating frequency	30 ± 0.5	Hz
Nominal displacer stroke	18 – 24	mm
Nominal piston stroke	18 – 24	mm
Generator output power (peak)	100	W

Engineering Practice (SEP) hazard category of South African National Standard 347 (SABS, 2012). To conform to statutory requirements, a comprehensive finite element stress analysis of the engine casing was performed using *Siemens NX 11.0* (2017) and is included in the dissertation's supplementary information file.

Inside the engine casing, the displacer and its shaft should align nearly frictionless with the power piston assembly, both also aligning with their respective bore cylinders. The displacer moves linearly between the hot and cold ends whilst 'shuttling' the working fluid along the annular heat exchanger (HX) channel through the heater, regenerator and cooler sections, as discussed in Chapter 3.1. Heating is supplied by a 1.0 kW electrical heater whereas a water cooling jacket is located around the cold end. A unique aspect of this engine configuration is that the displacer shaft is attached to a linear motor in the backspace. This allows for direct control over the

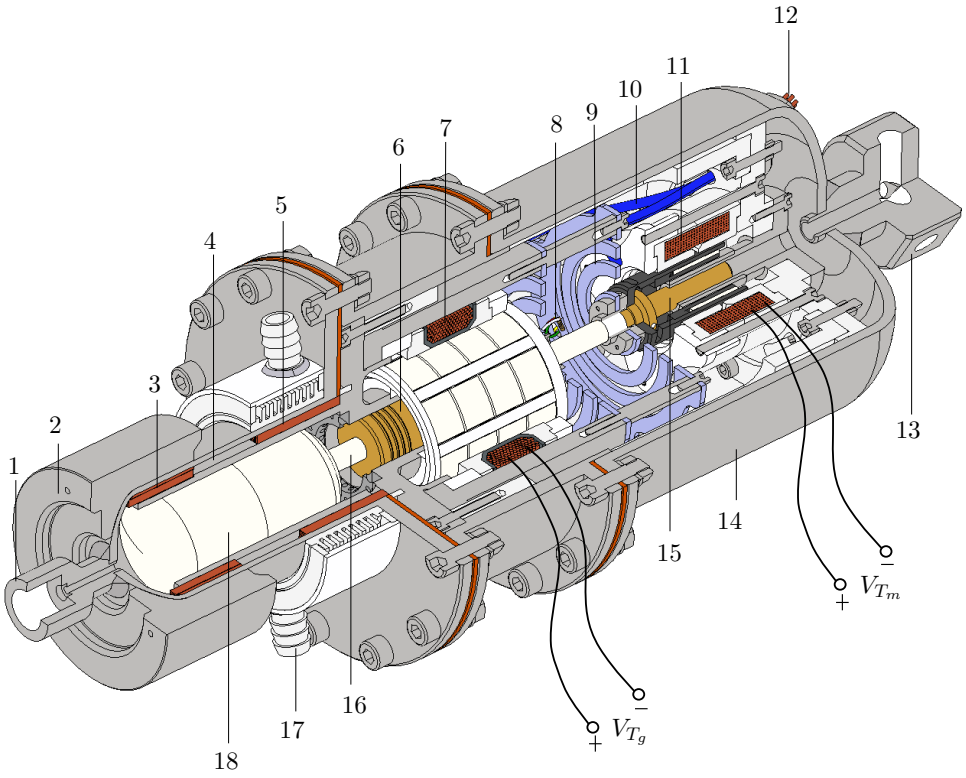

1	Expansion space pressure hub	10	Electrical wiring
2	Heater head	11	Linear electric motor
3	Heating fins	12	Electrical feed through
4	Regenerator	13	Backspace pressure hub
5	Cooling fins	14	Engine casing
6	Power piston assembly	15	Motor piston assembly
7	Linear electric generator	16	Displacer shaft
8	Strain gauge	17	Cooling water jacket
9	Flexure springs	18	Displacer

Figure 6.1: Illustration of the assembled free-piston Stirling engine prototype, depicting the principal engine components

displacer motion during experimental testing and in a future study, will allow for a direct displacer control strategy to be investigated. The displacer and power piston are each supported by their respective flexure springs which provide the restoring forces necessary to complete the Stirling cycle, being analogous to the flywheel in kinematic engines. The power piston is coupled to the generator magnet plunger, forming the *power piston assembly*. Labyrinth channels in the power piston serve as a dynamic gas seal between the compression and backspace, as illustrated in Figure 6.2. Nevertheless, a small piston-wall clearance allows for some gas leakage to induce a dynamic gas bearing between bore-cylinder and piston wall.

As further shown by the rendered illustration in Figure 6.2 and photograph in Figure 6.3 (a), the internal engine components assemble around the so-called *engine main body*, which was manufactured from case-hardened high tensile steel (grade EN24). After heat treating (hardening) the main body, the displacer and power piston bores were ground to size, having diameters of 48 mm and 30 mm respectively. The linear generator fits between the four flexure-supporting 'legs' of the main body, as seen from Figure H.4 in Appendix H. Four hexagon rods assemble the power piston flexure spring (with assembled power piston magnet train) to the main body, onto which the displacer flexure spring and attached displacer shaft is in turn bolted. This assembled main body further assembles within a supporting aluminium casing that serves to align the displacer motor to the linear generator and main body cylinder bore, as is shown by Figure H.1. The heater and cooler fins were manufactured from copper by electro-discharge machining (wire cutting) 135 axially-aligned channels into an annular cylinder, although shown in Figure 6.3 (a) is an earlier iteration of the heat exchanger fins made of aluminium.

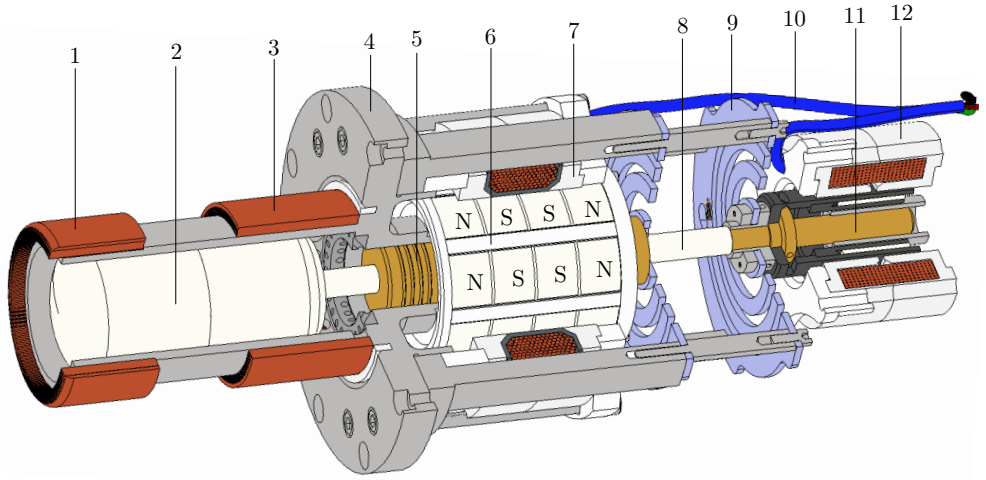

1	Heating fins HX	5	Power piston	9	Flexure spring
2	Displacer	6	Magnet plunger	10	Engine wiring
3	Cooling fins HX	7	Generator stator	11	Motor piston
4	Engine main body	8	Displacer shaft	12	Displacer motor stator

Figure 6.2: Rendered illustration of the internal engine assembly

Figure 6.3 (b) shows a photograph of the displacer and power piston magnet train assemblies. The hollowed displacer is assembled via an interference press-fit to the displacer shaft, which was manufactured from polished silver steel. The shaft fits through a tight-tolerance clearance-fit in the power piston, attaching to the displacer flexure spring and motor piston train via a connecting collar in the backspace. This collar allows the radial angle between the displacer shaft and power piston to be adjusted during assembly – as experience by trial-and-error has shown near-perfect concentric alignment to be difficult (if not impossible) to achieve using the resources available to this study. In contrast, the power piston assembly is bolted directly to its flexure spring and does not allow for any radial adjustment.

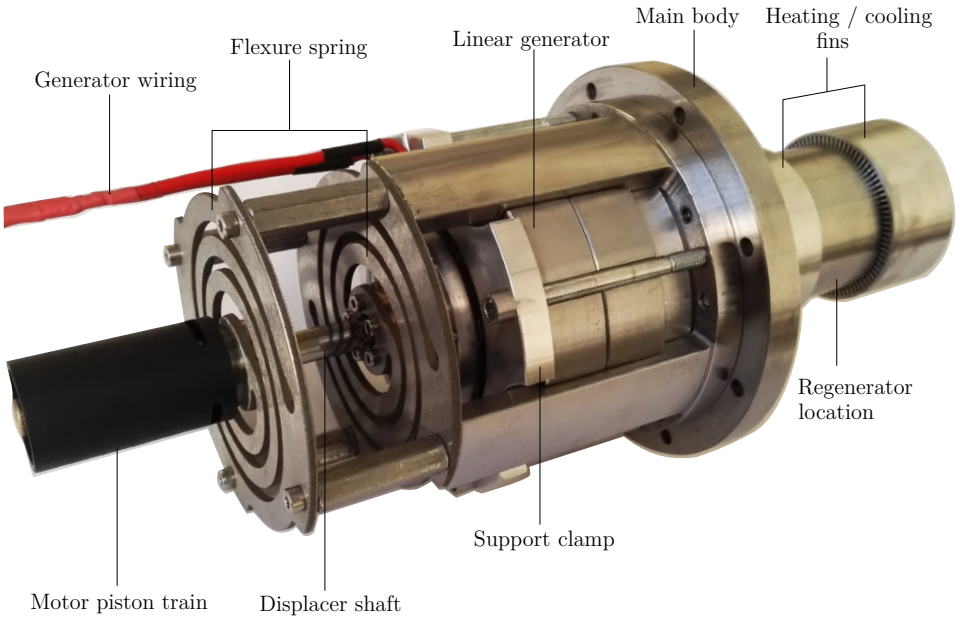

(a)

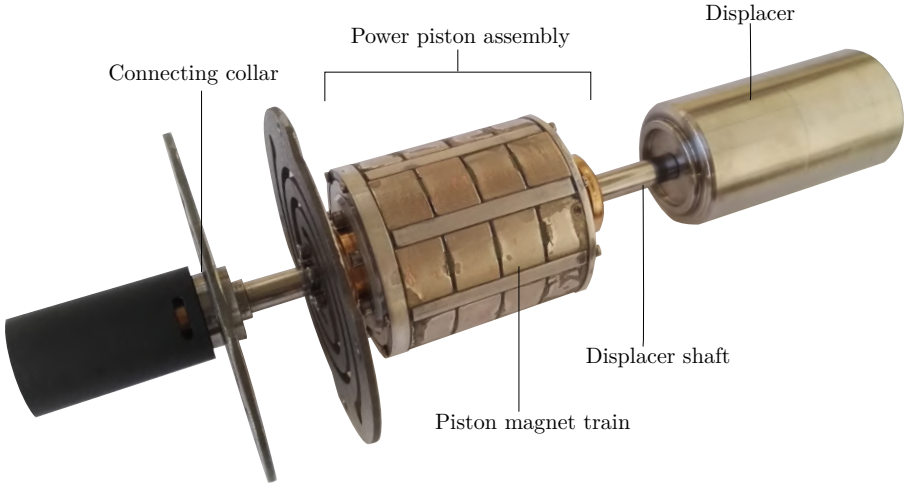

(b)

Figure 6.3: Photographs of (a) the assembled engine internals and (b) the displacer and power piston assemblies (excluding the internal sensor wiring)

6.2. Displacer, power piston and flexure springs

The displacer consists of two hollowed stainless steel shells (grade 304), with wall thicknesses of 1.5 mm, that assemble at the centre seam via a threaded connection. After assembling the displacer shells to the displacer shaft via interference press-fit, the entire assembly was ground to size to ensure a good geometric tolerance on concentricity. Using *Siemens NX 11.0*, a two-dimensional axisymmetric finite element analysis was performed on the displacer shell to investigate its expected thermal expansion and axial conductive heat losses. Figure 6.4 (a) shows the estimated thermal profile of the displacer and its bore, whereas (b) shows the resulting radial expansion of the displacer. At an assumed hot-end temperature of 500 °C the displacer dome expands by approximately 160 µm in the radial direction near the top dome, whereas the main body bore (not shown in (b)) expands by only 136 µm. To allow for a sufficient clearance even in a thermally expanded state, the displacer's cylinder bore was machined 100 µm larger in diameter than that of the displacer. Moreover, under the temperature profile simulated, the displacer wall conducts 24.2 W from the hot end to cold end. This is nearly negligible to the simulated 197.4 W being conducted in the bore cylinder wall – both closely resembling the axial conductive heat losses that were given in Figure 5.15 under a similar temperature gradient.

The power piston is not subject to such extreme temperatures as it reciprocates near the cold end of the engine. For its self-lubricating properties, the power piston was machined from phosphorous bronze with its diameter being 60 µm smaller than that of its bore cylinder. In theory, this should allow for a small amount of gas to leak

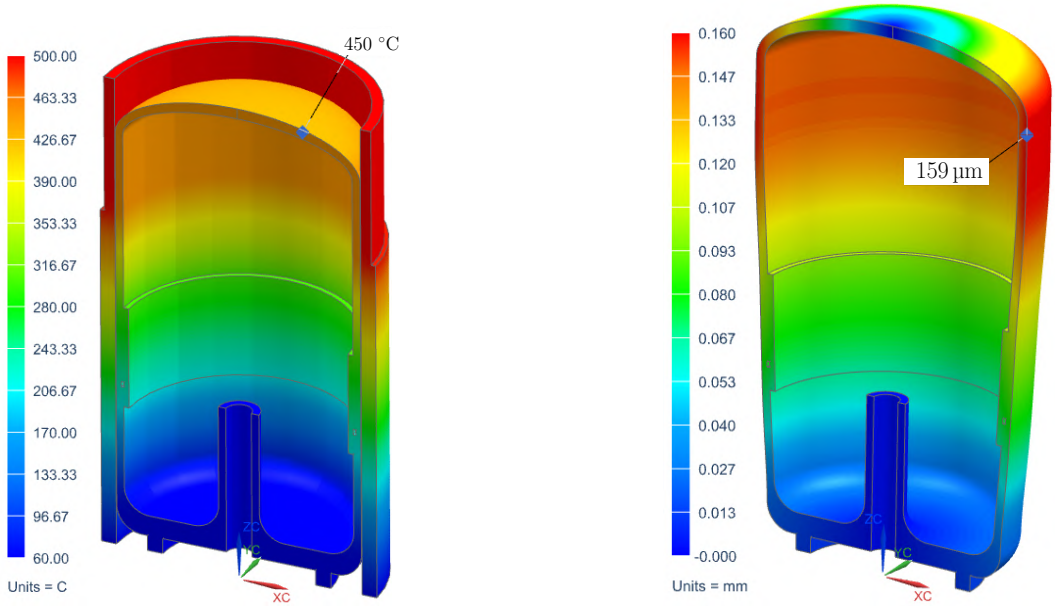

(a) **(b)**

Figure 6.4: Finite element analysis of the displacer dome, showing (a) the thermal profile used as a boundary condition and (b) the simulated radial expansion

back-and-forth between the compression space and backspace, and in so doing, act as a simple dynamic gas bearing/cushion to the piston. To limit this gas leakage at the piston head, four 0.5 mm deep radial grooves were machined into the piston head to form a *labyrinth* seal, as can be seen from the rendered illustration in Figure 6.7. An ISO H7/h6 reamed hole in the power piston allows the displacer shaft to slide through nearly frictionlessly, having a maximum clearance in the order of 25 µm on a diameter basis. By having a wall-to-wall clearance of 50 µm between displacer shell and bore wall, the displacer's alignment is predominately dependent on the power piston's alignment with its respective bore. This implies that the displacer is essentially *free-floating* within its cylinder.

As was seen from Figure 6.3, the displacer and power piston attach to respective flexure springs. Also taking into consideration the generator magnetic spring force, the respective flexure springs were designed by aid of FEA to ensure the displacer and power piston exhibit nearly identical first-mode natural frequencies. The final design settled upon, as shown in Figure 6.5, is a two-legged spiral profile similar to the *Oxford Aerospace Cryocooler* flexure spring (Peckham Engineering and Tool, 1994) and the work done by Stage (1991). The springs were fabricated from carbon spring steel (AISI 7050) by water jet cutting, after which the flexure spring surfaces were ground to eliminate surface imperfections and cutting burrs. Two sets of half-bridged strain gauges (HBM type L11-Y1) were attached to each flexure spring to infer the displacer and piston displacements and velocities. Spring stiffnesses were determined experimentally in a compression test during which the strain gauge sensitivity measurements were also calibrated for displacement measurement, as is discussed further in Appendix E.

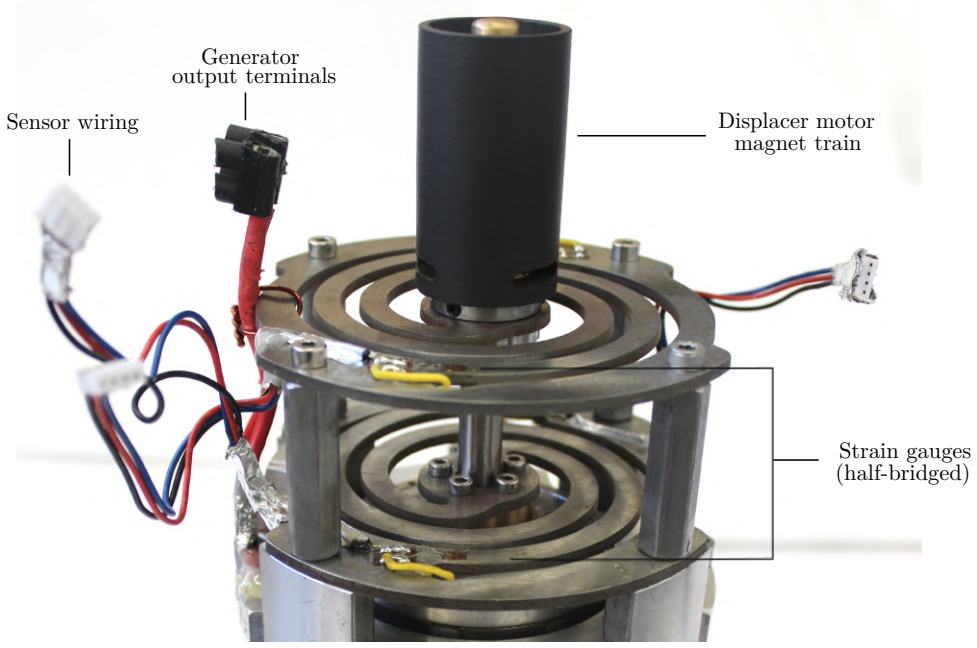

Figure 6.5: Photograph of the assembled flexure springs and strain gauges

6.3. Heater, regenerator and cooler

The engine heat load was supplied by a 1.0 kW ceramic-band electrical heater with a power density of 6 W/cm^2, assembled around the engine *heater head* as illustrated in Figure 6.6 (a). The heater head not only provides the interface between the electrical heater and engine casing, but serves to increase the thermal inertia of the hot-end so that experiments can be conducted at a more uniform temperature distribution. The electrical circuit diagram illustrates the heater feedback controller by which a 1.0 kV A single-phase variable transformer was used to supply an alternating current I to the heating coil. Three K-type thermocouples measure the temperature distribution along the height of the heater head; the average temperature $T_{h,avg}$ is used to trigger a National Instruments USB-6009 DAQ data logger to switch the heater on/off by means of a solid-state relay. In doing so, the hot-end temperature can be adjusted to a specified set-point temperature $T_{h,set}$ during experimental testing. The figure also shows a sectioned view of the radially-finned cooling jacket, for which the inlet and outlet water temperatures were recorded using T-type thermocouples. A ceramic-wool insulating jacket surrounds the entire top section of the engine – including heater and cooler – being covered with aluminium foil to keep wool particles from contaminating the work area, as is seen from Figure 6.9.

In Figure 6.6 (b) a photograph of the uncovered internal heat exchanger fins and regenerator is given. Despite the significant influence that well-designed compact heat exchangers may have on the overall engine thermal efficiency, under the scope limitations of this work, no design trade-off nor optimisation study has been carried out. Rather, for design-uniformity of this *first generation* prototype, the heater, regenerator and cooler were fabricated to have equal heights of approximately 35 mm each. A simple radially-wound wire-mesh regenerator was fabricated. As seen from the enlarged view, this was achieved by loosely winding strips of diameter 160 µm copper twill-weave 60-mesh in an annular canister to form a macroscopic void friction of approximately 77 %. Furthermore, the heater and cooler fins were machined to have a 100 µm clearance between internal fin diameter and the main body cylinder wall, upon which the engine casing (with attached heater head and cooling jacket) was assembled by an interference press-fit.

A post-experimental investigation revealed that after operating the engine to hot-end temperatures to a heater set-point temperature of 600 °C and internal gas pressures up to 1.80 MPa absolute, the heater-side fins have become thermally deformed and consequently 'shrink-fitted' to the main body cylinder. Although this thermal deformation allowed the engine pressure casing to be removed with greater ease, it complicated disassembly of the heating fins and regenerator canister from the main body without some damage to the heating fins. This thermal shrinking of the heater fins increased the thermal contact resistance between fin wall and engine casing, thereby reducing the heat rate into the heating fins. Additionally, both pairs of fins induce a thermal 'short-circuit' between the outer pressure casing and the main body bore-cylinder wall. This allows for large axial conductive heat transfer to occur arccos the bore-cylinder wall in addition to the already notable heat transfer across the regenerator in the engine casing. To decrease the axial conductive heat

transfer from hot to cold ends, the casing and bore cylinder walls' cross-sectional areas must be decreased in a revised design. Additionally, the surface contact area between the bore cylinder walls and the heater and cooler fins must be reduced to limit the otherwise thermal short-circuit.

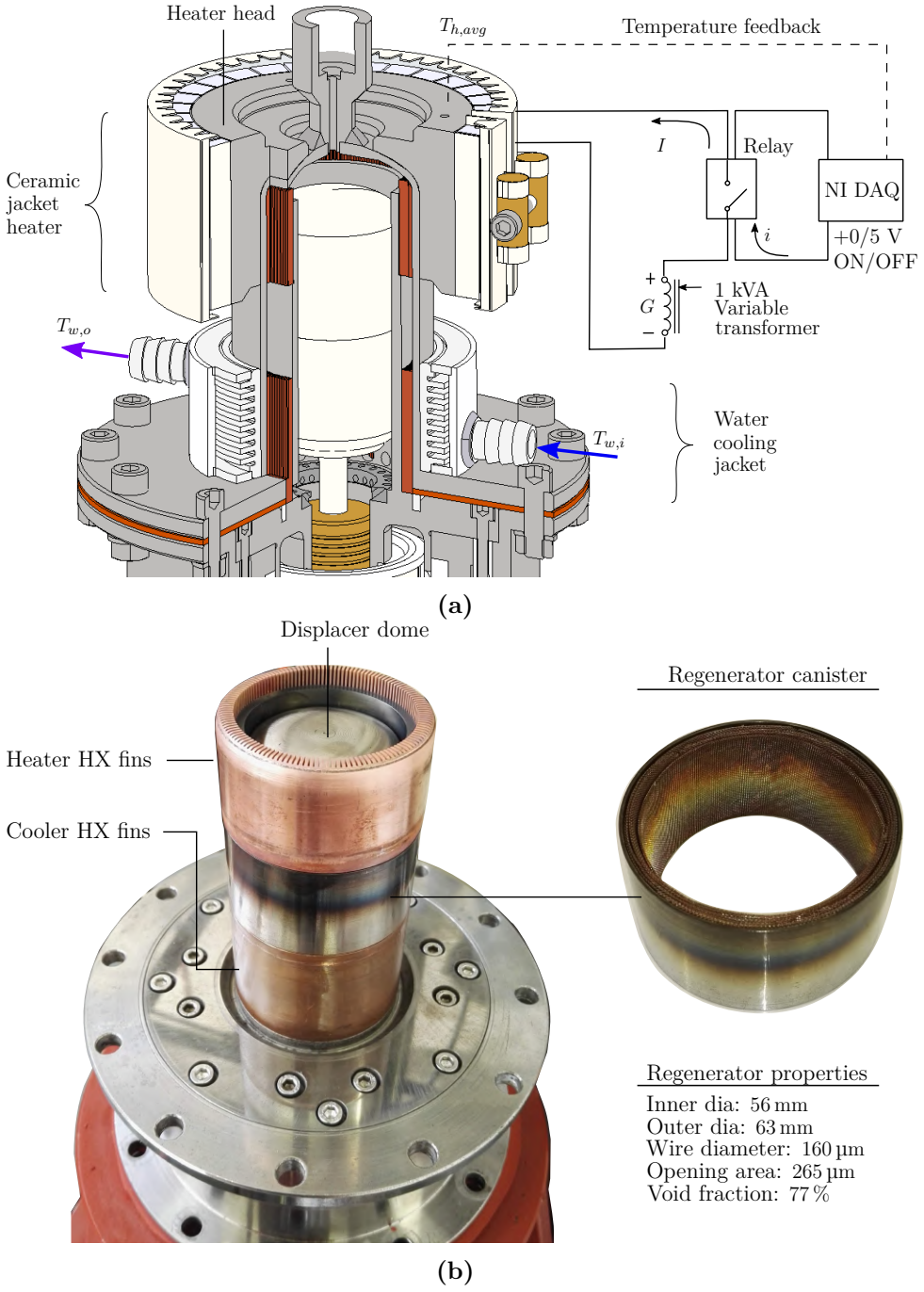

Figure 6.6: (a) Rendered illustration of the hot and cold ends with a schematic of the heater controller, (b) photograph of the uncovered heater and cooler fins with an enlarged view of the regenerator canister that is located in-between

6.4. Linear generator and displacer motor

As discussed in Chapter 4, the geometric layout of the linear electric generator was based on the work done by Dhar (1999) and design considerations of a finite element analysis that were performed in *ANSYS Maxwell 16.0*. The generator consists of the power piston and assembled magnet train that reciprocates through a stationary soft-iron core, as illustrated in Figure 6.7. The core consists of outer and inner mild-steel stators that assemble to the main body, as may be seen from Figure 6.3. Encased within the outer stator is a toroidally wound copper coil that is made up of 70 windings of Armoured Polyesterimide (API) AWG-14 magnet wire.

The magnet train consists of an aluminium (6082-T6 alloy) plunger with eight wedged-shaped slots running down its length, housing a total of 32 arc-shaped rare earth magnets (NdFeB grade 42H). These slots were manufactured by electro-discharge machining to provide a close tolerance sliding fit for the magnets. As seen from Figure 6.2, four magnets take up a slot and are arranged in a north-south-south-north orientation, approximating the radially magnetised ring-magnet geometry discussed in Chapter 4.1. Aluminium locking rings at each end of the plunger tightly secure the magnets in the slot, as seen from the illustration of Figure 6.7. Small plastic spacers (G11 plastic) were used to space magnets 1 mm apart, after which the voids were filled with high-temperature-resistant epoxy-resin to permanently attach the magnets to the plunger. Refer to Figure H.5 in Appendix H for a photograph of the power piston assembly, as seen before and after assembly and glueing of the magnets to the sleeved aluminium plunger.

Figure 6.8 illustrates the linear electric motor that attaches to the displacer shaft. The design of the motor is similar to that of the generator, but with a key distinction being that the motor magnet train consists of a single row of north-oriented magnets, thereby making for a more compact design. Eight rare earth block magnets (NdFeB grade 37) are located between an inner and outer cylinder to form the magnet

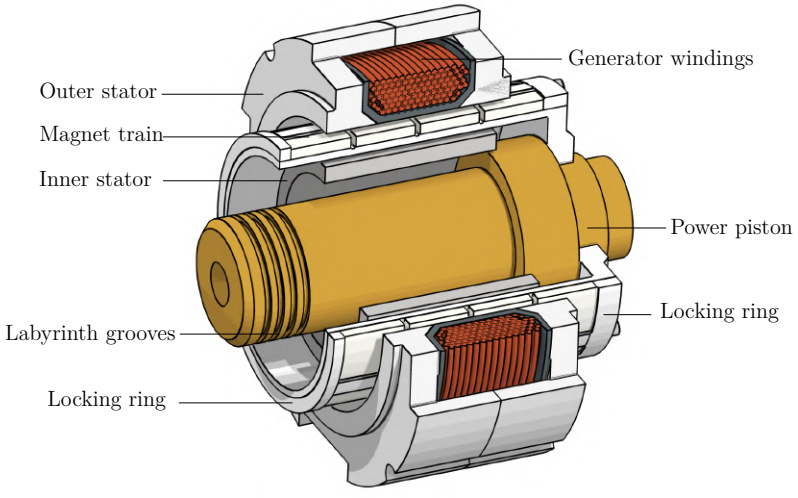

Figure 6.7: Illustration of the moving-magnet linear electric generator

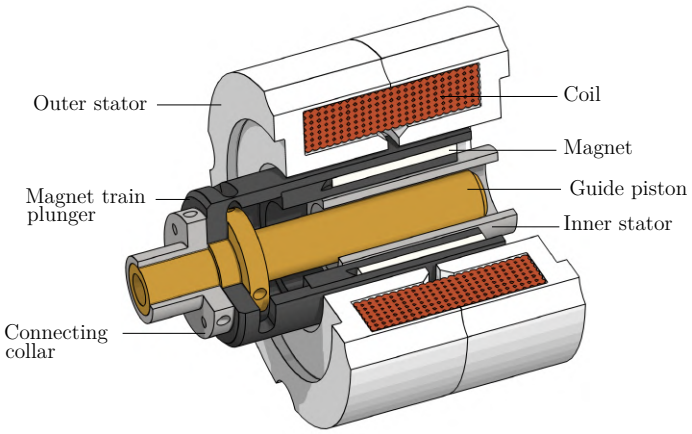

Figure 6.8: Illustration of the linear electric motor

plunger shown. The plunger was manufactured from carbon-filled PTFE-plastic and attaches to a phosphorous bronze guide piston, which centres the magnet train with respect to the inner and outer stators. The guide piston attaches to the displacer shaft and displacer flexure spring via a connecting collar, as was shown in Figure 6.3.

For the scope of this study, the linear motor was only used to excite the displacer motion. This has allowed for the evaluation of engine operation under relatively low charge pressures and hot-end temperatures where, due to large mechanical friction and piston electromagnetic load forces, the prototype engine could not be made to operate self-sustainingly. The motor coil terminals were connected to a Ling Dynamics PA100 sine-wave generator-amplifier, capable of delivering a maximum output power of 100 W at a current rating of 7 A peak. From a numerical simulation performed in *LTSpice IV*, one in which the motor coil inductance and resistance values were given as input parameters, it was estimated that the motor excitation voltage should not exceed 30 V in continuous operation to avoid coil burnout. Table 6.2 gives a summary of the linear generator and motor nominal design parameters. The electrical properties, such as the internal coil resistances and inductances, were determined experimentally as discussed in Chapter 7.2.1.

Table 6.2: Design parameters of the linear electric generator and motor

	Generator	Motor	[Unit]
Design parameters			
Peak terminal voltage	15	30	V
Peak rated current	10	5	A
Peak rated power	150	100	W
Mechanical-to-electrical efficiency	56	–	%
Magnet material and grade	NdFeB 42H	NdFeB 37	–
Stator material grade	Steel AISI 1018	Steel AISI 1018	–
Electrical properties			
Coil windings	70	170	–
Internal coil resistance	0.4	1.4	Ω
Coil inductance at 30 Hz	2.2	30	mH

6.5. Experimental setup

The experimental setup is depicted in Figure 6.9 along with the main equipment used. The assembled engine and its 'tripod' support stand were bolted to a steel test bench to adsorb and dissipate any engine vibrations. As shown by Figure H.8 in Appendix H.4, a safety blast cage was located over the assembled engine during testing with sensor wiring and coolant tubing passing underneath the table. The engine control instrumentation, such as the heater controller, motor excitation source and data-logging equipment were all fixed to the test bench, but were controlled remotely from a safe operating distance.

The engine heating load was supplied by an electrical ceramic heater, powered by the *heater variac*, whereas the cooling water was recirculated to the water reservoir depicted. The assembled engine was purged and pressurised with Grade 5.0 helium via the high pressure line shown. The displacer motor terminals are connected to a sinusoidal voltage generator $V_{m,t}$ that either *kick-starts* or operates the engine in displacer-driven operation, whereas the generator terminals are connected to the resistive load bank shown. An HBM QuantumX data acquisition computer (DAQ)

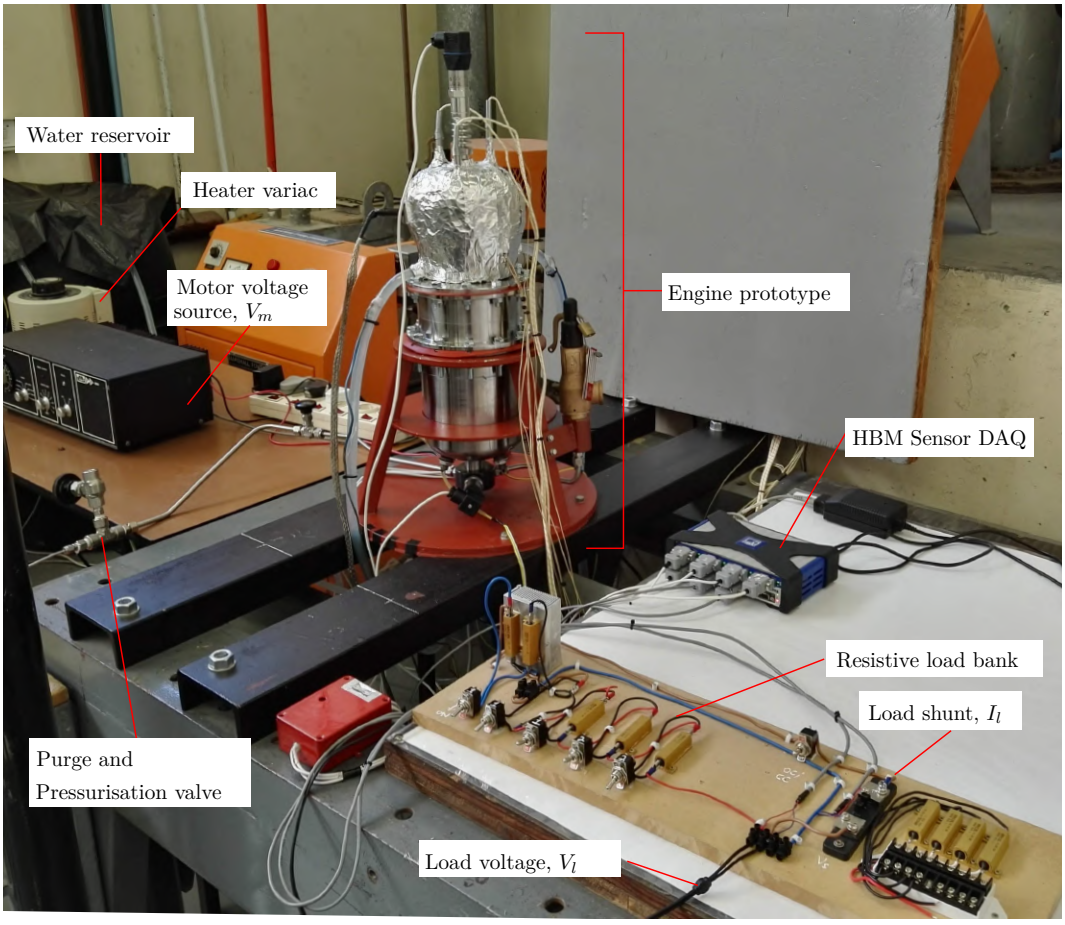

Figure 6.9: Photograph of the engine prototype and experimental test bed

was used to record high frequency test variables such as the gas pressures, generator voltages and currents, and additionally as a half-bridge amplifier to infer the displacer and piston motion from the strain gauge sensors attached to the respective flexure springs. Furthermore, a National Instruments DAQ (located underneath the table and not visible here) was used to record engine temperatures measurements. Refer to Appendix E for a detailed discussion relating to the setup and calibration of the measurement instrumentation used throughout the experiment.

Figure 6.10 shows both a photograph and illustrated cross-section of the assembled FPSE and its test-support stand, depicting the main components and measurement sensors that make up the test setup, along with the locations where these sensors are positioned. The pressure variation in the expansion space P_e was measured using a Wika S-20 pressure transducer with cooling fins, mounted at the top of the engine as shown. A similar transducer was used to measure the backspace pressure P_{bs} and is located at the bottom of the engine. Also connected to the backspace is a 2.0 MPa safety relief valve that limits the engine to over-pressurisation. The electrical heater with voltage G is controlled around a set-point temperature $T_{h,set}$, whereas at the cold-end heat is rejected to a water cooling jacket, with inlet and outlet water temperatures $T_{w,i}$ and $T_{w,o}$ respectively. Between the heater and cooler three additional K-type thermocouples measure the thermal gradient in the engine casing wall denoted $T_{r,top}$, T_r, $T_{r,bot}$. The cold-end temperature T_k and backspace wall temperature T_{bs} are also measured. All internal sensor and electrical wiring are passed through three removable feed-through plugs that are located at the bottom of the backspace. They allow for the pressure-tight feed-through of the strain gauge sensors wires (wiring in white) from which the displacer and piston displacements x_d and x_p are inferred, as discussed in Chapter 6.2, and for the generator and motor terminal wires (wiring in black and yellow) with voltages $V_{T,g}$ and $V_{T,m}$ respectively. The generator terminal wires connect to the resistive load bank shown in Figure 6.9, whereas the motor wires are connected to the signal amplifier V_m. The load bank allows for the manual adjustment of generator load between 1 and 7 Ω and can dissipate up to 100 W (RMS) in 1 Ω loaded operation.

6.6. Concluding remarks

In this chapter, an overview of the work done in fabricating and constructing a 100 W_e (peak) experimental engine prototype has been provided. The prototype engine has remained completely unoptimised in terms of efficiency and power density, as it serves only to verify and validate aspects of the theoretical simulation model. The geometrical layout of the engine has been based partially on Microgen's 1.0 kW_e FPSE, but with the unique addition of a linear motor attached to the displacer shaft. A discussion pertaining to the manufacture and assembly of principal engine components has been given. This includes the internal assembly; the displacer and piston; the flexure springs; the internal heat exchangers; the linear generator; and displacer motor. The chapter has concluded by presenting the experimental test setup. Following the assembly of the prototype in this experimental test layout, the engine was test operated under varying hot-end temperatures, charge pressures and generator loading conditions, as is discussed in the chapter that follows.

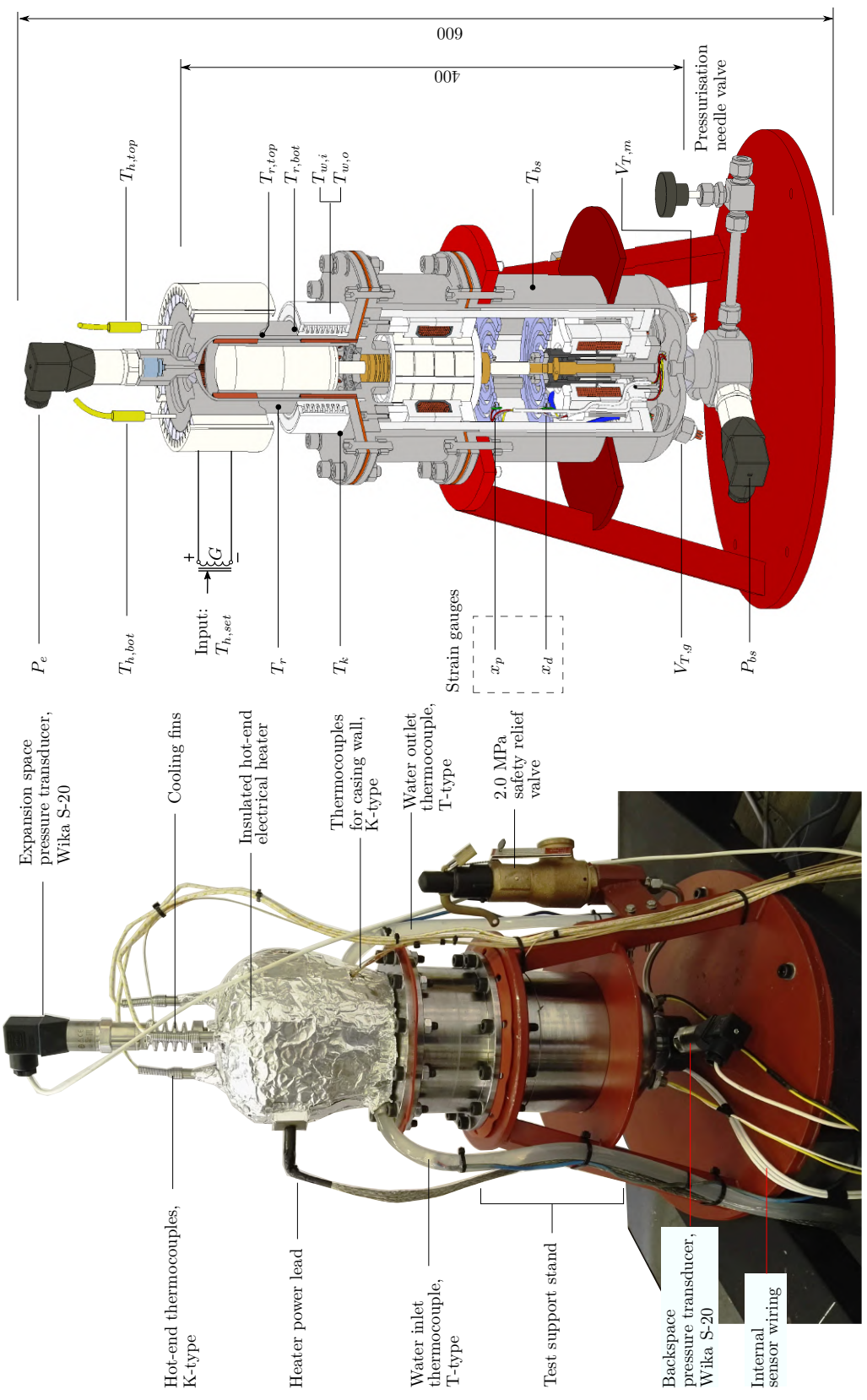

Figure 6.10: Photograph of the assembled prototype and test measurement instruments (left) and illustrated cross-section of the assembled engine (right), depicting the measurement sensors and locations where they were positioned

7. Experimental evaluation and validation

The experimental evaluation of the free-piston Stirling engine prototype serves to validate the theoretical simulation model. The chapter firstly discusses a free vibration response test that was performed to determine the friction forces acting on the as-manufactured displacer and power piston. Secondly, the performance of the linear generator is evaluated by reciprocating the piston assembly in a stand-alone experiment. The resulting generator voltage and current profiles validate the linear generator model that was outlined in Chapter 4. Thirdly, by comparing experimental and simulated results of seven selected sample test runs, the numerical model is validated for heater temperatures ranging from 300 to 600 °C and charge pressures between 1.0 and 1.80 MPa absolute. The chapter is concluded with a discussion relating to the main experimental limitations encountered as well as design and assembly suggestions for the improvement of the existing engine prototype.

7.1. Natural frequency and friction characterisation

The natural frequencies of the power piston and displacer were determined from a set of free vibration response tests (also known as ring-down response tests). To do so, the displacer and power piston were each subjected to an impulsive force and the resulting displacement-time responses were measured using the calibrated strain gauge sensors. The rate of decay in displacement was then investigated to estimate the viscous and Coulomb friction forces acting on the as-assembled experimental setup. An exponential decreasing displacement indicates viscous damping effects, for which a linearised viscous damping coefficient c_v was determined. According to Inman (2014), if the mass m, stiffness k and natural frequency ω_n of a spring-mass-damper system is known, the damping coefficient may be determined as:

$$c_v = \frac{-B}{\omega_n}\sqrt{2km} \tag{7.1}$$

where B is the exponential decay gradient, determined by curve-fitting an exponential function through the peaks of the resulting displacement-time response. On the contrary, a linear decreasing displacement is indicative of Coulomb or dry-sliding contact friction, for which the damping friction force may be determined as:

$$F_d = -\frac{a\pi k}{2\omega_n} \tag{7.2}$$

in which a represents the linear decay gradient. Moreover, the *damped* first mode natural frequencies listed in Table 7.1 were determined by taking the Discrete Fourier Transform (DFT) of the resulting displacement-time responses.

Figure 7.1 (a) shows the displacement-time response of the displacer, as assembled to the engine with the displacer shaft running through the power piston, but excluding the displacer motor at the shaft end. As shown, the rate of decay in displacement can reasonably be approximated as a form of viscous damping, although becoming

slightly more linear at displacement amplitudes smaller than 2 mm. This indicates that at small displacements, mechanical contact friction becomes dominant over the otherwise viscous damping effects such as air friction. When the displacer motor is included, the displacement decays linearly within approximately 0.6 seconds as shown in (b). This linear decay rate is indicative of dry-sliding contact friction between the displacer shaft and power piston, resulting from imperfect alignment between displacer shaft, displacer guide piston and power piston with the respective bore-cylinders. With each disassembly and reassembly of the engine this alignment changed slightly. Consequently, the Coulomb friction force in Figure 7.1 (b) varied between 1.74 N and 1.97 N for the test runs discussed throughout this chapter.

Figure 7.1 (c) shows the displacement-time response of the power piston that results when the magnet train and the displacer assembly have been removed completely. The displacement decays linearly over a period of nearly 2.6 seconds with a first-

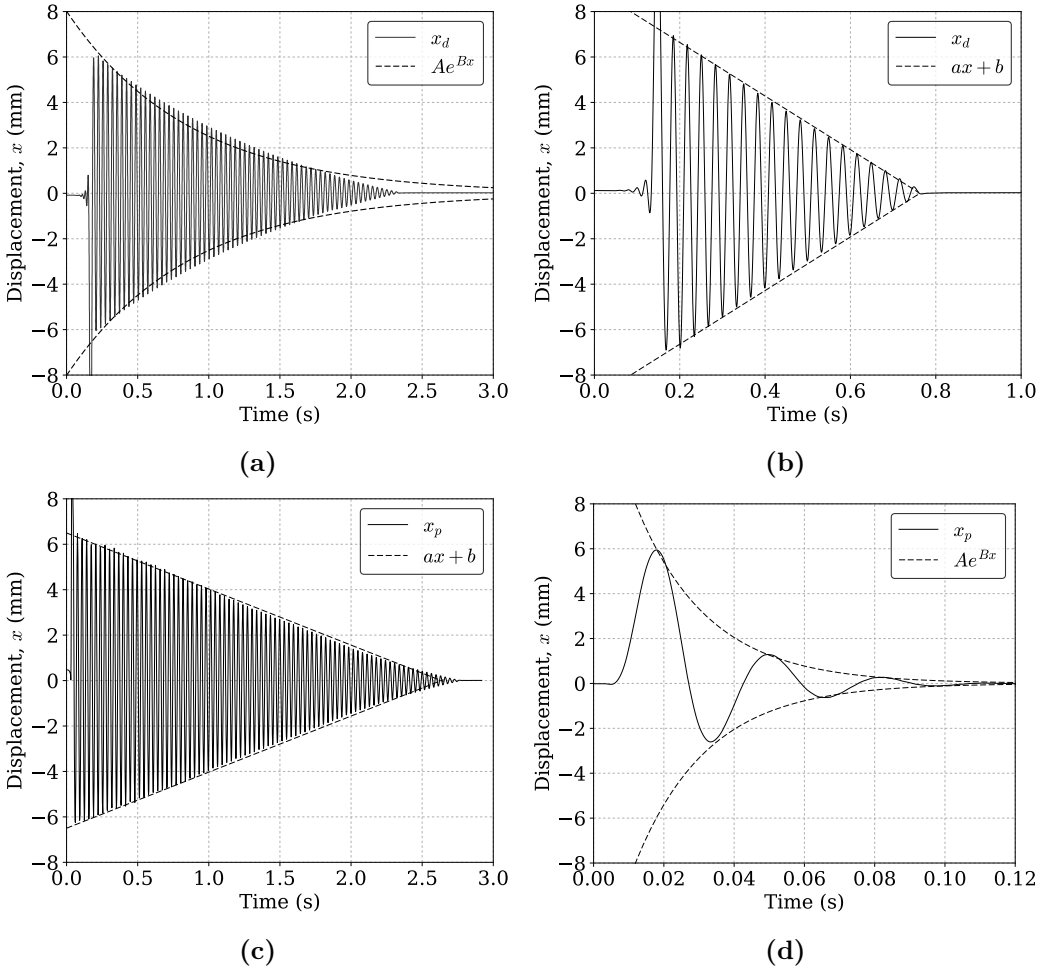

Figure 7.1: Free vibration response of: (a) the displacer assembled with power piston assembly but excluding displacer motor, (b) the displacer assembled with power piston assembly and including displacer motor, (c) the power piston without assembled magnet train, (d) the power piston with assembled magnet train

mode natural frequency of 31.1 Hz. This suggests that the power piston and piston-flexure spring are reasonably aligned with the piston bore cylinder, constituting to a Coulomb friction force of 0.49 N. When the magnet train is assembled with the power piston, a considerable damping force was found to act on the piston assembly, inducing stalling within only three oscillations, as is seen in Figure 7.1 (d). It is postulated that this large damping force results due to unevenly balanced magnetic side load forces that act between the magnet train and the generator stator, effectively pulling the piston assembly skew within its bore and thereby leading to significant mechanical friction. The unbalance of the generator magnetic forces are attributed to a miss-alignment of the arc-shaped magnets into the sleeved magnet holder shown in Figure 6.3 on page 85. Although from Figure 7.1 (d) a first-mode damped natural frequency of 30.5 Hz and a linearised damping coefficient of 77.4 N s/m were calculated, as this damping coefficient is based on only three oscillations, there remains some uncertainty to the validity of this finding.

To further investigate this damping force, the engine was pressurised to 1 MPa and the piston electromagnetically reciprocated using the linear generator, as outlined in Appendix G.2. The numerical model was used to simulate the equivalent piston-driven operation, by specifying the generator current as an input condition and then varying the simulated viscous friction coefficient between 40 and 80 N s/m in an effort to match the experimental behaviour. From this experiment, it was suggested that a simulated viscous damping force of 55 N s/m more accurately emulates the experiment. This lowered viscous damping coefficient can possibly be attributed to the formation of an induced gas cushion that is formed around the moving power piston by gas leakage. It is further postulated that as the piston stroke and gas pressure are increased, the effect of this *dynamic gas bearing* becomes more prominent and consequently, the linearised damping coefficient should be reduced, as was done for self-sustained engine operation in Chapter 7.3.4. Another explanation may be that the magnet-induced piston friction is not linear over the entire engine stroke.

Table 7.1 lists the first-mode natural frequencies and frictional forces that were determined for each of the four test scenarios illustrated in Figure 7.1. It is seen that the fully-assembled displacer and power piston exhibit nearly identical natural frequencies and closely matches the design-specified engine natural frequency of 30.0 Hz±0.5. The characterised damping friction forces refine the design parameters

Table 7.1: Summarised outcomes of the free vibration response tests

	Displacer		Power piston		[Unit]
	(a)	(b)	(c)	(d)	
Mover mass	0.38	0.526	0.582	0.952	kg
Spring stiffness	20 019	20 019	24 610	24 610	N s/m
Magnetic spring stiffness[1]	–	–	–	10 350	N s/m
Oscillation frequency	30.2	30.1	31.1	30.5	Hz
Damping friction force	$0.27 \times v_d$	1.74 – 1.97	0.492	$77.4 \times v_p$	N

[1] The piston magnetic spring stiffness for assembly (d) was calculated as the average slope of the force-displacement curve at the piston mid-stroke position ($x = 0$) from Figure 4.4.

that were given in Table 5.1 and allow for the more accurate numerical simulation of the as-manufactured and assembled prototype engine.

7.2. Experimental evaluation of the linear generator

The linear generator was experimentally investigated by first characterising the internal coil inductance over a range of operating frequencies. Thereafter the performance of the linear electric generator was evaluated by driving the power piston assembly with a linear reciprocator between 5 and 25 Hz, and measuring the terminal voltage under both open-circuit and 1 Ω loaded operation. Experimental results are compared against that of the finite element model derived throughout Chapter 4 to verify the linear generator model and inferred generator characteristic equations.

7.2.1. Characterising the generator inductance

The generator coil has an internal resistance R_{coil} and inductance L_{coil} that leads to a phase shift between the terminal voltage and current of the linear generator, as has been discussed in Chapter 4.1. To determine the combined inductance of the generator coil and soft-iron stator cores, the power piston assembly was removed from the engine and the generator coil terminals were connected in the electrical circuit arrangement shown in Figure 7.2. A Ling Dynamics PA100 sine-wave generator was used as the power supply V_s, whereas the external load R_{load} consisted of two 2 Ω, 50 W resistors (Arcol HS50 resistors) that were connected in parallel to form a 1 Ω load (more precisely 1.08 Ω). An HBM QuantumX MX840A data logger was used to measure the supply voltage using voltage probe V_{p1} with reference to common ground, whereas the current i and its phase was inferred from the voltage drop measured across the resistive load using voltage probe V_{p2}.

The voltage amplitude of the signal generator was retained at 10 V whilst the excitation frequency f was varied between 3 and 60 Hz. If the amplitude of the supply

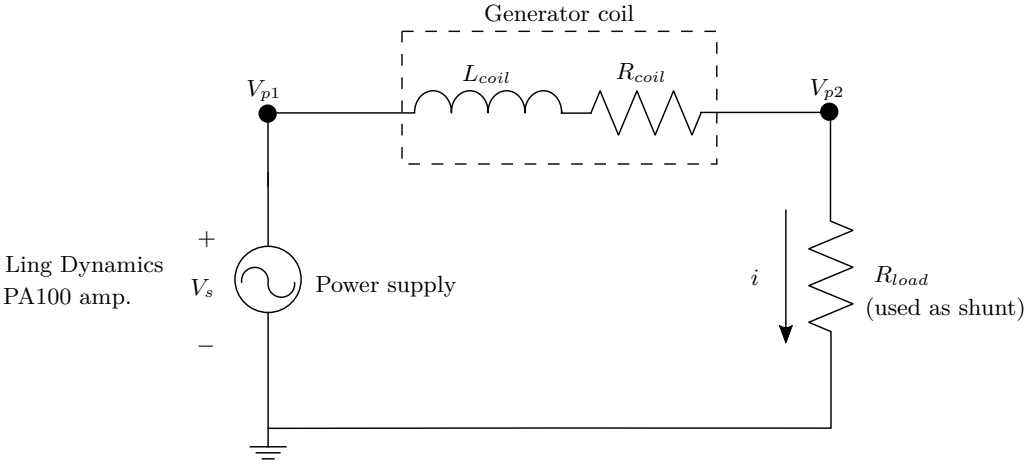

Figure 7.2: Electrical circuit setup to determine the generator coil inductance

voltage V_s and phase difference Φ with respect to current i is known, the inductance may be calculated from (Boldea and Nasar, 1997):

$$L_{coil} = \frac{Z \sin(\Phi)}{2\pi f} \tag{7.3}$$

where Z is the amplitude of the total circuit impedance, calculated according to:

$$Z = \frac{V_s}{i} \tag{7.4}$$

Figure 7.3 shows the experimentally determined coil inductance and current phase lag functions of excitation frequency. It is seen that the inductance varies exponentially from 2.8 down to 2.1 mH. As the excitation frequency increases, the coil reactance becomes more significant and the current phase lag increases. This effect can be opposed by either increasing the circuit resistance, or by including a series tuning capacitor in the load circuit. From this figure, the coil inductance can be estimated as a function of excitation (operating) frequency according to:

$$L_{coil}(f) = 3.183 f^{-0.1062} \tag{7.5}$$

At the generator design-specified operating frequency of 30 Hz, a current phase lag of 16.4° is induced, leading to a power factor of $\sin(\Phi) = 0.95$. However, should the generator be operated at 50 Hz, this phase lag will increase to nearly 25° and power factor will decrease to 0.9. To reduce the current phase lag, a series tuning capacitor C_t may be identified, based on the operating frequency according to:

$$C_t(f) = \frac{1}{(2\pi f)^2 L_{coil}} \tag{7.6}$$

However, since the power lost due to the current phase lag at 30 Hz is small (<5 %), a tuning capacitor did not form part of the engine performance tests that are to follow in Chapter 7.3. A similar methodology was used to determine the motor coil inductance at the design operating frequency, as was defined in Table 6.2.

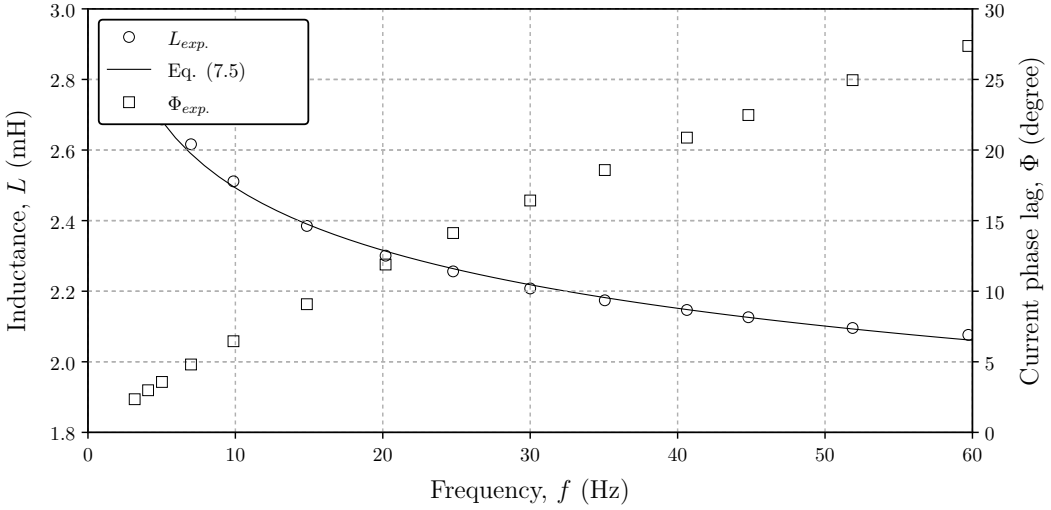

Figure 7.3: Generator coil inductance as a function of operating frequency

7.2.2. Verifying the linear generator model

To evaluate the performance of the linear electric generator, and in doing so verify the linear generator equations, the main body with the assembled linear generator was bolted to a stationary support base, as is illustrated in Figure 7.4. A crank-based reciprocator was used to drive the power piston assembly through the generator core at different operating speeds. As the crankshaft rotates, the connecting rod moves the piston through a fixed 20 mm stroke (10 mm displacement amplitude). The experimentally measured generator terminal voltage and load voltages profiles were used to validate the finite element model and subsequent generator characteristic functions that had been developed and derived throughout Chapter 4.

As shown in Figure 7.4, a three-phase, four-pole induction motor drives the crank. The motor is powered by a variable frequency drive, for which the driving frequency was varied between 10 and 50 Hz – correlating to a maximum reciprocator frequency of approximately 25 Hz on the four-pole motor. Experimental tests were performed first with no generator load (open-circuited condition) and thereafter with a purely resistive 1 Ω load being attached across generator terminals (closed-circuited condition). In each of these tests, the terminal voltage V_{T_g} was recorded using an HBM Quantum MX840A data logger. In the case of generator loaded operation, the *real* electrical power delivered to the purely resistive load was calculated. Refer to Appendix H.3 for photographs of the linear generator and reciprocator test setup.

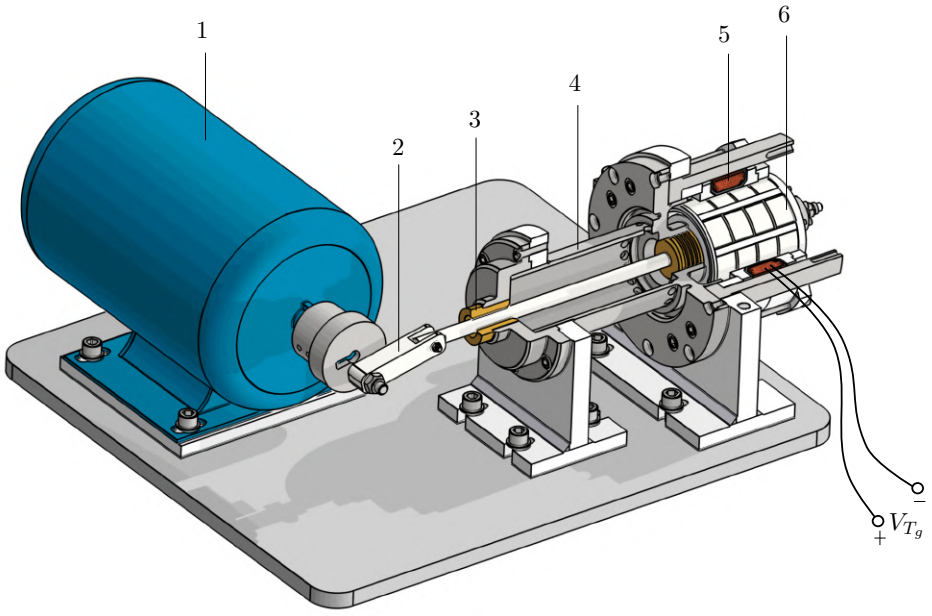

1	3-Phase induction motor	4	Internal engine main body
2	Crankshaft assembly	5	Generator stator and coil
3	Linear guide bush	6	Power piston assembly

Figure 7.4: Illustration of the linear generator connected to the reciprocator

Figure 7.5 compares the open-circuit voltage V_{OC} and closed-circuit load voltage V_L of the linear generator at an operating frequency of 20 Hz. In this figure the experimental measurements are overlaid with the simulated results, including piston displacement $x_{p,sim.}$, to depict the phase shift between the open- and closed-circuit voltages that result due to the generator's internal coil inductance. It is seen that the simulation is in good agreement with the experiment, although the open-circuit voltage amplitude is over-predicted by approximately 1.5 V from the experiment. This is due to unaccounted-for core loss effects that play a prominent role in opposing the magnetic flux density in the open-circuit operation. Unlike the simulated results, the experimental voltages appear slightly asymmetrical, likely indicating that the magnet train was in fact *not* reciprocated perfectly about the centre of the stator cores during testing. This could be due to a slight alignment-offset in the assembly of the reciprocator to the linear generator. Another explanation for this asymmetrical nature may well be that, as the magnet train moves closer to the main body flange, a small flux linkage 'short-circuit' is induced between the flange and the inner core stator. This asymmetrical flux linkage path is not captured in the model.

The simulated and experimentally determined voltage results for open-circuit and closed-circuit terminal conditions are shown in Figure 7.6 (a) for different reciprocation frequencies. Power trend lines visually depict the relationship between voltage and frequency between zero and 50 Hz. Both the open-circuit and closed-circuit results are seen to be in good agreement with the simulated results. At reciprocation frequencies above 20 Hz there appears to be an increasing over-prediction in the simulated open-circuit voltage results. However, since the experimental testing was limited to a maximum reciprocation frequency of 25 Hz, the actual performance of the generator can only be estimated at 30 Hz. Figure 7.6 (b) compares the simulated and experimentally produced load power P_L with increasing reciprocation frequency. The simulation estimates a peak generator output power of 120 W_e at the 30 Hz design-point frequency, whereas the experimental power trend line pre-

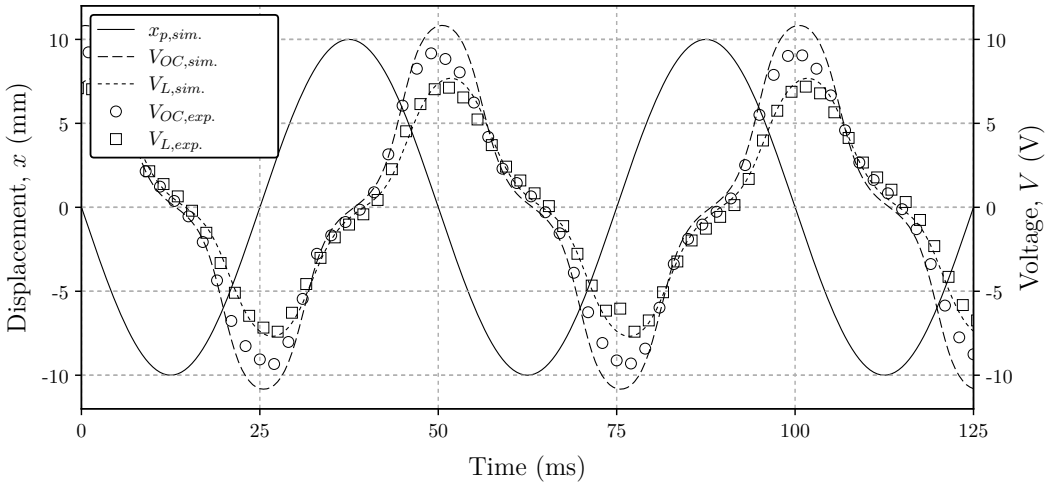

Figure 7.5: Comparison between experimental and simulated results at an operating frequency of 20 Hz

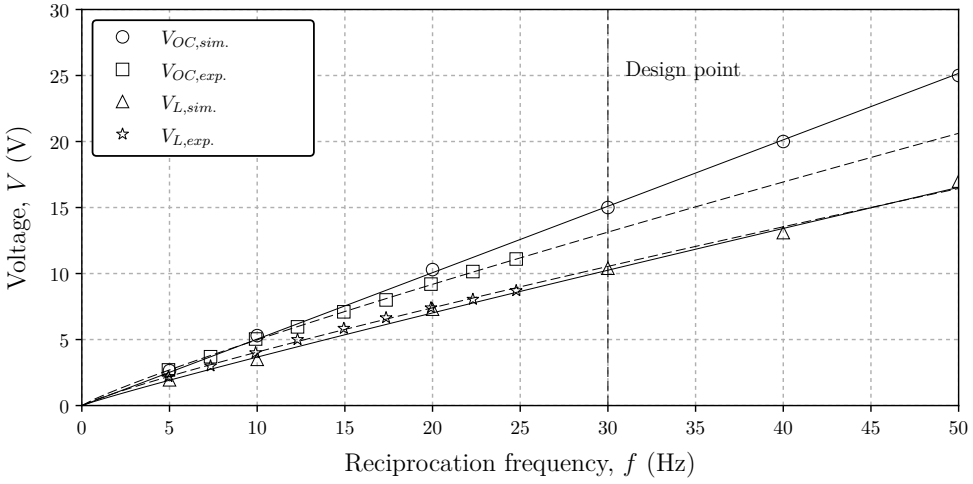

(a)

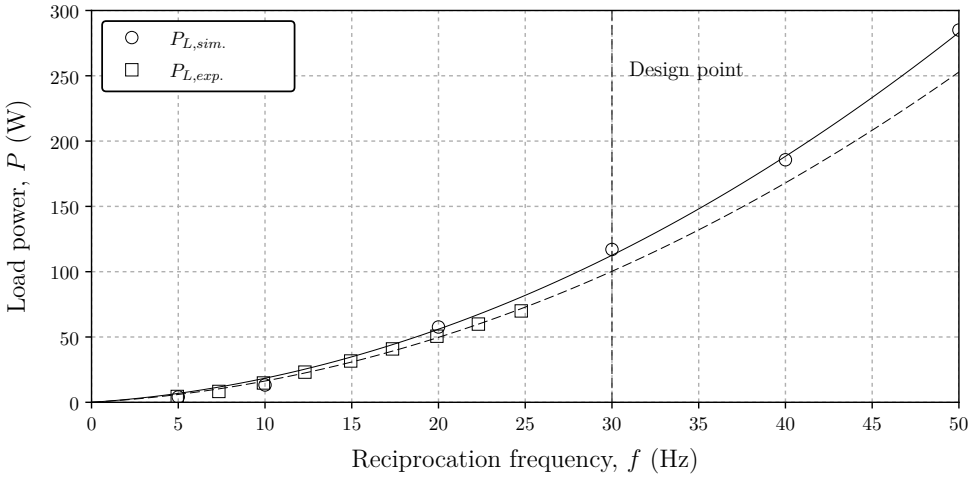

(b)

Figure 7.6: Comparison of the simulated and experimental results at different operating frequencies, showing the (a) open-circuit and closed-circuit voltages, (b) electrical power delivered to a 1 Ω purely resistive load

dicts approximately 100 W (peak) of electrical power output. This is nearly four times the 30 W_e power produced at 15 Hz, which should highlight the importance of increasing the engine operating frequency, should a larger power generating capacity be envisaged in a future engine design study.

Overall, the close correlation between simulated and experimental results presented validates the electromagnetic finite element analysis model of the linear generator. Therefore the analytical relations for flux linkage, magnetic force and magnetic flux density derived in Chapter 4.3 are also deemed verified. Moreover, the experimental results confirm that the linear generator is capable of inducing large current outputs; an important design prerequisite for damping the power piston motion when operating at high charge pressures and increasingly elevated temperatures.

7.3. Experimental evaluation of the assembled engine

Following the experimental evaluation of the linear generator, the prototype FPSE was assembled as per the experimental setup shown by Figure 6.9 on page 92. In this section, experimental results from seven selected sample test runs are qualitatively compared to simulation results achieved with identical setup parameters.

7.3.1. Methodology

Experimental testing of the engine was conducted with engine charge pressures ranging between 1.0 and 1.8 MPa absolute using helium as the working fluid, and with the heater set-point temperatures ranging from 300 to 600 °C. The methodology by which these experiments were performed is briefly outlined as follows:

- The prototype was firstly operated in a displacer-driven mode of operation with the magnet train removed from the power-piston assembly so as to eliminate any magnetic side-load forces induced by the magnets. This experiment serves as a pre-verification test to confirm that the model emulates the engine thermodynamic and piston kinematic behaviour accordingly, even in a completely unloaded condition of operation. It also makes for an interesting case study to see whether the engine would operate and behave in the absence of piston load forces.
- Secondly, the magnet train was reassembled to the power-piston and the engine was operated under open-circuit and closed-circuit generator conditions in a displacer-driven mode of operation. This experiment allows the model to be partially validated under *safe* operating conditions (low temperatures and pressures) in the absence of piston and displacer collisions. In this mode of operation the pressure forces were not able to overcome the engine friction forces to induce self-sustained operation.
- Thirdly, the engine charge pressure was increased until the internally acting pressure forces allowed for self-sustained operation to occur, at which point the displacer motor is switched off. Self-sustained operation was first achieved at an average heater temperature of 450 °C and charge pressure of 1.70 MPa absolute. Three sample test runs are performed under different hot-end temperatures, generator loading conditions and charge pressures. The experiment serves to validate the model in a completely self-sustained operational state.

In each test run presented the engine was first operated with 1 Ω load attached to the generator. The load was subsequently increased to 2 Ω, 3 Ω, 5 Ω and 7 Ω to finally being removed completely (i.e. open circuit condition) over the duration of the test run. It must be emphasised that the experimental evaluation was *not* meant to investigate the engine's sensitivity to changing operating parameters. Rather, the test runs presented allow for a qualitative assessment of the model's ability to emulate the FPSEs operational behaviour across different operating conditions. To do so, selected load cases were numerically simulated as 'snapshots in time' using the experimentally measured heater head temperature, cooling water inlet temperature, coolant flow rate and electrical load condition as model input parameters.

7.3.2. Displacer-driven operation with magnet train removed

In this experiment, the engine was operated in a completely unloaded condition. Since it was established that the magnetic side-load forces of the magnet train induce significant mechanical friction, the magnet train (shown in Figure 6.3) was removed from the power piston assembly. As this first test run would subject the engine to its first thermal cycle, the heater set-point temperature was limited to 400 °C. Displacer-driven engine operation was induced by exciting the displacer motor with a sinusoidal terminal voltage of 12 V, correlating to a peak motor current of approximately 2 A. Results from two sample test runs, denoted Test Run 1 and Test Run 2, with operating parameters listed in Table 7.2, are discussed.

Table 7.2: Operating parameters of Test Runs 1 and 2 in which the magnet train removed and the displacer resonated at 30.5 Hz

	Test Run 1	**Test Run 2**	[Unit]
Set-point temperature, $T_{h,set}$	350	400	°C
Charge pressure (abs.)	1.55	1.87	MPa
Piston friction, $F_{f,p}$	0.492	0.492	N
Heater top temperature, $T_{h,top}$	351.3	498.5	°C
Heater bottom temperature, $T_{h,bot}$	342.8	484.1	°C
Regen. top-wall temperature, $T_{r,top}$	282.2	315.5	°C
Regen. mid-wall temperature, T_r	176.2	218.4	°C
Regen. bot-wall temperature, $T_{r,bot}$	77.2	86.4	°C
Cold-end temperature, T_k	39.3	52.5	°C
Coolant inlet temperature, $T_{w,i}$	25.2	25.5	°C
Backspace wall temperature, T_{bs}	35.5	36.8	°C

Test Runs 1 and 2: Magnet train removed

In Figure 7.7 the experimental results of displacement and pressure of Test Run 1 and Test Run 2 are compared against simulation results of identical operating parameters. The heater casing wall was modelled as a linear temperature boundary condition varying between $T_{h,top}$ and $T_{h,bot}$, whereas the cooling water flow rate was set to 5.5 L/min. The backspace wall temperature T_{bs} was used as an initial estimate to the backspace working fluid temperature. By manually fine-tuning the displacer motor excitation frequency, it was found that the piston and displacer motor could be made to resonate at peak displacements in a shared natural frequency of 30.5 Hz. With reference to Table 7.1, this value is approximately the linear average between the displacer and power piston first mode frequencies. From Figure 7.7 (a) and (c) it is noted that the power piston closely follows the displacer motion with an almost negligible phase difference, calculated as approximately 10° in both cases. Although increasing the hot-end temperature and charge pressure from Test Run 1 to Test Run 2 increased the piston and displacer stroke amplitudes, it had almost no effect on the amplitude of the working fluid pressure swing, as seen from comparing (b) to (d). This is due to the piston-displacer phase difference that remains virtually unchanged as the piston remains unopposed by any load forces. The small phase difference is also indicative that almost no boundary work is being extracted by the engine, as the pressure and volume variations are virtually in phase.

Interestingly, from the simulated workspace pressure variations, two distinct peaks in pressure are visually noticeable. This is especially noticeable in Figure 7.7 (d). The first 'local' peak in pressure swing occurs as the displacer stroke reverses, thereby being related to the thermal expansion or contraction of the working fluid. The second peak occurs when the piston stroke reverses and is instantaneously brought to a standstill. In this instance the displacer, which slightly leads the piston, is already moving in the opposite direction and is thereby either compressing or expanding the working space by the inward or outward movement of its shaft.

In comparing the experimentally recorded and simulated pressure variations it is noted that the pressure transducers were not very sensitive to capturing such slight changes in gas pressure. For instance, when rapid changes in the workspace pressure occur, the experimentally recorded pressure seems to be missing data. Furthermore, in both sample test runs the simulated expansion space pressure swings are over-predicted by approximately 30 %. Arguably, the over-prediction in gas pressure could be attributed to the combined effects of unaccounted for dead-space, lower

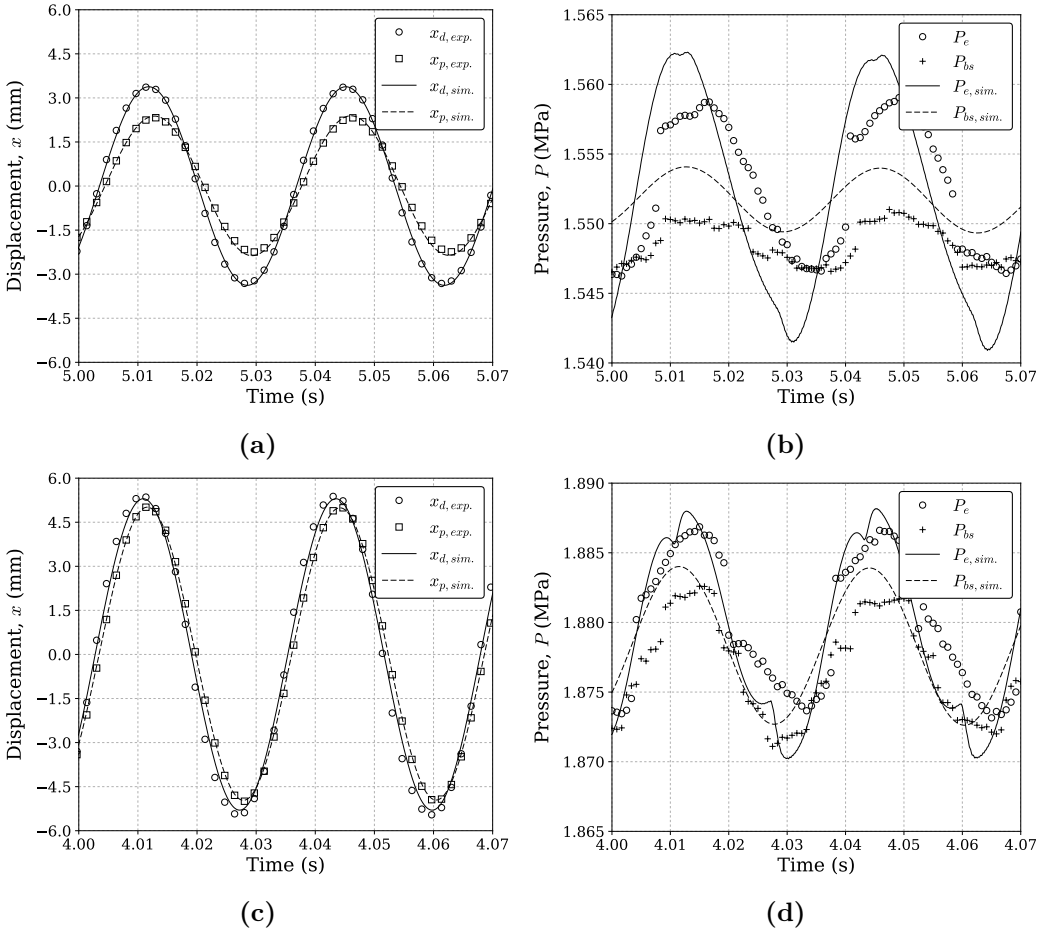

Figure 7.7: Comparison between experimental and simulated results, showing (a) displacement and (b) pressure graphs for Test Run 1, (c) displacement and (d) pressure graphs for Test Run 2

heat transfer rates and larger gas leakage to the backspace. It may also be possible that the thin-film pressure transducers used throughout the study are simply not sensitive enough to capture the peaks of the 30 Hz oscillatory pressure swing. This may be a result of the transducer response settling time, pressure range or internal voltage filtering that adversely affects the sensor's capability of accurately measuring the peaks in workspace and backspace pressure swing. Nevertheless, the overall trend of the simulated and experimentally measured pressure variation over time is seen to be in fair agreement with one another.

Summary of results

Table 7.3 summarises the results obtained for the Test Runs 1 and 2 and gives the simulation deviation percentage in terms of a 'percentage error', as a means of establishing how well the model predicts the experimental results. The deviation percentage is defined as:

$$\% \text{ Dev.} = (\phi_{sim.} - \phi_{exp.})/\phi_{sim.} \times 100\% \tag{7.7}$$

where ϕ represents the variable under consideration. From Table 7.3 it is seen that peak-to-peak (p-p) power piston stroke and phase lag correlate strongly to that of the simulation, exhibiting a simulation deviation of less than 5 %. This agreement verifies the flexure spring stiffnesses, mover masses and piston friction force quantified in Chapter 7.1. Although the increase in hot-end temperature and charge pressure from Test Run 1 to Test Run 2 led to an increase in the displacer and power piston stroke amplitudes, as the power piston remained unopposed by any load forces aside from a small mechanical friction force and inertial forces, the expansion space pressure variation remained nearly unchanged. Moreover, the small variation in working space pressure swing correlates directly with the relatively small piston stroke that, despite an average pressure of nearly 1.9 MPa absolute, barely reaches half its designed-for stroke of 20 mm. The small piston stroke is a result of the mismatch in piston and displacer resonant frequencies. With the piston magnet train removed the power piston assembly is significantly lighter and consequently, its resonant frequency is increased to 31.1 Hz, as shown in Table 7.1. This is in contrast to the displacer assembly having a resonant frequency of approximately 30 Hz and being excited at 30.5 Hz by the displacer motor. In spite of this mismatch in resonance frequency, the good overall correlation shown verifies the numerical model in displacer-driven operation with the magnet train removed.

Table 7.3: Summarised experimental and simulation results of Test Run 1 and Test Run 2, also giving the percentage deviation between them

	Test Run 1			**Test Run 2**			[Unit]
	Exp.	Sim.	Dev. [%]	Exp.	Sim.	Dev. [%]	
Displacer stroke (p-p)	6.7	6.7	[–]	10.8	10.8	[–]	mm
Piston stroke (p-p)	4.6	4.8	[4.2]	10.0	9.9	[-1.0]	mm
Operational frequency	30.5	30.5	[–]	30.5	30.5	[–]	Hz
Piston-displacer phase lag	10.8	11.2	[3.6]	10.3	10.0	[-3.0]	°
Pressure variation (p-p)	12.5	20.5	[39.0]	13.7	18.7	[26.7]	kPa

7.3.3. Displacer-driven operation with magnet train included

In this experiment, the magnet train was reassembled with the power piston. The magnet train not only subjects the power piston to the electromagnetic forces of the linear generator, but also to magnetic side-load forces that induces contact friction between the power piston and bore cylinder. The engine was tested in a displacer-driven mode of operation, by exciting the displacer motor with a 30 Hz sinusoidal voltage. Experimental results were used to validate the numerical model under moderately low charge pressures where, due to the engine mechanical friction and piston load forces, self-sustained engine operation could not be achieved otherwise.

Overview of displacer-driven engine dynamics

Figure 7.8 shows an overview of displacer-driven engine behaviour in three sample test runs of increasing charge pressure, subjected to differing generator loads and a constant hot-end set-point temperature of 450 °C. In each of these tests a 20.0 V, 30 Hz sinusoidal motor excitation voltage was used and the generator load switched between open-circuit to 7 Ω in discrete steps. The figure shows that in contrast to (a), where the engine is shown to operate stably under zero load, open-circuit operation induces a displacer and piston runaway condition in (b) (between six and seven minutes operating time). This erratic engine behaviour occurs when the pressure forces acting on the displacer rod, assisted by the displacer motor forces, are sufficiently large to overcome contact-sliding friction and fluid friction, thereby leading to excessive displacer resonance. As the displacer stroke increases the thermally-induced workspace pressure swing increases and so does the power piston stroke, in turn leading to even larger displacer driving pressure forces. In Figure 7.8 (c), under a charge pressure of 1.6 MPa, this runaway-resonating-behaviour is observed to occur even under loaded operation, starting at 2 Ω and increasing as the generator load resistance is increased. For loads up to 4 Ω the engine recovers from this so-called runaway condition, after undergoing approximately 30 seconds of transient *aliasing*. This apparent aliasing is attributed to a very slight mismatch in motor excitation frequency and the engine's *new* damped natural frequency, further indicating that the engine is close to becoming self-sustaining. When the generator load was increased to 5 Ω, however, the piston started colliding with the engine main body and consequently, the test was terminated after six minutes.

Figure 7.8 should emphasise the highly dynamic and transient nature of a real operating FPSE. As was seen, even the slightest mismatch between displacer excitation frequency and the engine's damped natural frequency can lead to dynamic instability and induce piston-casing collisions. This presents a significant challenge to controlling the engine dynamic behaviour via the displacer motor, especially as the precise damped natural frequency of the piston varies for different generator loads, hot-end temperatures and charge pressures. Therefore, in an effort to achieve greater control over the displacer motion and limit engine runaway (even in this displacer-driven mode of operation), subsequent displacer-driven operational tests were performed with an increased excitation voltage of 30 V. Additionally, the charge pressures were limited to below 1.40 MPa absolute to avoid any runaway-resonating behaviour.

To verify that the numerical model is capable of emulating the behaviour of the FPSE in a displacer-driven mode of operation, results from two sample test runs are qualitatively compared to simulation results of identical operation parameters. Table 7.4 lists the operating parameters and engine casing temperatures recorded for Test Runs 3 and 4 – also forming the modelling input parameters to validating the theoretical model for displacer-driven engine operation. In Table 7.5 on page 115 a comparative summary of the principal experimental and simulated results are given along with the simulation deviation percentage. In each of these tests the displacer motor excitation voltage was set to 30 V, correlating to a peak motor current of

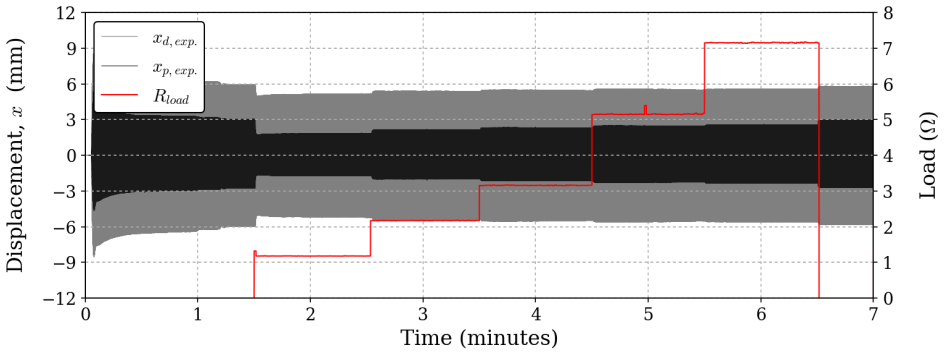

(a) P = 1.0 MPa abs., $T_{h,set}$ = 450 °C

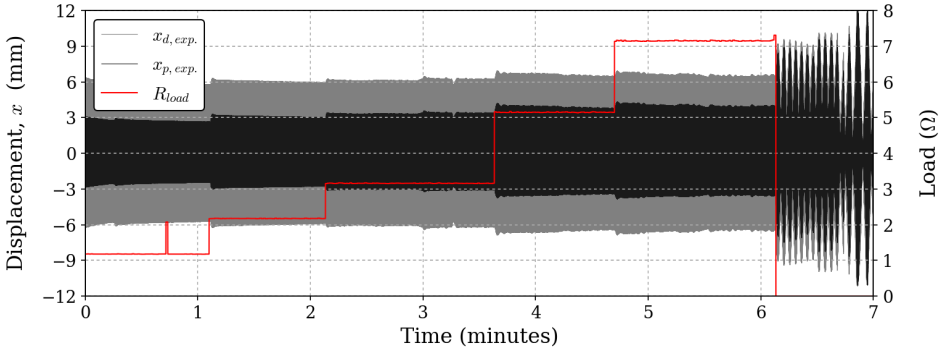

(b) P = 1.3 MPa abs., $T_{h,set}$ = 450 °C

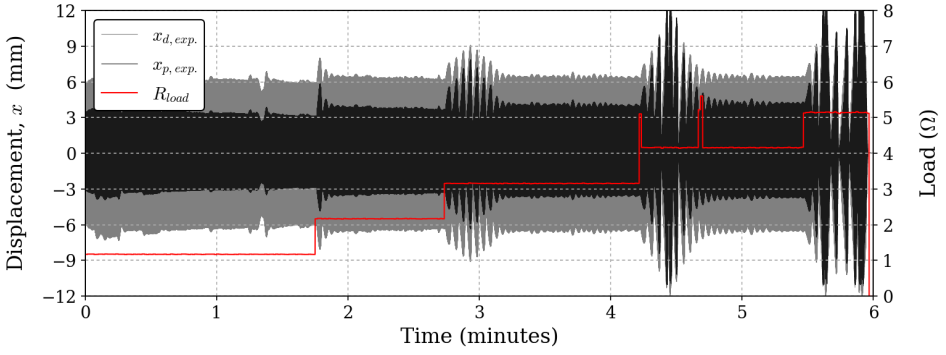

(c) P = 1.6 MPa abs., $T_{h,set}$ = 450 °C

Figure 7.8: Engine displacements over time for varying charge pressures and generator loading conditions, as operated in displacer-driven operation at 30.0 Hz

nearly 5 A, and the excitation frequency manually fine-tuned around 30 Hz until the peak displacer and piston motions were observed. The corresponding experimental displacer motion was then used as a model input parameter to omit the requirement of simulating the linear motor electrodynamic behaviour. The heater casing wall was modelled as a fixed temperature boundary condition, varying linearly from $T_{h,top}$ down to a linear average between $T_{h,bot}$ and $T_{r,top}$, whereas the coolant water inlet temperature was specified as measured from the experiment.

Table 7.4: Operating parameters of Test Runs 3 and 4 in which the magnet train is included and the displacer driven with a 30 V excitation voltage

		Test Run 3			**Test Run 4**		[Unit]
Set-point temperature, $T_{h,set}$			450			550	°C
Charge pressure (abs.)			1.15			1.35	MPa
Piston friction[1], $C_{f,p}$			55			55	Ns/m
Generator load, R_{load}	O.C.	1.18	2.18	7.18	1.18	2.18	Ω
Heater top temp., $T_{h,top}$	433.5	447.2	441.3	520.7	549.5	542.7	°C
Heater bottom temp., $T_{h,bot}$	431.2	440.5	435.1	519.3	542.7	539.1	°C
Regen. top-wall temp., $T_{r,top}$	370.3	382.3	377.1	427.7	453.4	444.8	°C
Regen. mid-wall temp., T_r	245.4	252.8	249.3	269.5	291.2	282.1	°C
Regen. bot-wall temp., $T_{r,bot}$	105.7	112.4	109.6	114.4	117.2	115.7	°C
Cold-end temp., T_k	49.5	47.2	48.3	52.1	49.9	51.5	°C
Coolant inlet temp., $T_{w,i}$	28.4	28.4	28.4	28.4	28.3	28.3	°C
Coolant outlet temp., $T_{w,o}$	30.4	30.4	30.4	30.9	30.7	30.7	°C
Backspace wall temp., T_{bs}	42.7	42.2	42.3	36.8	35.7	35.9	°C

[1] From trial-and-error by simulation, a viscous damping coefficient of 55 N s/m has been identified to be representative of the magnetically-induced piston mechanical friction.

Test Run 3: Open-circuited operation

Figure 7.9 shows the experimental and simulated results of displacement, pressure and voltage, as obtained for the open-circuit generator condition of Test Run 3. Although the simulated piston stroke in Figure 7.9 (a) is in good agreement with the experiment, the model under-predicts the piston-displacer phase difference as 64°, as opposed to the 84° that was calculated from the experiment. This is likely due to a slight mismatch between real and simulated piston friction forces or reciprocator masses. In Figure 7.9 (b) the expansion and backspace pressure swing is shown to be in good agreement with the model. In comparing (a) to (b) it is calculated that the workspace pressure swing is leading the displacer by 23.4° and the piston by 107.4°, as was denoted the phase differences β and α in Figure 5.5 on page 66.

The enclosed area within the pressure-volume (PV) diagram in Figure 7.9 (c) gives a net experimental indicated power of 38.0 W. This indicated power is solely dissipated in overcoming piston mechanical friction and generator open-circuit core loss effects, and is in good agreement with the simulated net indicated power being 39 W. This is despite Table 7.5 showing the expansion space and compression space model deviations to differ significantly for such small volume variations, in the order of 23 and 40 % respectively. As a result of the under-prediction in piston phase relative to the displacer, the simulated PV curve appears slightly tilted towards the right.

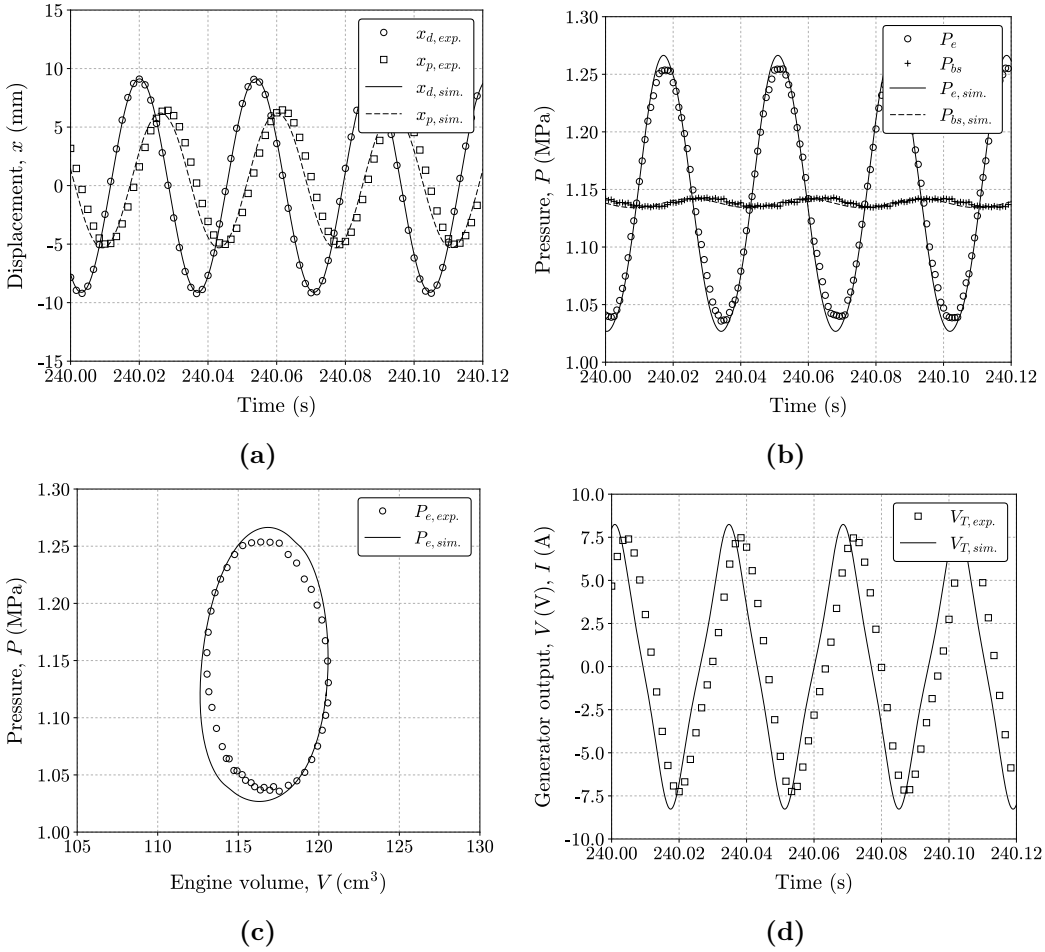

Figure 7.9: Experimental and simulated results for the open-circuit condition of Test Run 3, showing graphs for (a) displacement over time, (b) pressure over time, (c) pressure versus engine volume and (d) generator voltage over time

In spite of the good correlation in net indicated power it must be noted that, as has been discussed in Chapter 5.3, by integrating the expansion space pressure over the entire engine volume and thus assuming the expansion and compression space pressures to be equal, the frictional pressure losses are unaccounted for in this calculation of net indicated power. However, since the anticipated regenerator pressure drop is small, this experimental inaccuracy has been assumed to be negligible.

In Figure 7.9 (d) the experimental and simulated open-circuit terminal voltages of the linear generator are given. The simulation appears to be over-predicting the voltage amplitude by nearly 0.9 V and is leading the experiment by 37° in phase. This phase difference is partially attributed to the 20° difference in phase between modelled and measured piston phase. However, the nearly 17° of additional phase difference suggests that there are *inductive core-loss effects* in open-circuit operation that the theoretical simulation does not capture so accurately. With reference to Figure 4.3 on page 50, it is postulated that the widening of the flux linkage curve

about the simulated static case, which is not emulated by the numerical model, may be mainly responsible for this over-prediction in voltage and shift in its phase. This modelling limitation could certainly be improved upon in a future study study.

Test Run 3: One ohm loaded operation

Following the open-circuited operation, the engine was operated in an electrically loaded condition by attaching a purely resistive 1 Ω load across the generator terminals. Figure 7.10 (a) shows the displacer and power piston displacements, which are noticeably smaller in amplitude when compared to that of the open-circuit case presented in Figure 7.9. The attachment of the electrical load has nearly halved the power piston stroke to 6.6 mm, also reducing its phase lag behind the displacer to 61.7°. Accordingly, the simulation predicts this reduction in piston stroke. Corresponding to the reduction in piston stroke and phase difference with the displacer, the peak-to-peak variation in expansion space pressure in Figure 7.10 (b) has been reduced to 173 kPa. The numerical model over-predicts the expansion space pressure variation by approximately 20 %, whereas for the backspace, the model and experiment are in good agreement. In comparing (a) to (b) it is calculated that the workspace pressure swing is leading the displacer by only 13° and the piston by 75°.

Correlating to the reduction in piston stroke, the net indicated power calculated from Figure 7.10 (c) has been reduced to 16.7 W. Due to the over-prediction in simulated pressure swing, the model over-predicts the net indicated power by 15 %. The PV curves appear titled towards the right, indicating that the variation in engine workspace pressure is leading the volume variation by less than 90°. This is mainly due to the pressure swing being nearly in phase with the driven displacer's motion. As the power piston lags the displacer by less than 90°, and since the engine volume variation is mostly dependent on piston motion, the pressure-volume phase difference is also smaller than 90°. This orientation of the PV diagram is furthermore indicative that in its current operating state, the engine is consuming mechanical power rather than delivering a net positive output. Still, the model and the experiment are in good agreement. In Figure 7.10 (d) the induced load voltage and generator current is shown for the 1 Ω load. A small load voltage of 2.5 V is induced due to the piston's significantly smaller stroke. The generator delivers a peak electrical power output of 6.9 W, or 3.3 W if averaged over the cycle period.

Test Run 4: Seven ohm loaded operation

At the increased heater set-point temperature and charge pressure of Test Run 4, exciting the displacer motor in a generator open-circuit condition resulted in engine runaway behaviour and piston-casing collisions, as was shown in Figure 7.8 for example. From trial-and-error it was found that the engine could be operated stably if a load resistance of 7 Ω or smaller was applied. Consequently, in this section, 7 Ω loaded operation is discussed as opposed to open-circuited operation. Figure 7.11 (a) shows that the displacer and piston displacements are noticeably larger in comparison to that given by Figure 7.9 for Test Run 3. The displacer reciprocates nearly at its design-specified stroke of 20 mm whereas the piston stroke has increased to 14.9 mm, lagging 75° behind the displacer. The model correlates well with the experiment, also predicting the piston's displacement offset into the

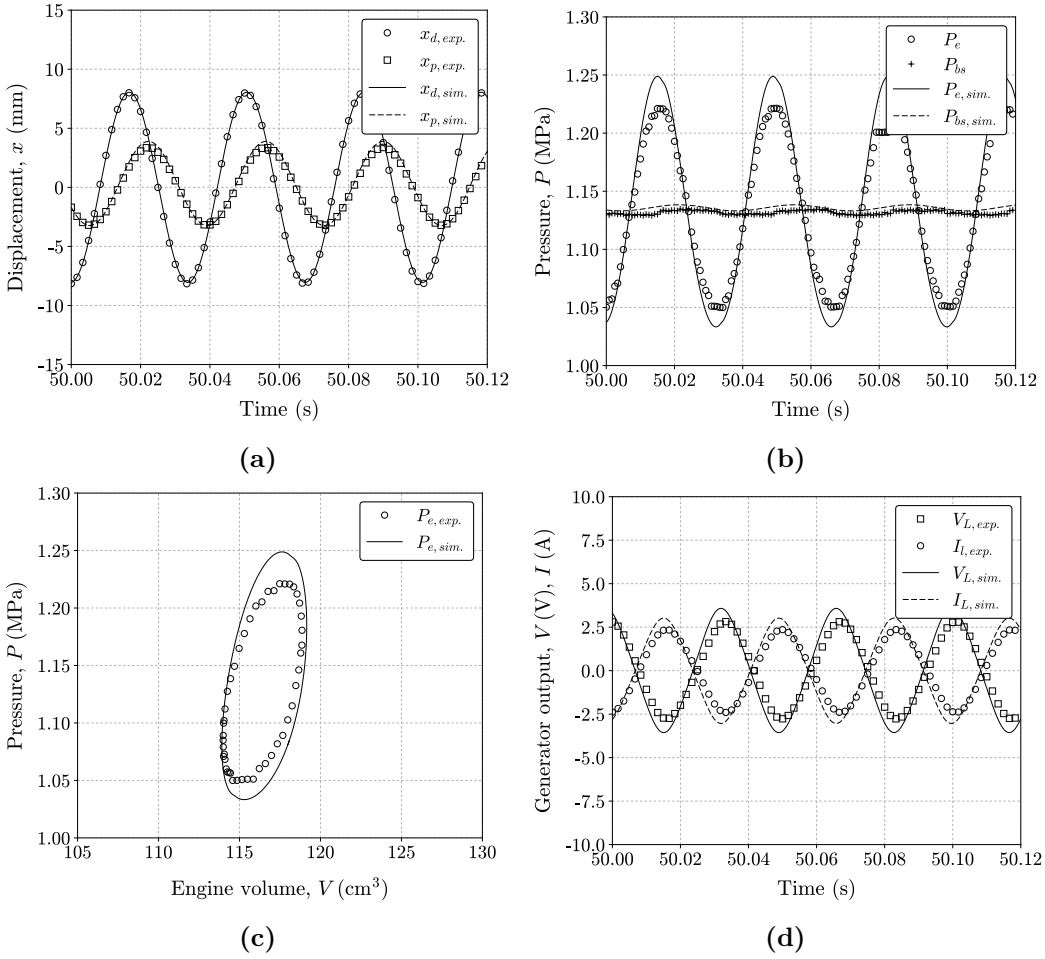

Figure 7.10: Experimental and simulated results for the 1 Ω load condition of Test Run 3, showing graphs for (a) displacement over time, (b) pressure over time, (c) pressure versus engine volume and (d) generator voltage and current over time

backspace. As was discussed in Chapter 5.3, this piston displacement offset evolves naturally as the engine finds its *new* thermodynamic equilibrium state and is the reason why operational FPSEs often make use of 'gas centring ports' (Karabulut, 2011). The simulated expansion space pressure variation in (b) is in good agreement with the experiment despite being over-predicted by 27 %. The measured pressure swing leads the displacer and piston by 36.8° and 111.5° respectively.

From the PV diagram in Figure 7.11 (c), the engine is calculated to deliver a net indicated power of nearly 61 W. This significant increase over Test Run 3 correlates to the larger piston stroke and pressure variation. The over-prediction in simulated pressure swing is seen to 'stretch' the PV curve vertically, thereby inducing an over-prediction of 25.6 % in indicated power. If this pressure over-prediction was to be accounted for by a model correction factor, the simulated and measured PV curves would be nearly indistinguishable. In Figure 7.11 (d) the generator is shown to deliver a peak load voltage of 8 V at a current of 1.2 A. As with the open-circuited

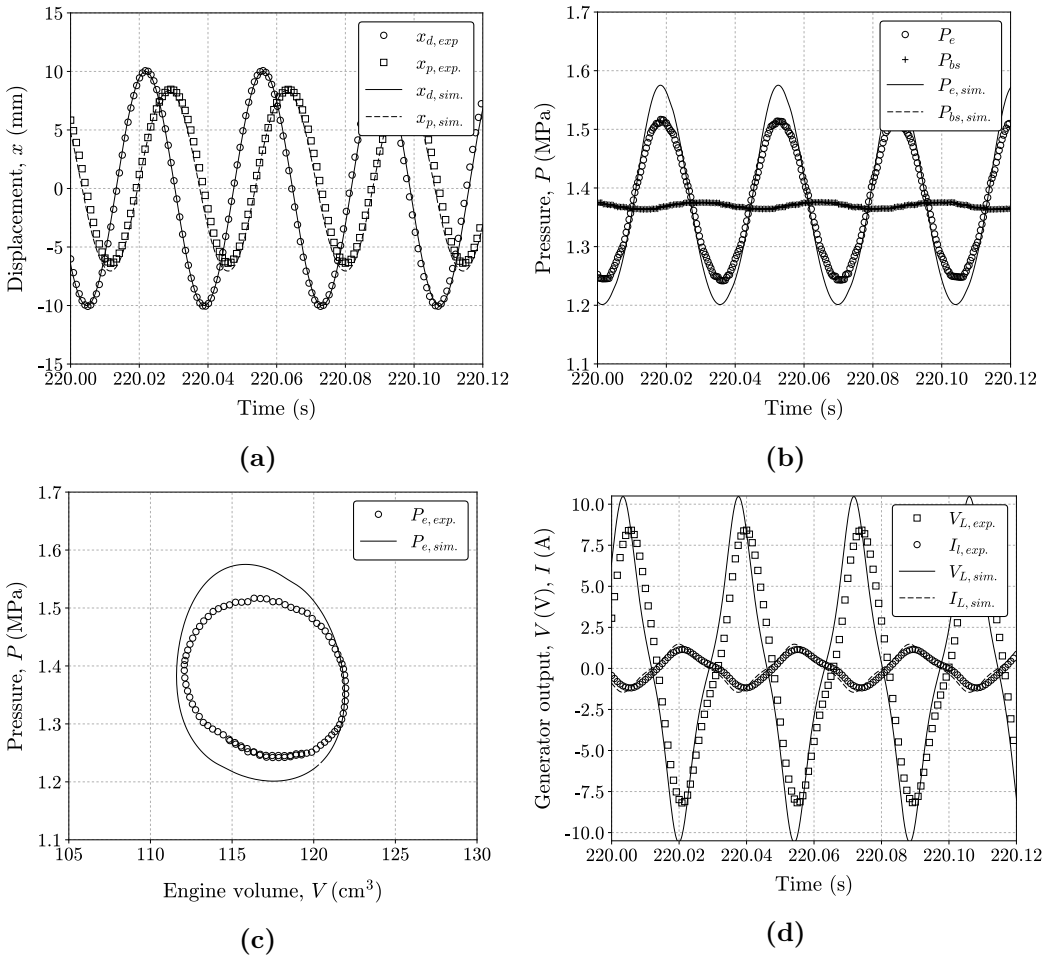

Figure 7.11: Experimental and simulated results for the 7 Ω load condition of Test Run 4, showing graphs for (a) displacement over time, (b) pressure over time, (c) pressure versus engine volume and (d) generator voltage and current over time

operation of Test Run 3, the model is slightly over-predictive of the voltage, with the model also leading the experiment in phase. But despite this slight deviation, the model accurately predicts the shape of this triangular voltage wave whilst delivering a peak electrical power of 10.2 W, or average power of 4.2 W.

Test Run 4: One ohm loaded operation

Figure 7.12 shows the displacement, pressure and voltage results as obtained for the 1 Ω loaded operation of Test Run 4. As was seen in Test Run 3, the attachment of a low-resistance electrical load leads to a reduction in piston stroke, down to 10.6 mm as seen from (a). The simulated piston stroke is in good agreement with the experiment, both in terms of amplitude and phase, and also predicts the piston's positive offset from its mid-stroke location. The simulated pressures in Figure 7.12 (b) are in good agreement with the experiment. The model over-predicts the peak-to-peak workspace pressure swing by nearly 29 % whilst the backspace pressure is indistinguishable from the experiment. The workspace pressure swing leads the displacer

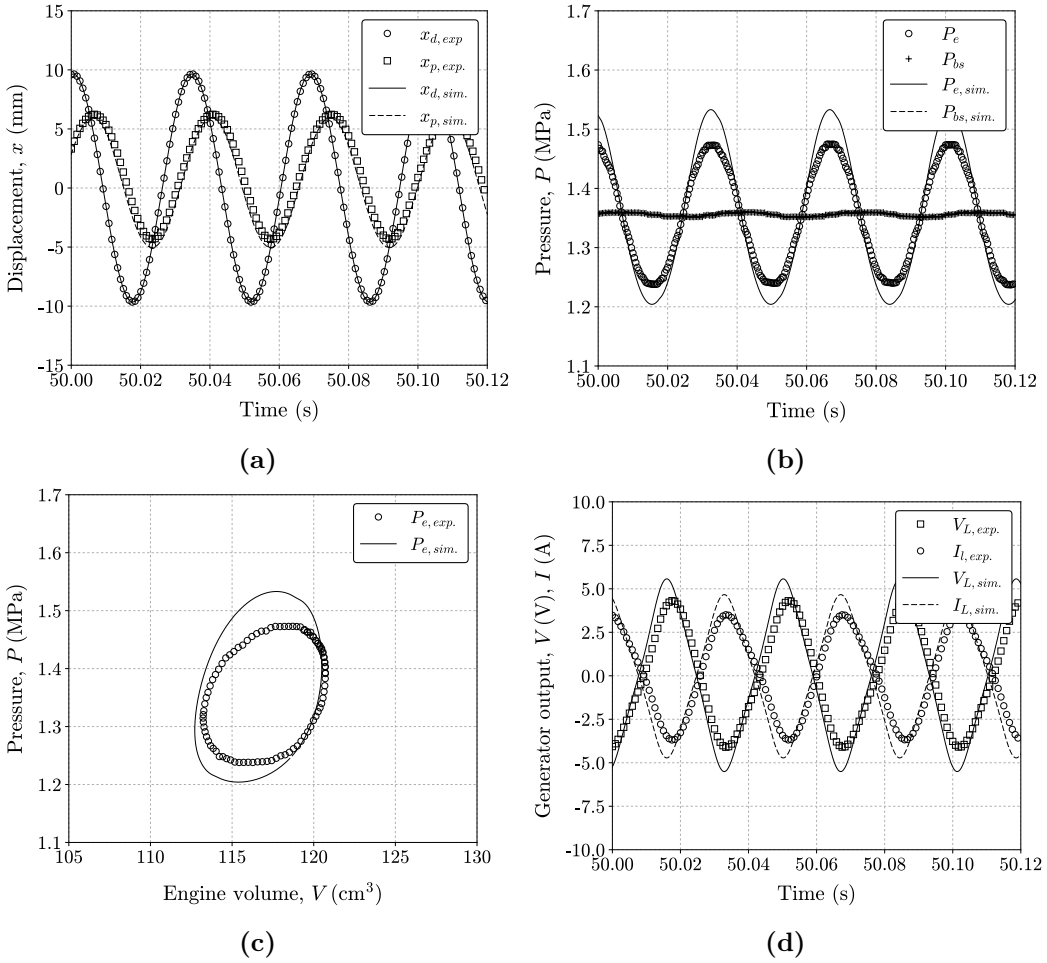

Figure 7.12: Experimental and simulated results for the 1 Ω load condition of Test Run 4, showing graphs for (a) displacement over time, (b) pressure over time, (c) pressure versus engine volume and (d) generator voltage and current over time

and piston motions by 24° and 63° respectively. From Figure 7.12 (c) it is noted that the reduction in piston swept volume, workspace pressure swing and piston-pressure phase difference correlate to a significant reduction in indicated power, from approximately 60.9 W to 38.7 W. As with the 1 Ω loaded operation of Test Run 3, the PV diagram is tilted towards the right as a result of the piston-pressure phase shift being smaller than 90°. The deviation in simulated and measured pressure contributes to the 23.9 % over-prediction in indicated power. A good correlation between load voltage and current is seen from Figure 7.12 (d), with the generator delivering on average 6.9 W of electrical power to the resistive load.

Summary of results

Experimental testing of the assembled prototype was conducted in two separate test runs of increasing hot-end temperature and pressure in which the engine was *forcefully* operated by exciting the displacer in a state of resonance using a 30 V motor voltage. This allowed the numerical model to be partially verified and validated un-

der moderate charge pressures where self-sustained operation would otherwise not be possible. In Table 7.5 the main experimental and simulation outcomes are summarised. The table additionally presents the summarised outcomes of 2 Ω loaded operation, which for its similarity to 1 Ω loaded operation, has been omitted from the aforementioned comparisons.

From Table 7.5 it is noted that the simulated piston stroke and phase differences α and θ are generally in good agreement with the experiment. However, from the qualitative comparisons it has been established that the model generally over-predicts the peak-to-peak pressure swing in the expansion space, ranging by between 10.6 to 28.9 % in the test cases presented. This is consistent with the over-predictions in pressure that was observed from Test Runs 1 and 2. It is hypothesised that this over-prediction is attributed to the effects of unaccounted for engine dead-space, larger gas leakage to the backspace and lower actual heat transfer rates occurring. However, the consistent over-prediction in pressure might also suggest that the pressure sensor used is simply inaccurate in measuring the 30 Hz pulsating pressure swing. The over-predicted pressure swing leads to engine boundary work rates being over-predicted. The model deviation with the expansion and compression space indicated powers is especially large when the displacer and piston strokes are small. The simulated load voltage is generally over-predicted by 20 % and so is the load current, leading to a deviation of up to 37.7 % in peak electrical power. The deviation in electrical power is attributed to the simplifying analytical relation used by which the generator flux linkage is represented. But despite the notable over-predictions in amplitude of pressure and electrical output power, the general trends of the simulated results were in all cases seen to be in fair agreement with the experiment.

Table 7.5: Summary of the principal experimental and simulated results of Test Runs 3 and 4 with the simulation deviation percentage given in brackets

		Displ. stroke [mm]	Piston stroke [mm]	Opp. freq. [Hz]	Phase diff α [°]	Phase diff θ [°]	Pres. (p-p) [kPa]	Volt. (p-p) [V]	Exp: $\dot{W}_e$ [W]	Comp: $\dot{W}_c$ [W]	Ind. power [W]	Peak power [W]	Avg. power [W]
Test Run 3: Set-point = 450 °C, P = 1.15 MPa													
O.C.	Exp.	18.2	11.5	29.6	107.4	84.0	214.6	14.8	65.3	27.3	38.0	–	–
	Sim.	18.2	11.5	29.6	94.7	63.8	240.0	16.5	84.9	45.9	38.8	–	–
	[% Dev.]	–	[0.3]	–	[-13.5]	[-31.8]	[10.6]	[10.6]	[23.1]	[40.5]	[2.6]	–	–
1 Ω	Exp.	16.1	6.6	29.6	74.5	61.7	172.8	5.1	21.5	4.8	16.7	6.9	3.3
	Sim.	16.1	7.1	29.6	78.7	63.8	216.3	7.1	39.0	19.3	19.6	10.9	5.1
	[% Dev.]	–	[7.6]	–	[5.4]	[3.3]	[20.1]	[28.8]	[44.9]	[75.1]	[15.2]	[36.4]	[36.5]
2 Ω	Exp.	16.7	7.5	29.6	79.8	63.8	177.8	7.6	29.4	9.3	20.1	7.0	3.2
	Sim.	16.7	8.1	29.6	78.7	60.6	214.6	9.4	47.3	24.3	23.0	10.2	4.7
	[% Dev.]	–	[7.9]	–	[-1.4]	[-5.3]	[17.1]	[19.0]	[37.8]	[61.6]	[12.4]	[31.3]	[31.4]
Test Run 4: Set-point = 550 °C, P = 1.35 MPA													
7 Ω	Exp.	20.1	14.9	29.2	115.5	74.7	272.2	16.7	105.9	45.0	60.9	10.2	4.2
	Sim.	20.1	15.4	29.2	110.5	71.5	373.7	20.9	168.5	86.7	81.8	10.6	5.6
	[% Dev.]	–	[3.6]	–	[-1.0]	[-4.4]	[27.2]	[20.3]	[37.2]	[48.1]	[25.6]	[4.5]	[24.6]
1 Ω	Exp.	19.3	10.6	29.2	87.3	63.1	234.5	8.5	65.3	26.5	38.7	16.0	6.9
	Sim.	19.3	11.0	29.2	85.2	60.9	329.9	11.0	99.5	48.6	50.9	25.7	11.4
	[% Dev.]	–	[3.1]	–	[-2.5]	[-5.3]	[28.9]	[22.7]	[33.4]	[45.4]	[23.9]	[37.8]	[38.9]
2 Ω	Exp.	19.6	12.5	29.2	99.9	64.2	256.7	11.9	119.1	67.1	52.0	17.2	7.2
	Sim.	19.6	12.8	29.2	96.8	65.2	341.6	15.1	127.3	63.6	63.7	26.5	10.7
	[% Dev.]	–	[2.4]	–	[-3.3]	[1.6]	[24.9]	[20.9]	[6.4]	[-5.6]	[18.4]	[35.0]	[33.0]

7.3.4. Self-sustained engine operation

Self-sustained operation becomes possible when the differential gas pressure forces acting on the displacer shaft are sufficiently large to overcome the frictional and gas shuttling losses over the engine heat exchanger channel. This mode of operation requires the piston to reciprocate over some minimum distance so that the boundary-work-induced pressure swing is large enough to overcome the aforementioned displacer load forces. When this is the case, the piston and displacer essentially *resonate* with the thermally induced engine internal pressure swing.

Figure 7.13 depicts a visual summary of experimental tests performed in which self-sustained operation could be achieved. The figure serves only to show the range of operating parameters initially investigated for self-sustaining operation (both under open and closed circuit conditions). The figure distinguishes the boundary where the hot-end temperature and charge pressure becomes sufficient to allow for self-sustaining operation to occur. Nevertheless, at internal charge pressures and heater temperatures below 1.7 MPa and 550 °C, engine operation could barely be sustained in a generator loaded state for more than thirty seconds. When the pressure was increased above 1.7 MPa, engine operation could be sustained for up to six minutes. Still, due to insufficient heating capacity by the 1.0 kW electrical heater, engine temperatures declined from the initial heater set-point with the onset of stalling occurring when the average heater temperature decreased below approximately 450 °C.

Throughout this section, self-sustained operation of the engine is investigated in greater detail for three sample test runs of increasing temperature and charge pressure – denoted Test Runs 5, 6 and 7. Test Runs 5 and 6 have been selected as they illustrate a clear pressure boundary to achieving self-sustained operation, whereas in Test Run 7, the engine was operated at the peak design-permitted charge pressure of 1.80 MPa and a maximum attainable heater temperature of nearly 600 °C.

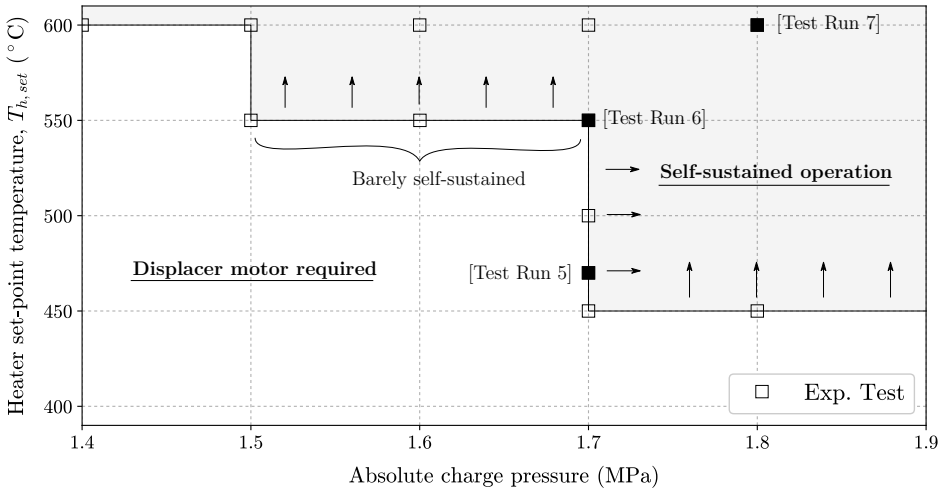

Figure 7.13: Experimental investigation into temperature and charge pressure dependency for self-sustained engine operation

Overview of self-sustained engine dynamics

Figure 7.14 shows graphs of displacement, pressure, generator voltage, current and electrical output power over time as the generator load was varied between one and seven ohms. The figure illustrates how a typical test run was conducted where, in this instance, the engine was operated to a heater set-point temperature of 470 °C and charge pressure of 1.70 MPa (e.g. Test Run 5). During the first twenty seconds of operation, the displacer motor was used to *kick-start* the engine into operation. When the displacer stroke first exceeded 20 mm, the motor was switched off.

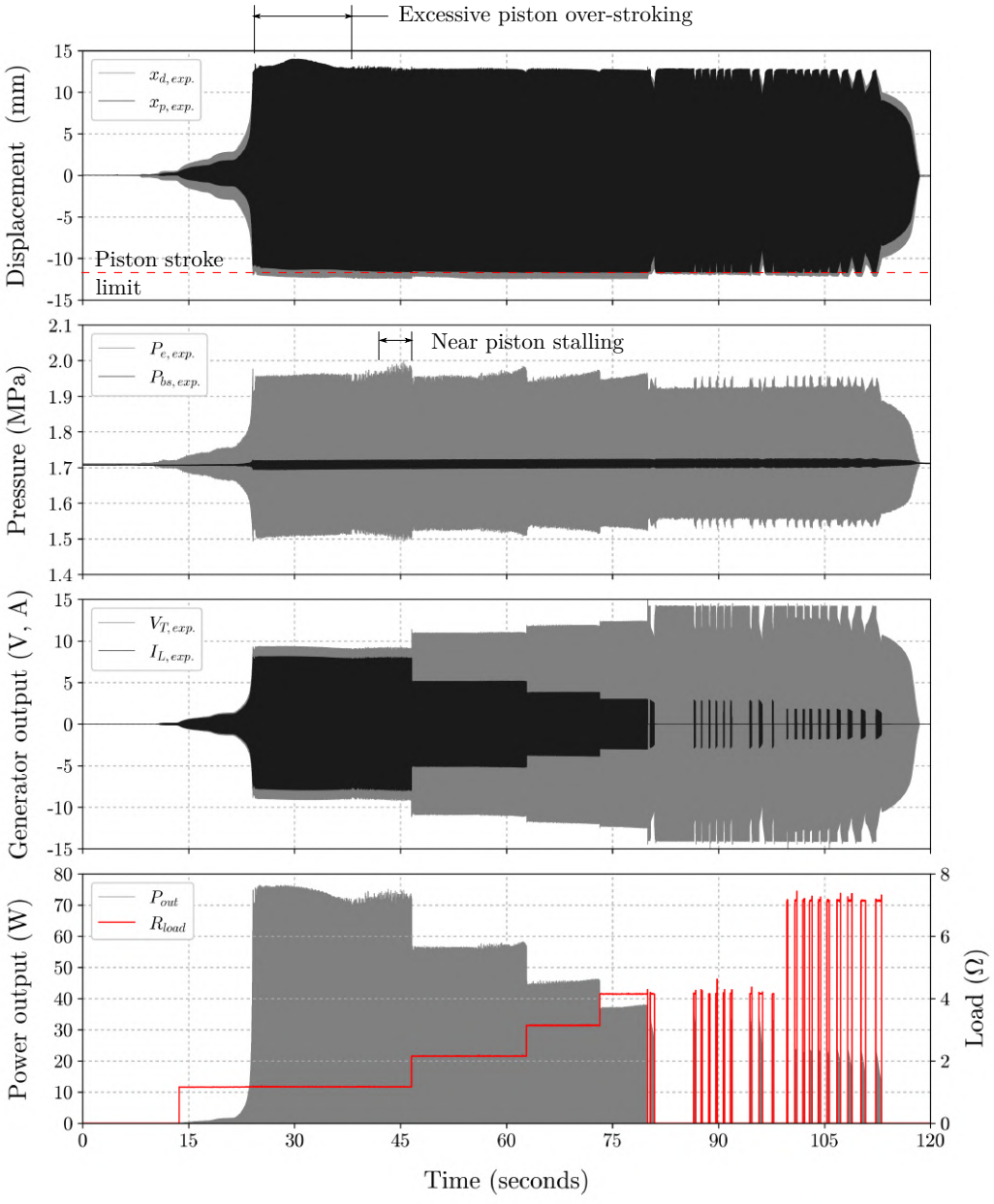

Figure 7.14: Engine displacements, pressures, generator output voltage, load current and peak electrical power output for the self-sustained operation of Test Run 5

During the first 80 seconds of operation the generator load was adjusted from 1 Ω to 4 Ω. This is followed by an additional 40 seconds of manually switching on/off the 4 Ω load and thereafter 7 Ω load in an effort to sustain engine operation. Interestingly it is seen that under all generator loading conditions tested, the power piston displacement approaches a physical-design limitation at −12 mm, consequently colliding with the engine main body as it *over-strokes* its intended 20 mm designed-for stroke. This limitation on piston stroke results in the nearly uniform pressure swing between 1.5 MPa and 1.95 MPa, as is seen for the expansion space. Another interesting phenomenon arises when the generator load is held constant, for example, that of 1 Ω: as the engine metal temperature decreases over time, the piston-displacer phase difference increases, from approximately 63° at start-up to nearly 77°, coinciding to a local increase in workspace pressure swing. This increase in piston-displacer phase difference correlates to a decrease in phase difference between the pressure swing and displacer amplitude, from approximately 45° to 37°. The decrease in phase shifts the peak in pressure further away from the displacer's peak velocity, thereby reducing the resonating effect that the pressure variation has on the displacer and consequently leading to engine stalling unless the generator load is reduced.

The engine temperature measurements depicted in Figure 7.15 show a clear decline in casing wall temperature over time, indicating that the 1.0 kW thermal output of the electric heater is insufficient to keep the engine operating at the 470 °C specified set-point temperature. The average wall temperature adjacent to the heater head denoted $T_{r,top}$ declines to 365 °C when the onset of stalling occurs. With reference to Figure 6.10, the temperature profile of the engine casing adjacent to the heater head can only be estimated as being somewhere in-between the metal temperatures

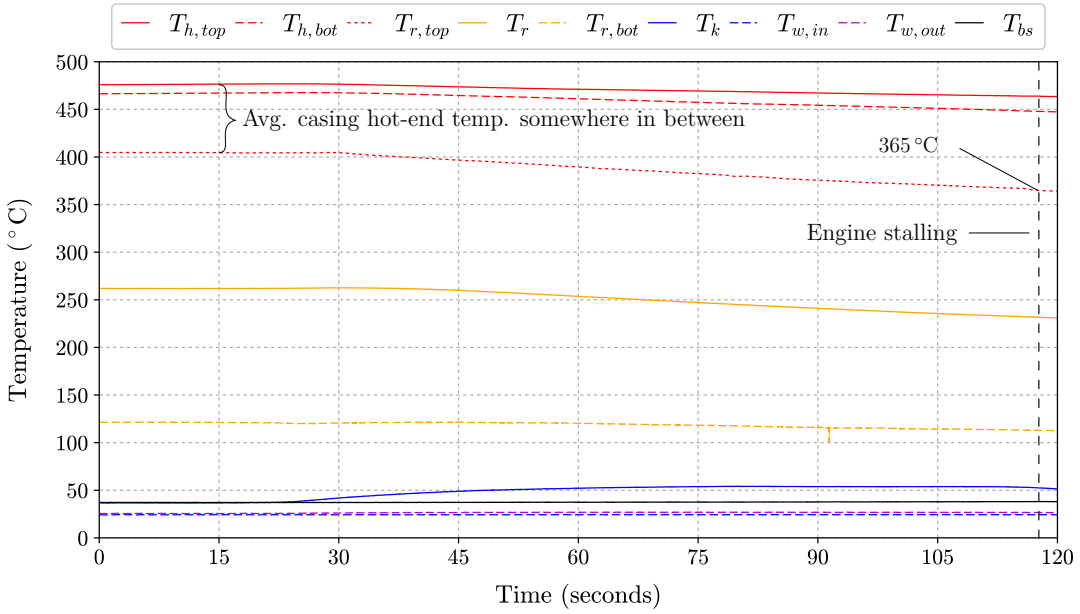

Figure 7.15: Engine temperatures measurements of Test Run 5, showing the decline casing wall temperature over time

Table 7.6: Operating parameters recorded for Test Runs 5, 6 and 7

	Test Run 5			**Test Run 6**			**Test Run 7**			[Unit]
Set-point temperature, $T_{h,set}$			470			550			600	°C
Charge pressure (abs.)			1.70			1.70			1.80	MPa
Piston friction [1], $C_{f,p}$			40			40			40	Ns/m
Generator load, R_{load}	O.C.	1.18	2.18	O.C.	1.18	2.18	O.C.	1.18	2.18	Ω
Heater top temp., $T_{h,top}$	468.2	476.8	471.1	536.2	549.4	541.6	506.4	576.5	558.3	°C
Heater bot. temp., $T_{h,bot}$	455.3	467.8	461.6	522.9	539.6	532.2	490.1	569.1	554.7	°C
Regen. top-wall temp., $T_{r,top}$	377.4	405.0	389.6	424.8	458.2	434.5	389.6	473.3	447.9	°C
Regen. mid-wall temp., T_r	243.5	262.6	253.8	264.6	295.1	273.1	243.7	307.1	281.3	°C
Regen. bot-wall temp., $T_{r,bot}$	116.8	116.4	117.1	114.9	118.1	118.5	110.8	117.1	119.9	°C
Cold-end temp., T_k	54.1	45.5	52.3	58.6	52.3	57.7	62.7	61.3	63.9	°C
Coolant inlet temp., $T_{w,i}$	24.3	24.3	24.3	27.7	27.7	27.7	30.8	30.7	30.7	°C
Coolant outlet temp., $T_{w,o}$	26.8	26.5	26.8	30.5	30.3	30.6	33.6	33.7	33.7	°C
Backspace wall, T_{bs}	37.6	37.1	37.5	35.2	34.3	34.9	38.9	34.2	35.2	°C

[1] From trial-and-error by simulation, a viscous damping coefficient of 40 N s/m has been identified to be representative of the magnetically-induced piston mechanical friction.

$T_{h,top}$ and $T_{r,top}$. When the engine is operating according to the parameters of Test Run 5, the casing wall adjacent to the cold end, T_k, increases to approximately 55 °C as heat is being shuttled there by the displacer. An increase of approximately 2.5 °C is measured in the cooling water, whereas from Table 7.6, it is seen that for Test Run 7 this temperature difference increases up to 3 °C. Depending on heater set-point temperature, this correlates to a cooler heat rejection rate of between 900 and 1100 W if the water flow rate is retained at 5.5 L/min. Due to the cooler heat rejection rate being sensitive to accurate knowledge of the cooling water flow rate and the change in water temperature, the cooler heat rejection rates of different test were not explicitly used as a way of verifying the numerical model.

To verify that the numerical model indeed emulates the completely self-sustained operational behaviour of the FPSE prototype, results from three sample test runs are qualitatively compared to simulation results of identical operating parameters. Table 7.6 lists the operating parameters and engine casing temperatures recorded for Test Runs 5, 6 and 7 – also forming modelling input parameters to validating the theoretical model for self-sustained engine operation. In Table 7.7 on page 134, a comparative summary of the principal experimental and simulated results are given along with the simulation deviation percentage, defined according to Equation (7.7).

Test Run 5: Open-circuited operation

Figure 7.16 shows graphs of displacement, pressure and generator voltage of four consecutive engine cycles of Test Run 5 that were recorded as a 'snapshot in time' to which simulated results may be compared to. As was done in the preceding section on displacer-driven operation, the heater casing wall was modelled as a fixed temperature boundary condition, varying linearly from $T_{h,top}$ down to the linear average of $T_{h,bot}$ and $T_{r,top}$. As an estimate of the model-converged engine metal and gas temperatures, the measured temperature profile through the casing wall (from $T_{r,top}$ to T_k) was used as model initialisation temperatures, and so was T_{bs} as an estimate of the backspace gas temperature. The cooling water inlet temperature $T_{w,i}$ and its 5.5 L/min flow rate were specified as fixed boundary conditions.

Figure 7.16 (a) shows the displacer and piston oscillating self-sustainingly over strokes of 23.6 mm and 24.7 mm respectively, at an operating frequency of 30.1 Hz, with the piston lagging behind the displacer by nearly 74°. As was shown in Figure 7.14, the piston collides with the engine main body during every compression stroke. Aside from not predicting piston-casing collisions, the modelled displacements are in good agreement with the experiment. In comparing (a) to (b) it may be calculated that the peak piston displacement lags 128° behind the peak in pressure swing, and that the displacer stoke lags 54° behind the peak in pressure swing denoted as phase differences β and α. The expansion space pressure swing in Figure 7.16 (b) is in reasonable agreement to that of the experiment, despite being over-predicted by 22.7 % for reasons that have previously been discussed in Chapter 7.3.3. With reference to (a), the model's over-estimation of the peak pressure swing is consistent with a slight deviation between the simulated and measured piston phases. The model's over-prediction of the workspace pressure swing leads to an over-prediction in simulated expansion and compression space boundary work, as seen from the PV curves in Figure 7.16 (c) and (d). The experimental expansion and compression space work rates are calculated as being 288.4 W and 164.0 W respectively. Consequently, the experiment yields a net positive indicated power of 124.4 W, whereas the simulation is more conservative at 141.2 W. As no electrical power is being extracted by the linear generator, it is deduced that this 124 W of indicated power is being dissipated to irreversible engine losses, mainly being mechanical friction losses, generator core losses and aerodynamic dissipation losses.

From trial-and-error it was found that the piston mechanical friction could reasonably be accounted for by simulating a 40 N s/m viscous damping load as acting on the piston. This damping load is nearly 20 % lower than that which was identified from Chapter 7.1 and simulated in the preceding subsection for displacer-driven operation. This reduction in friction can possibly be attributed to the formation of a lubricating *piston dynamic gas cushion* that is induced between the piston wall and bore cylinder wall by gas leakage. As gas leakage is proportional to the difference of the pressures squared, is postulated that this gas-lubricating-effect becomes more effective at increased piston strokes and charge pressures. Another explanation to the decreased friction may be that the magnetic piston side-load forces, that led to the large piston mechanical friction in the first place, are simply not linear over the nearly 25 mm piston stroke and consequently, a reduced damping friction coefficient more accurately emulates the experiment. These hypotheses could further be investigated in a follow-up study on decreasing the piston-mechanical friction forces.

The open-circuit terminal voltage shown in Figure 7.16 (e) is also in good agreement with the simulation results. The model appears capable of even predicting the distinctive inflexion point that occurs near the zero voltage cross-over. This open-circuit voltage, also known as the generator induced emf, is slightly larger than that predicted in Figure 7.6 (a) due to the increased piston stroke. As with the open-circuited case of Test Run 3, the simulated generator voltage is slightly over-predicted and is leading the experimental results in phase. This is attributed to inductive core-loss effects not accurately emulated by the model.

Test Run 5: One ohm loaded operation

By electrically loading the generator, the piston peak-to-peak stroke is reduced from 24.7 mm under open-circuited operation to 24.1 mm in closed-circuited operation, whilst the piston-displacer phase difference θ remains nearly unchanged at 73°, as seen from Figure 7.17 (a). The displacer stroke has increased from 23.6 mm to 24.2 mm in closed-circuit operation due to the increase in workspace pressure swing, as seen from Figure 7.17 (b). However, from Figure 7.17 (a), it is calculated that the model under-predicts the piston stroke by nearly 9 % and consequently, the model fails to predict the piston colliding with the engine main body at a displacement amplitude of −12 mm. It is postulated that this under-prediction of the model may be attributed to the numerical model in fact emulating engine operation as being at thermodynamic steady-state, whereas in the experiment, this is not the case. It is argued that, could operation be sustained for a longer period at the specified hot-end temperature, the experiment would ultimately approach the numerical solution.

In Figure 7.17 (b) the expansion space and backspace pressure swings are depicted. The experiment shows the expansion space pressure swing to be increasing-and-decreasing periodically, whilst the backspace pressure is nearly indistinguishable from the model. This periodic variation in pressure swing is induced by the piston colliding with the *engine main body* during the compression stroke. The metal-on-metal collisions 'bounce' the piston away from the main body wall, inducing a slight increase in piston frequency and decrease in piston-displacer phase difference θ directly after the occurrence of such a collision. Consequently, this reduction in piston-displacer phase difference decreases the peak-to-peak variation in workspace pressure, as less boundary work is done by the engine. Piston over-stroking is especially pronounced during the initial engine start-up transience – as illustrated in Figure 7.14 – when the temperature gradient between hot and cold end is large. But despite these periodic piston collisions, the PV curves in Figure 7.17 (c) and (d) are generally in good agreement with that of the experiment. It is, however, by coincidence that the experimental indicated power of 152.9 W is nearly identical to the simulated 152.1 W, since the volume and pressure variations are not the same.

From Figure 7.17 (e) it is seen that the simulated load voltage and generator current are in good agreement with that of the experiment. The 10 V load voltage is noticeably reduced from the induced emf shown in Figure 7.16 (e); this voltage reduction is attributed to the coil's reactance. The peak simulated load power given in Figure 7.17 (f) is also in reasonable agreement with the experimentally measured output power, despite being over-predicted by 13.1 %. The engine delivers on average 24.2 W electrical power. This power delivery is in accordance with the 28.5 W increase in net indicated above open-circuit operation. It must further be noted that the experimental load power indicates a linear 'ramp-up' in power output, from approximately 65 W up to 76 W over a period of four power strokes. This ramp-up period suggests that the piston collides with the engine casing only during every second engine cycle, correlating to the periodic decrease in workspace pressure swing in (b) that is seen to occur every second engine cycle.

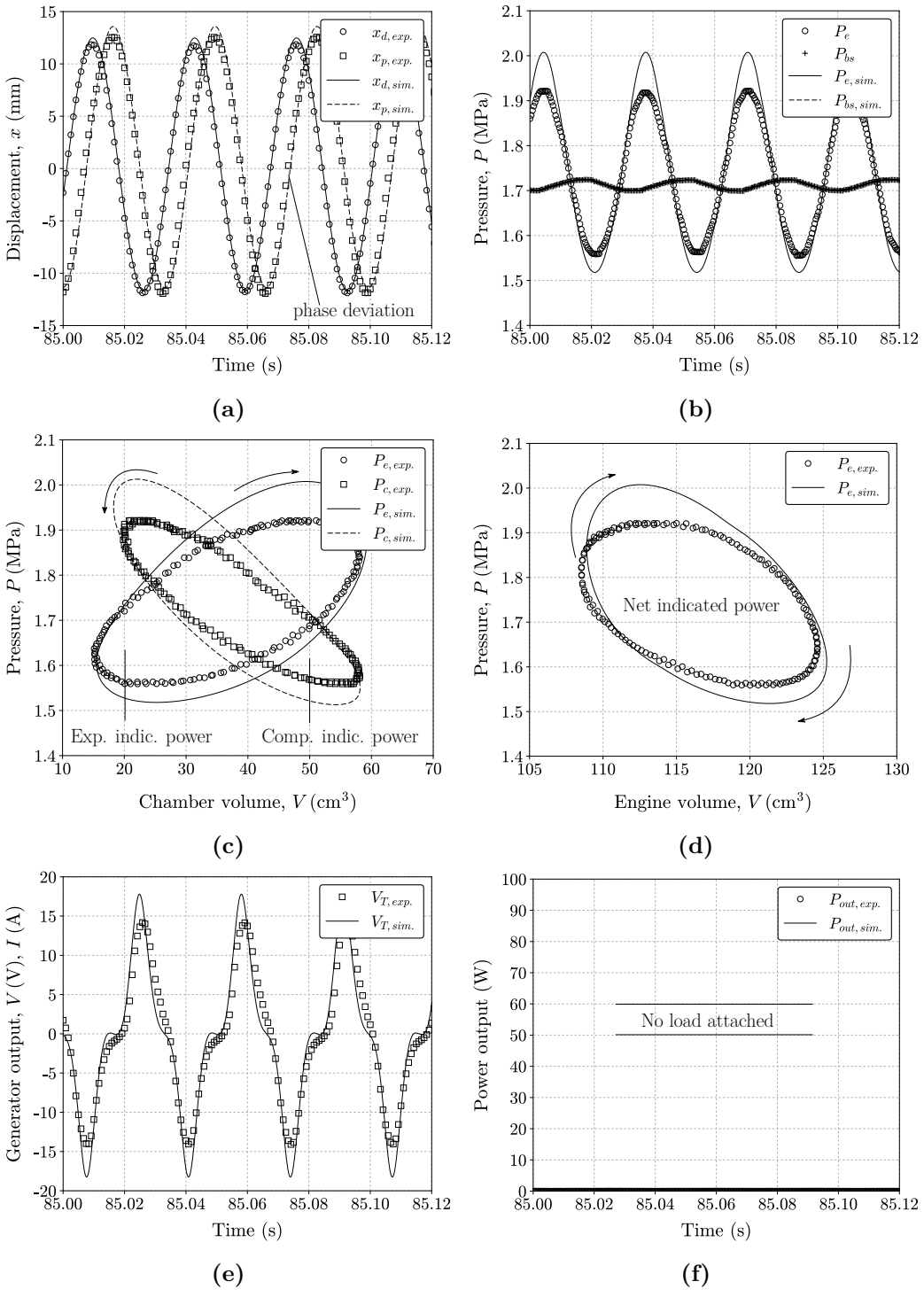

Figure 7.16: Experimental and simulated results for the open-circuit condition of Test Run 5, showing (a) displacement over time, (b) pressure over time, (c) pressure versus chamber volume, (d) pressure versus engine workspace volume, (e) generator terminal voltage over time and (f) electrical power output over time

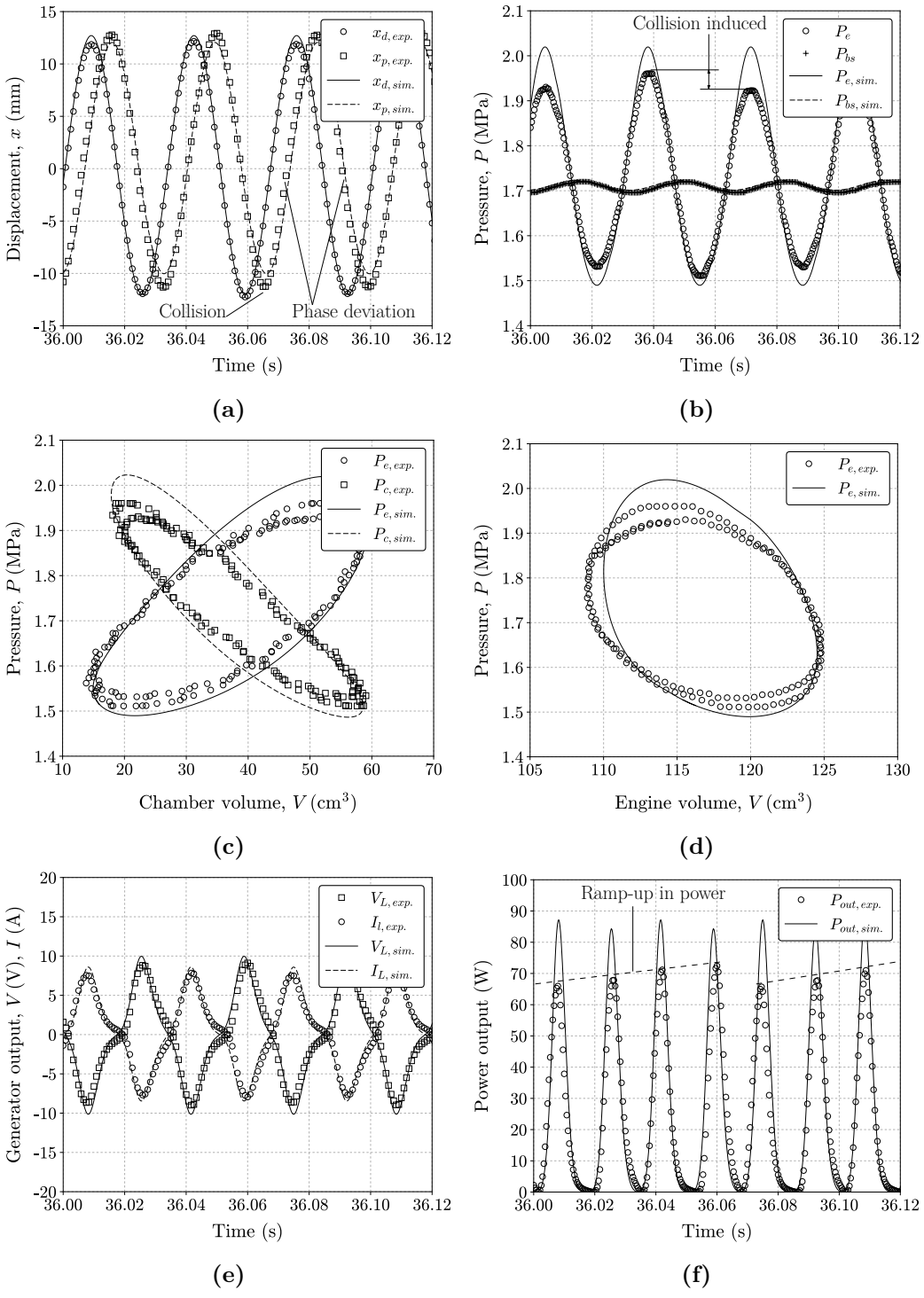

Figure 7.17: Experimental and simulated results for the 1 Ω load condition of Test Run 5, showing (a) displacement over time, (b) pressure over time, (c) pressure versus chamber volume, (d) pressure versus engine workspace volume, (e) generator output over time and (f) electrical power output over time

Test Run 6: One ohm loaded operation

By increasing the heater temperature to 550 °C, generator electrical-loaded operation could be sustained for up to nearly three minutes at a time. This is in contrast to the barely one minute of loaded operation shown in Test Run 5. But apart from being able to sustain operation for longer, the overall engine performance was found to be very similar to that of Test Run 5, mainly due to the mechanical limitation on the power piston displacement amplitude at −12 mm.

Figure 7.18 (a) shows graphs of displacement, pressure, voltage and load power output for the self-sustained, 1 Ω loaded operation of Test Run 6. The increase in hot-end temperature over Test Run 5 has not only induced an increase in the displacer and piston strokes, to 25.8 mm and 25.1 mm respectively, but a decrease in the average piston-displacer phase lag to 63.5°. In fact, due to piston-casing collisions, the piston-displacer phase difference varies from 58° to 71°. As with Test Run 5, the simulation fails to predict these piston-casing collisions due to simulating thermodynamic steady-state operation, whereas the experimental results presented are in reality closer to engine start-up transience. As a consequence of the model under-predicting the piston stroke, the modelled results do not show a periodic increase-and-decrease in workspace pressure swing in (b), as this phenomenon is induced by an increase in piston frequency (and decrease in piston-displacer phase difference) directly after the occurrence of a collision. Furthermore, in comparing (a) to (b), it is noted that the pressure-piston phase difference α is varying from 113 to 121°. This is a direct result of the piston collisions with the engine main body.

From Figure 7.18 (c) it is should be noted how the modelled over-prediction in workspace pressure leads to a large over-prediction in the expansion and compression space pressure-volume diagrams. In fact, from the experiment, it is calculated that the engine delivers 319 W on indicated power in expanding the working fluid, whereas 157 W of indicated power is required to compress the working fluid. This leads to a net positive indicated power of 162 W, as is visually depicted in (d), whereas the model predicts 176 W. The piston collisions also contribute to the experimental indicated power being smaller, as the collisions reduce the piston-displacer phase difference and thereby inducing the growing-shrinking pressure swings. But despite these notable over-predictions of the model, the general shapes of the simulated PV curves of both (c) and (d) appear to be in reasonable agreement to the experiment.

The modelled load voltage and current profiles shown in Figure 7.18 (e) appear to correlate well with the experiment, despite the model over-predicting the voltage and current by 17 %. This over-prediction in voltage is attributed to the simplifying relation used to model the generator flux linkage that consequently does not consider the widening or flattening of the flux linkage curve in closed-circuited operation. Although the overall voltage and current shapes correlate well with that of the experiment, the over-prediction in voltage and current are compounded in simulating the electrical power output. As shown in (f), the peak simulated load power of 101.3 W over-predicts the experimental result of 72.6 W by nearly 28 %. As with Test Run 5, a four-period ramp-up in experimental load power is observed. This is still indicative of the piston collisions occurring once every second engine cycle.

Test Run 6: Two ohm loaded operation

Figure 7.19 (a) shows that when the load resistance is increased to 2 Ω after approximately a minute into self-sustained operation, the displacer and piston strokes are increased slightly to 26.2 and 25.6 mm respectively. The average piston-displacer phase difference θ has increased to a more steady 72.6°. This increase in phase difference over 1 Ω loaded operation is attributed to the decrease in temperature difference between hot and cold end over time, as is evident from the temperature measurements given in Table 7.6. The model indicates piston collisions to occur once every two engine cycles at a displacement amplitude of −12 mm, which is in agreement with the experiment. In comparison to 1 Ω loaded operation, despite the engine load being reduced, the actual piston collisions were found to be considerably softer. This is again attributed to the decrease in workspace temperature gradient.

In comparing Figure 7.19 (a) and (b) it is calculated that the experimental pressure swing is leading the displacer by 49° and the piston by 122°. From (b) it is seen that the simulated and experimentally measured pressure swings are in reasonable agreement despite the model over-predicting the peak-to-peak variation by 24 % for reasons that have been discussed. Both the simulated and measured workspace pressure plots show a significantly smaller periodic variation in pressure swing than that of the one ohm loaded case. This is consistent with the less severe piston-casing collisions that do not significantly influence the piston's phasing and consequently, the measured and simulated piston phases are in good agreement. From the PV diagram in Figure 7.19 (c), it is calculated that the expansion space delivers 347 W in expanding the working gas, whereas the compression space exerts 190 W onto the gas to compress it. Consequently, the engine it is calculated to deliver 157 W of net indicated power, whereas the model estimates a more conservative net indicated power of 187 W due to the over-estimation in pressure swing. The simulated PV curve in Figure 7.19 (d), that represents the total engine pressure-volume diagram, is also seen to be in good agreement with the experiment.

Figure 7.19 (e) shows that the simulated load voltage and current are also in good agreement with the experiment. The increase in load resistance has led to the generator current being reduced to approximately 5 A peak and an increase in the generator terminal voltage to above 10 V. In Figure 7.19 (f) the simulated electrical load power is compared to the experimental load power. The model is over-predictive of the peak load power by nearly 37 %. When averaged over the engine cycle period, the experimental FPSE delivers 18.8 W to the electrical load whereas the model is over-predictive at 25.7 W. Moreover, when compared to that of the 1 Ω loaded case, it is calculated that the engine delivers on average 5 W less electrical power. This is consistent with the decrease in net indicated power between the tests.

Test Run 7: Overview

In Test Run 7 the engine was operated at its physical design limits: that is at a maximum attainable hot-end temperature of 580 °C and maximum permissible charge pressure of 1.80 MPa, using helium as the working fluid. In contrast to Test Runs 5 and 6, engine operation could be sustained for nearly six minutes before the casing wall adjacent to the heater bottom wall, $T_{r,top}$, declined to below 380 °C and

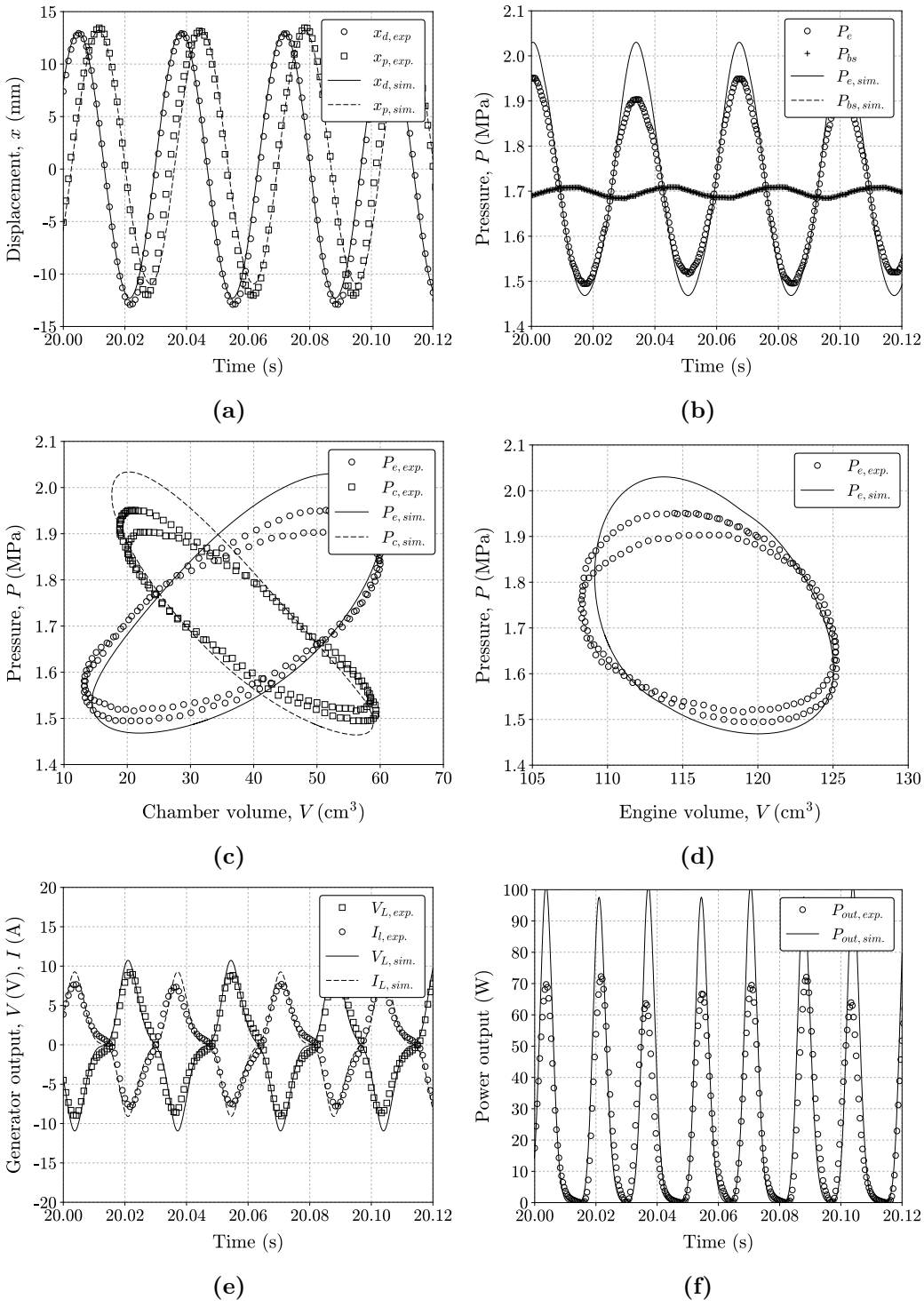

Figure 7.18: Experimental and simulated results for the 1 Ω load condition of Test Run 6, showing (a) displacement over time, (b) pressure over time, (c) pressure versus chamber volume, (d) pressure versus engine workspace volume, (e) generator output over time and (f) electrical power output over time

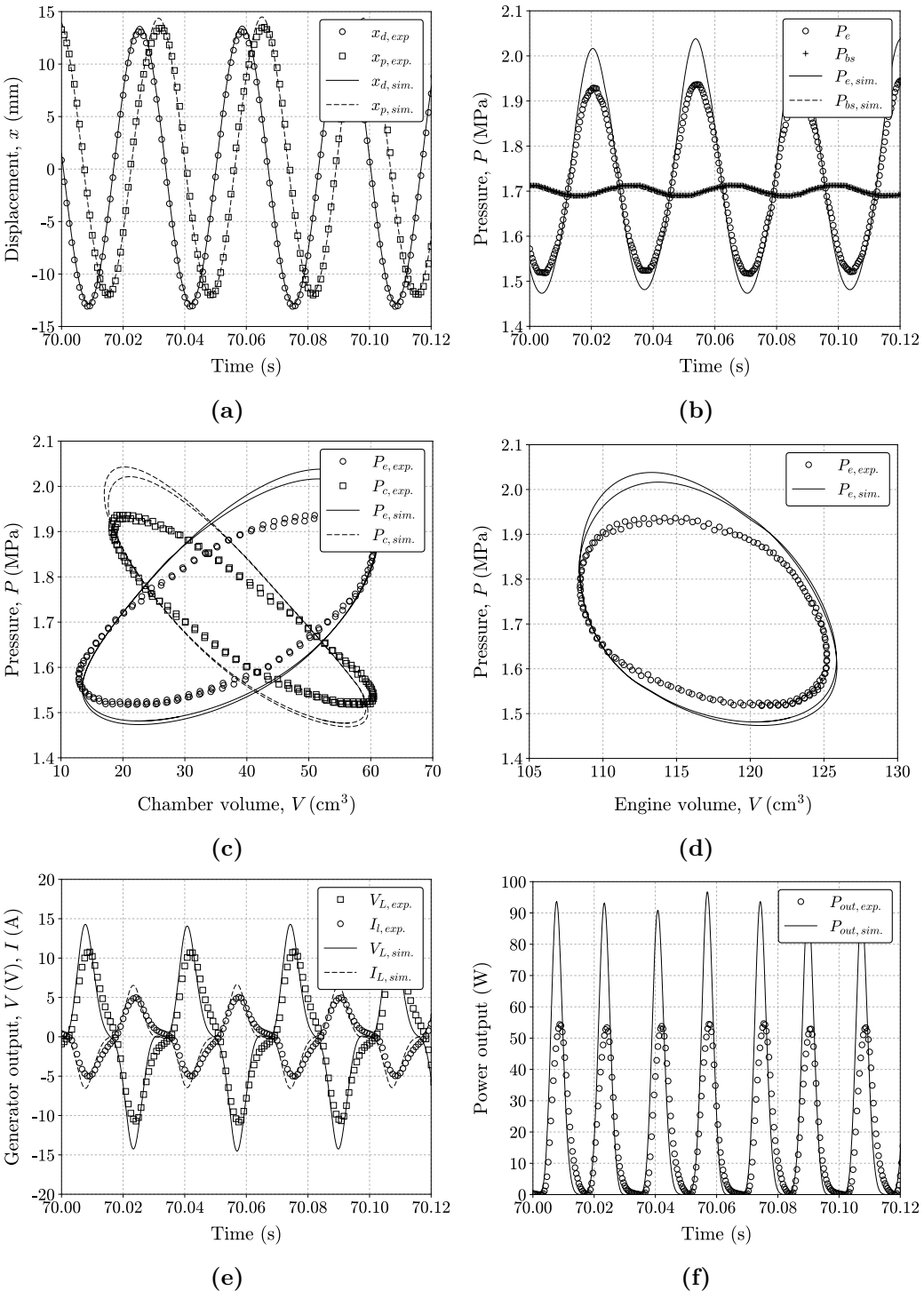

Figure 7.19: Experimental and simulated results for the 2 Ω load condition of Test Run 6, showing (a) displacement over time, (b) pressure over time, (c) pressure versus chamber volume, (d) pressure versus engine workspace volume, (e) generator output over time and (f) electrical power output over time

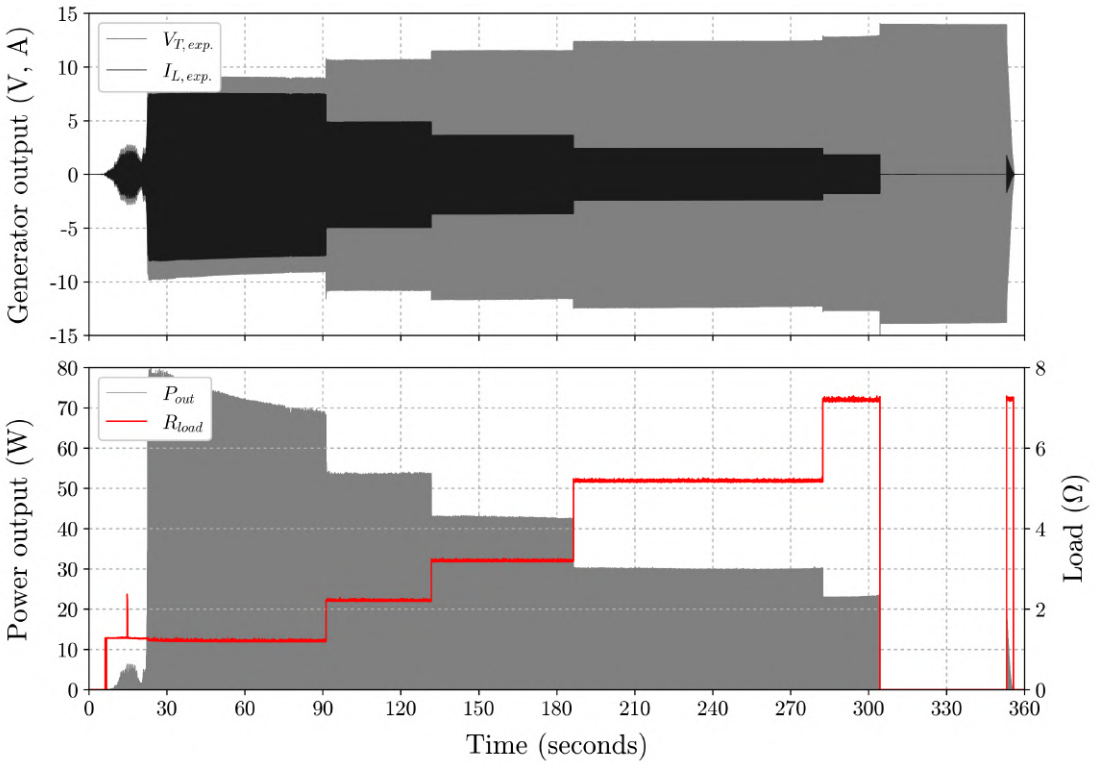

Figure 7.20: Generator voltage, load current and peak electrical power output for the self-sustained operation of Test Run 7

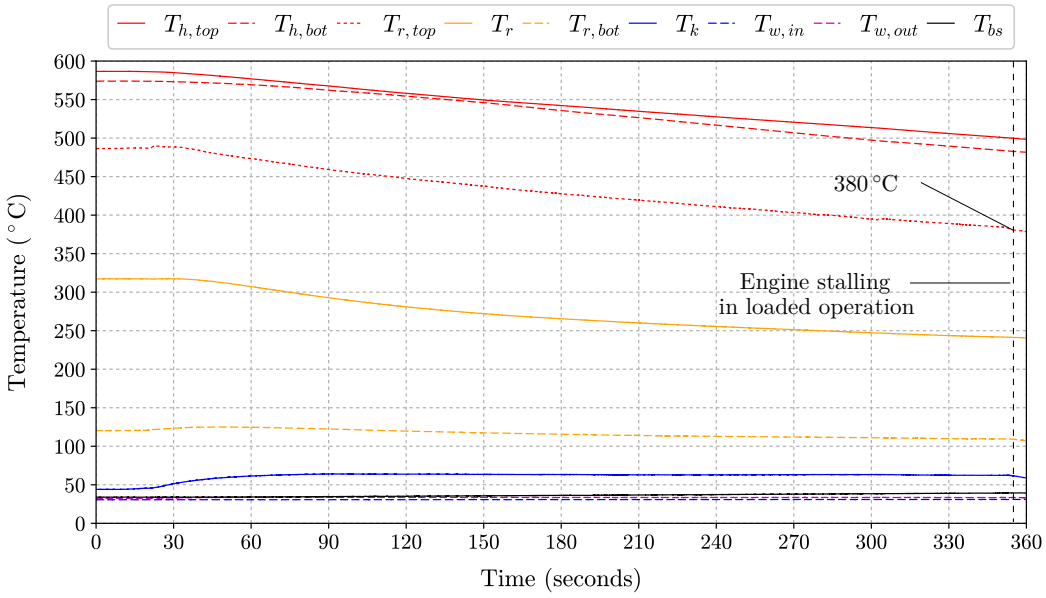

Figure 7.21: Engine temperatures measurements of Test Run 7, showing a decline in casing wall temperature over time

stalling occurred, as is shown from Figures 7.20 and 7.21. This apparent temperature limitation to self-sustained operation is in good agreement with the 365 °C limiting temperature previously seen from Figure 7.15, in which stalling occurred under open-circuited operation. Moreover, the temperature measurements show an approximately linear decline in hot side temperature, with the heater top decreasing from 580 °C to 500 °C at an average rate of 20 °C per minute. This notable decline highlights the inadequacy of the electrical heater to sustain the specified set-point temperature. The water cooling jacket maintains a nearly constant cold-end temperature T_k of 62 °C, rejecting heat at a significant rate of 1150 W to the water.

It must be emphasised that *only* in Test Run 7 could generator-loaded engine operation be sustained for longer than five minutes at a time. However, operating the engine at this most elevated temperature and charge pressure conditions resulted in more violent piston collisions that not only led to the destruction of the strain gauge sensors, but ultimately, mechanical failure of the piston flexure spring.

Test Run 7: One ohm loaded operation

Figure 7.22 shows the graphs of displacement, pressure, voltage and load power output for the self-sustained operation of Test Run 7 with a 1 Ω load attached across the generator terminals. In comparison to Test Run 5, from (a) it is seen that the displacer stroke has remained nearly unchanged at 25.8 mm, whereas the piston stroke has increased from 25.1 mm to 25.9 mm. As with the preceding tests presented the piston collides with the engine main body during every second compression stroke at the −12 mm displacement limitation. Consequently, the piston-displacer phase difference varies from 68° just before an impending collision, to 55° just after the collision, as the metal-on-metal collisions induce an increase in piston reciprocation frequency. In contrast to the periodic collisions encountered in the experiment, the model predicts a uniform piston-displacer phase difference of 68.7° as it is slightly under-predictive of the piston stroke and consequently does not predict collisions.

In comparing (a) to (b) in Figure 7.22 it is calculated that the piston lags the pressure swing by between 103 and 119° – the smaller phase lag correlating to when the piston is reciprocating at the slightly increased frequency. As with the preceding tests, the increased piston frequency induced by engine collisions periodically reduces the piston-displacer phase difference and peak-to-peak workspace pressure swing in (b). The model over-predicts the peak pressure swing by 16 % for reasons that have been discussed, leading to over-predictions in expansion and compression boundary work. From the PV curves in Figure 7.22 (c) it is calculated that 344 W of indicated power is delivered in expanding the working fluid, whilst compressing it requires 178 W. Consequently, the engine delivers a net positive indicated power of 165 W, as is represented by the encapsulating area of the total workspace PV diagram in (d) if the viscous dissipative losses in the engine heat exchangers are assumed negligible (i.e. if the expansion and compression space pressures are assumed equal). The PV diagrams from both (c) and (d) are remarkably similar to that presented in Test Runs 5 and 6, despite the curves being shifted upwards by 0.1 MPa. The measured generator voltage and load current depicted in Figure 7.22 (e) are also in good agreement with the simulation results, both appearing nearly indistinguishable from

that of Test Runs 5 and 6. In Figure 7.22 (f) it is seen that the generator delivers a peak electrical power of 73 W, closely resembling the power delivered in Test Runs 5 and 6. The linear 'ramp-up' in output power confirms that the piston collides with the main body only once every second engine cycle. From the experiment, an average electrical power output of 24.1 W is calculated, whereas the model suggests that on average, 31.6 W of electrical load power is being delivered.

Test Run 7: Two ohm loaded operation

In Figure 7.23 graphs are given of displacement, pressure, voltage and load power for the self-sustained 2 Ω loaded engine operation. Although having increased the load resistance two-fold, the experimentally measured displacer and piston strokes in (a) have remained nearly unchanged from 1 Ω loaded operation. However, at the reduced load, the model predicts piston casing collisions to occur once every second cycle at a displacement amplitude of −12 mm. In contrast to the model, from the experiment, the piston collisions were found to be more steady and occurring once during *every* engine cycle, with the actual piston-displacer phase difference increasing slightly to a steady 67.7°. The more steady nature of the engine is confirmed from the measured expansion space pressure swing in (b) that is varying cyclically – but only very slightly. As the piston collides with the casing wall once during every cycle, the piston-displacer phase difference is not varying cyclically over two engine cycles as was the case with one ohm loaded operation.

In Figure 7.23 (b) the influence piston collisions have on the engine workspace pressure swing should be noted. The piston collisions occurring once during every compression stroke is consistent with the lowered peak-to-peak pressure swing if the results are compared to that of 1 Ω loaded operation. This lowered, more steady swing in pressure is attributed to the piston-displacer phase lag being steady at 68°. This is in contrast to Figure 7.22 (b), where the cyclic piston collisions led to the piston-displacer phase difference varying between 55 and 68°. The model over-predicts the peak-to-peak swing in pressure by 24 % – with the maximum over-prediction being consistent to a slight deviation between modelled and measured piston phase. From the PV diagram in Figure 7.23 (c) it is calculated that the experimental engine delivers 348 W of indicated power in expanding the working fluid, whilst requiring 192 W to compress it. This amounts to a net positive indicated power of 155 W. The simulation predicts 187 W; this deviation being attributed to the over-estimation in workspace pressure swing, as seen from (d). Also in good agreement are the simulated and measured load voltage and current profiles shown in Figure 7.23 (e). The model appears to accurately predict the shape of the load voltage curve despite the peak-to-peak voltage variation being over-predicted by 24 %. The model is also over-predictive of the peak electrical output power shown in Figure 7.23 (f) by nearly 40 %. When averaged over the engine cycle, the generator delivers 18.3 W whereas the model predicts 25.7 W; the simulation deviation being 28.6 %. Note that the electrical power delivered in (f) is similar to that delivered under 2 Ω loaded operation in Test Runs 5 and 6. This is mainly due to the piston being limited by the collisions to having approximately the same stroke.

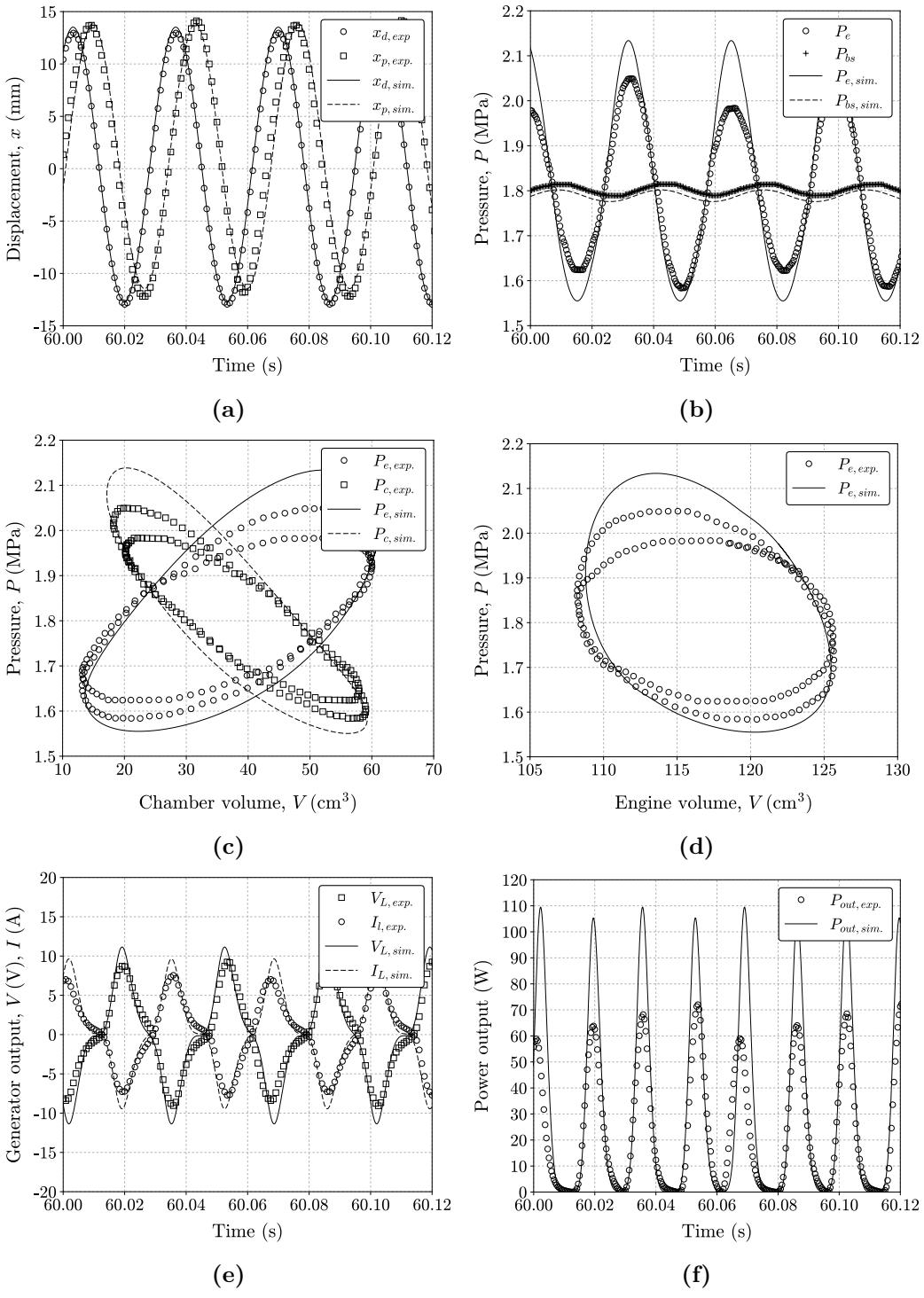

Figure 7.22: Experimental and simulated results for the 1 Ω load condition of Test Run 7, showing (a) displacement over time, (b) pressure over time, (c) pressure versus chamber volume, (d) pressure versus engine workspace volume, (e) generator output over time and (f) electrical power output over time

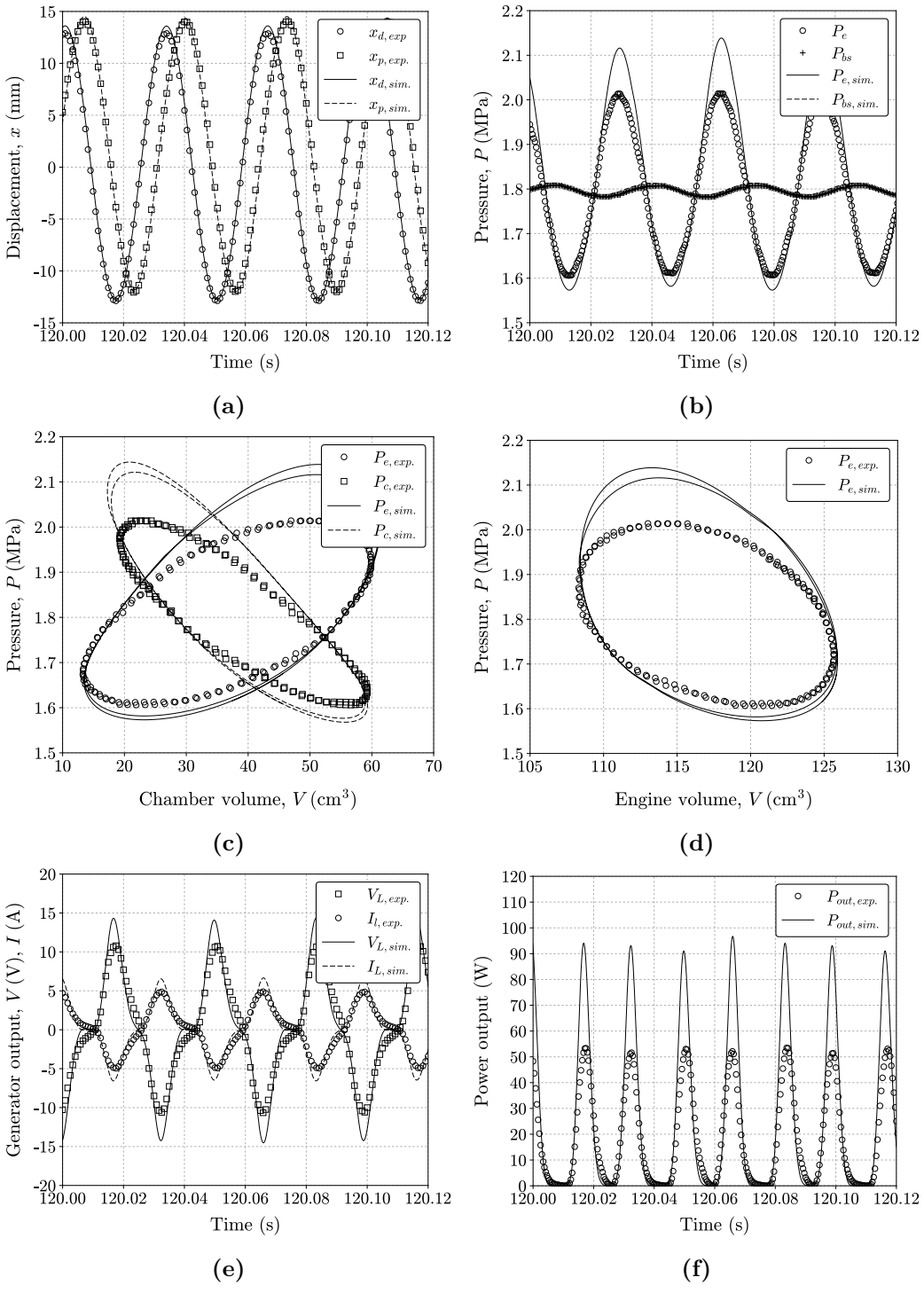

Figure 7.23: Experimental and simulated results for the 2 Ω load condition of Test Run 7, showing (a) displacement over time, (b) pressure over time, (c) pressure versus chamber volume, (d) pressure versus engine workspace volume, (e) generator output over time and (f) electrical power output over time

Summary of results

Experimental testing of the assembled prototype was conducted in two separate test run cases of increasing hot-end temperature, and a third of increased temperature and pressure. Throughout this section, graphical comparisons and discussions relating to two selected load cases have been presented for each of the test runs. In Table 7.7, the main experimental and simulated outcomes are listed. Additionally, the table gives the summarised outcomes of 2 Ω loaded operation of Test Run 5 and the open-circuited results of Test Runs 6 and 7. The simulation deviation percentage, as defined from Equation (7.7), is given in an effort to quantify the agreement that is seen between the experiment and the model.

From Table 7.7 it is noted that the displacer and piston strokes, and the phase difference between them, are generally in good agreement with the experiment. Aside from the 1 Ω loaded operation of Test Run 5, the stroke amplitudes deviate by less than 5 % from the experiment. The open-circuit operation of Test Runs 5 and 6 show a deviation in piston-displacer phase difference θ of up to −16.5 %. The experiment showed the occurrence of piston-casing collisions for all test cases, which were not apparent for all the simulated cases. Piston collisions not only led to an increase in operational frequency, but also a reduction in piston-displacer phase difference and the simulated peak-to-peak workspace pressure swing. A notable finding has been that, in nearly all the test cases presented, the numerical model over-predicted the peak-to-peak pressure swing by between 14 % and 24 %. Due to the deviation in modelled and measured pressure swing, the corresponding expansion and compression space boundary work rates are over-estimated in the range of 24 to 38 % from the experiment. This agreement is nevertheless a considerable improvement over the displacer-driven operation summarised in Table 7.5.

It is postulated that the over-prediction in pressure swing by the model resulted due to the combined effects of simulating larger-than-actual heat transfer rates, not accurately accounting for unmeasured engine deadspace (including the void in the pressure sensor cooling fin and thin-film dome), not considering gas hysteresis effects, and likely, larger-than-simulated engine gas leakages occurring between the workspace and backspace. As a counter argument to the pressure variation being over-predicted by the model, it may also be argued that the experimental pressure variation is, in fact, *under-measured*. This may be a consequence of the thin-film sensors not being sensitive enough to accurately measuring the 30 Hz oscillatory peaks in pressure. However, it must be stated that as the presented sample tests have consistently shown the *lower* pressure swing to be in good agreement with the model, under-performance of the pressure transducers seem less likely. Another contributing factor to the deviation between simulated and measured pressure swing is certainly the slight mismatch in simulated and measured piston phasing during the expanding stroke that directly follows the occurrence of a piston-casing collisions. Although piston-casing collisions further resulted in a slight deviation between simulated and measured piston phase, the general shapes of the PV curves were shown to be in reasonably good agreement with the experiment. This affirms the model's capability of predicting engine thermodynamic performance to a reasonable degree of accuracy, entirely from first principles. However, to confirm whether the model is

over-predicting the pressure variation due to thermodynamic effects not accurately being considered, or whether the experimental pressure swing is in fact slightly under-measured by the sensors and to what degree the piston-casing collisions influence the peak pressure variation, would require additional engine testing (without piston-casing collisions occurring) using more accurate and faster-responding pressure transducers than those that were available to this study.

Relating to the generator electrical output, Table 7.7 shows the simulated and measured load voltage to deviate by between 9 and 24 %, and so does load current (although not listed here). The deviation error in predicting the load voltage and current are compounded in calculating the peak in generator output power, which consequently was over-predicted by between 21.3 and 45.7 %. Still, the per-cycled average power deviated by only 12.0 to 28.6 % from the experiment, suggesting that the real electrical power output curve is slightly wider and flatter than that which was simulated. The model's deviation with the experiment has largely been attributed to magnetic hysteresis and core loss effects in the generator stators that are not considered by the analytical flux linkage relationship used to emulate the induced emf.

Table 7.7: Summary of the principal experimental and simulated results of Test Runs 5, 6 and 7 with the simulation deviation percentage given in brackets

		Displ. stroke [mm]	Piston stroke [mm]	Opp. freq. [Hz]	Phase diff α [°]	Phase diff θ [°]	Pres. (p-p) [kPa]	Volt. (p-p) [V]	Exp: $\dot{W}_e$ [W]	Comp: $\dot{W}_c$ [W]	Ind. power [W]	Peak power [W]	Avg. power [W]
Test Run 5: Set-point = 470 °C, P = 1.70 MPa													
O.C.	Exp.	23.6	24.7	30.1	127.9	73.6	362.2	28.3	288.3	164.0	124.4	–	–
	Sim.	24.2	25.0	30.2	127.4	72.3	468.4	37.0	399.1	257.9	141.2	–	–
	[Dev. %]	[2.4]	[1.2]	[0.1]	[-0.4]	[-1.8]	[22.7]	[23.5]	[27.8]	[36.4]	[11.9]	–	–
1 Ω	Exp.	24.2	24.1	29.9	122.8	73.2	456.9	18.3	301.0	148.1	152.9	75.9	24.2
	Sim.	24.7	22.1	29.9	116.9	72.8	529.8	20.2	375.0	222.9	152.1	87.4	27.4
	[Dev. %]	[2.2]	[-9.2]	[0.1]	[-5.0]	[-0.5]	[13.7]	[9.2]	[19.7]	[33.5]	[-0.5]	[13.1]	[12.0]
2 Ω	Exp.	24.9	24.5	30.0	127.2	74.6	436.4	21.9	326.9	174.4	152.5	57.3	19.6
	Sim.	25.6	23.9	30.0	120.8	72.9	533.1	26.4	416.0	257.2	158.8	78.3	23.3
	[Dev. %]	[2.9]	[-2.5]	[0.2]	[-5.4]	[-2.4]	[18.1]	[16.9]	[21.4]	[32.2]	[3.9]	[26.8]	[16.0]
Test Run 6: Set-point = 550 °C, P = 1.70 MPa													
O.C.	Exp.	24.6	25.7	30.0	123.4	67.7	391.1	28.8	291.6	158.4	133.2	–	–
	Sim.	25.0	26.6	30.3	113.0	58.1	454.6	37.0	385.7	223.9	161.8	–	–
	[Dev. %]	[1.5]	[3.4]	[0.8]	[-9.2]	[-16.5]	[14.0]	[22.1]	[24.4]	[29.2]	[17.7]	–	–
1 Ω	Exp.	25.8	25.1	29.9	116.0	63.5	456.9	17.9	318.7	156.6	162.0	72.6	23.8
	Sim.	25.4	24.2	29.9	117.4	71.1	562.8	21.7	422.6	246.6	176.0	101.3	30.2
	[Dev. %]	[-1.7]	[-3.9]	[0.2]	[1.1]	[10.7]	[18.8]	[17.3]	[24.6]	[36.5]	[7.9]	[28.3]	[21.3]
2 Ω	Exp.	26.2	25.6	30.0	121.8	72.6	421.5	21.6	346.7	189.6	157.0	56.9	18.8
	Sim.	26.5	26.5	30.0	118.9	67.4	533.6	28.6	471.3	275.4	186.9	90.1	25.7
	[Dev. %]	[1.0]	[3.5]	[0.2]	[-2.4]	[-7.8]	[21.0]	[24.3]	[26.4]	[31.2]	[16.0]	[36.9]	[26.9]
Test Run 7: Set-point = 600 °C, P = 1.80 MPa													
O.C.	Exp.	25.2	25.3	30.1	129.4	72.3	404.3	28.3	306.5	168.3	138.2	–	–
	Sim.	25.1	26.4	30.2	123.5	65.3	476.8	37.3	425.4	270.3	155.3	–	–
	[Dev. %]	[-0.5]	[4.0]	[0.5]	[-4.8]	[-10.8]	[15.2]	[24.0]	[27.9]	[37.7]	[11.0]	–	–
1 Ω	Exp.	25.8	25.9	30.0	110.0	60.2	467.1	18.2	343.5	178.4	165.0	72.5	24.1
	Sim.	26.2	25.3	30.0	116.4	68.7	557.6	22.2	468.6	279.1	189.5	109.7	31.6
	[Dev. %]	[1.6]	[-2.6]	[-0.1]	[4.7]	[12.4]	[16.2]	[18.4]	[26.7]	[36.1]	[12.9]	[33.9]	[23.8]
2 Ω	Exp.	25.7	26.0	30.0	119.1	67.7	407.2	21.7	347.5	192.9	154.6	54.8	18.3
	Sim.	26.4	26.3	30.1	116.7	65.9	535.1	28.5	471.9	284.7	187.1	93.4	25.7
	[Dev. %]	[2.4]	[1.2]	[0.3]	[-2.0]	[-2.8]	[23.9]	[24.0]	[26.4]	[32.2]	[17.4]	[41.3]	[28.6]]

7.4. Operating limitations and design improvements

The chapter is concluded with a discussion pertaining to physical limitations encountered during the operation of the engine in a self-sustaining manner. This is followed by suggested design and manufacturing improvements to the existing prototype.

7.4.1. Piston and displacer friction

Mechanical contact friction between the piston and its bore has been identified as a significant operating obstacle to self-sustained operation. This *dry-sliding contact friction* is induced by strong magnetic side-load forces acting between the magnet plunger and the generator stators that, in effect, pull the piston 'skew' within its bore. It is hypothesised that the large mechanical friction acting on the power piston is the primary reason why self-sustained operation could not be achieved indefinitely, as was envisaged in Chapter 5. However, Test Run 5 indicated that by increasing the average charge pressure to 1.70 MPa absolute, self-sustaining engine operation could temporarily be maintained with both open- and closed-circuited loading conditions. By first operating the engine in an open-circuited generator condition, the irreversible engine losses were estimated from the net indicated power to be in the range of 120 W to 140 W. From trial-and-error it was estimated that the power piston mechanical friction could be reasonably accurately simplified to a viscous damping coefficient of 40 N s/m. This value is slightly larger at 55 N s/m for smaller piston strokes in displacer-driven operation. It is hypothesised that this decrease in viscous damping may be attributed to the formation of a dynamic gas cushion that is induced by gas leaking back and forth between the piston and cylinder bore. Another explanation might be that the magnetically-induced side load forces are simply not linear as the piston moves through its power stroke.

In Figure 7.24 the scuff marks of mechanical friction are shown to be significant for the displacer and power piston. The displacer shows scuffing along the rim of its dome where the effect of its misalignment is most pronounced. To mitigate displacer and bore cylinder wear it is recommended to further decrease the displacer's diameter along the top dome. In an improved design layout, the two halves of the displacer should be joined nearer to the cold-end (bottom of the displacer) where

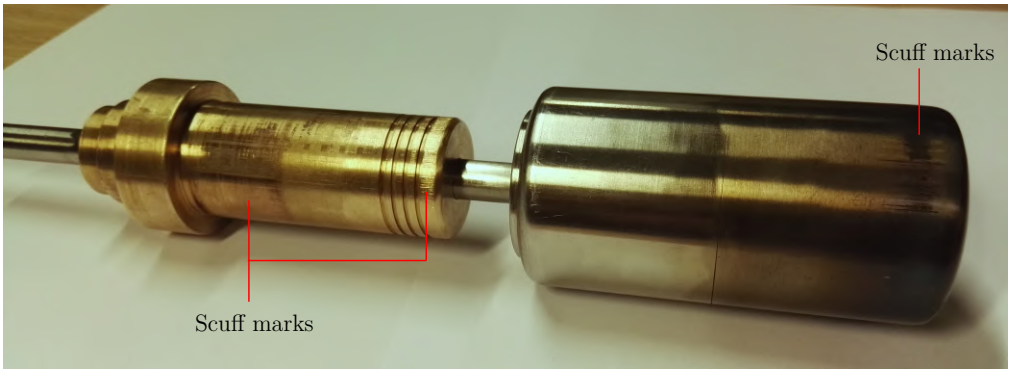

Figure 7.24: Photograph of piston and displacer scuff marks

thermal expansion is less significant. The considerable wear seen on the power piston not only decreased the piston's concentricity, but also led to the formation of small metal particulates that contaminated the sliding surfaces. Mechanical Technology Incorporated (1999) effectively eliminated mechanical friction in their FPSEs by incorporating a static gas bearing system, whereas Sunpower Inc. (2016) and Microgen (2018) employ dynamic gas bearings in their engines. However, for a gas bearing to function, the close-tolerance alignment between the piston, displacer and bores are critically important. To reduce mechanical friction acting on the existing power piston, it is strongly recommended to investigate using an improved, re-manufactured magnet train. This revised magnet train should consist of four radially magnetised *ring magnets* as opposed to the arc-magnets, whose imperfect seating is thought to have induced large magnetic side-load forces. As a secondary improvement, the use of a functional dynamic gas bearing – incorporating an internally-located piston pressure plenum and one-way check valve system – should be investigated.

7.4.2. Heater power delivery and thermal losses

The 1.0 kW electrical heater failed in maintaining the required heat input rate to sustain engine operation above 365 °C, as was shown in Figure 7.15, and consequently, self-sustained engine operation could not be maintained indefinitely. This failure of the heater to sustain the specified hot-end temperatures is largely attributed to considerable parasitic heat losses that exist in the engine metal sections. The heater performance test given in Appendix F revealed that in the order of 360 W of thermal power is lost to the cooling jacket via axial conduction in the casing wall. Additionally, it has been estimated that in the order of 200 W of heat is conducted axially from heater side to cooler water via the engine bore cylinder, if a set-point temperature of 600 °C is to be maintained. These findings suggest that, even in the most idealised case of having a perfectly insulated heater head, a limited amount of 440 W of heating power would remain to thermally expand the working fluid.

From a post-experimental investigation of the engine internals it was revealed that the copper heater fins, shown in Figure 6.6, have become thermally shrunk to the main body cylinder. The top section of the engine pressure casing has also become thermally deformed with the internal diameter being enlarged by between 10 and 30 µm. This deformation in both the heating fins and the engine casing is considered to have severely increased the thermal contact resistance between pressure casing wall and the outer wall of the internal heating fin, thereby limiting the heat transfer rate to the working fluid. It is argued that this increased thermal resistance, which is not accounted for by the numerical model, contributes to the lower-than-simulated experimental pressure swing that has been observed in all sample test runs. Test Runs five through seven proved that self-sustained operation of the prototype could be obtained. However, self-sustained operation could generally only be sustained in the order of two to six minutes due to insufficient output power from the electrical heater. It is apparent that, in order to sustain engine temperatures above 500 °C (using the existing heater design), the axial conductive heat losses in the engine casing and bore cylinder walls must be reduced. This could either be accomplished by reducing the pressure casing and bore cylinder wall thicknesses, fabricating these

components from less conductive materials, or elongating the regenerator channel in a revised engine design. For future experimental testing, it may be sensible to investigate using a completely new heater head design, such as the thin-tubed-bundle heat exchanger used by Qnergy (2018) and Qiu *et al.* (2019).

7.4.3. Engine stability and feedback control

Displacer-driven operation in Chapter 7.3.3 showed that the engine is easily induced into a *runaway* condition when the motor driving frequency and engine natural frequency are not matched precisely. From Test Runs five through seven in Chapter 7.3.4 it was seen that, when the engine operated self-sustainingly, the power piston collided with the main body during the compression stroke. By increasing the heater temperature, self-sustaining operation could be sustained for longer. However, when the heater bottom temperature declined below 365 °C, stalling occurred, as was seen in Figure 7.15. In the course of this study, no definite stable operating region could be established where neither collisions nor engine stalling occurs. It may be argued that the experimental prototype is inherently unstable (i.e. it will naturally over-stroke and collide with the engine casing as it fails to reach a stable limit cycle), but since thermodynamic steady-state operation could not be achieved due to the declining heater temperature, this finding may yet be inconclusive.

In all of the test cases presented, the power piston collided with the engine main body during the compression stroke, consequently being limited to a displacement amplitude of −12 mm. It is argued that the piston collisions resulted due to the non-linear *decrease* in opposing magnetic force acting between magnet train and generator stators, as was seen from Figure 4.4 for example. The decrease in magnetic force decreases the piston's equivalent 'spring stiffness' and consequently allows for piston over-stroking. To mitigate these collisions, the piston's physical stroke limits could be increased. However, this would correlate to an enlarged workspace pressure swing which, in turn, would lead to a further increase in the displacer and piston strokes. A more fitting solution to limit this apparent over-stroking could be to introduce an additional non-linear opposing force to act on the piston. This could be achieved by employing mechanical strain hardening springs, or, by using additional generator magnets to exert a 'pull-back' force onto the power piston at the end of its envisaged stroke, as done by Wood *et al.* (2010) and Kim *et al.* (2017) for example. It is further recommended that some form of dynamic engine control strategy be investigated in which either the linear generator, displacer motor or both are subject to feedback control. Such an engine controller should allow for controlled start-up and shutdown of the engine, but could also limit the piston and displacer displacement amplitudes to some pre-defined values for different heat input and loading conditions. In its simplest form, a generator load controller could be used to modulate the load voltage and current-draw to a design-specified range. By varying the generator current and so indirectly influencing the piston electromagnetic load, the piston can be limited to a pre-defined stroke range (Berchowitz *et al.*, 1987). However, before the development of any engine feedback controller be undertaken, it is essential that the preceding operating limitations and design improvements first be addressed and a revised prototype be assembled.

7.5. Summary of findings

Throughout this chapter a series of experimental evaluation tests of the prototype engine were conducted to characterise, refine and verify principal assumptions made in the development of the theoretical simulation model. The main findings of the chapter are briefly summarised in this subsection.

The mechanical friction forces acting on the as-assembled displacer and power piston were investigated from a ring-down free-vibration test. It was found that when the piston was assembled to its magnet train, a considerably large damping force acts on the power piston assembly. For simplicity this damping force has been represented as a form of viscous friction, which was estimated to be in the range of 40 and 55 N s/m depending on the piston stroke and charge pressure. The generator coil inductance was characterised and a performance test of the linear generator was conducted in which the magnet train was forcefully reciprocated. Good correlations between the simulated and experimentally measured load voltage and electrical power output results were shown, thereby validating the linear generator finite element analyses.

The assembled prototype was first operated in a displacer-driven mode of operation but with the magnet train removed. Two sample test runs (denoted Test Runs 1 and 2) were presented and qualitative comparisons were made to simulated results of identical setup parameters. It was found that the engine could not be made to operate self-sustainingly in the absence of the magnet train, as the displacer and piston reciprocated with nearly any phase difference. Thereafter, the engine was operated in a displacer-driven mode of operation with the magnet train included. It was found that engine runaway behaviour would be induced by the continuous excitation of the displacer motor if the charge pressure exceeded 1.4 MPa. This was seen as a result of transient aliasing between the motor excitation voltage and engine natural frequency. Two sample test runs (denoted Test Runs 3 and 4) were conducted at different hot-end temperatures and charge pressures. A qualitative comparison with an equivalent simulation study showed a reasonably good correlation, with the workspace pressure swing typically being over-predicted by between 20 and 30 %.

Three sample test runs (denoted Test Run 5, 6 and 7) were presented of self-sustained engine operation, with heater set-point temperatures ranging from 470 °C to 600 °C and charge pressures between 1.70 and 1.80 MPa. Engine stalling was seen to occur when the casing wall temperature adjacent to the heater bottom declined to below the range of 365 °C to 380 °C. A good qualitative correlation between modelled and experimental test data was shown for selected load conditions. Typically, the model over-predicted the workspace pressure swing by between 14 and 24 % and consequently, the expansion and compression indicated powers were over-predicted. In spite of the operating limitations that were encountered, an overall good correlation was shown across all seven selected engine test run cases. This verifies that the theoretical model is indeed capable of simulating the linked thermodynamic, kinematic and electrodynamic behaviour of a free-piston Stirling engine. Consequently, the theoretical model is deemed validated, with further experimental testing being recommended only *after* the identified operating limitations have been addressed.

8. Concluding remarks and recommendations

The principal objectives of the study were to develop a comprehensive theoretical simulation model, to design and manufacture a testable prototype free-piston Stirling engine electric generator, and to evaluate the performance of the prototype engine – and in doing so, validate the underlying theoretical model. In this chapter, final conclusions are drawn relating to each of the research objectives. Design improvements and recommendations for future work are given to aid with the ongoing development of a task-suited free-piston Stirling engine.

8.1. Derivation and simulation of the theoretical model

In this study, a comprehensive theoretical simulation model was developed from first principles. As has been outlined in Chapter 3, the thermodynamic Stirling cycle was modelled by applying and solving the principles of conservation of mass, momentum and energy for a discretised network of one-dimensional working fluid and metal control volumes. The working fluid thermodynamics, displacer and power piston dynamics, and linear generator electrodynamics simultaneously influence one another. The governing equations of this *linked* system were solved using a fully-explicit numerical method, programmed in Fortran. To simplify modelling the generator electrodynamics, in Chapter 4, the linear electric generator was simulated and characterised in a transient finite element analysis model. The generator model was integrated into the theoretical simulation model by means of generator characteristic functions. By using nano-scale time-steps to apply the momentum equation and by so doing, calculate the fluid velocity profile explicitly, the simulation was capable of even resolving induced sonic stress waves in the working fluid that would typically result from the piston or displacer colliding with the engine casing. A temperature adjusting scheme was employed to accelerate the evolution of the numerical method towards thermodynamic steady-state. This significantly reduced the required computational resources to simulating steady-state operation.

A demonstrative case study of envisaged engine operation has been simulated in which the heater input power is limited to 1.0 kW and the initial charge pressure is set to 1.5 MPa absolute, as was outlined in Chapter 5. The engine metal and gas temperature distribution, and the free-running displacer and piston kinematic behaviour, evolve naturally as model outputs. Under these operating conditions, but with a lower piston damping load force of 30 N s/m, the engine is expected produce a net positive indicated power of 151 W and an average electrical load power of 39 W. The simulation indicates that a significant percentage of the heater input power is rejected to the cooling jacket, thereby leading to a low thermal efficiency of 15.1 %. To increase the net thermal efficiency, it is suggested that a larger amount of boundary work should be extracted from the working fluid, as would be achieved by increasing the power piston swept volume. Due to large mechanical friction, a mechanical efficiency of 54 % was shown, and as a result of large generator core

and ohmic losses, an even lower electrical efficiency of 48 % resulted. Nevertheless, despite these notable losses, the simulation results affirmed that the principal engine design parameters would yield a self-sustaining and operating engine.

8.2. Design and manufacture of an experimental prototype

In Chapter 6 the design and manufacture of a 100 W_e (peak) free-piston Stirling engine electric generator was outlined. An especially unique aspect about the testable engine prototype is that for the first time, an internally located linear electric motor was attached directly to the displacer shaft. Although not operationally proven in the scope of this work, the motor is envisaged as a possible means of providing direct control over the displacer motion in forming part of a feedback control system. The manufacture and assembly of the FPSE was shown to be a complex undertaking, for which the close-tolerance alignment of the piston, displacer and displacer shaft were identified as being critically important. For nearly frictionless reciprocating operation, the design layout of the assembled FPSE requires that the power piston and displacer should both align perfectly within their bores, and that the displacer shaft should align perfectly through the power piston and with the displacer motor. The clearance gap between the displacer and bore must be minimised in order to ensure that the bulk of the working fluid is displaced through the regenerator channel. The amount of working fluid leaking between the power piston and its bore must be minimised without their surfaces actually making contact, so as to minimise gas enthalpy losses to the backspace.

The power piston magnet train was identified to be a design-critical component. Ill-manufacturing of the magnets and assembly thereof into the sleeved magnet plunger resulted in strong, unbalanced magnetic side-load forces. These forces pulled the power piston skew within its bore, thereby inducing large piston-sliding contact friction forces that dissipated a significant amount of mechanical energy during operation. This misalignment of the power piston also induced a misalignment of the displacer shaft, consequently leading to displacer-sliding contact friction. It is deemed critical to reduce the piston mechanical friction, as this friction force is thought to have severely limited self-sustained operation of the prototype. The strain gauges attached to the flexure springs delivered a reliable means of determining the displacer and piston displacements. However, during self-sustained engine operation, uncontrolled displacer and piston collisions with the engine casing led to the destruction of the strain gauge sensors. This should reaffirm the necessity of employing a feedback-based control system for operating the FPSE in a self-sustaining oscillatory state without destructive collisions occurring.

8.3. Experimental evaluation and model validation

Throughout Chapter 7, the free-piston Stirling engine prototype was experimentally evaluated and validated in parts. Firstly, the as-assembled displacer and power piston mechanical friction forces were determined from a free vibration response test. It was concluded that the power piston assembly is subject to a considerably

large friction force resulting from the magnetic side-load force of the magnet train. Secondly, the performance of the linear electric generator was evaluated in the reciprocator test setup shown in Figure 7.4. It was concluded that the experimental and simulated voltage output results are in good agreement, as was shown in Figure 7.5 for example. Thirdly, the assembled FPSE was evaluated under different charge pressures, hot-end temperatures and piston loading conditions. These operational tests were conducted first in a displacer-driven mode. Thereafter, the completely self-sustained operation of the engine prototype was investigated.

To adhere to statutory safety regulations, the static engine charge pressure was limited to 1.80 MPa. A maximum hot-end temperature of 580 °C could be achieved with the 1.0 kW electrical heater, but only after allowing sufficient time for thermal build-up in the heater head. However, during operational testing, this temperature could not be sustained indefinitely due to the large axial heat losses and insufficient power output of the heater. Engine stalling typically occurred when the casing wall temperature adjacent to the heater bottom declined below 365 to 380 °C. Consequently, self-sustained engine operation could not be achieved at a charge pressure of 1.50 MPa and heater temperature of 500 °C, as was initially simulated in Chapter 5. This is also due to the large piston mechanical friction forces. To operate the engine and validate the numerical model at lower heater temperatures and charge pressures, the displacer motor was used to excite induce displacer reciprocation. Self-sustained operation could for a first time be achieved at a heater set-point temperature of 470 °C and charge pressure of 1.70 MPa absolute. When the heater temperature was increased further to nearly 600 °C and the charge pressure to 1.80 MPa, up to six minutes of self-sustained operation could be achieved. The engine delivered a peak electrical power of approximately 73 W or per-cycle average power of 24 W.

Experimental results from seven sample test runs were compared to modelled results based on identical setup parameters. Apart from estimating the assumed viscous damping load acting on the piston by trial-and-error, no effort has been made to 'fine-tune' the model by any form of correction factor. Throughout Chapter 7, qualitative comparisons were made regarding the displacer and piston displacement, expansion space and backspace pressure variation, indicated power and electrical power delivery. It was concluded that the simulation generally over-predicts the pressure variation by between 10 % to 29 % in Test Runs 3 and 4, and by between 14 % to 24 % in Test Runs 5 to 7. From the experiment, it was seen that the piston typically over-stroked its 10 mm displacement amplitude during every second engine cycle and consequently collided with the engine main body during the compression stroke. These physical piston collisions induced a slight increase in piston reciprocation frequency during the following stroke cycle. This slightly reduces the phase difference between displacer and piston, and phase difference between piston and peak pressure swing. As a consequence, the engine volume variation is lowered and so less indicated power is delivered by the engine. Accordingly, the experimental pressure swing is also lower during the following piston stroke. These cyclical deviations in pressure swing induced similar deviations in the engine indicated powers. But despite the general over-predictions in pressure swing the simulated engine displacements, and their phase differences relative to the pressure swing, was shown to

be in good agreement to the experiment, typically deviating by less than ten percentage points from the experiment. Moreover, the simulated load voltage was shown to be in reasonable agreement with the experiment, with typically the peak-to-peak voltage variation being over-predicted by 20 to 24 %.

It was hypothesised that the model could be refined to more accurately predict the pressure variation, by possibly accounting for increased engine dead-space and lower heat transfer rates occurring especially during the Stirling expansion cycle. As a counter argument, it was suggested that the experimental pressure variation measured by the expansion space transducer could also be understated. This could be as a result of sensor range insensitivity, lowered sensor response settling times or even be ascribed to the internally performed signal conditioning on the measurement signal. On the other hand, if the measured pressure is indeed accurate, the good agreement of the simulated engine displacements may be fortuitous as a result of the frictional damping coefficients that were inferred by trial-and-error. Consequently, if the model were to be refined to more accurately match the experimental pressure variation, the assumed frictional damping force acting on the piston should also be reduced. These contrasting arguments could be further investigated in a follow-up study using higher fidelity, temperature-compensated pressure sensors so that the pressure measurements presented in this study can be verified.

Despite some notable differences in amplitude between the simulated and measured pressure peaks, their general shapes were shown to be in good agreement with each other. It is concluded that the numerical model has overall succeeded in emulating the dynamic operational behaviour of the FPSE prototype to a reasonable degree of accuracy and consequently, is deemed validated over the range of parameters tested.

8.4. Final conclusion

As detailed through sections 8.1 to 8.3, it has been shown that the research objectives were realised. The main goal of the study has been achieved, which was to provide a validated, in-depth theoretical simulation model of a free-piston Stirling engine electric generator. It is to the author's best knowledge that, at the time of writing, no other such comprehensive theoretical model was available from published literature. Consequently, this study has presented a significant contribution to the still limited knowledge-base surrounding in-depth modelling and experimental testing of free-piston Stirling engines. It is further postulated that the use of this validated model can indeed be of use as a practical yet powerful design tool by which a more task-suited FPSE may be developed from the ground up.

The study has identified design critical components, complexities and physical limitations that are associated with the manufacture and operation of a working prototype. These limitations should be addressed in order to achieve self-sustained and steady operation of a functional free-piston Stirling engine. The close tolerance alignment between power piston, displacer and bore cylinder is the most critical design and assembly prerequisite to ensuring that near frictionless operation is achieved.

8.5. Future work and recommendations

From the aforementioned discussions, it should be apparent that self-sustained operation of the existing prototype was limited by large axial parasitic heat losses, insufficient output power of the electrical heater, and significant mechanical friction forces acting on the power piston. Moreover, stable engine operation could not be achieved, with the piston over-stroking its 20 mm design-for stroke and so leading to collisions with the engine main body. To improve upon the operational performance of the engine, the following recommendations are made for future work:

- To increase the engine's thermal efficiency and in doing so, possibly allow for longer sustained engine operation, it is deemed critically important to reduce the large axial heat losses in the engine pressure casing and main body cylinder. This could be achieved by reducing the casing and cylinder wall thicknesses; by ensuring that the inside of the heater and cooler fins are not in contact with the main body cylinder; by using less conductive materials for the engine metal casing; by elongating the distance between heater and cooler, or even; by developing a completely new heater that is based on a thin-tube-bundled heat exchanger. In addition to decreasing parasitic heat losses, it is recommended that a more powerful electrical cartridge heater be installed to replace the existing 1.0 kW ceramic jacket heater which, by design, is limited to having a 6 W/cm^2 power density. The electrical cartridge heater could be interfaced with the existing heater controller.
- It has been identified as critically important to reduce the large mechanical friction that acts most prominently on the power piston. To do so it was recommended that the 32 individual arc-shaped magnets be replaced with four radially magnetised ring magnets, as imperfect alignment of these magnets into the sleeved magnet plunger resulted in large magnetic side-load forces. As an additional recommendation to decreasing power piston mechanical friction, the study recommends investigating the use of a dynamic gas bearing system. This investigation could form the scope of an entire stand-alone study in which the design, numerical simulation and experimental characterisation of such a gas lubricating piston must ultimately be accomplished. This newly developed theory and insight gained into the functioning of a dynamic gas bearing system would be a welcomed addition to the theoretical simulation model.
- From the generator finite element analysis performed in Chapter 4, it was suggested that large ohmic losses and the inner generator stator becoming magnetically saturated are primarily responsible for the low mechanical-to-electrical efficiency of approximately 50 %. A redesign of the linear generator is consequently recommended so that these significant losses may be reduced. It is recommended that the newly designed generator should exhibit a non-linear magnetic 'pull-back' force on the power piston so that over-stroking can be magnetically limited to an envisaged stroke amplitude.
- In addition to the redesigned generator, this study strongly recommends that a feedback control system be developed to ensure the continual steady operation of the engine (without collisions occurring). This controller may either be

based on directly influencing the displacer motion, by use of the included displacer motor, or by performing active generator load control. Furthermore, the controller could be based on a multi-input-multi-output strategy – using the hot-end temperature, charge pressure, displacer and piston motions and generator output as input parameters to effectively control the generator current. Additionally, a current-feedback controller may be employed for the displacer motor to also limit or influence the displacer motor. These considerations can make for a complete stand-alone study using the experimental engine that was delivered in this study engine.

- Only when the aforementioned design improvements and recommendations have been addressed should additional experimental testing be conducted. To reaffirm whether the numerical model is over-predicting the pressure variation – as has been hypothesised in this study – or whether the workspace pressure variation is slightly under-measured, it is recommended that the use of quicker-responding piezoelectric pressure transducers be investigated. Furthermore, it is recommended that future experimental testing efforts be aimed at achieving longer, self-sustaining steady-state operation.

Pertaining to the theoretical simulation model developed throughout this work, two follow-up studies are recommended:

- Firstly, although the numerical model has verified that it is indeed capable of emulating FPSE operational dynamics from first principles, it is recommended that the validity of the model be extended beyond the scope of the existing prototype. Engine design parameters and experimental test data derived from the Sunpower's RE-1000 and General Motor's GPU-3 kinematic Stirling engine could, for example, be used accordingly as input parameters to the numerical model. These engines could then be studied in a 'reverse engineering' approach using the as-developed model. Alternatively, Stellenbosch University's recently acquired 1.0 kW_e dish-Stirling engine based on the Microgen FPSE architecture could be deconstructed, experimentally characterised, and the lab-based operation of the engine numerically simulated with and without employing engine load control. By reconfiguring this existing off-the-shelf engine into a lab-based unit with controlled heating and loading, validation of the numerical model could be extended to Microgen's engine.
- Secondly, after having proven the model's fidelity beyond the existing prototype, it is recommended that a comprehensive parametric study be undertaken of geometrical design considerations so that a more *optimised* and task-suited engine be developed. It is recommended that the design-study of a larger-output engine should start with the development of the linear generator. Only when the linear generator has been characterised and designed should the numerical simulation model be employed as a design tool to further investigate and refine the engine geometrical considerations. The experimental insight gained and documented throughout this study should be considered as a guide towards developing a second-revision prototype.

List of References

Alger, D.L. (1988). Component Improvement of Free-Piston Stirling Engine Key Technology for Space Power. In: *4th International Conference on Stirling Engines*. National Aeronautics and Space Administration, Japan.

Anderson, S.K. (2006). *Numerical Simulation of Cyclic Thermodynamic Processes*. Ph.D. thesis, Technical University of Denmark, Department of Mechanical Engineering, Denmark.

ANSYS (2017). ANSYS Maxwell. [Online]. Available at: `http://www.ansys.com/products/electronics/ansys-maxwell`, [2017, January 23].

ARPA-E (2019). Sustainable Economic MCHP Stirling (SEMS) Generator. [Online]. Available at: `https://arpa-e.energy.gov/?q=slick-sheet-project/sustainable-economic-mchp-stirling-sems-generator`, [2019, April 4].

Azelio (2019). Azelio Demonstrates Game-Changing Technology for Low Cost Solar Energy Etorage. [Online]. Available at: `https://www.azelio.com/investors/press-releases/2018/azelio-demonstrates-game-changing-technology-for-low-cost-solar-energy-storage/`, [2019, February 6].

Azetsu, A. (1982). The Analysis of Performance of Stirling Engines: 1st Report, Computer Simulation Model. *Bulletin of the Japan Society of Mechanicah Engineers*.

Beale, W.T. (1969). Free Piston Stirling Engines - Some Model Tests and Simulations. *SAE International*.

Benvenuto, G., De Monte, F. and Farina, F. (1990). Dynamic Behaviour Prediction of Free-Piston Stirling Engines. In: *Proceedings of the 25th Intersociety Energy Conversion Engineering Conference*. Nevada, U.S.A.

Berchowitz, D. (1986). *Stirling Cycle Engine Design and Optimisation*. Ph.D. thesis, Faculty of Engineering, University of the Witwatersrand, Johannesburg, South Africa.

Berchowitz, D. (1988). Operational Characteristics of Free-Piston Stirling Engines. In: *23rd Intersociety Energy Conversion Engineering Conference*, vol. 1, pp. 107–112. Denver, Colorado, U.S.A.

Berchowitz, D., Richter, M. and Shade, D. (1987). Development and Performance of a 3 kW(e) Air Charged Free-Piston Stirling Engine with Linear Alternator. In:

22nd Intersociety Energy Conversion Engineering Conference, pp. 1834–1840. American Institute of Aeronautics and Astronautics, Pennsylvania, U.S.A.

Bird, R., Stewart, W. and Lightfoot, E. (2002). *Transport Phenomena*. 2nd edn. John Wiley and Sons Inc., New York, U.S.A. ISBN 0471410772.

Boldea, I. and Nasar, S.A. (1997). *Linear Electric Actuators and Generators*. Cambridge University Press, Cambridge, U.K. ISBN 978-0-521-48017-8.

Boucher, J., Lanzetta, F. and Nika, P. (2007). Optimization of a Dual Free Piston Stirling Engine. *Applied Thermal Engineering*, vol. 27, no. 4, pp. 802–811.

Briggs, M. (2015). *Improving Free-Piston Stirling Engine Power Density*. Ph.D. thesis, Case Western Reserve University, Ohio, U.S.A.

Bulbulia, T. (2018). Swedish stirling signs exclusivity agreement with glencore south africa for clean tech. [Online]. Available at: `https://www.miningweekly.com/article/swedish-stirling-signs-exclusivity-agreement-with-glencore-south-africa-for-clean-tech-2019-07-05/rep_id:3650`, [2019, July 17].

Caballero, G.E.C., Mendoza, L.S., Martinez, A.M., Silva, E.E., Melian, V.R., Venturini, O.J. and del Olmo, O.A. (2017). Optimization of a Dish Stirling System Working with DIR-Type Receiver Using Multi-Objective Techniques. *Applied Energy*, vol. 204, pp. 271 – 286.

Camarinha-Matos, L.M. (2016). Collaborative Smart Ggrids – A Survey on Trends. *Renewable and Sustainable Energy Reviews*, vol. 65, pp. 283–294.

Çengel, Y.A. and Ghajar, A.J. (2011). *Heat and Mass Transfer: Fundamentals and Applications*. 4th edn. McGraw-Hill, New York, U.S.A. ISBN 978-0-07-339818-1.

Chen, N.C.J. and Griffin, F.P. (1983). *A Review of Stirling Engine Mathematical Models*. Oak Ridge National Laboratory, Oak Ridge, Tennessee, U.S.A.

Collins, M. (2019). Snowbasin Resort Partners With Qnergy to Install the "SmartGen," Temote-Power Unit. [Online]. Available at: `https://www.snowbasin.com/blog/snowbasin-resort-partners-with-qnergy-to-install-the-smartgen-remote-power`, [2019, May 5].

Costa, S., Barreno, I., Tutar, M., Esnaola, J. and Barrutia, H. (2015). The Thermal Non-Equilibrium Porous Media Modelling for CFD Study of Woven Wire Matrix of a Stirling Rgenerator. *Energy Conversion and Management*, vol. 89, pp. 473 – 483.

Costa, S., Barrutia, H., Esnaola, J.A. and Tutar, M. (2013). Numerical Study of the Pressure Drop Phenomena in Wound Woven Wire Matrix of a Stirling Regenerator. *Energy Conversion and Management*, vol. 67, pp. 57 – 65.

Costa, S., Tutar, M., Barreno, I., Esnaola, J., Barrutia, H., García, D., González, M. and Prieto, J. (2014). Experimental and Numerical Flow Investigation of Stirling Engine Regenerator. *Energy*, vol. 72, pp. 800 – 812.

Courant, R., Friedrichs, K. and Lewy, H. (1928). Über die Partiellen Differenzengleichungen der Mathematischen Physik. *Mathematische Annalen*, vol. 100, no. 1, pp. 32–74.

Craig, O. (2018). *Concentrating Solar Power (CSP) Technology Adoption in South Africa*. Ph.D. thesis, Faculty of Engineering, Stellenbosch University, South Africa.

CSP World (2013). The end for dish-Stirling CSP Technology? Infinia files for bankruptcy. [Online]. Available at:`http://www.csp-world.com/news/20130929/001196/end-dish-stirling-csp-technology-infinia-files-bankruptcy`, [2015, March 3].

Deetlefs, I.N. (2014). *Design, Simulation, Manufacture and Testing of a Free-Piston Stirling Engine*. Master's thesis, Faculty of Engineering, University of Stellenbosch, South Africa.

Dhar, M. (1999). *Stirling Space Engine Program, Final Report*. Mechanical Technology Inc., Latham, New York, U.S.A.

Dochat, G.R. (1979). Design Study of a 15 kW Free-Piston Stirling Engine - Linear Alternator For Dispersed Solar Electric Power Systems. techreport DOE/NASA/0056-79/1, Mechanical Technology Incorporated, Latham, New York, U.S.A.

Dochat, G.R. (1987). Stirling Space Power Demonstrator Engine Test/Analytical Comparison. *Acta Astronautica*, vol. 15, no. 6, pp. 341–346.

Dyson, R., Geng, S., Tew, R. and Adelino, M. (2008). Towards Fully Three-Dimensional Virtual Stirling Converters For Multi-Physics Analysis and Optimization. *Engineering Applications of Computational Fluid Mechanics*, vol. 2, no. 1, pp. 95–118.

Finkelstein, T. (1960). Generalized Thermodynamic Analysis of Stirling Engines. S.A.E. Paper No. 118B. SAE International.

Finkelstein, T. (1975). Computer Analysis of Stirling Engines. *Advances in Cryogenic Engineering*, vol. 20, p. 269.

Formosa, F. (2011). Coupled Thermodynamic-Dynamic Semi-Analytical Model of Free Piston Stirling Engines. *Energy Conversion and Management*, vol. 52, no. 5, pp. 2098–2109.

Gedeon, D. (2016). *Sage User's Manual*. Gedeon Associates, Athens, Ohio, U.S.A, 11th edn.

Gedeon, D. and Wood, J. (1996). Oscillating-Flow Regenerator Test Rig: Hardware and Theory With Derived Correlations for Screen and Felts. Technical Publication NASA TECH-REPORT-198442, National Aeronautics and Space Administration (NASA) Lewis Research Center, Ohio, U.S.A.

Geng, S., Mason, L., Dyson, R. and Penswick, L. (2008). Overview of Multi-Kilowatt Free-Piston Stirling Power Conversion Research at Glenn Research Center. Tech. Rep. NASA/TM—2008-215061, National Aeronautics and Space Administration (NASA) Glenn Research Center, Ohio, U.S.A.

Gibson, M., Mason, L., Bowman, C., Poston, D., McClure, P., Creasy, J. and Robinson, C. (2015). Development of NASA's Small Fission Power System for Science and Human Exploration. techreport NASA/TM-2015-218460, National Aeronautics and Space Administration (NASA) Glenn Research Center, Ohio, U.S.A.

Gibson, M., Oleson, S., Poston, D. and McClure, P. (2017). NASA's Kilopower Reactor Development and the Path to Higher Power Missions. techreport NASA/TM-2017-219467, National Aeronautics and Space Administration (NASA) Glenn Research Center, Ohio, U.S.A.

Gibson, M.A., Poston, D.I., McClure, P., Godfroy, T.J., Briggs, M.H. and Sanzi, J.L. (2018). Kilopower Reactor Using Stirling TechnologY (KRUSTY) Nuclear Ground Test Results and Lessons Learned. Technical Report NASA/TM-2018-219941, National Aeronautics and Space Administration (NASA) Glenn Research Center, Ohio, U.S.A.

Goldberg, L.F. (1987). *A State Space and Continuum Mechanics Analysis of Stirling Cycle Machines*. Ph.D. thesis, Faculty of Engineering, University of the Witwatersrand, Johannesburg, South Africa.

Goldberg, L.F. (1990). One- and Two-Dimensional Stirling Machine Simulation Using Experimentally Generated Reversing Flow Turubulence Models. Tech. Rep. NASA-CR-185285, National Aeronautics and Space Administration (NASA) Lewis Research Center, Ohio, U.S.A.

Goldwater, B., Piller, S., Rauch, J. and Cella, A. (1977). Demonstration of a Free Piston Stirling Engine Driven Linear Alternator. Tech. Rep. EY-76-C-2764, Mechanical Technology Incorporated, Latham, New York.

Grinnell, S. (1956). Flow of a Compressible Fluid in a Thin Passage. *Transactions of ASME: Paper No. 55-SA-13*, pp. 765–776.

Hargreaves, C.M. (1991). *The Philips Stirling Engine*. Elsevier; Distributors for the U.S. and Canada, Elsevier Science Pub. Co., Amsterdam, Netherlands; New York, U.S.A. ISBN 0444884637.

Hart-Davis, A. (ed.) (2012). *Engineers: From The Great Pyramids to the Pioneers of Space Travel*. 1st edn. London: Dorling Kindersley. ISBN 978-1-4053-7569-6.

H.M. Hashemian and Jin Jiang (2009). Pressure Transmitter Accuracy. *ISA Transactions*, vol. 48, no. 4, pp. 383–388.

Hudson, H. (2013). *From Rural Village to Global Village: Telecommunications for Development in the Information Age*. 1st edn. Taylor and Francis, New York, U.S.A. ISBN 9780805860160.

Ibrahim, M.B. and Tew, R.C. (2012). *Stirling Converter Regenerators*. CRC Press: Taylor & Francis Group, Florida, U.S.A. ISBN 978-1-4398-3007-9.

Inman, D.J. (2014). *Engineering Vibration, International Edition*. 4th edn. Pearson, Harlow, England. ISBN 9780273785217.

Jakubowski, A.K. (1980). Radioisotope-Powered Free-Piston Stirling Engine for Space Applications. *Acta Astronautica*, vol. 7, no. 2, pp. 169–181.

Kankam, M. and Rauch, J. (1991). Comparitive Survey of the Dynamic Analyses of Free-Piston Stirling Engines. In: *Proceedings of the 26th Intersociety Energy Conversion Engineering Conference*. Boston, Massachusetts, U.S.A.

Karabulut, H. (2011). Dynamic Analysis of a Free Piston Stirling Engine Working with Closed and Open Thermodynamic Cycles. *Renewable Energy*, vol. 36, pp. 1704–1709.

Kayofa, L. (2015). *Feasibility Study and Business Plan for Manufacturing a 3 kW-Electrical Solar Stirling Engine and Dish for Stand-Alone Power Supply Units*. Master's thesis, Faculty of Engineering, University of Stellenbosch, South Africa.

Kays, W.M. and London, A.L. (1984). *Compact Heat Exchangers*. 3rd edn. McGraw-Hill, New York, U.S.A.

Kim, J.-M., Choi, J.-Y., Lee, K.-S. and Lee, S.-H. (2017 mar). Design and Analysis of Linear Oscillatory Single-Phase Permanent Magnet Generator for Free-Piston Stirling Engine Systems. *AIP Advances*, vol. 7, no. 5, p. 056667.

Konangi, S., Palakurthi, N.K. and Ghia, U. (2018). Von Neumann Stability Analysis of First-Order Accurate Discretization Schemes for One-Dimensional (1D) and Two-Dimensional (2D) Fluid Flow Equations. *Computers & Mathematics with Applications*, vol. 75, no. 2, pp. 643 – 665.

Kröger, D. (1998). *Air-cooled Heat Exchangers and Cooling Towers*. 1st edn. University of Stellenbosch, Stellenbosch, South Africa.

Lenand, D.K., Priest, J.F., Keiter, D.E. and Schreiber, J.G. (2008). Development of a Power Electronics Controller for the Advanced Stirling Radioisotope Generator. Technical Publication NASA/TM-2008-215031, National Aeronautics and Space Administration (NASA) Glenn Research Center, Cleveland, Ohio, U.S.A.

Lewis, M. and Radebaugh, R. (2011). Measurement of Heat Conduction Through Metal Spheres. In: R.G. Ross, J. (ed.), *Cryocoolers*, vol. 11, pp. 419–425. Kluwer Academic/Plenum Publishers, New York, U.S.A.

Mahkamov, K. (2006). Design Improvements to a Biomass Stirling Engine Using Mathematical Analysis and 3D CFD Modeling. *Journal of Energy Ressources Technology*, vol. 128, pp. 209–215.

Martini, W.R. (1983). *Stirling Engine Design Manual*. National Aeronautics and Space Administration (NASA), Cleveland, Ohio, U.S.A., 2nd edn.

Meijer, R.J. (1960). *The Philips Stirling Thermal Engine: Analysis of the rhombic drive mechanism and efficiency measurements*. Ph.D. thesis, Technische Hogeschool Delft, Netherlands.

Microgen (2018). Microgen Engine Corporation. [Online]. Available at: `http://www.microgen-engine.com/`, [2018, April 1].

Mikalsen, R. and Roskilly, A.P. (2007). A Review of Free-Piston Engine History and Applications. *Applied Thermal Engineering*, vol. 27, no. 14-15, pp. 2339–2352.

Mills, A. and Ganesan, V. (1999). *Heat Transfer*. 2nd edn. Dorling Kindersley, India. ISBN 9780139476242.

Mohammadi, M.A. and Jafarian, A. (2018). CFD Simulation to Investigate Hydrodynamics of Oscillating Flow in a Beta-Type Stirling Engine. *Energy*, vol. 153, pp. 287 – 300.

Murugan, S. and Horák, B. (2016). A Review of Micro Combined Heat and Power Systems for Residential Applications. *Renewable and Sustainable Energy Reviews*, vol. 64, pp. 144 – 162.

Ökofen (2018). Microgen Stirling Engine. [Online]. Available at: `http://www.okofen-e.com/en/pellematic_smart_e/`, [2018, February 21].

Organ, A.J. (1992). *Thermodynamics and Gas Dynamics of the Stirling Cycle Machine*. Cambridge University Press, Cambridgeshire, U.K. ISBN 9780521131797.

Organ, A.J. (2014). *Stirling Cycle Engines: Inner Workings and Design*. 1st edn. John Wiley & Sons, West Sussex, U.K. ISBN 978-1-118-81843-5.

Oriti, S. and Scott, W. (2011). *Advanced Stirling Convertor (ASC-E2) Performance Testing at NASA Glenn Research Cent*. National Aeronautics and Space Administration (NASA) Glenn Research Center, Cleveland, Ohio, U.S.A.

Patankar, S. and Spalding, D. (1972). A Calculation Procedure for Heat, Mass and Momentum Transfer in Three-Dimensional Parabolic Flows. *International Journal of Heat and Mass Transfer*, vol. 15, no. 10, pp. 1787–1806.

Paul, C.J. and Engeda, A. (2015). Modeling a Complete Stirling Engine. *Energy*, vol. 80, pp. 85 – 97.

Peckham Engineering and Tool (1994). *Precision Linear Flexure Bearing Cartridge*. Philips Laboratory, Kirtland Air Force Base, Albuquerque, New Mexico, U.S.A.

Prinsloo, G.J. (2018). *Synthesis of an Off-Grid Solar Thermal Cogeneration and Intelligent Smartgrid Control System for Rural Rpplications*. Ph.D. thesis, Faculty of Engineering, University of Stellenbosch, South Africa.

Qiu, S., Gao, Y., Rinker, G. and Yanaga, K. (2019). Development of an Advanced Free-Piston Stirling Engine for Micro Combined Heating and Power Application. *Applied Energy*, vol. 235, pp. 987–1000.

Qnergy (2018). Smart, Efficient, Reliable Energy Solutions with the Stirling Engine. [Online]. Available at: `https://www.qnergy.com/`, [2018, February 6].

Ramos, J.A. (2015). *Thermodynamic Analysis of Stirling Engine Systems*. Ph.D. thesis, KTH Royal Institute of Technology, School of Industrial Engineering and Management, Sweden.

Redlich, R.W. and Berchowitz, D. (1985). Linear Dynamics of Free-Piston Stirling Engines. In: *Proceedings of the Institution of Mechanical Engineers*, vol. 199, pp. 203–213. Ohio, U.S.A. ISSN 0263-7138.

Renzi, M. and Brandoni, C. (2014). Study and Application of a Regenerative Stirling Cogeneration Device Based on Biomass Combustion. *Applied Thermal Engineering*, vol. 67, no. 1, pp. 341 – 351.

Rinker, G., Solomon, L. and Qiu, S. (2018). Optimal Placement of Radiation Shields in the Displacer of a Stirling Engine. *Applied Thermal Engineering*, vol. 144, pp. 65–70.

Riofrio, J.A., Al-dakkan, K., Hofacker, M.E. and Barth, E.J. (2008). Control-Based Design of Free-Piston Stirling Engines. pp. 1533–1538.

SABS (2012). *South African National Standard 347:2012 Categorization and Conformity Assessment Criteria for all Presure Equipment*. South African Bureau of Standards.

Sayyaadi, H. and Ghasemi, H. (2018). A Novel Second-Order Thermal Model of Stirling Engines with Consideration of Losses due to the Speed of the Crack System. *Energy Conversion and Management*, vol. 168, pp. 505–521.

Schmidt, G. (1871). The Theory of Lehmans Calorimetric Machine. *Z Vereines Deutcher Ingenieure*, vol. 15.

Schmitz, P.C., Mason, L.S. and Schifer, N.A. (2016). Modular Stirling Radioisotope Generator. Technical Publication NASA/TM—2016-218911, National Aeronautics and Space Administration (NASA) Glenn Research Center, Glenn Research Center, Ohio, U.S.A.

Schock, A. (1978). Stirling Engine Nodal Analysis Program. *Journal of Energy*, vol. 2, no. 6, pp. 354–362. ISSN 0146-0412.

Schreiber, J.G. and Geng, S.M. (1987). *RE 1000 Free-Piston Stirling Engine Hydraulic Output System Description*. National Aeronautics and Space Administration, Cleveland, Ohio, U.S.A.

Senda, F.M. (2012). *Aspects of Waste Heat Recovery and Utilisation (WHRU) in Pebble Bed Modular Reactor (PBMR) Technology*. Master's thesis, Faculty of Engineering, University of Stellenbosch, South Africa.

Shunmin, Z., Guoyao, Y., Jongmin, O., Tao, X., Zhanghua, W., Wei, D. and Ercang, L. (2018). Modeling and Experimental Investigation of a Free-Piston Stirling Engine-Based Micro-Combined Heat and Power System. *Applied Energy*, vol. 226, pp. 522–533.

Siemens PLM (2017). NX 11 Product Engineering Software. [Online]. Available at: `https://www.plm.automation.siemens.com/en/products/nx/11/`, [2017, June 7].

Smith, G. (2006). *Building, Testing and Modelling of a Pulse Tube Cryogenic Cooler*. Master's thesis, Faculty of Engineering, University of Stellenbosch, South Africa.

Snyman, H. (2007). *Second Order Analysis Methods for Stirling Engine Design*. Master's thesis, Faculty of Engineering, University of Stellenbosch, South Africa.

SpaceFlight Insider (2018). It Keeps Going and Going: Stirling Engine Test Sets Long-Duration Record at NASA Glenn. [Online]. Available at: `https://www.spaceflightinsider.com/space-centers/glenn-research-center/it-keeps-going-and-going-stirling-engine-test-sets-long-duration-record-at-nasa-glenn/`, [2019, February 1].

Stage, R. (1991). *Analysis of a Planar Spiral Displacer Spring for use in Free-Piston Stiring Engines*. Master's thesis, Faculty of Engineering and Technology, Ohio University, Ohio, U.S.A.

Stevens, L., Wilcox, M., Leopold, A., Taylor, C. and Waters, L. (2016). *Poor People's Energy Outlook*. 1st edn. Practical Action Publishing Ltd, Warwickshire, U.K.

Steyn, L. (2019). Swedish Cleantech Turns Waste Gas to Cash in Krugersdorp. [Online]. Available at: `https://www.businesslive.co.za/bd/companies/energy/2019-01-15-swedish-cleantech-turns-waste-gas-to-cash-in-krugersdorp/`, [2019, February 1].

Strauss, J.M. (2013). *Direct Piston Displacement Control of Free-Piston Stirling Engines*. Ph.D. thesis, Faculty of Engineering, University of Stellenbosch, South Africa.

Sullivan, T.J. (1989). NASA Lewis Stirling Engine Computer Code Evaluation. Tech. Rep. NASA-CR-182248, National Aeronautics and Space Administration (NASA) Lewis Research Center, Ohio, U.S.A.

Sunpower Incorporated (2016). Linear Alternators and Motors. [Online]. Available at: `http://sunpowerinc.com/engineering-services/technology/linear-alt/`, [2016, July 8].

Tanaka, M., Yasamashita, I. and Chisaka, F. (1990). Flow and Heat Transfer Characteristics of the Stirling Engine Regenerator in an Oscillating Flow. *JSME International Journal*, vol. 33, no. 2, pp. 283–289.

Tavakolpour-Saleh, A., Zare, S. and Omidvar, A. (2016 dec). Applying perturbation technique to analysis of a free piston Stirling engine possessing nonlinear springs. *Applied Energy*, vol. 183, pp. 526–541.

Tew, R.C. (1983). Computer Program for Stirling Engine Performance Calculations. Tech. Rep. NASA-TM-82960, National Aeronautics and Space Administration (NASA) Lewis Research Center, Ohio, U.S.A.

Thieme, L.G. (1979). Low-Power Baseline Test Results For the GPU-3 Stirling Engine. Tech. Rep. NASA TM-79103, National Aeronautics and Space Administration (NASA) Lewis Research Center, Ohio, U.S.A.

Thieme, L.G. (1981). High-Power Baseline and Motoring Test Results for the GPU-3 Stirling Engine. Technical Publication DOEINAW51040-31 (NASA TM-82646), National Aeronautics and Space Administration (NASA) Lewis Research Center, Ohio, U.S.A.

Ulusoy, N. (1994). *Dynamic Analysis of Free Piston Stirling Engines*. Ph.D. thesis, Department of Mechanical and Aerospace Engineering, Case Western Reserve University, Ohio, U.S.A.

United Nations (2015). *Transforming Our World: The 2030 Agenda For Sustainable Development*.

Urieli, I. (1977). *A Computer Simulation Of Stirling Cycle Machines*. Ph.D. thesis, Faculty of Engieering, University of the Witwatersrand, South Africa.

Urieli, I. and Berchowitz, D. (1984). *Stirling Cycle Engine Analysis (Modern Energy Studies)*. 1st edn. CRC Press. ISBN 978052744352.

Urieli, I. and Rallis, C.J. (1976). A New Regenerator Model for Stirling Cycle Machines. Research Report 67, University of the Witwatersrand, South Africa.

VDI-GVC (2015). *VDI Heat Atlas*. 2nd edn. Springer, Dusseldorf, Germany. ISBN 978-3-540-77876-9.

Versteeg, H. and Malalasekera, W. (2007). *An Introduction to Computational Fluid Dynamics: The Finite Volume Method*. 2nd edn. Pearson, Harlow, U.K. ISBN 9780131274983.

Walker, G. (1980). *Stirling Engines*. Clarendon Press ; Oxford University Press, Oxford, U.K.; New York, U.S.A. ISBN 0198562098 9780198562092.

Walker, G. and Senft, J. (1985). *Lecture Notes in Engineering: Free Piston Stirling Engines*. 1st edn. Springer-Verslag, Heidelberg, Germany. ISBN 3-540-15495-7.

White, F.M. (2006). *Viscous Fluid Flow*. 3rd edn. McGraw-Hill. ISBN 007-124493-X.

Wilson, S.D., Schifer, N.A., Williams, Z.D. and Metscher, J.F. (2016). Overview of Stirling Technology Research at NASA Glenn Research Center. Technical Publication NASA/TM—2016-218909, National Aeronautics and Space Administration (NASA), Glenn Research Center, Ohio, U.S.A.

Wood, J., Buffalino, A., Holliday, E., Penswick, B. and Gedeon, D. (2010). Free-Piston Stirling Power Conversion Unit for Fission Surface Power, Phase I Final Report. techreport NASA/CR-2010-216750, National Aeronautics and Space Administration (NASA), Ohio, U.S.A.

World Bank (2017). State of Electricity Access Report 2017 (Vol. 2) : Full Report (English).
Available at: `http://documents.worldbank.org/curated/en/364571494517675149/full-report`

Yuan, S. and Spradley, I. (1992). A Third Order Computer Model For Stirling Refrigerators. *Advances in Cryogenic Engineering*, vol. 37, pp. 1055–1062.

Zare, S. and Tavakolpour-Saleh, A. (2016). Frequency-Based Design of a Free Piston Stirling Engine Using Genetic Algorithm. *Energy*, vol. 109, pp. 466–480.

Zare, S. and Tavakolpour-Saleh, A. (2019). Free piston Stirling engines: A review. *International Journal of Energy Research*, pp. 1–32.

Appendices

A. A derivation of the fluid dynamic transport equations

This appendix derives the governing transport equations for the working fluid from first principles, following the procedures outlined by Bird *et al.* (2002). The derivation is based on applying the principle of conservation of mass, momentum and energy to a finite control volume element of an infinitesimal size. The governing equations are first derived for the generalised three-dimensional flow case and are then simplified to a one-dimensional plug-flow model.

A.1. Conservation of mass

The principle of conservation of mass states that mass cannot be created or destroyed, but that the total mass of a closed system is always conserved. When applied to a finite control volume V, the conservation of mass may be worded as follows:

$$\left\{\begin{matrix}\text{Rate of increase of}\\ \text{mass within the}\\ \text{control volume } V\end{matrix}\right\} = \left\{\begin{matrix}\text{Rate of mass flow}\\ \text{entering the}\\ \text{control volume}\end{matrix}\right\} - \left\{\begin{matrix}\text{Rate of mass flow}\\ \text{exiting the}\\ \text{control volume}\end{matrix}\right\}$$

To express this mathematically, a fixed control volume is defined through which the working fluid may flow, as shown in Figure A.1. The control volume depicts the one-dimensional inflow and outflow of working fluid with density ρ and velocity v in the x-direction, crossing the interface area $\Delta y \Delta z$ at locations x and $x + \Delta x$. For the fixed control volume V, the conservation of mass in the direction of x is first derived as:

$$\Delta x \Delta y \Delta z \frac{\partial \rho}{\partial t} = \Delta y \Delta z \left[(\rho v)|_x - (\rho v)|_{x+\Delta x}\right] \tag{A.1}$$

If the mass balance is extended include flow in the y and z dimensions; the resulting equation set divided by the volume $\Delta x \Delta y \Delta z$; and the equation taken to the limit as $\Delta \to 0$, then the three-dimensional form of the continuity equation results as:

$$\frac{\partial \rho}{\partial t} = -\left(\frac{\partial}{\partial x}\rho v_x + \frac{\partial}{\partial y}\rho v_y + \frac{\partial}{\partial z}\rho v_z\right) \tag{A.2}$$

which is more concisely written in vector notation by:

$$\frac{\partial \rho}{\partial t} = -(\nabla \cdot \rho \vec{v}) \tag{A.3}$$

For the one-dimensional case in x, the continuity equation reduces to:

$$\boxed{\frac{\partial \rho}{\partial t} = -\frac{\partial}{\partial x}\rho v} \tag{A.4}$$

which is the final form of the continuity equation as used throughout this study.

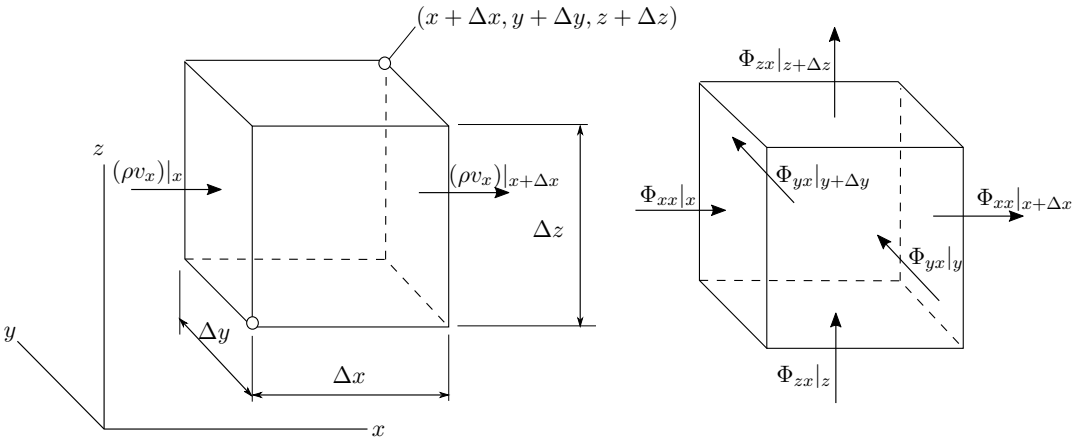

Figure A.1: Finite control volume V through which the working fluid is flowing, showing the x-components of mass flux (left) and momentum flux (right)

A.2. Conservation of momentum

The conservation of momentum equation is derived from application of Newton's second law of motion, which states that the rate of change in momentum of a body is equal to the net force acting on it. For a fixed control volume V this may be worded as follows:

$$\left\{\begin{array}{l}\text{Rate of increase of}\\ \text{momentum within the}\\ \text{control volume } V\end{array}\right\} = \left\{\begin{array}{l}\text{Rate of momentum}\\ \text{convected into the}\\ \text{control volume}\end{array}\right\}$$

$$- \left\{\begin{array}{l}\text{Rate of momentum}\\ \text{convected out of the}\\ \text{control volume}\end{array}\right\} + \left\{\begin{array}{l}\text{Net body and external force}\\ \text{acting on the working fluid}\\ \text{within the control volume}\end{array}\right\}$$

Momentum transfer occurs by two principal mechanisms that are convective and molecular in nature. For simplicity and clarity of this derivation, the symbol Φ has been used throughout as an encapsulating term of both these mechanisms. The momentum balance equation is first derived only using the rate of change in momentum acting in the x-direction. Thereafter the equation set is expanded to include the y and z directions and the generalised form of the momentum balance equation is derived. Referring to Figure A.1, it is seen how the x-component representing the rate of momentum flux Φ enters and leaves through the faces y and z at locations x and $x+\Delta x$, being $\Phi_{xx}|_x$ and $\Phi_{xx}|_{x+\Delta x}$ respectively. Additionally the rates of momentum flux entering and leaving the faces at y and $y+\Delta y$ are $\Phi_{yx}|_y$ and $\Phi_{yx}|_{y+\Delta y}$ respectively, and the rate of momentum flux entering and leaving the faces at z and $z+\Delta z$ are $\Phi_{zx}|_z$ and $\Phi_{zx}|_{z+\Delta z}$.

Expressed mathematically for fluid flow in the x-direction, Newton's second law of motion states:

$$\frac{\partial}{\partial t}(\Delta x \Delta y \Delta z \rho v_x) = \sum F_{x,s} + \sum F_{x,b} \tag{A.5}$$

where the subscripts 's' and 'b' refer to surface and body forces respectively. The net surface force acting on the control volume in the x-direction is given by:

$$\begin{aligned}\sum F_x = \Delta y\Delta z(\Phi_{xx}|_x - \Phi_{xx}|_{x+\Delta x}) \\ +\Delta z\Delta x(\Phi_{yx}|_y - \Phi_{yx}|_{y+\Delta y}) \\ +\Delta x\Delta y(\Phi_{zx}|_z - \Phi_{zx}|_{z+\Delta z})\end{aligned} \tag{A.6}$$

Dividing by $\Delta x\Delta y\Delta z$ and taking the limit as $\Delta \to 0$:

$$\frac{\partial}{\partial t}\rho v_x = -(\frac{\partial}{\partial x}\Phi_{xx} + \frac{\partial}{\partial y}\Phi_{yx} + \frac{\partial}{\partial z}\Phi_{zx}) + \rho g_x \tag{A.7}$$

where ρg_x is the only body force assumed to be acting on the fluid. By following the same approach as for the continuity equation (i.e. extending the momentum flux terms to three dimensions) yields the momentum balance equation in vector notation:

$$\frac{\partial}{\partial t}\rho\vec{v} = -[\nabla\cdot\vec{\Phi}] + \rho\vec{g} \tag{A.8}$$

When the momentum flux term is expanded into its convective and molecular constituents, that are $\Phi = \rho\vec{v}\vec{v} + P\vec{\delta} + \vec{\tau}$, the more generalised momentum-balance equation in vector notation is given by:

$$\frac{\partial}{\partial t}(\rho\vec{v}) = -[\nabla\cdot\rho\vec{v}\vec{v}] - \nabla P - [\nabla\cdot\vec{\tau}] + \rho\vec{g} \tag{A.9}$$

Note that term $-[\nabla\cdot\rho\vec{v}\vec{v}]$ represents the rate of momentum addition by convection per unit volume, the terms $-\nabla P - [\nabla\cdot\vec{\tau}]$ the rate of momentum addition by molecular transport and $\rho\vec{g}$ the external force on the fluid per unit volume.

If the effect of gravity is assumed negligible and the only one-dimensional flow is considered in x (i.e. $v_y = v_z = 0$), the momentum balance equation reduces to:

$$\boxed{\frac{\partial}{\partial t}(\rho v) = -\frac{\partial}{\partial x}(\rho vv) - \frac{\partial}{\partial x}(P) - [\frac{\partial\tau_{xx}}{\partial x} + \frac{\partial\tau_{yx}}{\partial y} + \frac{\partial\tau_{zx}}{\partial z}]} \tag{A.10}$$

If the assumption of one-dimensional plug flow is inferred (i.e. $v_y = v_z = 0$ and $\partial v_x/\partial y = \partial v_x/\partial z = 0$), then the last two terms within parenthesis fall away. Equation (A.10) is the final form of the one-dimensional momentum equation used throughout this study.

A.3. Conservation of energy

A.3.1. Derivation of the total energy equation

The derivation of the total energy equation starts by applying the principle of conservation of energy to the stationary control volume V depicted in Figure A.1. The total energy equation may be expressed in a number of equally applicable forms (Bird *et al.*, 2002). One such form, commonly known as the *thermal energy equation,* is derived by subtracting *mechanical energy equation* from the total energy equation. For a fixed control volume V, the principle of conservation of energy may

be worded as follows:

$$\left\{\begin{array}{l}\text{Rate of increase of}\\ \text{internal and kinetic energy}\\ \text{within the control volume}\end{array}\right\} = -\left\{\begin{array}{l}\text{Net rate of internal and}\\ \text{kinetic energy exiting}\\ \text{the control volume}\end{array}\right\}$$

$$+\left\{\begin{array}{l}\text{Net rate of}\\ \text{heat addition to}\\ \text{the control volume}\end{array}\right\} - \left\{\begin{array}{l}\text{Net rate of work done by the}\\ \text{fluid within the control volume}\\ \text{onto the external surroundings}\end{array}\right\}$$

Expressed mathematically, Bird *et al.* (2002) gives the total energy equation in vector notation as follows:

$$\begin{aligned}\frac{\partial}{\partial t}(\rho u + \frac{1}{2}\rho v^2) = &-(\nabla\cdot(\rho u + \frac{1}{2}\rho v^2)\vec{v}) - (\nabla\cdot\vec{q}) - (\nabla\cdot P\vec{v})\\ &-(\nabla\cdot[\vec{\tau}\cdot\vec{v}]) + \rho(\vec{v}\cdot\vec{g})\end{aligned} \tag{A.11}$$

in which u represents internal energy and the term containing $v^2/2$ the kinetic energy. Further note that the first of Equation (A.11) represents the per unit volume rate of energy addition by convective transport; the second term, the rate of energy addition by heat conduction; the third term, the rate of work done on the fluid by pressure forces; the fourth term, the rate of work done on the fluid by viscous forces; and the fifth term, the rate of work done on the fluid by external forces.

In order to extract the thermal energy equation, the Equation (A.11) is first written in substantial form. This is accomplished by rearranging Equation (A.11) in carrying out the indicated differentiations on the left-hand side (LHS) and substituting for the continuity equation, Equation (A.3). Bird *et al.* (2002) shows that after a lengthy rearrangement the total energy equation is given in vector notation by:

$$\rho\frac{D}{Dt}(u + \frac{v^2}{2}) = (\nabla\cdot\vec{q}) - (\nabla\cdot P\vec{v}) - (\nabla\cdot[\vec{\tau}\cdot\vec{v}]) + (\vec{v}\cdot\vec{g}) \tag{A.12}$$

A.3.2. Derivation of the mechanical energy equation

The mechanical energy equation is produced for the generalised three-dimensional case by taking the dot product of the momentum equation, given by Equation (A.9), and velocity vector $\vec{v}$. Substitution of the continuity equation and rearrangement yields the mechanical energy equation in terms of $(\frac{1}{2}\rho v^2)$:

$$\begin{aligned}\frac{\partial}{\partial t}(\frac{1}{2}\rho v^2) = &-(\nabla\cdot\frac{1}{2}\rho v^2\vec{v}) - (\nabla\cdot P\vec{v}) - P(-\nabla\cdot\vec{v})\\ &-(\nabla\cdot(\vec{\tau}\cdot\vec{v})) - (-\vec{\tau}:\nabla\vec{v}) + \rho(\vec{v}\cdot\vec{g})\end{aligned} \tag{A.13}$$

Written in substantial form, the mechanical energy equation is given by:

$$\rho\frac{D}{Dt}(\frac{1}{2}v^2) = -(\nabla\cdot P\vec{v}) + (P\nabla\cdot\vec{v}) - (\nabla\cdot(\vec{\tau}\cdot\vec{v})) + (\vec{\tau}:\nabla\vec{v}) + \rho(\vec{v}\cdot\vec{g}) \tag{A.14}$$

A.3.3. Derivation of the thermal energy equation

The thermal energy equation is derived by subtracting the mechanical energy equation from the total energy equation. This yields a more convenient equation for expressing the thermal energy u and therefore temperature of the working fluid. Subtracting Equation (A.14) from Equation (A.12) yields:

$$\rho\frac{Du}{Dt} = -\nabla\cdot\vec{q} - P(\nabla\cdot\vec{v}) - (\vec{\tau}:\nabla\vec{v}) \tag{A.15}$$

A closer inspection of the individual constituents of Equation (A.15) reveals that:

(i) The term $\nabla\cdot\vec{q}$ represents the net heat conduced to the control volume per unit volume.

(ii) The term $-P(\nabla\cdot\vec{v})$ represents the *reversible* rate of internal energy increase per unit volume by boundary work.

(iii) The term $-(\vec{\tau}:\nabla\vec{v})$ represents the *irreversible* rate of internal energy increase per unit volume by viscous dissipation. This term is always positive as viscous fluid friction always acts against the direction of movement.

In the case of one-dimensional flow in x, the viscous dissipation term reduces to:

$$(\vec{\tau}:\nabla\vec{v}) \rightarrow \tau_{xx}\frac{\partial v_x}{\partial x} + \tau_{xy}\frac{\partial v_x}{\partial y} + \tau_{xz}\frac{\partial v_x}{\partial z} \tag{A.16}$$

If the assumption of one-dimensional plug flow is inferred, the velocity gradients in the y and z axes are zero and consequently the second and third terms of Equation (A.16) fall away. The one-dimensional form of the energy equation is then rewritten as:

$$\boxed{\frac{\partial}{\partial t}(\rho u) = -\frac{\partial}{\partial x}(\rho u v) - \frac{\partial q}{\partial x} - P\frac{\partial v}{\partial x} - \tau_{xx}\frac{\partial v}{\partial x}} \tag{A.17}$$

which is considered the final form of the energy equation as used throughout this study. The energy equation may be used to model the change in working fluid internal energy. Then, using the appropriate state functions, the change in internal energy may be related to a change in working fluid temperature. This is two steps short of the methodology followed by Bird *et al.* (2002) and White (2006), in which the energy equation is thereafter further rewritten in a form for enthalpy, and by accordingly substituting an equation of state for pressure, modified to yield a relation for temperature. The author argues that this is not necessary, since the transport equations are solved numerically in finite difference form. Care should however be taken to ensure that the appropriate equations of state are employed accordingly.

B. Discretisation of the transport equations

This appendix presents the discretisation of the governing transport equations to a one-dimensional plug flow model consisting of finite control volume elements. It was assumed that external interactions including heat transfer and fluid friction may be applied uniformly over the entire control volume. By discretising the conservation equations of mass, momentum and energy, solvable finite difference equations are devised. The appendix concludes by temporally integrating the finite difference equations to a fully-explicit integral form, which may then be solved numerically to compute the following time-step mass, momentum and thermal energy using a digital computer.

B.1. Conservation of mass

The conservation of mass equation A.4 was applied to a finite control volume element i with interface area A_x, length Δx and volume $V = A_x \Delta x$. By use of Gauss's Divergence theorem, spatial integration of the differential equation was performed over the length of the element, between two control volume interface areas. The rate of change in mass for a finite volume element i may then be expressed by:

$$\frac{\partial m_i}{\partial t} = \frac{\partial}{\partial t}(\rho_i A_{x_i} \Delta x_i) = \left[\rho_j v_j A_j - \rho_{j+1} v_{j+1} A_{j+1}\right] \tag{B.1}$$

where the subscript '$_j$' denotes the interface between two finite control volumes, and is called a vector node. Nodes were used to store information about velocity in a grid-staggered manner, whereas scalar properties such as density and pressure were assumed uniform for the control volume element and are stored at cell centres i. The density at the node ρ_j was calculated from first-order upwind differencing from the adjacent scalar control volumes, whereas the interface area at the node A_j represents the smallest fluid-to-fluid contact area between two adjacent control volumes, through which flow occurs.

Equation B.1 was integrated temporally using a fully-explicit forwards differencing scheme, in which the rate of change of a variable at a following time-step may be determined fully from its current time-step variables (Versteeg and Malalasekera, 2007), as given by:

$$\frac{\Delta m_i}{\Delta t} = \left[\rho_j v_j A_j - \rho_{j+1} v_{j+1} A_{j+1}\right]^t \tag{B.2}$$

where Δt represents the finite time-step duration and superscript '^{t}' denotes the current time-step. If the LHS of equation B.2 is expanded, the equation may be rewritten to solve the control volume mass at the following time-step:

$$\boxed{m_i^{t+\Delta t} = m_i^t + \Delta t\left[\rho_j v_j A_j - \rho_{j+1} v_{j+1} A_{j+1}\right]^t} \tag{B.3}$$

Equation (B.3) is the final form of the solution to the discretised continuity equation as used through this study. It states that the new time-step control volume mass

may be computed using the previous control volume mass and time-step mass fluxes.

B.2. Conservation of momentum

The conservation of momentum equation A.12 was discretised over a staggered-stacked vector control volume defined about the interface node j, consisting of half the upwind and downwind scalar control volumes. This so-called grid staggering technique couples the pressure and velocity terms, stored at cell centres and interface nodes respectively, to avoid the so-called checker-board pressure field phenomenon (Versteeg and Malalasekera, 2007). While staggering control volumes in this fashion is no longer practice in modern computational fluid dynamic analyses, in the context of an orthogonal Cartesian structured grid it is given preference as an accurate, transparent and robust numerical approach.

Figure B.1 depicts the generalised vector control volume that was staggered-stacked over half the upwind and downwind scalar control volumes, which may even be of different cross-sectional face areas A_x. Scalar thermodynamic properties such as pressure, density and internal energy were defined and stored at the scalar control volumes with centres indicated '$\bullet$' and numbered 'i'. In contrast, the vector velocities were defined and stored at the interface nodes indicated by '$\circ$' and numbered 'j'. The figure also depicts the forces acting on the vector control volume, excluding gravity, which was assumed negligibly small.

Spatial integration of equation A.10 was performed by use of Gauss's Divergence theorem. For the assumed one-dimensional plug flow control volume this yields:

$$\frac{\partial}{\partial t}(m_j v_j) = \left[\rho_{i-1} v_{i-1}^2 A_{x_{i-1}} - \rho_i v_i^2 A_{x_i}\right] + \left[P_{i-1} A_j - P_i A_j\right] - \left[\tau_{s_{i-1}} \frac{A_{z_{i-1}}}{2} + \tau_{s_i} \frac{A_{z_i}}{2}\right] \tag{B.4}$$

where the fluid shear forces at the wall have been simplified to empirical relations of wall friction, as given by the last two terms within parenthesis. The mass m_j represents half the adjacent scalar control volume masses, whereas the velocity v_i may be determined from a volumetric flow interpolation between neighbouring interface velocities v_j (Urieli, 1977). In addition, A_j represents the fluid-to-fluid interface area upon which the working fluid pressure forces are acting.

In the momentum balance equation is then integrated temporally over a finite time-step Δt as in the case of the continuity equation, the finite difference form results:

$$\frac{\Delta}{\Delta t}(m_j v_j) = \left[\rho_{i-1} v_{i-1}^2 A_{x_{i-1}} - \rho_i v_i^2 A_{x_i}\right]^t + \left[P_{i-1} A_j - P_i A_j\right]^t - \left[\tau_{s_{i-1}} \frac{A_{z_{i-1}}}{2} + \tau_{s_i} \frac{A_{z_i}}{2}\right]^t \tag{B.5}$$

By expanding the LHS of Equation (B.5) and rearranging, the following time-step

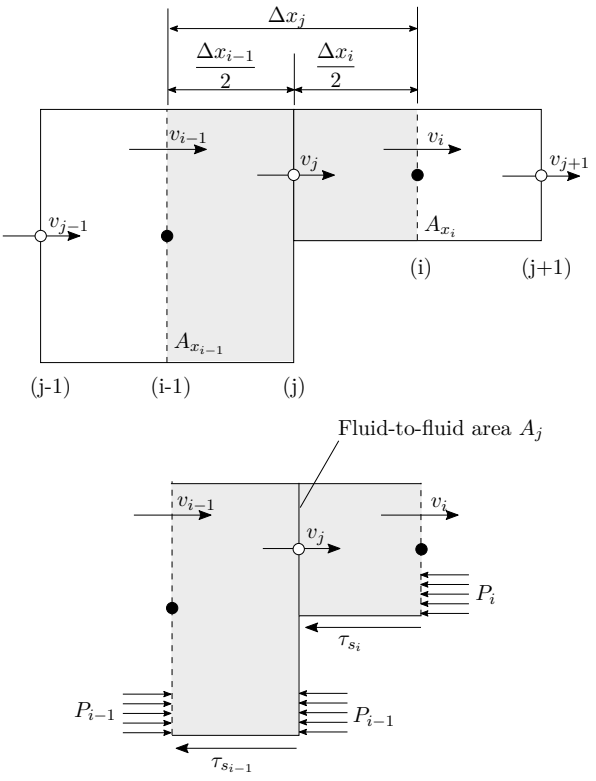

Figure B.1: Schematic depiction of the generalised vector control volume j, as staggered over two unequally sized scalar control volumes i-1 and i

velocity is calculated using a fully-explicit method as:

$$\boxed{{v_j}^{t+\Delta t} = \frac{\left(m_j v_j\right)^t + \Delta t\left[DM + DP + DF\right]^t}{m_j^{t+\Delta t}}} \tag{B.6}$$

where DM, DP and DF represent the first, second and third terms of Equation (B.5) respectively. It should be noted that Equation (B.6) is the final form of the transient solution to the vector velocity v_j as used throughout this study. This equation may be solved numerically if the new time-step mass is known.

B.3. Conservation of energy

The conservation of thermal energy Equation (A.17) was discretised for the generalised scalar control volume i as depicted by Figure B.2. The figure shows the thermal energy inflow and outflow, as well as work done by pressure forces. For simplicity in integrating the thermal energy equation into the model, the rate of boundary work done was decoupled from reversible compression and expansion and is represented by $\dot{W}_b$. Irreversible heat generation by viscous dissipation was modelled by surface wall friction, for which the velocity magnitude $|\overline{v_i}|$ indicates that the internal thermal energy increases regardless of flow direction. Fluid flow occurs through the smallest interface area A_j, with thermodynamic properties determined from first-order upwind differencing.

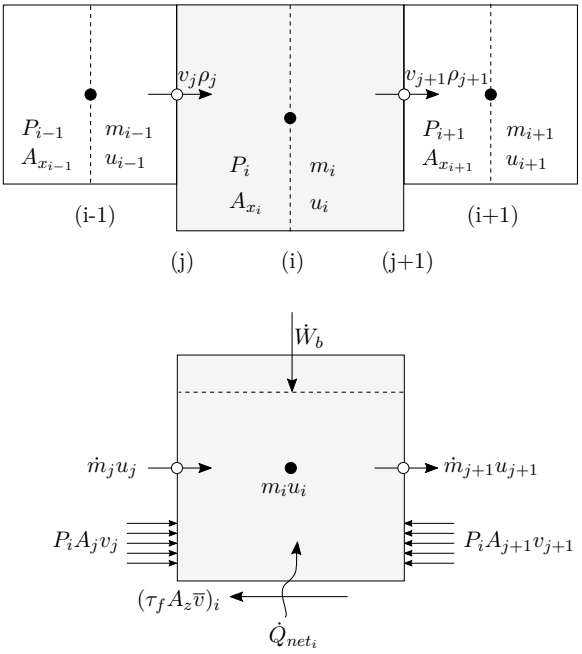

Figure B.2: Schematic depiction of the generalised scalar control volume i, to which the continuity and thermal energy equations were applied

Spatial integration of Equation (A.17) was achieved by use of Gauss's Divergence theorem to yield:

$$\frac{\partial}{\partial t}(m_i u_i) = \left[\rho_j v_j A_j u_j - \rho_{j+1} v_{j+1} A_{j+1} u_{j+1}\right] + \dot{Q}_{net} + P_i\left[v_j A_j - v_{j+1} A_{j+1}\right] + \dot{W}_b + \tau_{f_i} A_{z_i} |\overline{v_i}| \tag{B.7}$$

Equation (B.7) is then integrated temporally with the fully-explicit forwards differencing scheme to yield the energy equation in finite difference form:

$$\frac{\Delta}{\Delta t}(m_i u_i) = \left[DM_e + \dot{Q}_{net} + DP_e + \dot{W}_b + DF_e\right]^t \tag{B.8}$$

where DM_e, DP_e and DF_e represents the first, third and fifth terms of the thermal energy Equation (B.7). The following time-step thermal energy is then determined by rearranging Equation (B.8) to yield:

$$\boxed{(m_i u_i)^{t+\Delta t} = (m_i u_i)^t + \Delta t\left[DM_e + \dot{Q}_{net} + DP_e + \dot{W}_b + DF_e\right]^t} \tag{B.9}$$

Equation (B.9) is the final form of the discretised thermal energy equation used throughout this study. Equation (B.9) may be solved numerically using the rates of change in momentum of the previous time-step. Then, by dividing the new time-step internal energy by the new time-step mass calculated from the continuity equation, the specific internal energy of the control volume may be computed. The change in internal thermal energy is then related to a change in fluid temperature using the appropriate state functions for a constant volume process.

C. Finite element analysis model of the linear generator

The operation of the linear electric generator was simulated in a two-dimensional axisymmetric FEA that was performed in *ANSYS Maxwell 16.0*. Maxwell's transient magnetic solver was used to determine the open-circuit and closed-circuit flux linkage, terminal voltage, load current and generator magnetic forces as functions of magnet train displacement, in order to arrive at the generator characteristic functions given in Chapter 4.3 on page 49.

C.1. Geometry and mesh setup

Due to geometrical symmetry, only a simplified two-dimensional axisymmetric slice of the generator was modelled, as depicted in Figure C.1. As shown, the Z-axis forms a symmetry axis about which the two-dimensional model may be revolved. Only the ferro-magnetic and electrically conductive generator components that partake in the operation were included in the program solver. Because the magnetic flux densities through the bronze power piston and aluminium magnet train do not vary with time, these components were neglected from the solver. The 32 arc-shaped magnets making up the magnet train were approximated by four radially magnetised ring magnets. The magnetic field in the outer two magnets (red) were aligned with the positive X-direction in a north orientation, whereas the inner two magnets (blue) were aligned in a south orientation (negative X-direction). The magnetic field within the magnets were assumed to remain constant. The components were assigned materials properties from Maxwell's built-in material library, as listed in Table C.1.

The model geometry was meshed using Maxwell's default triangular meshing tool, as shown in Figure C.2. The generator components were defined to have a maximum element size of 1 mm, whereas the surrounding air elements in the 'balloon boundary' were defined to have a maximum element size of 5 mm. The mesh refinement boundary region has a maximum element size of 2 mm

Table C.1: Materials assigned to the generator components

Model component	Material
Balloon boundary, moving band	Air
Outer and inner stator	Mild steel, AISI 1008
Coil	Copper, 70 windings
Coil bobbin, coil insulation	PVC plastic
Magnets	NdFeB 42H
Magnet plunger	Aluminium

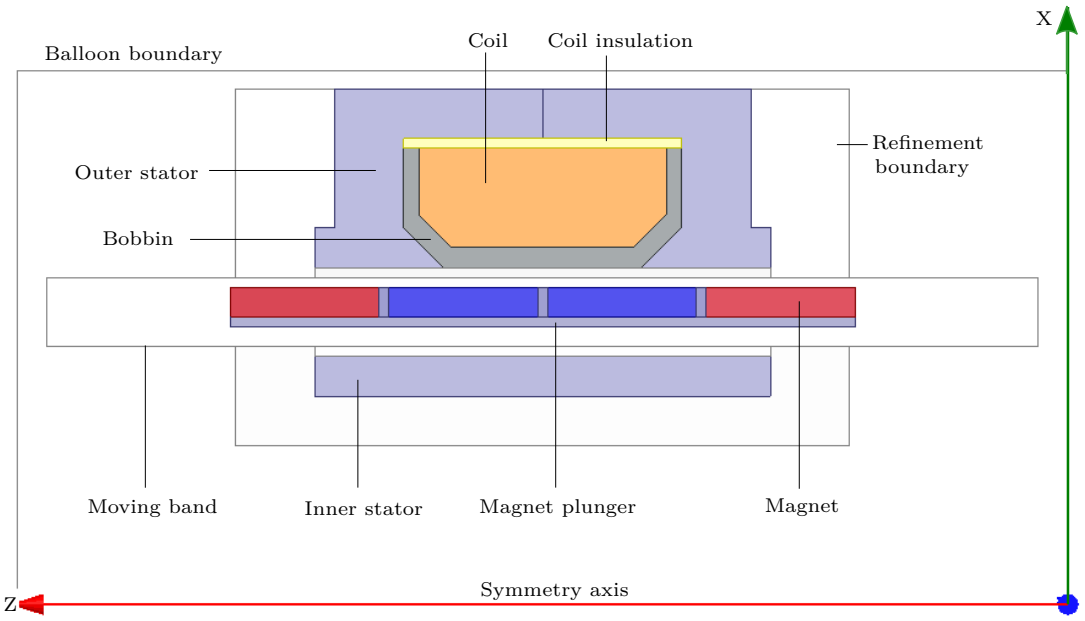

Figure C.1: Two-dimensional axisymmetric slice of the linear generator, depicting the principal modelling components

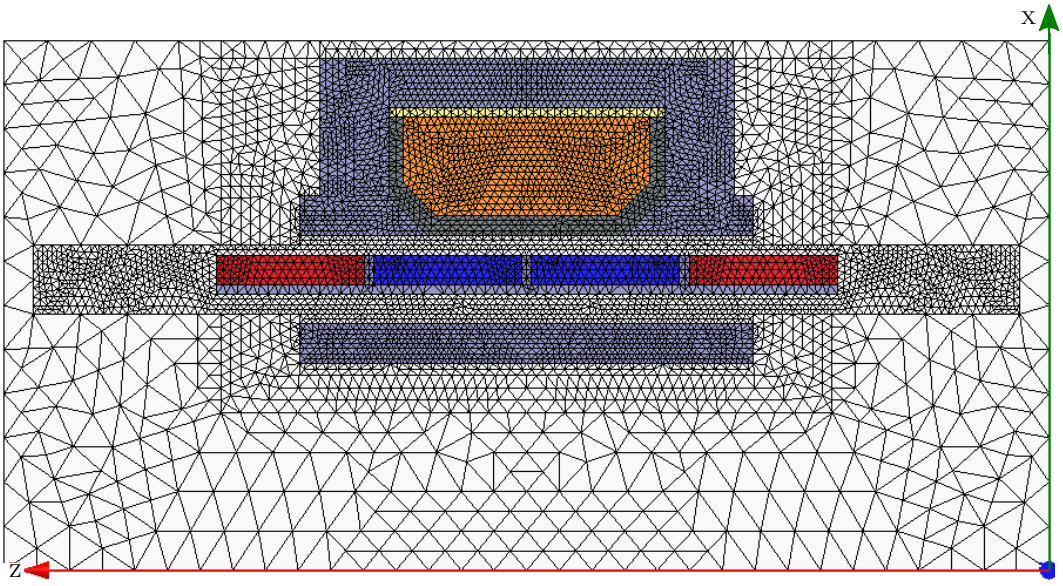

Figure C.2: Triangular meshing setup applied to the two-dimensional model geometry, showing the progressive mesh refinement from the air boundary towards the physical generator components

C.2. Boundary conditions

The principal model boundary conditions are briefly outlined as follows:

Balloon boundary
A finite modelling region was created to encapsulate the linear generator, to which Maxwell's 'Balloon Boundary' condition was applied. This allows stray magnetic fields to fringe infinitely across the boundary edges. Maxwell automatically defines a symmetry boundary condition at the symmetry edge of the balloon boundary, with the solution type set to 'Symmetric about Z-axis'.

Moving band
The moving band region encapsulates the four moving magnets to which Maxwell's 'Moving Band' boundary condition was applied. This was achieved by defining a 'Translation Motion Setup' in the positive Z-axis of model. A sinusoidal velocity profile v_p was defined for the moving band, and is given by:

$$v_p(t) = 2\pi f(x_p \cos(2\pi f t)) \tag{C.1}$$

where f is the frequency at which the magnet train reciprocates and x_p is magnet train displacement stroke amplitude, which was set to 10 mm. A 'Force Parameter' was defined to monitor the total magnetic force exerted by the moving magnets on the generator stators and was used to infer the open-circuit, closed-circuit and electromagnetic load force components.

Eddy effects
Maxwell's transient solver also allows the calculation of eddy current power losses. Because the prototype stator cores are not laminated, yet are subject to an alternating magnetic flux, eddy losses were included in order to predict a more realistic generator output power. A non-linear B-H curve for the mild steel stators was selected from Maxwell's built in materials library. Eddy losses are not expected for the aluminium plunger or phosphorous bronze power piston, since these components remain stationary relative to the magnets and are therefore not subject to significant rates of change in magnetic flux.

Coil and external load circuit
A 'Coil Excitation' boundary condition was applied to the copper coil and the 'Number of Conductors' (windings) was set to 70. A so-called 'Coil Winding' boundary condition was created for the coil, for which a prescribed voltage or current may be defined. To simulated open-circuit operation the coil current was set to zero. However, to simulate closed-circuit operation, a purely resistive 1 Ω load was attached across the coil terminals. This was achieved by creating a *.netlist* file of electrical circuit in *Maxwell Circuit Editor* and linking it to the coil winding as an externally defined boundary condition. The electrical circuit also accounts for the 350 mΩ internal coil resistance, which was determined from experimental investigation into the engine prototype.

C.3. Sample simulation results

Maxwell's 'Transient Magnetic' solver with 'Symmetry about Z-axis' was selected to simulate the operation of the generator. The default two-dimensional iterative solver was initialised, which employs a 'Backward Euler' time integration method with a non-linear solver residual of 1E-06. Simulations were performed by reciprocating the magnet train at operating frequencies ranging between 1 and 40 Hz. Simulation results obtained were mapped against magnet displacement, as shown in Chapter 4.3, thereby characterising the linear generator performance. For each operating frequency simulated, the solver's linear progressing time-step was set to 1/100 times the period of oscillation, with the final simulation time set to three times the oscillation time period.

Figure C.3 shows the simulated open-circuit and closed-circuit load voltages V_{OC} and V_L obtained when the magnet train oscillates at its design-specified frequency of 30 Hz. Also shown is the magnet train displacement, x_p. The closed-circuit voltage is seen to lag behind the open-circuit voltage due to the coil's internal inductance. A peak current of approximately 10 A flows through the 1 Ω load

The magnetic forces acting on the magnet train are shown in Figure C.4, as simulated for the open-circuit and closed-circuit conditions. The Lorentz electromagnetic force F_m induced by the current flow is determined by subtracting the open-circuit force from the closed-circuit force, $F_m = F_{CC} - F_{OC}$. The peak Lorentz force occurs when the magnet train crosses its inflection point at zero displacement, also moving at its peak velocity.

Figure C.5 compares the peak electrical power generated P_{gen} with the open-circuit and closed-circuit core losses. A considerable 50 W peak power dissipation loss

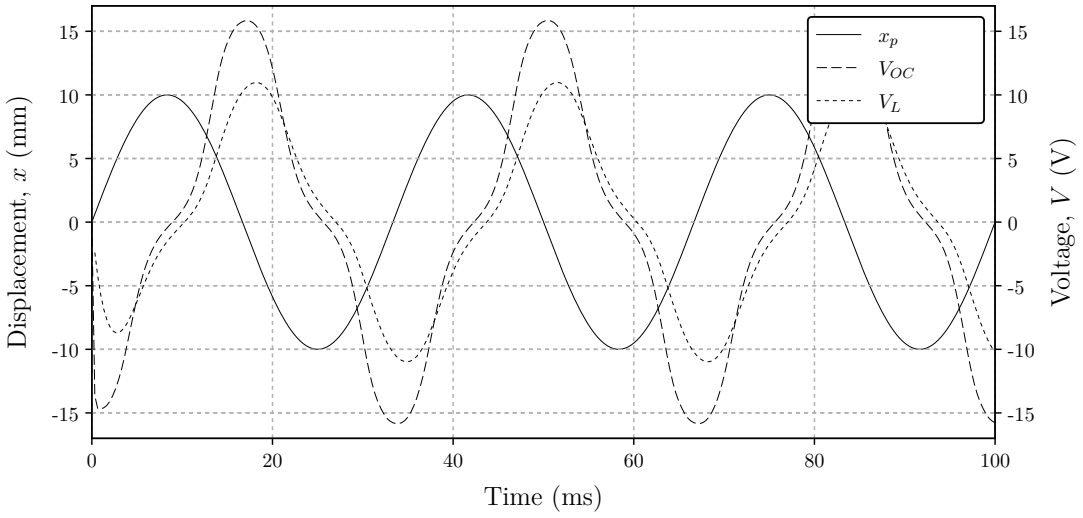

Figure C.3: Generator open-circuit voltage and closed-circuit load voltage over time, as simulated for operation at 30 Hz

occurs in the closed-circuit operation, as induced by swirling eddy currents inside the generator stators. A peak electrical power output of approximately 110 W_e is expected, but this could be increased to in the range of 160 W_e should the stator cores be laminated (and the eddy currents eliminated) in a refined design.

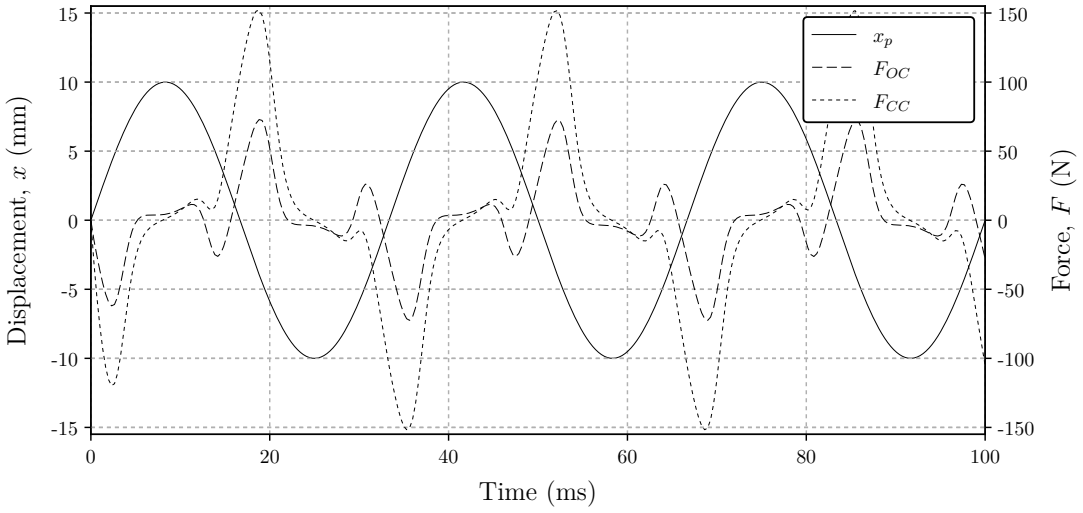

Figure C.4: Generator open-circuit and closed-circuit magnetic force over time, as simulated for operation at 30 Hz

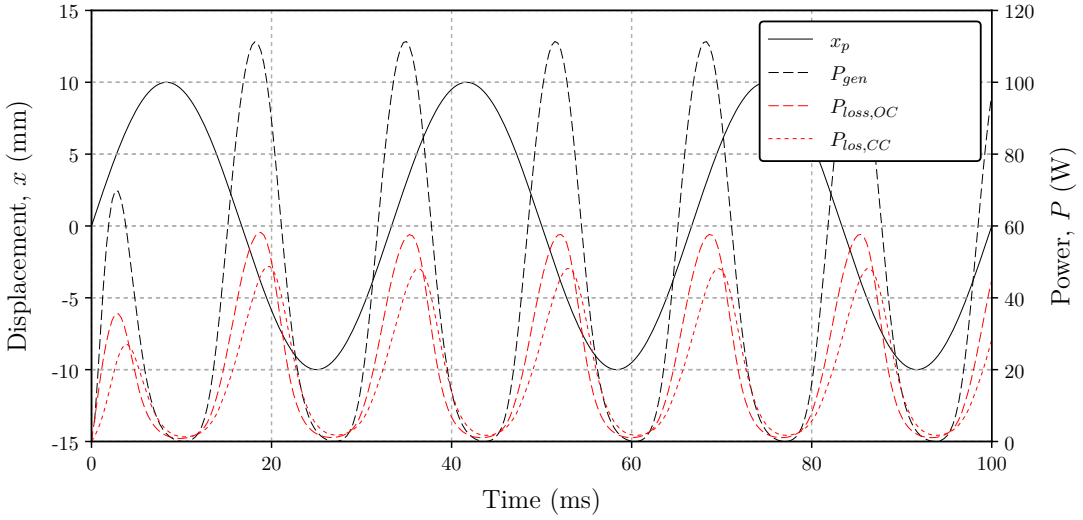

Figure C.5: Electrical power delivered to a 1 Ω load over time, with the predicted open-circuit and closed-circuit core losses

D. Engine geometry

As an extension of Table 5.1 in Chapter 5, this appendix provides a more complete list of the engine geometry and design parameters.

Table D.1: Engine design parameters

Parameter		**Unit**
Heater		
Heat exchanger type	Axially aligned fins	
Fin length	35	mm
Fin base inner diameter	62	mm
Fin base outer diameter	65	mm
Fin tip inner diameter	54	mm
Fin thickness	0.72	mm
No. of fins	135	–
Cross-sectional flow area	389.56	mm^2
Channel void volume	13.63	cm^2
Heat transfer surface area	412.08	cm^2
Material	copper	–
Regenerator		
Heat exchanger type	Wire screen HX	–
Canister length	34.5	mm
Canister outer diameter	63	mm
Canister inner diameter	56	mm
Mesh type	Winder mesh-60 twill screen	–
Macroscopic void fraction	77.8	%
Cross-sectional flow area	509.2	mm^2
Canister void volume	17.57	cm^3
Heat transfer surface area	1251.34	cm^2
Material	copper	–
Cooler		
Heat exchanger type	Axially aligned fins	–
Fin length	36	mm
Fin base inner diameter	62	mm
Fin base outer diameter	65	mm
Fin tip inner diameter	56	mm
Fin thickness	0.7	mm
No. of fins	135	–
Cross-sectional flow area	389.56	mm^2
Channel void volume	10.52	cm^2
Heat transfer surface area	326.66	cm^2
Material	copper	–

Table D.1: Engine design parameters

Parameter		Unit
Water cooling jacket		
Heat exchanger type	Radially spiralled fins	–
Fin base inner diameter	71	mm
Fin base outer diameter	77	mm
Fin tip outer diameter	91	mm
Jacket outer diameter	95	mm
Jacket length	36	mm
Fin pitch	4	mm/rot
Fin thickness	2	mm
Heat transfer surface area	37605	mm^2
Material	aluminium	–
Piston		
Bore diameter	30	mm
Piston diameter	29.94	mm
Piston hole diameter	10.025	mm
Length	98	mm
Mass (incl. magnet plunger)	0.952	kg
Spring stiffness	24610	N/m
Displacer		
Bore diameter	48	mm
Displacer diameter	47.90	mm
Shaft diameter	10	mm
Dome length	93	mm
Shaft length	166.5	mm
Mass (incl. shaft)	0.526	kg
Spring stiffness	20019	N/m
Expansion space		
Displacer-casing-distance at mid-stroke	13.7	mm
Add. manifold void volume	11.806	cm^3
Compression space		
Displacer-step-distance at mid-stroke	13.7	mm
Piston-step-distance at mid-stroke	11	mm
Add. Manifold void volume	7.609	cm^3
Backspace		
Casing diameter	135	mm
Casing length	238.5	mm
Volume of backspace components	1443.43	cm^3

E. Sensor setup and calibration

This appendix presents the setup and calibration of the test measurement sensors. Referring to Figure 6.10 on page 94, measurement sensors include the pressure transducers, thermocouples and strain gauges. In order to calibrate the strain gauge sensors for displacement measurement, the displacer and piston flexure springs stiffness's were first determined. Thereafter a block layout diagram of the measurement sensors and data acquisition instrumentation is given. Calibration coefficient for the strain gauges, pressure sensors and thermocouples are lastly presented.

E.1. Flexure stiffness evaluation

The force-displacement relationship of the flexures springs were determined experimentally in a compression test, performed on a *MTS Criterion Universal Test Machine* (model 445) using a 30 kN load cell (MTS LPS 304). This test also served to calibrate the strain gauge voltage measurements to spring displacement.

The measured force-displacement curves of the displacer and piston flexure springs are shown in Figure E.1. A linear trend line was fit through the data, of which the gradient represents a constant spring stiffness. The springs show a slight non-linear behaviour, especially noticeable at displacements greater than 8 mm, resulting due to twisting in the flexure spring legs. However, for the design-specified displacement operating range of 10 mm, this is insignificant. The strain gauge sensors are calibrated for displacement in the following section, after describing the instrumentation layout.

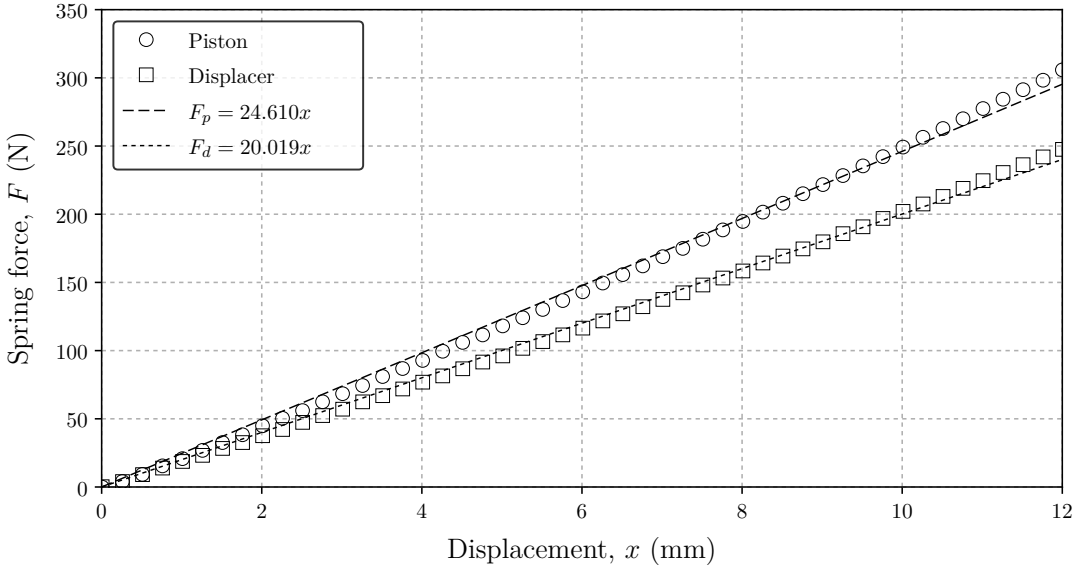

Figure E.1: Flexure springs force-displacement curves

E.2. Instrumentation layout

National Instruments (NI) data acquisition (DAQ) devices were used to record the thermocouple temperature measurements, for which the average hot-end temperature measurement $T_{h,avg}$ formed an input signal to the electric heater controller. An HBM QuantumX universal amplifier was used to record the flexure springs displacements, working space pressure variation and terminal voltages of the linear generator and motor. Table E.1 gives the specifications of the measurement instrumentation that were used.

Figure E.2 depicts a block layout diagram of the measurement sensors and data acquisition devices used throughout the study. As shown, the temperature measurements were recorded with the NI-9123 thermocouple card embedded in a cDAQ-9184 chassis (Serial number 19045B-01). An HBM QuantumX MX840A was used to record the flexure springs strains, pressure variation and generator terminal voltages. Both the NI cDAQ and QuantumX were connected to a network switch so that a single RJ45 ethernet connection could be made to a measurement computer, located at a safe distance from the experiment. As has been discussed in Chapter 6.3, a NI USB-6009 DAQ was employed as a feedback controller for the electrical heater. To log temperature measurements and to control the electric heater operation, National Instruments' *LabView 2015* was used. HBM's *catmanEasy 4.1* software was

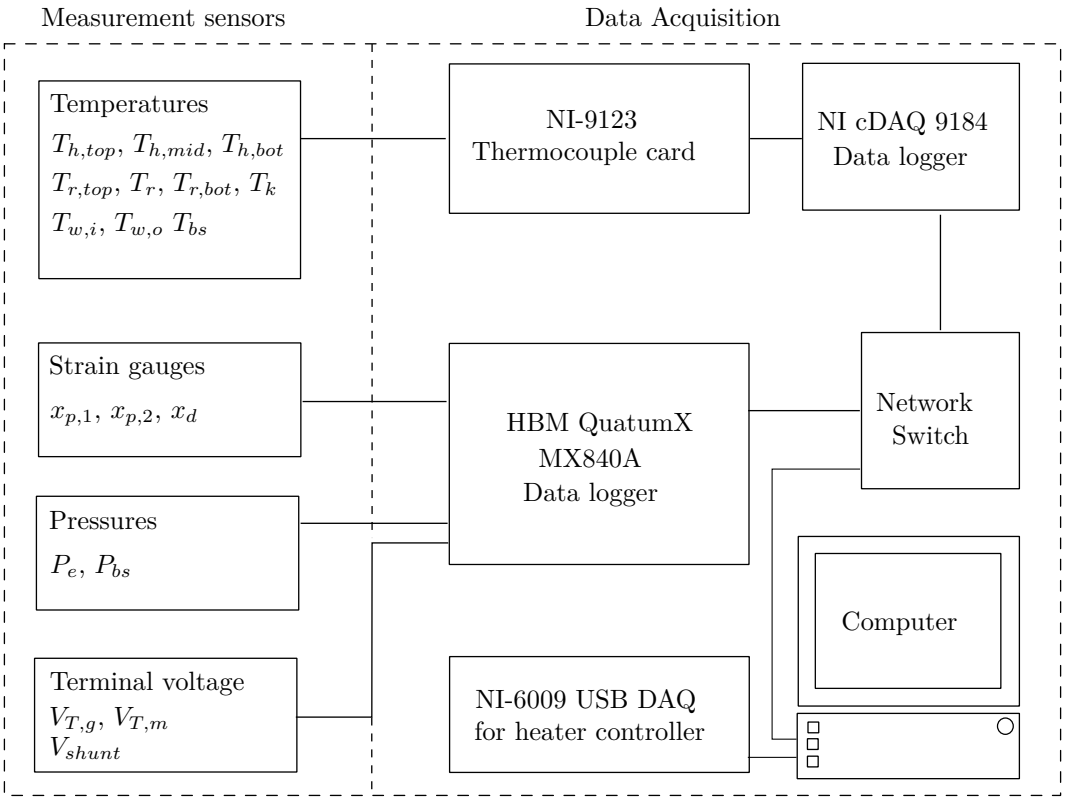

Figure E.2: Block layout diagram, showing how the measurements sensors and data acquisition instrumentation were connected to a central data logging computer

Table E.1: Measurement instrumentation specifications

	NI-9213	**HBM QuantumX MX840A**	**NI-6009 USB**
Description	16-Channel, 24-bit thermocouple input module with 0.77 °C measurement accuracy	8-Channel universal data acquisition and amplifier device	14-Bit multifunctional data acquisition and analog output device
Signals measured	Thermocouples	Pressure transducers, strain gauges, generator and motor terminal voltage	Heater controller (ON/OFF analog output)
Serial number	198854C-01L-19B8F07	009E50038A2	196FAD0
Sampling rate	0.5 Hz	2400 Hz	10 Hz
Active filtering	No	Yes, 120 Hz low-pass filter with phase correction applied to strain gauge measurements in results post-processing	No

used to record the strain gauge, pressure and terminal voltage measurements obtained from the QuantumX. No active filtering was applied to the measured signals during experimental testing. However, in the post-experimental results processing, a 120 Hz low-pass Butterworth filter was applied to the strain gauge measurements with phase correction, to reduce the piston-collision induced measurement noise.

E.3. Sensor calibration

This section discusses the calibration procedures of the strain gauge, pressure transducer and thermocouple measurement sensors.

E.3.1. Strain gauge displacement calibration

The voltage measurements of the half-bridge strain gauges were calibrated to cross-head displacement in the same compression test used to determine the flexure spring stiffness. As shown in Figure 6.5 on page 87, a half-bridge setup is comprised of two HBM type L11-Y1 strain gauges mounted on the opposing sides of the flexure spring to record pure bending. The power piston flexure spring contains two sets of half-bridged strain gauges (with displacements x_{p1} and x_{p2}), whereas the displacer flexure spring only has one. The QuantumX was used to amplify (using a 1 V excitation voltage) and record the strain gauge sensitivity at different cross-head displacements, as shown in Figure E.3.

The calibrated flexure spring displacements are given as a function of strain gauge sensitivity by the three second-order polynomials (with $R^2 > 0.99$):

$$\begin{aligned} x_{p1} &= -5.9827v^2 + 19.09v + 0.0877 \\ x_{p2} &= -9.601v^2 + 25.411v + 0.0288 \\ x_d &= -14.104v^2 + 28.588v + 0.1617 \end{aligned} \tag{E.1}$$

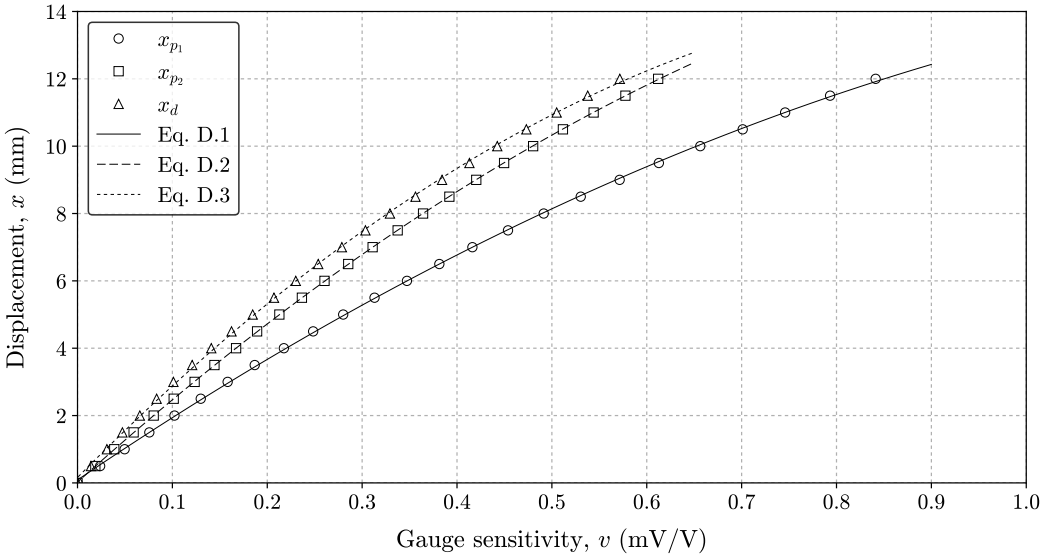

Figure E.3: Strain gauge calibration curve, depicting displacement as a function of gauge sensitivity

where v is the gauge sensitivity, measured in millivolts per voltage excitation, and x is the displacement in millimetre. The relations were reflected about the X- and Y-axis in order to determine negative displacements.

E.3.2. Pressure transducer calibration

Two Wika S-20 pressure transducers, with specifications given in Table E.2, were used to measure the variations in expansion space and backspace working fluid pressure. The pressure transducers were imported from Germany with certified calibration certificates, reporting an error band of ±0.5 % due to non-linearity over the transducer's span at the calibrated temperature range of 25 °C. However, as the temperature of the working fluid at the thin-film dome is likely to be in the range of 30 to 80 °C, an additional ±1.0 % of span measurement error can be expected

Table E.2: Pressure transducer specifications

	Expansion space pressure transducer, P_e	**Backspace pressure transducer**, P_{bs}
Manufacturer	Wika	Wika
Model	S-20 with cooling fin, 3-wire 0-10 V signal	S-20, 2-wire 4-20 mA signal
Serial number	1A00EG2WH2K	1A00BT98A26
Measurement range	0 - 40 bar gauge	0 - 25 bar gauge
Non-linearity	±0.5 % of span	±0.5 % of span
Temperature error	±1.0 % of span	±1.0 % of span
Settling time	1 ms	1 ms
Data capture equipment	HBM QuantumX MX840A	HBM QuantumX MX840A
Sampling rate	2400 Hz	2400 Hz
Active filter	None	None

according to the transducers' data sheets. If sensor drift and signal hysteresis is neglected (as typically being below 0.1 %, the total error as a percentage value of transducer span is then given by (H.M. Hashemian and Jin Jiang, 2009):

$$\text{Tot. error} = \sqrt{(0.5)^2 + (1.0)^2} = 1.18\% \text{ of span} \tag{E.2}$$

For the expansion space transducer this relates to an error band of ±45 kPa and ±30 kPa for the backspace. It must be noted however that as the thin-film traducers used apply internal signal conditioning (i.e. filtering), the measured pressure signal does not vary between the upper and lower error band limits (i.e. the measured signal represents the effective linear average between these two bounds).

In Table E.3 the transducer calibration coefficients a and b are given, along with their coefficients of determination R^2. The experimentally measured (actual) pressure is related to the calibrated traducer output signal S, by:

$$P_{actual} = (S - b)/a \tag{E.3}$$

Table E.3: Pressure transducer calibration coefficients

Transducer signal, S	a	b	R^2
S_e (V)	0.2499	-0.0089	0.9997
S_c (mA)	0.6404	4.0047	0.9998

E.3.3. Thermocouple calibration

Referring to Figure 6.10 on page 94 , K-type thermocouples were used to measure the average heater head temperature and thermal gradient between the heater and cooling jacket. The cooling water inlet and outlet temperatures were measured using T-type thermocouples. As depicted in Figure E.2 the thermocouple lead wires were connected to a NI-9213 thermocouple card, embedded in the NI cDAQ-9184 chassis. Table E.4 lists the instrumentation that were used to calibrate the thermocouples over their expected operating ranges. An ISOTECH platinum resistance thermometer (serial number 191069) was used as reference temperature T_{ref} for the lower temperature measurements (between 5 and 120 °C) of the FLUKE 9142. For the higher temperature measurements (between 150 and 600 °C), the FLUKE 9150's on-screen temperature indication was used as reference.

Figure E.4 shows the calibration curves for two of the thermocouples probes. The hot-end thermocouple $T_{h,top}$ was calibrated using the FLUKE 9150 Thermocouple Furnace, whereas the cold-side thermocouple T_k was calibrated using the FLUKE 9423 Field Metrology well and ISOTECH thermometer. For each of the respective thermocouples a linear trend line was fit through the calibration data in order to represent the relation between measured and reference temperature, with trend line constants and coefficients of determination listed in Table E.5. The *actual* temperature is determined from the *measured* temperature and straight line calibration constants a and b using a similar calibration equation as Equation (E.3).

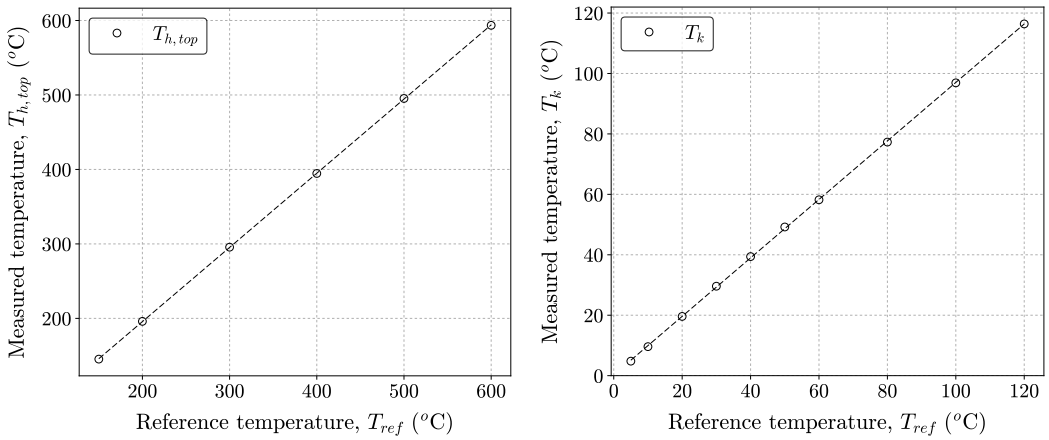

(a) **(b)**

Figure E.4: Sample thermocouple calibration curves of (a) $T_{h,top}$ and (b) T_k

Table E.4: Thermocouple calibration equipment

Instrument description	**Calibrated range**	**Thermocouples**	**Accuracy**
Heart Scientific FLUKE 9142 Field Metrology well	5 to 120 °C	T_k, $T_{w,i}$, $T_{w,o}$, T_{bs}	T-Type, ±0.5 °C or ±0.4 %
Heart Scientific FLUKE 9150 Thermocouple Furnace	150 to 600 °C	$T_{h,top}$, $T_{h,mid}$, $T_{h,bot}$, $T_{r,top}$, T_r, $T_{r,bot}$	K-Type, ±1.5 °C or ±0.4 %
ISOTECH Platinum Resistance Thermometer 931472	5 to 120 °C	T_{ref}	reference

Table E.5: Thermocouple calibration coefficients

Thermocouple sensor (S), T (°C)	a	b	R^2
$T_{h,top}$	0.987	-3.554	>0.99
$T_{h,mid}$	0.986	-3.231	>0.99
$T_{h,bot}$	0.987	-3.656	>0.99
$T_{r,top}$	0.983	-3.430	>0.99
T_r	0.973	-2.830	>0.99
$T_{r,bot}$	0.977	-4.302	>0.99
T_k	0.967	0.267	>0.99
$T_{w,i}$	0.965	0.393	>0.99
$T_{w,o}$	0.963	0.539	>0.99
T_{bs}	0.971	0.439	>0.99

F. Heater performance test

This appendix presents a thermal performance test of the electrical heater and accompanying controller – in which the heater was subjected to different set-point temperatures and the axial heat losses through the engine casing quantified.

The electrical heater and controller was tested with the engine casing depressurised and the internal engine components removed. The test was performed to investigate whether the average hot-end temperature $T_{h,avg}$ could safely be limited to a set-point temperature, and to quantify the axial conductive heat loss in the engine casing. During testing the set-point temperature was adjusted from 300 to 600 °C in steps of 100 °C, with temperature measurements shown in Figure F.1. The ripple in hot-end temperature observed about the set-points occur as the electric heater is switched on/off by the National Instruments USB-6009 DAQ controller in an effort to keep the hot-end temperature constant, as described in Chapter 6.3 on page 88.

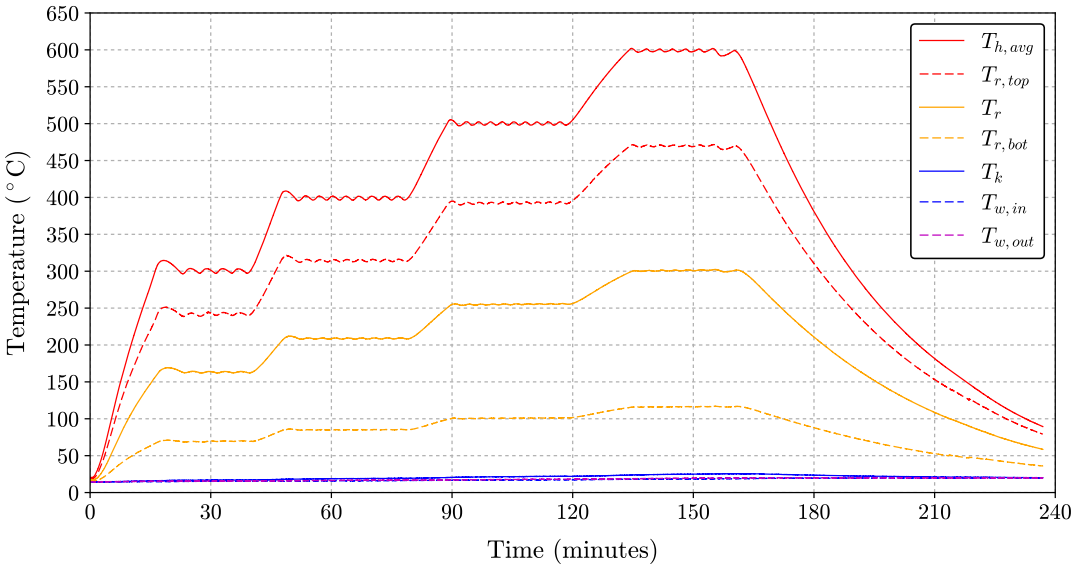

Figure F.1: Temperature measurements recorded in the heater control test, with set-point temperatures varying between 300 and 600 °C

As shown in Fig. F.1, an approximately linear temperature profile is seen between the hot-end $T_{h,avg}$ and cold-end T_k, resulting due to axial conductive heat transfer in the engine casing wall. A heat-up period of 18 minutes is required to reach the first set-point temperature of 300 °C from cold start-up. When the set-point temperature is increased from 500 °C to 600 °C – in the temperature range at which the engine is planned to operate – the heater requires a approximately 15 minutes to reach its new thermal equilibrium, despite only increasing the hot-end temperature by 500 °C.

This more sluggish thermal response of the heater is indicative of large heat losses that become significant at elevated hot-end temperatures.

The axial conduction heat loss from heater to cooler may be estimated from the steady-state conduction equation, given by:

$$\dot{Q}_{cond} = kA_x \frac{(T_{r,top} - T_{r,bot})}{l_r} \tag{F.1}$$

where $T_{r,top}$ is the temperature at the bottom of the heating channel (at the top of the regenerator channel), $T_{r,bot}$ is the temperature at the bottom of the regenerator channel and l_r the length of the regenerator channel. The axial condition heat loss was compared to the steady-state heat rejection rate of the water cooling jacket, as determined from the energy balance equation:

$$\dot{Q}_{rej} = \dot{m}_w C_{p,w}(T_{w,o} - T_{w,i}) \tag{F.2}$$

where $\dot{m}_w$ is the water mass flow rate in kg/s and $T_{w,o}$ and $T_{w,i}$ the respective outlet and inlet water temperatures. The average axial conduction heat loss rates and average cooler heat rejection rates are given in Table F.1 for hot-end temperatures of 400, 500 and 600 °C respectively. The heat losses determined from the conduction equation are shown to correlate reasonably well to that rejected by the cooling jacket. At a hot-end temperature of 600 °C, approximately 350 W of thermal heat loss occurs by axial conduction in the engine casing and is rejected by the water cooling jacket. This makes up a significant 35.7 % of the 1.0 kW heater thermal capacity, also subjecting the water cooling jacket to a permanent load even when the engine is not being operated.

Table F.1: Engine casing conductive heat losses at different set-point temperatures

	400 °C	500 °C	600 °C	[Units]
Coolant mass flow rate, $\dot{m}_c$	0.0917	0.0917	0.0917	kg/s
Coolant inlet temperature, $T_{w,i}$	15.88	16.98	18.53	°C
Coolant outlet temperature, $T_{w,o}$	16.44	17.71	19.46	°C
Conduction heat loss rate, Eq. F.1	202	265	332	W
Cooler heat rejection rate, Eq. F.2	215	280	357	W

In addition to the heat loss through the casing wall, when the engine is assembled, conductive heat losses occur through the internal heat exchanger channels (heater, regenerator and cooler), displacer bore and displacer wall. It is postulated that due to the relative thickness of the displacer bore and displacer wall in relation to the axial flow channel width, these heat losses may be as significant. However, for risk of damaging the engine internals, this heat loss was not investigated prior to operating the prototype and is only discussed in Chapter 7.4, after conducting a range of operational tests.

G. Supplementary verification tests

This appendix presents two supplementary tests that were performed to partially verify the theoretical simulation model. Firstly, the free vibration response tests were used as a way of verifying the behaviour of the theoretical model. Secondly, the power piston was electrically driven and the resulting pressure variation and displacer motion (as induced by the pressure variation) was used to verify experimentally determined displacer friction and empirically related regenerator friction factor.

G.1. Verification by free vibration response

The theoretical model was partially verified by comparing the experimentally determined free vibration response of the power piston and displacer against simulation results with identical setup parameters. The model was simulated with the experimentally determined mechanical friction forces derived in Chapter 7.1.

Fig. G.1 compares the experimentally determined displacement-time response of the power piston assembly against that of the simulated response. To simulate this behaviour, the power piston assembly was given an initial velocity of 1.4 m/s and was subjected to the experimentally determined piston damping force of 77.4 N s/m. It is seen that the simulation results and behaviour are in good agreement with the experiment, thereby validating the free vibration behaviour of the model. However, as discussed in Appendix G.2, this considerably large damping load is only valid for small piston velocities, as it does not account for any reduction in piston friction by

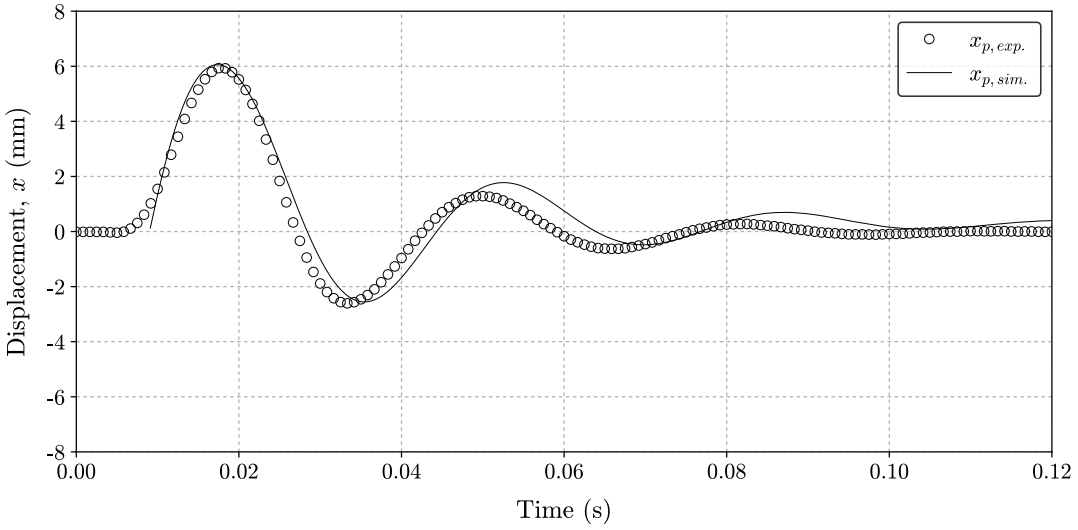

Figure G.1: Comparison between experimental and simulated displacement-time of the power piston, as subject to an impulsive load

the piston-induced dynamic gas bearing.

Figure G.2 shows the experimental and simulated free vibration displacement-time response of the displacer. To simulate this behaviour the displacer was given an initial velocity of 1.5 m/s and was subject to a Coulomb friction force of 1.74 N opposing the displacer motion. The skin coefficient of friction within the heater, regenerator and cooler channels was set to 0.01 in the theoretical model so that the displacer shuttling losses would become negligent and thereby representative of the conditions in which the experiment was performed. The good agreement between the simulation and experimental data validates the non-linear free vibratory response of the simulation model.

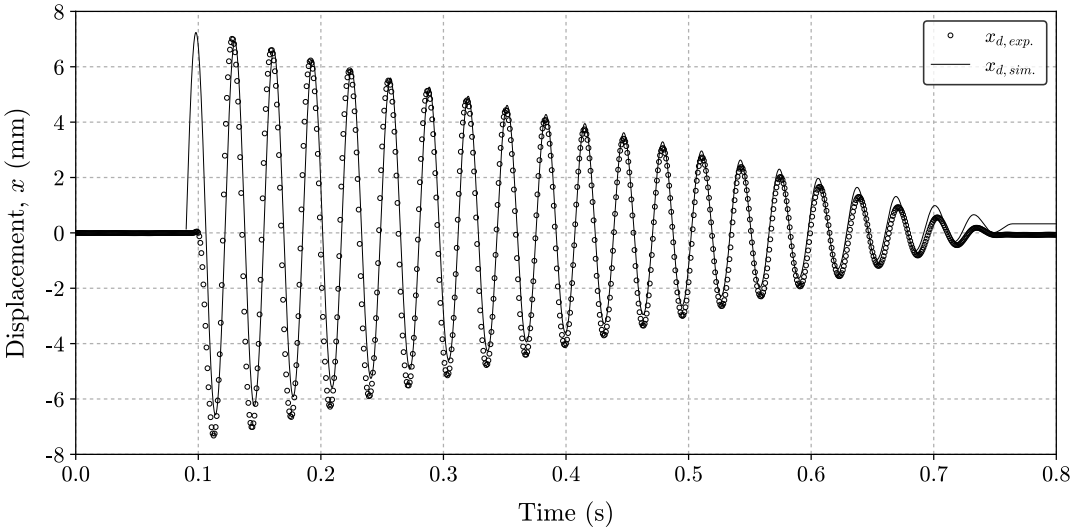

Figure G.2: Comparison between experimental and simulated displacement-time response of the displacer, as subject to an impulsive load

G.2. Verification by piston reciprocation

The theoretical simulation model was partially verified by electrically reciprocating the power-piston and in so doing induce a pressure variation in the working fluid (gas). The induced pressure variation was compared to a simulated case using identical setup parameters. From this experiment the resonant frequency of the as-assembled displacer was verified, and by comparing the experimental and simulated displacer stroke's, displacer and regenerator friction factors were also verified. The experiment also served to refine the power-piston friction force (listed in Table 7.1 on page 97).

The FPSE prototype was fully assembled as shown in Fig. 6.10 of page 94 and pressurised with helium gas to a charge pressure of 1.18 MPa (absolute). For this experiment the electrical heater and cooler were not used. The linear generator coil terminals were connected to a Ling Dynamics PA100WA sine-wave generator and

amplifier, thereby inverting the generator to function as a linear motor for the power piston.

The power piston was electrically driven at frequencies ranging from 28 to 32 Hz with a motor excitation voltage of 10 V (current limited to 10 A by the PA100WA amplifier). The piston-induced pressure variation in the working fluid acts on the displacer shaft and leads to displacer resonance. From trial-and-error the maximum displacer stroke, and thus the displacer's resonating frequency, was obtained at a piston excitation frequency of 30.35 Hz, where in contrast the piston's resonant frequency is closer to 28 Hz. This piston-driven behaviour was emulated by simulating a 10 V sinusoidal voltage boundary condition across the linear generator terminals, V_T, with current given by:

$$i^{t+\Delta t} = i^t + \frac{\Delta t}{L_{coil}}(V_T - i^t R_{coil}) \tag{G.1}$$

where L_{coil} is the generator coil inductance and R_{coil} its internal resistance.

Figure G.3 shows that the experimental displacement of both displacer and power piston agree well to that of the simulated case. This partially verifies that the displacer friction force identified from the free vibration test in Figure 7.1 (b) on page 96, and the empirically related regenerator friction factor used, given by Equation (3.58) on page 41.

However, the power piston friction, represented in Figure 7.1 (d) as a form of viscous damping, is not well matched as it over-damps the piston displacement. In contrast to the 77.4 N s/m calculated from the free vibration response test, the simulated piston displacement correlates best with the experimental results if a refined value of 55 N s/m is simulated. It is hypothesised that this noticeable decrease in piston friction is a result of the dynamic gas 'cushion' created between the piston and bore-cylinder wall when the piston is reciprocating. This so-called *dynamic gas bearing*

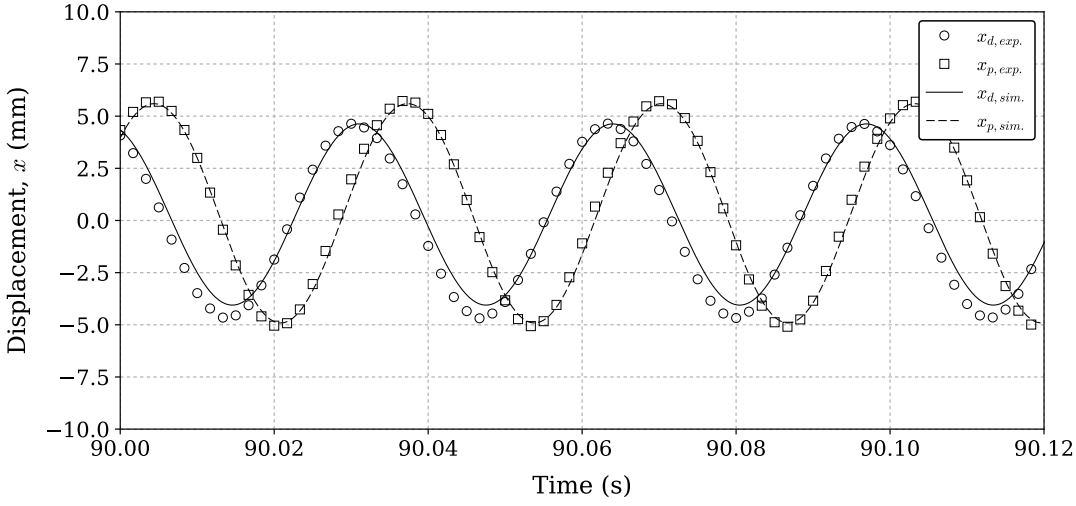

Figure G.3: Experimental and simulated displacer and piston displacements

acts to centre the power-piston in its bore, in-turn leading to a reduction in the strong side-load forces of the magnet train that, in the first place, is postulated to have induced the considerable piston damping force shown in Fig. G.1.

Correlating to the displacement graph, from Figure G.4 it is seen that the simulated pressure variation in the expansion space P_e over-predicts the experimental results by approximately 27 kPa. This may be attributed to the combined effects of un-accounted for dead-space in the working space, additional dead-space and friction pressure drop in the pressure traducer cooling fin channel, and larger gas leakage rates to the backspace. It may also be postulated that the 4 MPa-rated WIKA S-20 pressure transducer used to record the experimental pressure variation is insensitive to capturing the peaks in pressure in this lower range.

The overall good correlation between the simulated and experimental behaviour, both in displacement and pressure variation, tends to verify the displacer mechanical friction, the regenerator friction relation and refines the linearised power piston friction. Should a stronger signal generator be used with current output exceeding the 10 A limit, verification of the power piston friction force may be extended to larger piston strokes.

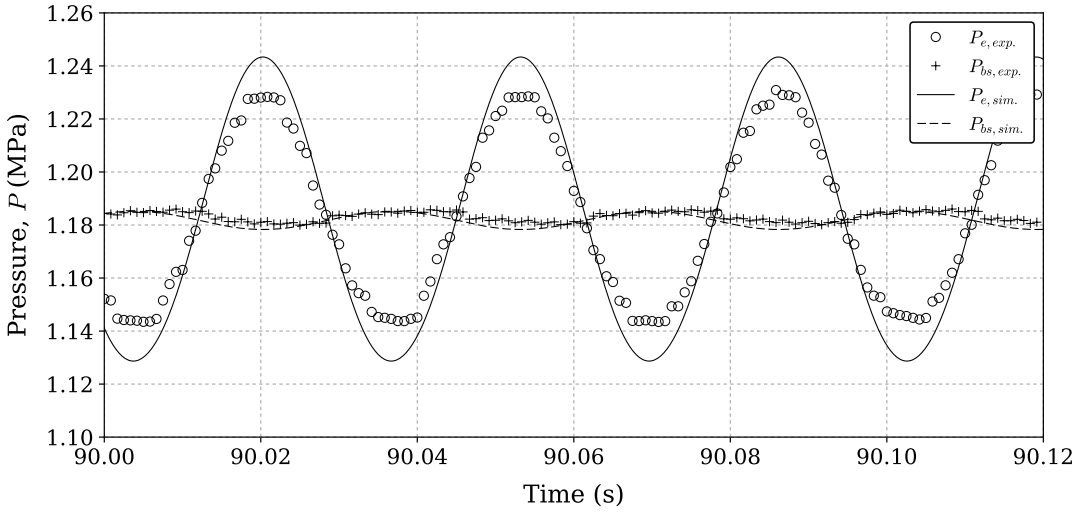

Figure G.4: Experimental and simulated pressure variation in the working space, as induced by reciprocating the power piston

H. Photographs of the prototype engine

This appendix provides photographs of the FPSE prototype's internal assembly, the generator reciprocator test setup and the assembled engine test layout.

H.1. Internal assembly

Figure H.1 gives a photograph of the internal assembly of the FPSE before experimental testing was commenced. The internally located engine components are assembled within and held together by an aluminium sleeved body that essentially acts as the internal 'skeleton' of the engine. In this photograph, however, the heater, cooler and regenerator heat exchangers were removed. The linear electric generator and flexure springs can be seen through the longitudinal slots in the body.

In Figure H.2, a photograph of the engine internal assembly is given with the aluminium sleeved body and displacer motor core removed. From this photograph the flexure spring strain gauges and internal engine wiring are visible, and so are the internally located heater and regenerator heat exchangers. Figure H.3 gives a photograph of only the displacer and power piston assemblies with the engine main body and linear generator core having been removed.

Figure H.1: Internal engine assembly that is held together by the aluminium sleeved body, as seen with the removable of the pressure retaining engine casing

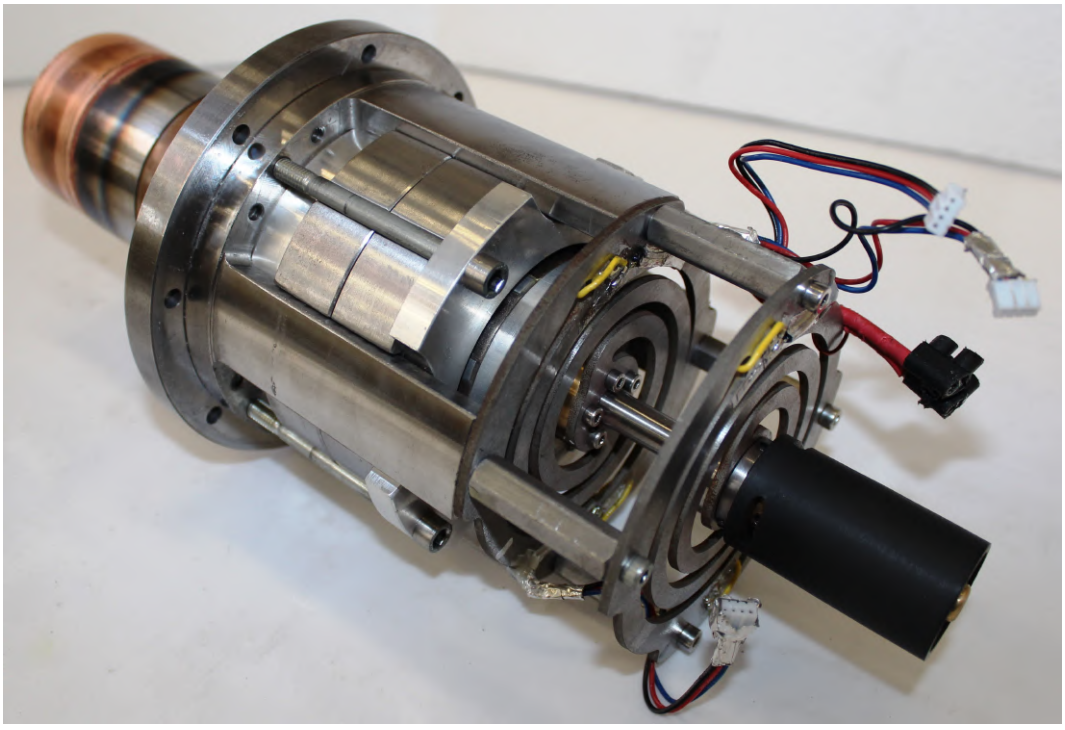

Figure H.2: Internal engine assembly, as seen with the removal of the aluminium sleeved body and the displacer motor core

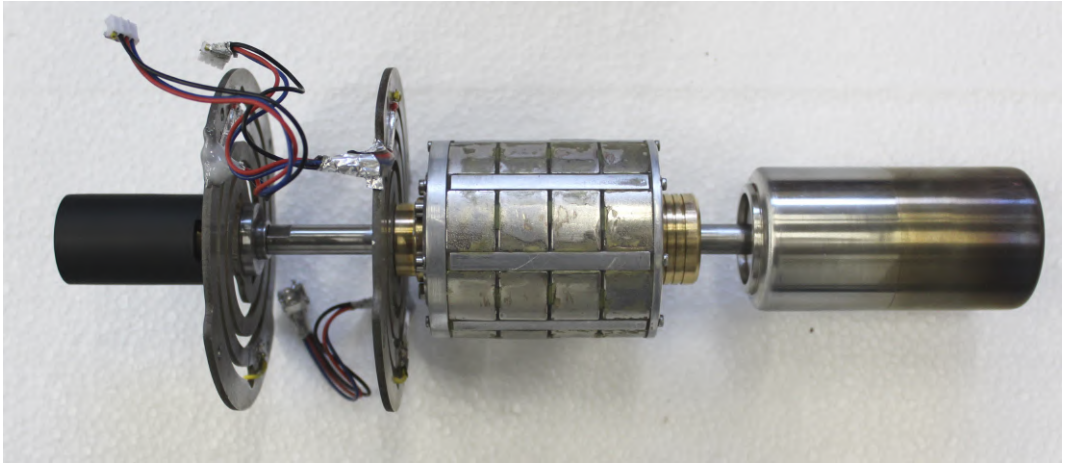

Figure H.3: Isolated view of the displacer and power piston assemblies

H.2. Main body and generator assembly

In Figure H.4, the disassembled engine 'main body' and linear generator core is shown. The flexure legs bolt onto the flanged main body; the linear generator core then assembled between the four 'legs' by location fit. Figure H.5 depicts the power piston assembly before and after the glueing of the 32 arc magnets to the aluminium-sleeved plunger.

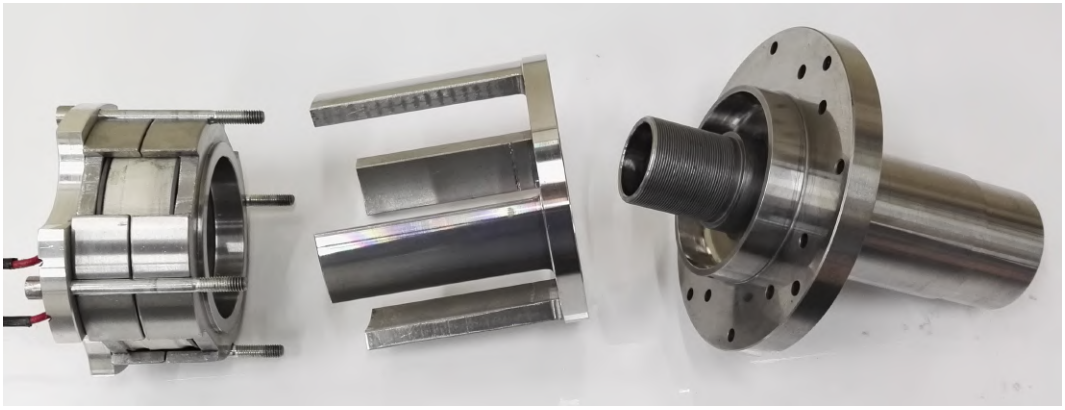

Figure H.4: Disassembled internal engine components, showing the linear generator core (left) , the flexure legs (centre) and the flanged main body with piston and displacer bores (right)

(a) **(b)**

Figure H.5: Power piston assembly, showing (a) the piston and magnet train plunger before assembly with arc magnets, and (b) the piston and magnet train after assembly and glueing of arc magnets (notice the relatively poor quality of assembly and glueing)

H.3. Generator reciprocator

Figures H.6 and H.7 show the linear generator assembled with the reciprocator, as was done to test the performance of the linear generator. Refer to the illustration in Figure 7.4 on page 100 for a components description.

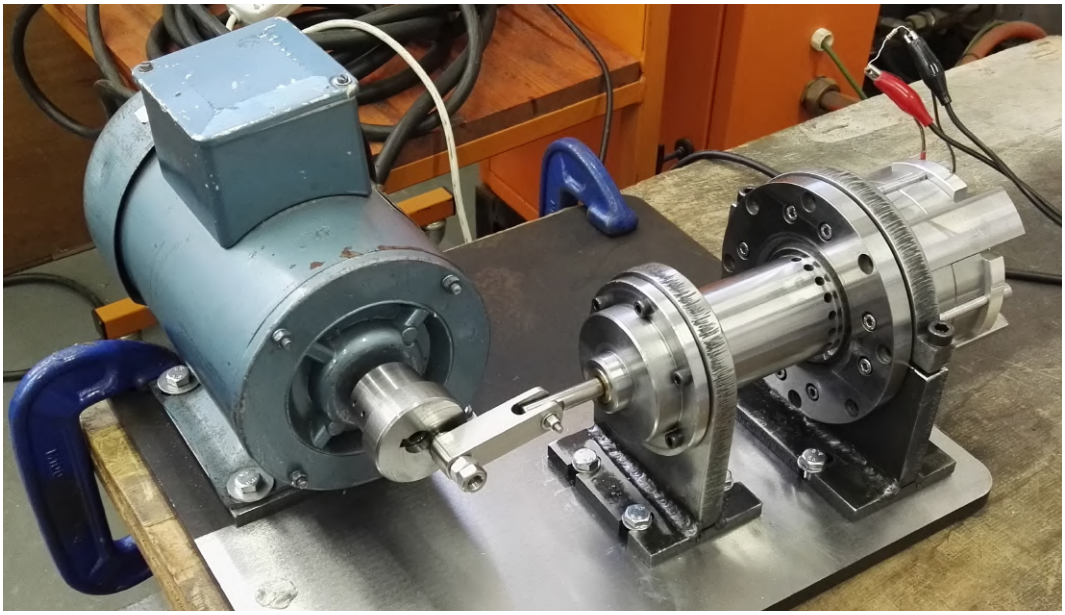

Figure H.6: Main body and linear generator as assembled with the reciprocator, to emulate and test the operation of the linear generator

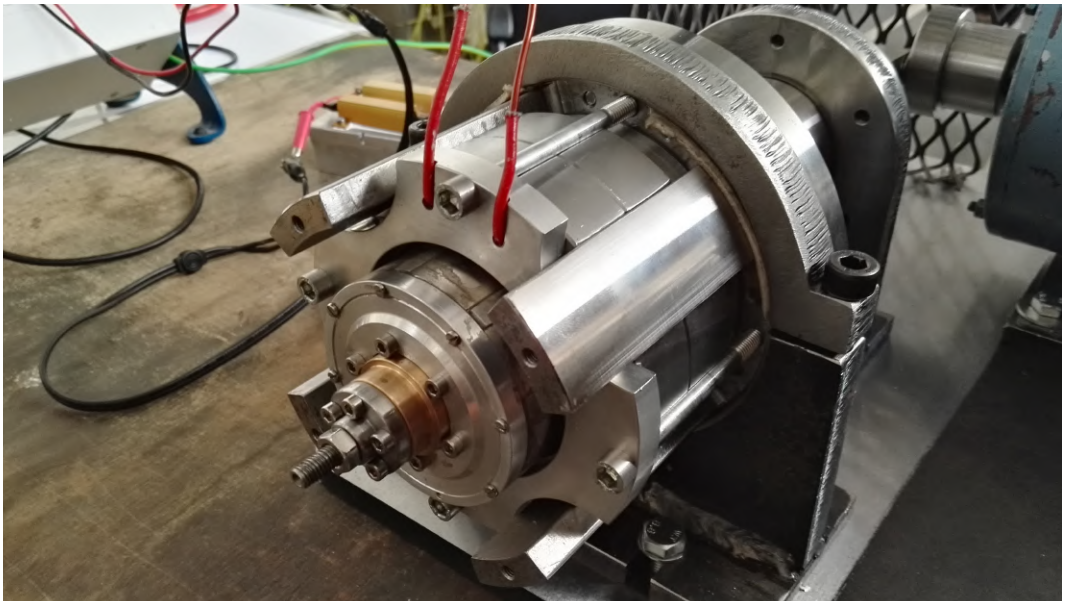

Figure H.7: Photograph showing the back view of the power piston and magnet train assembly, as assembled to the linear reciprocator

H.4. Assembled engine and test stand

During experimental operation the assembled engine prototype was covered by a 'safety blast cage' as shown in Figure H.8. This so-called blast cage was clamped to the steel frame of the engine test bed, with instrumentation wiring passing underneath. A ventilation fan is attached to the top cover of the blast cage to cool the electronic sensor component of the expansion space pressure transducer. The engine was pressurised and depressurised manually via a pressure purge line, of which the connecting engine tubing is barely visible in this figure. Then, during engine testing, operating parameters including the generator load, hot-end temperature and displacer motor excitation voltage were controlled from a safe operating distance.

Figure H.8: Blast cage in which the assembled prototype engine was operated

Figure H.9 shows the insulated hot-end with a secondary ventilation fan located in the side-wall of the blast cage to limit the pressure transducer from overheating. Figure H.10 shows the bottom pressure transducer and two of the three sensor feed-through plugs that pass through wiring from the backspace.

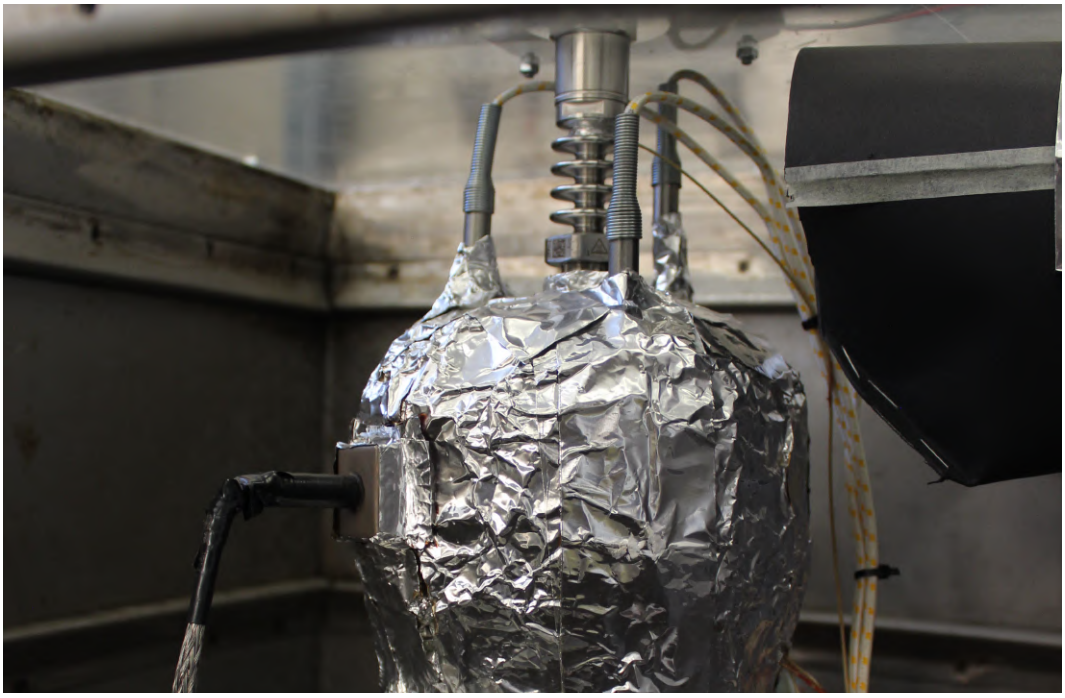

Figure H.9: Photograph showing the insulated hot-end and the forced-air ventilation duct used to cool the pressure transducer

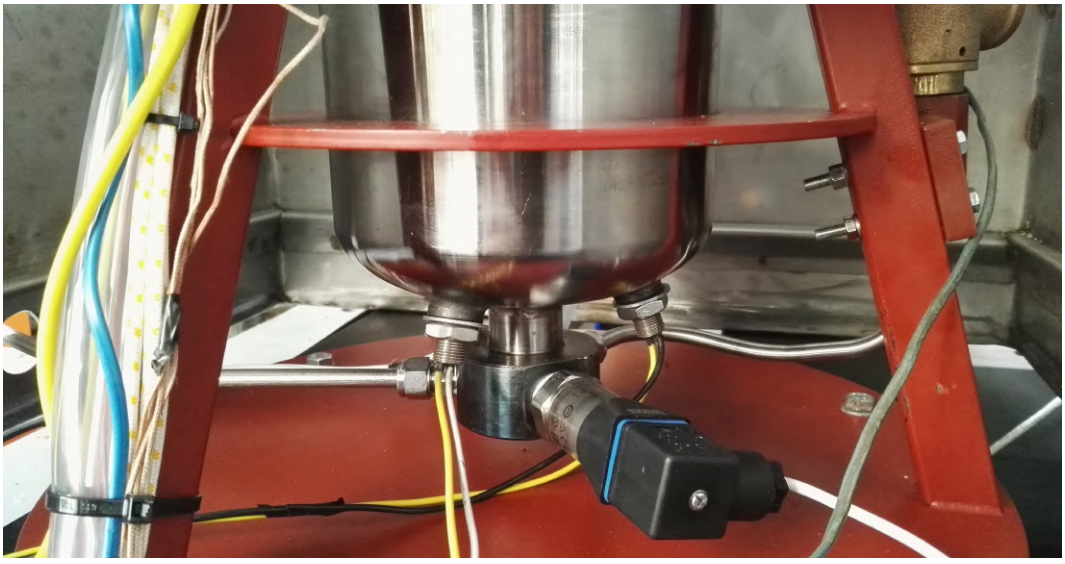

Figure H.10: Photograph of the bottom pressure transducer, also showing two of the three wire feed-through plugs